Site U1351[1]

Expedition 317 Scientists[2]

Chapter contents

Background and objectives

Hole U1351A

Position: 44°53.0307′S, 171°50.4037′E
Start hole: 0931 h, 18 November 2009
End hole: 2330 h, 18 November 2009
Time on hole (d): 0.58
Seafloor (drill pipe measurement from rig floor, m DRF): 133.3 (APC mudline)
Distance between rig floor and sea level (m): 11.0
Water depth (drill pipe measurement from sea level, m): 122.3
Total depth (drill pipe measurement from rig floor, m DRF): 161.3
Total penetration (m DSF): 28.0
Total length of cored section (m): 28.0
Total core recovered (m): 27.3
Core recovery (%): 98
Total number of cores: 6

Hole U1351B

Position: 44°53.0422′S, 171°50.4065′E
Start hole: 2330 h, 19 November 2009
End hole: 1800 h, 25 November 2009
Time on hole (d): 6.77
Seafloor (drill pipe measurement from rig floor, m DRF): 132.7 (APC mudline)
Distance between rig floor and sea level (m): 11.0
Water depth (drill pipe measurement from sea level, m): 121.7
Total depth (drill pipe measurement from rig floor, m DRF): 1163.3
Total penetration (m DSF): 1030.6
Total length of cored section (m): 1030.6
Total core recovered (m): 304.5
Core recovery (%): 30
Total number of cores: 116

Hole U1351C

Position: 44°53.0572′S, 171°50.4057′E
Start hole: 1800 h, 25 November 2009
End hole: 0200 h, 30 November 2009
Time on hole (d): 4.33

Seafloor (drill pipe measurement from rig floor, m DRF): 132.7 (by proxy, Hole U1351B)

Distance between rig floor and sea level (m): 11.0

Water depth (drill pipe measurement from sea level, m): 121.7

Total depth (drill pipe measurement from rig floor, m DRF): 1100.0

Total penetration (m DSF): 967.3

Total length of cored section (m): 0.00

Total core recovered (m): 0.0

Core recovery (%): 0.0

Total number of cores: 0

Integrated Ocean Drilling Program (IODP) Site U1351 (proposed Site CB-03B) is located on the outer shelf (122 m water depth) within the Canterbury Bight and is the most basinward shelf site of the Canterbury Basin drilling transect. This location was chosen as a primary site in response to an Environmental Protection and Safety Panel (EPSP) request (December 2005) to avoid the high seismic amplitudes observed at ~1.05 s two-way traveltime at proposed Site CB-03A. Site U1351 is located on dip seismic Profile EW00-01-66, updip from Site CB-03A (Fig. F1). Because of the move from Site CB-03A, there is no EW00-01 crossing strike profile at Site U1351. However, this site is located on crossing strike Profile CB-82-25, a line acquired for hydrocarbon exploration purposes in 1982 (Figs. F1, F2).

In order to determine the impact of global sea level change on deposition cyclicity, it is important to drill each sedimentary sequence in at least two locations: landward of the rollover or clinoform break representing the paleoshelf edge, where paleowater depths critical for eustatic amplitude estimates are best constrained by benthic foraminiferal biofacies, and on paleoslopes, where increased pelagic microfossil abundance provides optimal age control. Obtaining such information for a number of prograding sequences requires a transect of boreholes crossing the margin in the dip direction.

Furthermore, the facies, paleoenvironments, and depositional processes associated with sequence stratigraphic models of prograding continental margins, where sequences are best resolved seismically, have yet to be adequately constrained by scientific ocean drilling. Prediction of the distribution of sediments within sequences is highly model dependent (e.g., systems tract models of Posamentier et al., 1988; Vail et al., 1991). These models offer great potential for understanding oil and gas resources and for ground water–pollution remediation issues. However, the fundamental assumptions and predictive capabilities of these models can only be tested by drilling on shallow continental shelves within a well-defined seismic stratigraphic framework.

Operations at Site U1351 began in accordance with the proposed drilling strategy, which stipulated that drilling should begin at the deepwater end of the shelf transect if weather conditions allowed. The distal location of this site allowed the initial attempt at shelf drilling to occur at the deepest water depth of any of the proposed shelf sites and at a location where sediments were presumably finer grained than at more proximal proposed shelf sites such as Site U1353 (proposed Site CB-01A). This approach provided experience in shelf sediment drilling before drilling was attempted at more challenging inboard shelf sites. The planned maximum penetration was 1249 m. Actual penetration was 1031 m drilling depth below seafloor (DSF) in Hole U1351B.

Nineteen regional seismic surfaces interpreted as seismic sequence boundaries (U1–U19) have been identified in the middle Miocene to recent shelf-slope sediment prism (Lu and Fulthorpe, 2004). Seismic sequence boundaries U6–U19 were penetrated at Site U1351. Upper Miocene–lower Pliocene sequence boundaries (below U10) feature smooth onlapped paleoshelves and rounded rollovers with sigmoid internal reflection geometries. In contrast, middle Pliocene–Holocene sequence boundaries (U10 and above) display eroded and incised downlapped paleoshelves and more pronounced rollovers with oblique reflection geometries. Drilling tested the hypothesis that these contrasting characteristics occur because paleoshelves below U10 were not subaerially exposed at lowstand, whereas those above U10 were exposed, probably because of increasing eustatic amplitudes during the Pliocene–Holocene.

The principal objectives at Site U1351 were as follows:

1. To sample facies landward of, but close to, rollovers of progradational sequence boundaries, particularly U8–U19. A particular goal was to use benthic foraminiferal biofacies to estimate paleowater depths both above and below sequence boundaries. This information will be used to calculate eustatic amplitudes using two-dimensional backstripping.

2. To sample slope facies of U4–U7 to provide age control.

3. To investigate facies, paleoenvironments, and depositional processes associated with the sequence stratigraphic model on a prograding continental margin where sequence architecture is well constrained by seismic imaging.

Operations

Transit to Site U1351

After a 1 day transit from Wellington, New Zealand, covering 257 nmi at an average speed of 11.4 kt, the R/V *JOIDES Resolution* was positioned over Site U1351 on 18 November 2009 at 0931 h (all times are ship local time, Universal Time Coordinated [UTC] + 13 h). The position reference was a combination of Global Positioning System (GPS) and an acoustic beacon on the seafloor, weighted heavily toward the acoustic beacon (80%). The positioning beacon (FSI BAP-547W, SN 1025, 14.0 kHz, 200 dB) was deployed at 1030 h.

Site U1351 overview

Three holes were drilled at this site (Table **T1**). The first two holes were cored with the advanced piston corer (APC)/extended core barrel (XCB) coring systems. Total core recovery was 332 m. Average recovery rates for Site U1351 were 87% with the APC coring system, 23% with the XCB coring system, and 31% for all cores. Hole U1351B was logged with limited success. The third hole was drilled with a 9⅞ inch tricone bit for logging purposes. Logging was attempted, but the tool became stuck and had to be recovered. The third-generation advanced piston corer temperature tool (APCT-3) was deployed three times, and the Sediment Temperature (SET) tool was deployed twice. Data from four out of five deployments were severely compromised, probably because of sediment that had fallen to the bottom of the hole and/or motion at the bit.

Hole U1351A

Rig floor operations commenced at 0931 h on 18 November. The drill string was spaced out, placing the bit at 126.5 m drilling depth below rig floor (DRF) or 4.9 m above the "corrected" precision depth recorder (PDR) depth of 131.4 m DRF. The first APC barrel recovered ~2.7 m of core, and an official seafloor depth was established at 133.3 m DRF. APC coring continued through Core 317-U1351A-6H to 28 m DSF using standard steel coring assemblies. All cores after Core 317-U1351A-2H were partial stroke cores, indicating very firm near-surface sediments. The hole was terminated after Core 317-U1351A-6H.

Contamination testing was done on all cores with perfluoromethylcyclohexane (PFT) and microspheres. A temperature measurement was taken with the APCT-3 at Core 317-U1351A-4H. Average recovery for Hole U1351A using the APC coring system was 98%. The drill string was pulled back to the sea-floor, and the bit cleared the seabed at 2330 h on 18 November.

Hole U1351B

Hole U1351B officially began at 2330 h on 18 November. The vessel was offset 20 m south of Hole U1351A, and coring in Hole U1351B began at 0045 h on 19 November. Hole U1351B was piston cored to 94.7 m, with a total recovery of 81.12 m (81% recovery). Orientation was measured on the first five cores, and then poor APC coring conditions forced the tool to be removed. The XCB system was deployed for most of the remaining interval (Cores 317-U1351B-14X through 116X [94.7–1030.6 m DSF]). Recovery was acceptable (ranging from 20% to 100%) from the top of the XCB interval to ~429 m DSF, where it dropped to nearly zero for seven cores. The decision was made to switch back to the APC system three times (Cores 317-U1351B-57H through 59H, 65H, and 78H) in an attempt to improve recovery. However, penetration was short each time (0.8–4 m; recovery was nominally high but was based on recovered length), and XCB coring was resumed. The average core recovery for all XCB cores was 23%. Coring was terminated at 1030.6 m DSF after the XCB core barrel became stuck inside the bottom-hole assembly (BHA).

After the core barrel was freed, a decision was made to stop coring and log Hole U1351B. A 50 bbl high-viscosity mud sweep was pumped to clean the hole, and the hole was displaced with 420 bbl of 9.0 ppg mud with a 100+ Marsh funnel viscosity. The drill string was tripped back to 80 m DSF, and the triple combination (triple combo) tool string was rigged up and run to the bottom. Hole conditions before logging were good, but the gauge of the hole was largely unknown. The first logging run revealed that the hole was oversized over most of its length. Next, the Formation MicroScanner (FMS)-sonic tool string was rigged up and deployed. The tool failed to pass 618 m wireline log depth below rig floor (WRF), indicating that the hole had collapsed and bridged near that depth. The hole was logged from that point upward. A 12 bbl cement plug was pumped according to IODP policies for drilling on a continental shelf, with the string at 283 m DSF. The drill string was tripped back to the surface, and the bit cleared the rotary table at 1800 h on 25 November, ending Hole U1351B.

Contamination testing for microbiology was done at regular intervals (every ~50 m) throughout Hole U1351B. Both PFTs and microspheres were deployed. Temperature measurements were taken with the APCT-3 at Cores 317-U1351B-10H and 12H and with

the SET tool at Cores 317-U1351B-16X and 42X, with mostly poor results.

Average core recovery in Hole U1351B was 84% for the APC system and 23% for the XCB system. Total recovery for Hole U1351B was 304.5 m out of a cored interval of 1030.6 m (30% recovery rate).

Hole U1351C

The objective of drilling Hole U1351C was to provide a dedicated, fresh hole for wireline logging without coring, and operations officially began at 1800 h on 25 November. The ship was offset 30 m south of Hole U1351B. A new BHA was made up with a 9⅞ inch tricone bit fitted with a mechanical bit release. After tripping the BHA to the seafloor and picking up the top drive, drilling in Hole U1351C began at 2335 h on 25 November. The hole was drilled to 1100 m DRF and swept clean with a 50 bbl high-viscosity mud sweep.

At 1915 h on 27 November, while the hole was being swept clean with mud in preparation for logging, a sudden wind change forced the vessel outside its maximum positioning offset (8% of water depth, or ~10 m). The vessel lost power to three of its six forward thrusters while trying to respond to the sudden wind shift. Position and power were reestablished within 15 min. The maximum excursion from the hole was 38 m. With all drilling parameters still normal, Hole U1351C was displaced with logging mud in preparation for logging. The drill string was tripped to 80 m DSF, and the section of drill pipe that was located at the seabed during the excursion was inspected after it was recovered at the surface. No damage to the drill string was visible.

The triple combo logging string was assembled and run into Hole U1351C. When the tool was at ~912 m wireline log depth below seafloor (WSF), the winch lost weight, indicating that the tool was stuck. The tool could not be moved either up or down, so the logging line was cut, and the drill pipe was tripped in over the logging line in an attempt to recover the triple combo logging string. The logging tools were eventually recovered after tripping over the wireline from 80 to 708 m DRF. The tools were pulled up into the drill string, and the logging line was pulled up onto the rig floor using T-bars until sufficient length was recovered to attach the line to the coring winch. After the line was spooled onto the coring winch, the coring winch was used to recover the logging tools. The logging tools were set back on the rig floor, the drill string was pulled back to ~285 m DRF, and the hole was cemented with 10 bbl of 14 ppg cement. The drill string was then tripped back to the rig floor and secured for the 8 nmi transit to the next site, ending Hole U1351C at 0200 h on 30 November.

Lithostratigraphy

Two holes were cored at outer shelf Site U1351. Hole U1351A was drilled to 28 m core depth below seafloor (CSF-A; unless otherwise noted, all depths in this section are reported in m CSF-A), and Hole U1351B was drilled to 1031 m. Holes U1351A and U1351B were APC cored to 95 m. The XCB was then used to drill to total depth, with occasional use of the APC in attempts to improve core recovery.

Core recovery in lithologic Unit I in Hole U1351B was moderate (average = 62%); recovery was higher with APC drilling and lower with XCB drilling (86% and 48%, respectively). Recovery in Unit II was very poor, averaging ~19% (Figs. **F3, F4**).

Although the sedimentary succession at Site U1351 can be divided into two lithostratigraphic end-member units based on lithology and sedimentary structures, the exact boundary location is uncertain (see **"Unit I/II boundary,"** below and Fig. **F5**) and lies somewhere within the interval between Cores 317-U1351B-30X and 36X (247–300 m). We tentatively place the unit boundary at the single lithologic boundary recovered within this depth range, at Section 317-U1351B-31X-4, 68 cm (262 m). The transitional interval also contains the break between logging Units 1 and 2 (see **"Downhole logging"**) and roughly corresponds to a change in macro- and microfauna, indicating a shift from inner-middle to middle shelf settings (see **"Biostratigraphy"**). Unit I is Holocene–Pleistocene to early Pliocene in age, whereas Unit II is early Pliocene to late Miocene in age (Table **T2**).

Cores recovered from Holes U1351A and U1351B show a fairly gradual downhole transition from a heterolithic section with abrupt contacts at the top to a more featureless sedimentary section at the base, suggesting progressive changes in sedimentary styles as the margin evolved (Figs. **F3, F4**). This gradational change is also reflected in sediment physical properties (see **"Physical properties"**).

Description of lithologic units

Unit I

Intervals: Cores 317-U1351A-1H through 6H and 317-U1351B-1H through Section 317-U1351B-31X-4, 70 cm

Depths: Hole U1351A: 0–28 m (total depth) and Hole U1351B: 0–262.0 m

Age: Holocene–Pleistocene

Holes U1351A and U1351B are offset ~20 m from each other (Figs. F6, F7) and exhibit slightly different stratigraphies (e.g., slump in Core 317-U1351A-4H; Fig. F8). The following lithologic summary of Unit I is largely based on Hole U1351B because a significant number of whole-round samples were taken from Hole U1351A for geochemical, microbiological, and geotechnical analyses and thus were not available for sedimentologic description. Although this resulted in a less complete stratigraphy in Hole U1351A, key surfaces and associated sediments (abrupt-based sand beds) allow for correlation between holes (dashed lines in Fig. F6). These key lithologic surfaces are designated U1351A-S1, U1351A-S2, U1351B-S1, and U1351B-S2 and are more fully described in "Description of lithologic surfaces and associated sediment facies."

Drilling disturbance increased downhole with the XCB method, becoming more prominent in Cores 317-U1351B-21X and below, where pronounced biscuiting was observed (Fig. F9). In many instances, intervals of shell hash or sand at the tops of cores were considered to represent downhole contamination by caved sediment (Fig. F10). This interpretation is supported by caliper logs that show the upper section of Hole U1351B to be washed out (see "Downhole logging"). In addition, intervals of suspected shell-hash cavings are also commonly associated with anomalously high magnetic remanence values (see "Paleomagnetism").

Lithologies include dark gray and dark greenish gray to olive-gray fossiliferous mud and sandy mud, dark gray very fine to medium well-sorted sand, olive-gray muddy sand, gray mud (high clay content), and shell hash. Bioclastic material includes gastropods, bivalves, barnacle plates, and bryozoans, which in places form centimeter-thick shelly beds. These lithologies are illustrated in Figures F11, F12, and F13.

As partly observed with a hand lens and verified by smear slide analysis (see "Site U1351 core descriptions"), sand- and silt-sized grains are dominated by quartz and feldspar, with common to rare mica (biotite and muscovite), chlorite, ferromagnesian minerals (various amphiboles), other dense minerals (zircon, clinozoisite, epidote, tourmaline, and others), and glauconite. Clay minerals are also present; however, the clay-sized fraction contains not only clay but a significant proportion of nonclay mineral grains. Rock fragments common in the sand-sized fraction are mainly low-grade metamorphic fragments (e.g., phyllite/slate or semi-opaque, unidentifiable polycrystalline fragments; see Fig. F14). Authigenic minerals are mainly opaque minerals (e.g., pyrite occurring as framboids and as infill in microfossils) and carbonate. A variable biogenic component consisting of bioclasts (mollusk and barnacle fragments) as well as more readily distinguishable foraminifers (whole and fragmented), echinoderm spicules and plate fragments, calcareous and siliceous spicules, and bryozoa fragments is also present. The biogenic silt- to clay-sized fraction includes nannofossils and other spicules.

The assemblage of mineral components identified visually (e.g., quartz, feldspar, mica, chlorite, clay minerals, carbonate, pyrite, and the amphibole and epidote group minerals) compares well with data from X-ray diffraction (XRD) analysis (see XRD in "Supplementary material"). XRD data indicate that the main carbonate mineral is calcite and the main feldspar is plagioclase, with lesser orthoclase and microcline. Unfortunately, because of peak interference with the sheet silicates, it was not possible to conclusively identify glauconite in the XRD analysis.

Bedding contacts are locally abrupt to gradational, and there are a few decimeter- to meter-thick examples of coarsening-upward or fining-upward beds and color banding. Lamination and convolute bedding are rare (Figs. F8, F13). Bioturbation is common in finer grained units (ichnofabric index of 1–5) and includes discrete burrows of *Chondrites* and *Thalassinoides*. *Thalassinoides* burrows tend to be associated with abrupt contacts and extend as far as 50 cm below these contacts (Fig. F7).

Diagenetic changes in the lower part of Unit I are indicated by authigenic carbonate cements and limestone concretions in Cores 317-U1351B-19X, 22X, 25X, and 30X. Thin section analysis of glauconitic limestones (cemented shell-hash beds) from the core catchers of Cores 317-U1351B-19X (147 m) and 22X (175 m) shows these concretions to similarly consist of gravel-sized barnacle, bryozoa, brachiopod, bivalve, and echinoderm fragments (Fig. F15). One sample exhibits a micritic matrix; the other, more porous, sample is partly cemented by carbonate microspar. Pores within fossils have also been filled with sparry calcite. Some sand- and silt-sized quartz, feldspar, and accessory grains are also present. The moderate (10%–15%) glauconite content results mainly from the epigenetic growth of glauconite within fossil void spaces, although a few "grains" of glauconite may be allochthonous.

Within the uppermost part of Unit I, two dominant facies assemblages recur (Figs. F16, F17). The first facies assemblage (Type 1; ~5 examples in uppermost 30 m of both Holes U1351A and U1351B, as indicated in Fig. F16A) is several meters thick and consists mainly of bioturbated, very fine sandy mud (silt-dominated) with scattered common shell fragments of gastropods and bivalves (*Tawera*). The base of the assemblage is rich in shell fragments and con-

tains centimeter- to decimeter-thick shell-hash beds mixed with siliciclastic materials (fine to medium sand) that fine upward into overlying sandy silt at the top of the assemblage (Fig. F17). The boundaries of each assemblage range from sharp (e.g., Core 317-U1351B-3H) to gradual (e.g., Sections 317-U1351B-4H-2 through 4H-4). However, each boundary is characterized by a concentration of shell fragments above the contact and sometimes by abundant burrows filled with shell fragments below the contact. A distinct color change from greenish gray in the shelly sandy mud above the sharp boundary grading into gray sandy mud with extensive burrowing beneath the boundary was observed only in Cores 317-U1351B-1H and 2H.

The second facies assemblage (Type 2) characterizes the middle (30–170 m) of Unit I. This facies assemblage can be as thick as ~20 m (much thicker than Type 1; see Figs. F16, F17). Examples of the Type 2 assemblage are best defined in intervals 317-U1351B-5H-1, 120 cm, through 8H-4, 5 cm (29.4–52.25 m); 8H-4, 5 cm, through 11H-2, 113 cm (52.25–72.33 m); and 19X-2, 103 cm, through 21X-CC, 26 cm (144.13–168.36 m). This assemblage consists of a greenish gray (calcareous), shelly, bioturbated mud with scattered common shell fragments of gastropods and bivalves overlying a sharp contact (Fig. F12). In Core 317-U1351B-8H, a few meter-thick shelly intervals also exist above the lower boundary. This shelly facies is followed by a transition uphole into a dark gray, micaceous very fine sandy mud that contains alternating color bands of light and dark gray clay beds (e.g., Fig. F13C) with diffuse to sharp contacts and slight upward-coarsening into interbedded very fine sand and mud. The dark gray mud is homogeneous and contains very rare shell fragments (e.g., Fig. F13B). In Core 317-U1351B-5H, this facies assemblage also contains in its uppermost interval a 2 m thick, gray, very well sorted quartz-rich very fine sand interval (Fig. F12A). Note that an alternative interpretation places this sand at the base of a Type 1 facies assemblage (Fig. F6; see "Interpretation of Unit I").

In contrast to the heterolithic middle and upper part of Unit I, a monotonous repetition of two lithologies characterizes the base of Unit I (interval 317-U1351B-27X through 31X [~218–264 m]): (1) very dark gray homogeneous clay-rich mud without shell fragments and (2) dark greenish gray sandy shelly mud (e.g., Fig. F13A). The abundant shell material in the sandy mud is dominated by barnacle plates. Contacts between lithologies are more gradational and do not appear distinctly erosional like those in the upper part of Unit I, nor are they heavily bioturbated. Furthermore, the shelly sandy mud intervals tend to be thicker (1–3.5 m) than the intervening clay-rich mud intervals (0.5–1.0 m).

Unit I/II boundary

The Unit I/II boundary is not defined at a particular point in the succession because imperfect core recovery hampered interpretation of both the exact location of the unit boundary and its nature (gradational or abrupt). Each of the two units has a distinct lithology, and the transition interval is defined as occurring between 247 and 300 m. A range of options for the location of the Unit I/II boundary is presented in "Discussion and interpretation" (Figs. F5, F18, F19). The only lithologic contact recovered in this interval (at Section 317-U1351B-31X-4, 70 cm [262.0 m]) was selected as the unit boundary for the purpose of unit description.

Unit II

Interval: Sections 317-U1351B-31X-4, 70 cm, to 116X-CC, 44 cm
Depth: 262.0–1024.4 m
Age: early Pliocene to late Miocene

The main lithologies of Unit II are dark greenish gray very fine sandy mud and greenish black to dark greenish gray mud (Fig. F20), both of which may be shell bearing. A less abundant lithology is dark greenish gray very fine muddy sand. Millimeter- to centimeter-thick dark greenish gray, well-sorted very fine to fine sand occurs sporadically throughout the unit. Shells are common in the upper portion of the unit and include bivalves, gastropods, echinoid spines, and barnacle plates, but they become less frequent below Core 317-U1351B-40X and are absent below Core 101X. Many shells are fragments or partially altered fragments. Shell-hash units that occur at the tops of cores are thought to represent material derived from downhole cave-in, as also noted in Unit I. Bioturbation is not common and rarely reaches an ichnofabric index of 5; it is absent below Core 317-U1351B-113X. No distinct sedimentary structures were observed, but in higher recovery zones such structures could be masked by the locally intense biscuiting observed throughout this generally poorly recovered (recovery = ~18%) unit (Fig. F9). The terrigenous and biogenic components noted in smear slides and in XRD analyses from Unit II are similar to those listed above in the Unit I description. One exception is the presence of minor amounts of authigenic zeolite(?) cements in Core 317-U1351B-111X and deeper. The proportion of minerals and components differs slightly between units, as discussed in the following section.

More indurated intervals of clayey or sandy mud are present in many core catchers in the lower part of

the hole, where drilling disturbance noticeably increased (Table T3; Fig. F21E, F21F). This induration is drilling induced and related to high temperatures generated by frictional grinding when the cutting shoe in the XCB was not properly cooled because of clogged ports in the bit (cores smelled "baked" upon splitting). However, other indurated intervals within the less indurated host sediment are in situ and a product of incipient to well-developed carbonate cementation, as shown by the presence of authigenic carbonate in smear slides and thin sections (Table T3; Fig. F21A–F21D). Such cemented intervals, defined as "nodules" when smaller than the core diameter and "concretions" when wider (truncated) than the core diameter, are present throughout the unit, particularly in Core 317-U1351B-87X and below. Petrographic examination of seven of these cemented rocks showed them to be carbonate-cemented silty sandstone to sandy marlstone. They are generally bioturbated, quartzo-feldspathic, and micaceous but variably fossiliferous and matrix rich.

No hard lithologies were recovered in the low (15%) recovery zone in Unit II between Cores 317-U1351B-42X and 87X (352–745 m), whereas the higher (27%) recovery zone between Cores 317-U1351B-87X and 116X (745–1024 m) contains more hard lithologies, which could have potentially caused poor recovery. Therefore, the low recovery rate between Cores 317-U1351B-42X and 87X must be attributed to this interval's lithology rather than to the presence of cemented or indurated beds.

This thick unit includes some gradual lithologic changes (Fig. F4). For example, the lowermost part of Unit II comprises slightly more calcareous sandy mud and is generally greenish gray in color (Fig. F20).

Downhole trends in sediment composition and mineralogy

In general, Site U1351 mineralogy and composition is fairly consistent downhole, with the relative abundances of most minerals apparently varying according to sediment texture (Fig. F22). Unit I mineralogy consists of quartz, total clays, micas (muscovite/biotite), chlorite, plagioclase, K-feldspar, and pyrite. Dolomite and siderite were occasionally observed, but peak intensities are close to the limit of detection (see XRD in "Supplementary material"). The relative intensity of the calcite peak correlates ($R = 0.7$, $N = 47$) with the total calcium carbonate concentration determined by coulometry (with the exception of seven outliers, all in the uppermost 250 m). This indicates that calcite is the dominant carbonate mineral. The outliers likely represent heterogeneities in carbonate shell content between the samples used

for each analysis. Overall, the depth trends in calcite peak intensity follow smear slide and bulk $CaCO_3$ concentrations (Figs. F22, F23). There is a notable downhole decrease in the occurrence of hornblende, with a 50% decrease below ~90 m. Dense mineral percentages, as identified in smear slides, appear to be more variable (Fig. F23). The diffraction peaks for pyrite are close to the limit of detection, and the maximum intensities of these peaks show no particular downhole trend. This trend matches smear slide observations, which show fluctuating opaque mineral concentrations that lack a trend with depth. Siliceous bioclast concentrations did not exceed 1%, except for a few isolated samples in the uppermost 50 m (see "Site U1351 core descriptions").

The composition and mineralogy of Unit II is similar to that of Unit I, but several changes are worth noting. In addition to the less variable bulk carbonate percentage trends from smear slides and coulometry data seen in Unit II, the most useful trend for differentiating units appears to be the percentages of clay and, conversely, quartz/feldspar and glauconite. Glauconite content is highest in Unit I and lowest in Unit II, whereas clay and quartz/feldspar percentages are extremely variable in Unit I and much less so in Unit II. XRD peak intensities of quartz and plagioclase (dominantly albite) increase downhole and are significantly higher ($p = 0.05$, $N = 60$) below the Unit I/II boundary, possibly corresponding to an increase in very fine sandy mud in Unit II. Note that in the context of this discussion the clay percentage is a smear slide estimate of the clay-sized fraction (<4 µm), which probably contains a significant proportion of clay-sized quartz and other detrital grains, as suggested by thermal conductivity data (see "Heat flow").

Correlation with wireline logs

The triple combo tool string (measuring gamma ray, porosity, density, and resistivity) was run in Hole U1351B from the seafloor to the bottom of the hole at 1032 m WSF. The FMS-sonic tool string (measuring microresistivity and sonic velocity) was run from ~80 to ~486 m WSF. In addition, gamma ray and resistivity logs were acquired from 84 to ~782 m WSF in Hole U1351C (see "Downhole logging"). Three logging units were identified at Site U1351. The boundary between logging Units 1 and 2 (at 260 m wireline log matched depth below seafloor [WMSF]) corresponds within the error of core-log depth matching to the lithologic Unit I/II boundary. Although the caliper log from Hole U1351B indicates a large-diameter hole in the uppermost 600 m, comparison of wireline logs with measurements from cores from equivalent depths indicates that the

gamma ray, resistivity, and density logs were not seriously affected by the enlarged hole (see "Downhole logging").

Gamma ray logs from siliciclastic settings are primarily interpreted as delineating relative changes in the amount of fine-grained sediments (clay) and thus grain size (Doveton, 1994). However, in settings such as the Canterbury Basin that have an appreciable amount of nonclay minerals in the clay-sized fraction (e.g., rock flour), increased mica and feldspar content in the silt- to sand-sized fraction, and a mixture of siliciclastic and carbonate lithologies, the downhole trends in absolute gamma ray values represent changes not only in grain size but in lithology and mineralogy. For example, low gamma ray values may be caused by carbonate-rich (coarse or fine) intervals. In addition to reflecting an increase in clay content, an increase in gamma ray values could also stem from an increase in the mica, feldspar, or dense mineral content of sands, or it may simply reflect a decrease in rock flour in the mud-sized fraction.

Standard gamma ray (SGR) and computed gamma ray (CGR) logs (Figs. F5, F18, F19) were used to examine downhole changes in lithology. SGR is the total gamma ray count from all sources, whereas CGR reflects the subtraction of the uranium contribution from the SGR (Doveton, 1994). Sandy layers of meter- and submeter-scale thickness described in the cored interval of Hole U1351B correspond to low peaks in CGR, suggesting that low gamma ray values can be used as a proxy for a coarse-grained lithology (see "Downhole logging"). However, large-scale trends of increasing gamma ray values are possibly caused by both textural and compositional changes, as discussed above and elaborated below.

The gamma ray log varies within the uppermost 300 m WMSF, having high-amplitude (~70 gAPI) swings over <10 m vertical distances. The higher amplitude swings in SGR are reflected in the CGR logs, supporting the interpretation that the variation in gamma radiation over this interval results largely from textural changes, likely intercalated sand and mud, consistent with the heterolithic record of recovered sediments from lithologic Unit I. Above 200 m WMSF within Unit I, considerable variability in the logging data is apparent in what are interpreted as alternating sand and mud intervals. The interval between 250 and 300 m WMSF reveals an overall upsection decrease in CGR, likely reflecting a coarsening-upward trend. This log can be interpreted to reflect more lithologic variability, similar to the more heterolithic log character of Unit I.

Although the uppermost 300 m WMSF has a variable gamma ray log over relatively short vertical distances, the interval below has more gradual trends. From 300 to 530 m WMSF, there is a steadily increasing upsection trend in the SGR record. This trend is evident in the CGR record as well, but to a lesser extent. This suggests that the increase in total gamma ray intensity over this interval is due to both textural and compositional change. An increase in total gamma ray units between 530 and 560 m WMSF corresponds to an increase in total clays seen in XRD analysis, suggesting that this interval has higher clay content. From 650 m WMSF to total depth, the SGR has interbeds of higher values interpreted as clay-rich beds and relatively thin (<5 m thick), low-value layers interpreted as beds of sand with both fining- and coarsening-upward trends. Where low gamma ray and resistivity peaks co-occur deeper in Hole U1351B, these intervals are interpreted as the result of irregular hole size rather than a change in lithology (see "Downhole logging"). The presence of hard surfaces or features in Cores 317-U1351B-87X through 116X correlates well with positive changes in the gamma ray signature and density values in the lower part of the hole (Table T3; Fig. F21).

Description of lithologic surfaces and associated sediment facies

The testing of sequence stratigraphic concepts (i.e., sequence boundaries, maximum flooding surfaces, and lowstand, transgressive, and highstand systems tracts, as defined by Posamentier et al., 1988) was a major objective of Expedition 317. As a result, the identification and description of lithologic surfaces and their associated sedimentary packages that mark transitions and discontinuities has the potential of providing information about sequence stratigraphy. These lithologic surfaces and their associated sediments are detailed in this section.

Because of time restrictions on board the ship, surfaces were only examined close to the predicted depths of seismic sequence boundaries; therefore, the lithologic surfaces identified here are implicitly linked to the predicted occurrences of sequence boundaries identified on the seismic (Lu and Fulthorpe, 2004). A similar approach was used on board Ocean Drilling Program (ODP) Legs 150 and 174A, the objectives of which were also to study sea level changes. Postcruise study will attempt to clarify the exact relationship of all lithologic surfaces and facies associations to sea level changes and seismic stratigraphy. The lithologic surface numbering system used in the site chapters, tables, and summary diagrams comprises a hole-specific prefix and a surface designation (e.g., U1351A-S1) that links each surface to a seismic sequence boundary; therefore, these litho-

logic surfaces and associated sediments are thought to be correlative between sites across the transect.

Lithologic surfaces at Site U1351 are labeled U1351A-S1 to U1351A-S2 and U1351B-S1 to U1351B-S8 (Tables T4, T5). Depositional packages were identified and characterized by their lithologic composition (sand, muddy sand, sandy mud, and mud) and the nature of their upper and lower contacts (sharp or gradational). Hole U1351A recovered only the uppermost 28 m, and only two lithologic surfaces were identified. Potential surfaces in poorly recovered or nonrecovered intervals are based on gamma log signatures. In some instances, the basal contacts of these packages are near the predicted depths of seismic sequence boundaries (Lu and Fulthorpe, 2004), allowing for a preliminary and tentative correlation of the lithology to seismically defined sequence boundaries (see "Interpretation of lithologic surfaces and associated sediment facies" and the "Expedition 317 summary" chapter).

Generally, the surfaces and/or discontinuities in Hole U1351A and the uppermost 200 m of Hole U1351B are sharp and separate coarse lithologies above the surface and fine mud beneath (Figs. F11, F12). Each contact is generally extensively bioturbated, and the burrows extend below the contacts by as much as 50 cm. Above the contacts, coarse-grained lithologies are represented by shell-rich mud, sandy mud, and fine-grained, well-sorted quartz-rich sand that contains green ferromagnesian accessory minerals and fines upward.

Surfaces U1351A-S1 and U1351B-S1

Of particular importance is the correlation of two surfaces recovered from Holes U1351A and U1351B, located ~20 m apart. Surfaces U1351A-S1 and U1351B-S1 were recovered at Sections 317-U1351A-3H-3, 77 cm, and 317-U1351B-2H-6, 65 cm, respectively, both at ~16 m (Figs. F6, F7). The lithologic expression of this surface is a sharp basal contact that is heavily burrowed and overlain by a shell bed (<30 cm thick in Hole U1351B).

Surfaces U1351A-S2 and U1351B-S2

A second pair of surfaces (U1351A-S2 and U1351B-S2) was tentatively identified as having been recovered at Sections 317-U1351A-6H-1, 26 cm (22.76 m), and 317-U1351B-5H-3, 3 cm (31.00 m), although the actual U1351A-S2 may not have been recovered. These surfaces may be overprinted and/or masked by drilling disturbance (cave-in) at the tops of Cores 317-U1351A-6H and 317-U1351B-5H (Fig. F6). The tops of the sand beds associated with these surfaces roughly align, and their compositions are similar:

very fine grained, well-sorted, quartz-rich sand containing ferromagnesian accessory minerals.

Surfaces U1351B-S3, U1351B-S4, and U1351B-S5

Surface U1351B-S3 at Section 317-U1351B-8H-4, 5 cm (52.25 m), is represented by a sharp basal contact and heavy bioturbation overlain by 5 cm thick muddy gravelly sand.

The sharp boundary at Section 317-U1351B-10H-2, 45 cm (67.27 m), separating dark greenish gray sandy mud with shells from underlying gray shelly sand is described as U1351B-S4 but may be associated with caved material. The underlying shelly sand is 40 cm thick and grades downward into coarse, poorly sorted shelly sand. The bottom portions of intervals 317-U1351B-10H-2, 50–150 cm, and 10H-3, 0–121 cm, which are composed of shelly coarse sand, are also suspected to be caved material.

A 70 cm thick, very fine grained, partly cemented muddy sand was recovered in interval 317-U1531B-12H-1, 50–120 cm (76.2–76.9 m). The sand is similar in character to that recovered above U1351B-S2 in that it is quartz rich, fine grained, and well sorted; however, it is partly cemented and greenish to bluish gray as opposed to the very dark gray color that occurs in Core 317-U1351B-5H. Surface U1351B-S5 is placed at the presumed base of the recovered sand interval. A lithologic break is implied by the gamma ray logs at 87 m WSF.

Surfaces U1351B-S6 and U1351B-S7

Surface U1351B-S6 is a sharp basal contact at Section 317-U1351B-19X-2, 104 cm (144.14 m), between a 1.15 m thick shelly sand bed and an underlying mud with scattered shell fragments. Surface U1351B-S7 is a heavily burrowed, sharp contact separating clayey mud below from a 1 m thick shelly sandy mud above, located at Section 317-U1351B-22X-1, 102 cm (171.4 m).

Surface U1351B-S8

Surface U1351B-S8 is a sharp, heavily bioturbated contact at Section 317-U1351B-30X-5, 80 cm (253.9 m), separating mud from an overlying shelly, muddy, fine sand bed 6.7 m thick. This bed contains a bimodal population of shells, with some shell fragments of millimeter to 1 cm thickness and bivalves that are several centimeters long and have both valves preserved.

Additionally, nodules/concretions and cemented beds that could be potential sources of seismic reflectivity were recovered from Cores 317-U1351B-9H through 116X (Table T3).

Discussion and interpretation

Interpretation of Unit I

Upper to middle part of Unit I (Cores 317-U1351B-1H through 22X)

A depositional environmental interpretation of Unit I is best accomplished in the framework of the facies assemblages (Types 1 and 2) described above, starting with the thicker, more complete Type 2. Starting at a sharp basal contact, the Type 2 facies assemblage contains upward-fining shelly sandy mud transitioning into mud that, in turn, coarsens upward into sandy mud. The formation of a shelly lag deposit, followed by a fining-upward sandy mud just above an erosional contact in the lowermost part of the facies assemblage (Fig. F17), indicates a transgressive systems tract passing up into highstand mud. Subsequent regressive facies deposition, namely the coarsening-upward sandy mud, can be attributed to shoreline progradation during periods of limited accommodation. The diverse facies assemblage of the Type 2 assemblage includes decimeter- to centimeter-thick dark to light gray clay beds (e.g., Fig. F13C). Similar clay-rich beds are observed on modern muddy continental shelves and are formed by rapid deposition following flood events (Suter, 2006; Wheatcroft et al., 1997, 2006). The preservation of such beds and the lack of subsequent bioturbation indicate relatively high sediment accumulation rates and/or frequent (subdecadal) flood events, which are typical near sediment-rich fluvial systems (Bentley et al., 2006). The upper boundary of the Type 2 facies assemblage generally ends at a truncated surface within sandy mud, except in Core 317-U1351B-5H, where the sandy mud grades upward into a very well sorted, quartz-rich very fine sand bed; in this case, the facies assemblage boundary is placed at a truncated surface above the sand, as depicted in Figure F17, rather than at the gradational base of this sand. This sand indicates a possible inner shelf, high-energy coastal environment, suggesting that this part of the facies assemblage may represent the offshore progradation of the coastline.

The components and depositional processes of the Type 1 facies assemblage are similar to those of the lower part of the Type 2 facies assemblage, although they lack the well-developed clay beds discussed above. The stacking pattern of the Type 1 assemblage indicates frequent erosion during marine transgression, indicated by the deposition of shell fragments and bioturbated mud (Fig. F16). This likely represents a transgressive-lag deposit, followed by a maximum flooding surface or the earliest phases of regression (e.g., Clifton, 2006; Suter, 2006; Saul et al., 1999). Both Type 1 and Type 2 assemblages are similar to Pliocene–Pleistocene shelf facies from the Wanganui Basin (Abbott and Carter, 1999; Saul et al., 1999; Abbott et al., 2005; Naish et al., 2005). The greenish gray color indicates more calcareous sand content, as determined by smear slide observations.

Evidence for reworking comes from thin section petrography of the limestone pieces recovered from Cores 317-U1351B-19X and 22X. Many of the rounded fossil fragments from these cores exhibit narrow borings that are generally filled with glauconite, whereas other components (foraminifers, small brachiopod shells, and bryozoa fragments) are never bored (Fig. F15). This may imply that the bored fragments were transported from some distance, whereas the other fragments represent a population originating much closer to the environment of deposition. The few "grains" of glauconite present may also have been transported. Shell beds are likely to be lag deposits, a concentration of material from several different ages, presumably created by a winnowing process of some sort.

Unit I/II boundary

Lower part of Unit I to Unit II transition (Cores 317-U1351B-29X through 36X)

The character of lithofacies assemblages—from more heterogeneous lithologies toward the top of Unit I to interbedded clayey mud and sandy shelly mud at the base—can be related to changing environmental conditions. This change occurs at ~200 m and is primarily revealed by lithology and substantiated by biostratigraphy, gamma ray logs, and seismic reflection profiles. These results reveal downhole changes in margin sedimentation processes and paleoenvironments from an inner middle shelf setting to an outer shelf–upper slope setting.

As mentioned in **"Description of lithologic units,"** a range of options exists for a more precise definition of the Unit I/II boundary, based on both lithologic variations and interpretation of the available downhole gamma logs (Figs. F5, F18, F19). These potential boundary options are as follows:

- Option A, 247 m: An abrupt increase in downhole total gamma ray values corresponds to a change in lithology in the recovered cores from homogeneous mud at the base of Section 317-U1351B-29X-CC (247.37 m) to muddy sand at the top of Section 30X-1 (247.1 m). Although the actual boundary was not recovered, the abrupt change in gamma ray values suggests a sharp contact.

- Option B, 262 m: A sharp lithologic boundary occurs at the base of a thick, clay-rich mud (Section 317-U1351B-31X-4, 68 cm). Below this recovered interval, boundaries between green sandy lithologies and gray muddy lithologies are grada-

tional or unclear, whereas clear, sharp, or slightly bioturbated boundaries, as well as a more heterolithic assemblage of lithologies, exist above this interval. This option is used in the descriptions of Units I and II, above.

- Option C, 264 m WSF: A rapid decrease in downhole gamma readings correlates to the interval from Cores 317-U1351B-31X through 32X, within the depth uncertainty corresponding to a change from a more uniform gamma profile below to a more serrate profile above.

- Option D, 280 m WSF: The top of an overall increasing trend in CGR and SGR values and the base of a more variable pattern above can be correlated to the interval from Cores 317-U1351B-33X through 34X, within depth scale uncertainties.

- Option E, 300 m WSF: The top of a trend of gradually increasing SGR and CGR values that change above this point to a more variable log pattern with smaller scale increasing uphole trends can be correlated to the interval from Cores 317-U1351B-35X through 36X, within depth scale uncertainties.

Interpretation of Unit II

Poor core recovery and moderate to intense drilling disturbance in Unit II prevented detailed interpretation of the depositional environment within the generally texturally uniform sandy mud and muddy sand lithologies of Unit II.

The gradual downhole increase of planktonic foraminifers from ~600 m to the base of Unit II and the downhole transition from an inner neritic planktonic and middle shelf benthic foraminiferal assemblage at the top of Unit II to an extraneritic planktonic and outer shelf to uppermost bathyal benthic foraminiferal assemblage at the base of Unit II demonstrate a transition within Unit II from a continental shelf environment to more open ocean, continental slope conditions, as proposed by Lu and Fulthorpe (2004) and Carter (2007). The presence of reworked barnacle plates and bivalve and gastropod shell fragments in the uppermost intervals of Unit II (Cores 317-U1351B-33X through 49X) also attest to a higher energy shelf-slope environment than that which existed during the early stages of Unit II deposition (see **"Biostratigraphy"**).

Site U1351 falls within the Canterbury Drift succession of Carter (2007), which is defined as sediment drifts that underlie the eastern South Island coastal plain, shelf, and slope, ranging in age from latest Oligocene–early Miocene on shore to Holocene on the continental slope. On shore, these strata are exposed as the Tokama Siltstone (Field and Browne, 1989),

which is also called the Bluecliffs Formation (Carter, 2007). Offshore, the Canterbury Drift succession is found within Units II–III (0.28–3.92 Ma) of ODP Site 1119 (Carter and Gammon, 2004). By combining textural results from both the Tokama Siltstone and Site 1119, Carter (2007) contended that the Canterbury Drift succession formed by along-strike northward sediment transport. An overall fining-upward succession within the Canterbury Drift succession is hypothesized to result from the progressive increase in sediment transport distance from the source, coupled with a tectonic/climatic overprint that led to an increase in mud deposition over sand. These more proximal and distal equivalents provide additional insight into the depositional environment of Unit II at Site U1351.

The gross lithology of Unit II is similar to that observed at both the Tokama Siltstone and Site 1119, which, in combination with well logging results and biostratigraphy, suggests that Unit II is likely an equivalent sedimentary package. Texturally, the generally uniform nature of the sandy mud and muddy sand lithology of Unit II is similar to the massive silty mudstone of the Tokama Siltstone and Site 1119. The higher calcareous content below 600 m and the increasing occurrence of cemented concretions and nodules at depth are similar to observed lithologies from the Tokama Siltstone. Furthermore, downhole gamma ray logs from Site U1351 reveal an overall fining-upward trend above ~725 m that may be similar to the temporal textural trends observed by Carter (2007) for the Canterbury Drift succession.

Sediment composition and diagenesis

XRD peak intensities of quartz and plagioclase correlate ($R = 0.7$, $N = 60$), but there is no correlation between the combination of micas and/or total clays versus quartz and plagioclase (also observed in smear slides), suggesting that different depositional processes control the relative concentration of each mineral component within Site U1351 sediment. The abundant fine clay–sized (<4 µm) nonclay mineral fraction in these sediments can be attributed to onshore glacial processes that likely produced large quantities of glacial flour that were transported offshore by some combination of meltwater discharge, eolian processes, and marine dispersal mechanisms. This fine mineral fraction significantly affects the physical properties of the sediments (see **"Physical properties"**).

Terrigenous minerals (quartz, feldspar, mica, chlorite, amphibole group, and epidote group minerals) and minor lithic components observed in smear slides (mainly silt to fine sand) and thin sections of sandstones from deeper in the hole are consistent

with a metamorphic source. There is evidence of grain reworking (e.g., well-rounded grains), so the metamorphic detritus may be partly recycled rather than being only first-cycle material derived from more southerly schist outcrops. Evaluating potential downhole contributions from nonschist lithologies will require more detailed petrologic and mineralogic study.

The downhole decrease in percent amphibole minerals is likely a function of burial dissolution rather than a signal of provenance change because serrate (cockscomb) dissolution textures of ferromagnesian minerals were noted in smear slides. Other downhole trends include an increase in carbonate cementation, first appearing as micrite crystals and later as more pervasive cements. This lithification first affects more calcareous lithologies, and at depth there is local pervasive carbonate cementation of sandy lithologies. The minor amount of zeolite(?) identified in smear slides and thin sections at the bottom of the hole could be linked to an unconformity (long-term exposure surface) or to dissolution of trace amounts of volcanic glass components in the sediment. Unfortunately, the quantities were insufficient for precise zeolite mineral identification with the XRD technique.

Interpretation of lithologic surfaces and associated sediment facies

Previous analyses of seismic records using the EW00-01 seismic reflection grid allowed interpretation of seismic sequence boundaries U19–U4 and their predicted depths and ages (Lu et al., 2003, 2005; Lu and Fulthorpe 2004). These seismic sequence boundaries provide large-scale understanding of the margins' subsurface seismic facies. The lithologic surfaces and their associated sedimentary packages identified are in some instances near the predicted depths of seismic sequence boundaries (Lu and Fulthorpe, 2004), allowing a tentative correlation of lithology to seismically defined surfaces (Tables **T4, T5**).

Surfaces U1351A-S1 and U1351A-S2 and U1351B-S1 to U1351B-S6

Lithologic surfaces U1351A-S1 and U1351A-S2 and U1351B-S1 to U1351B-S6 and their associated facies are characterized by sharp basal contacts and heavy burrowing beneath (Table **T4**). Shelly sandy mud is present above the contact for 50 to 100 cm. These lithologic surfaces and their associated packages show pronounced lithologic variability and are easy to identify in the cores. The lithologic surfaces and their associated packages were tentatively correlated with U19–U13. The surfaces and their associated facies developed on the inner to middle shelf, and in

some of these packages stratal relations suggest that erosion and/or sediment bypass are associated with the formation of the discontinuity. Additionally, the facies within the upper part of Site U1351 show considerable lithologic variability.

Surfaces U1351B-S7 and U1351B-S8

Surface U1351B-S7 is correlated with U12, which has a predicted depth of 166 m. Surface U1351B-S8 is tentatively correlated with U10, which has a predicted depth of 237 m.

Surfaces deeper than U1351B-S8

Several issues contribute to the lack of lithologic correlation to seismic sequence boundaries in the lower part of Site U1351 (~240–900 m). Primarily, recovery gaps at 308–313, 316–323, 394–400, 611–620, and 890–899 m prevented lithologic correlation to U9, U8, U7, and U6, which have predicted depths of 312, 394, 614, and 895 m, respectively. Additionally, sharp contacts and/or discontinuities are difficult to identify visually in cores from the lower part of Hole U1351B associated with U9–U6. These sediments were deposited when the position of Hole U1351B was on the middle to outer shelf (U8–U9) or slope (U6–U8), resulting in less heterolithic variability compared to the uppermost 240 m, where the position of Site U1351 was progressively farther landward of the shelf break. Finally, many nodules, concretions, and cemented beds that could be potential sources of seismic reflectivity are present in the lower part of Hole U1351B, making identification of lithologic surfaces likely to be the cause of seismic sequence boundaries more complex. Further correlation and identification of lithologic surfaces will form part of postcruise research.

Biostratigraphy

Calcareous nannofossils, diatoms, and planktonic and benthic foraminifers from core catcher samples from Holes U1351A and U1351B were examined to develop a shipboard biostratigraphic framework for recovered sediments (Fig. **F24;** Table **T6**). Biostratigraphic control was achieved primarily with calcareous nannofossils in the Pleistocene section and with planktonic foraminifers in the middle Pliocene to late Miocene section where species of the *Globoconella miotumida* lineage were well represented. Occasional infill sampling for calcareous nannofossils between core catchers helped to constrain some bioevents and evaluate abundance distributions of nannofossils across sequence boundaries. Diatoms were absent from all but one core catcher sample. The abundance of calcareous microfossils was variable, and several

samples were barren. Benthic foraminifers were primarily used for determining paleowater depths and depositional environments. All depths in this section are reported in m CSF-A.

A Holocene–late Miocene succession was recovered at Site U1351. The Pliocene/Pleistocene boundary was identified between Samples 317-U1351B-18X-CC and 19X-CC (134.48–147.55 m), based on calcareous nannofossil and foraminiferal biostratigraphic evidence. The Miocene/Pliocene boundary was reliably constrained with planktonic foraminiferal evidence between Samples 317-U1351B-94X-CC and 95X-CC (819.12–822.69 m).

The sedimentary succession at Site U1351 was interrupted by two major unconformities. The first hiatus occurred between the Pleistocene and Pliocene (Samples 317-U1351B-18X-CC and 19X-CC [134.48–147.55 m]), where most, if not all, of the upper Pliocene was missing. The second was an intra-late Miocene unconformity between Samples 317-U1351B-113X-CC and 114X-CC (998.34–1005.34 m), where at least 3.4 m.y. was missing. Other hiatuses, identified on biostratigraphic and/or lithostratigraphic evidence, are shown in Figure F24.

Older, reworked material was evident in nannofossil assemblages throughout this succession, especially in the Pliocene and Miocene, where reworked material constituted a major component of the nannofossil assemblages. In addition, the Pliocene–Miocene sequence lacked all standard low-latitude nannofossil zonal markers except *Reticulofenestra pseudoumbilicus*.

Benthic foraminifers suggest that water depths varied throughout the Pleistocene but generally deepened downcore from inner to middle shelf depths to middle to outer shelf depths before shallowing to inner shelf depths in the middle Pliocene. Water depths then increased downcore to outer shelf to uppermost bathyal depths in the early Pliocene section, below 700 m. Outer shelf to uppermost bathyal water depths persisted throughout the cored Miocene succession, except for an excursion to middle to outer shelf depths in Core 317-U1351B-98X-CC (851.7 m).

Calcareous nannofossils

Nannofossil abundance was highly variable in the cored sections of Holes U1351A and U1351B (Table T7). Preservation was generally good to moderate and poor in only a few cases. Age assignment by means of nannofossils was problematic for the interval between Cores 317-U1351B-20X and 116X (160.16–1024.39 m), where standard warm-water zonal markers were absent. Nannofossil datums used

for age determination for this site are summarized in Table T6.

Pleistocene

All sediments recovered from Hole U1351A (Samples 317-U1351A-1H-CC through 5H-CC [2.56–27.50 m]) were biostratigraphically zoned in NN21, the base of which was defined by the lowest occurrence (LO) of *Emiliania huxleyi* (Table T6; 0.29 Ma). The deepest core catcher sample for this hole (Sample 317-U1351A-6H-CC [28.00 m]) was barren of nannofossils. The frequent but not abundant presence of *E. huxleyi* likely places these samples in Zone NN21a, below the Holocene acme of *E. huxleyi* (i.e., >0.08 Ma).

The Pleistocene in Hole U1351B spanned Samples 317-U1351B-1H-CC through 19X-CC (7.71–147.55 m). The late Pleistocene *E. huxleyi* Zone (NN21a; Fig. F24) was recognized between Samples 317-U1351B-1H-CC and 5H-CC (7.71–32.34 m). The base of this event was dated at 0.29 Ma (Lourens et al., 2004); however, an acme of *Gephyrocapsa aperta* in Samples 317-U1351B-4H-CC and 5H-CC (28.17–32.34 m; dated at ~0.1 Ma) and marked reworking in Sample 317-U1351B-6H-CC (39.27 m) suggest an unconformable boundary. Zone NN20 (0.29–0.44 Ma), a gap zone demarcated by the LO of *E. huxleyi* at its top and the highest occurrence (HO) of *Pseudoemiliania lacunosa* at its base, was identified between Samples 317-U1351B-6H-CC and 10H-CC (39.27–69.83 m). The top of Zone NN19 (0.44 Ma) was robustly constrained between Samples 317-U1351B-10H-CC and 11H-1, 128 cm (69.83–70.98 m); however, its base (1.93 Ma) was loosely placed around Sample 20X-CC (160.16 m).

An unconformity was recognized between 76.92 and 90.02 m (Samples 317-U1351B-12H-CC and 13H-CC), evidenced by the concurrence of two nannofossil bioevents in Sample 317-U1351B-13H-CC: the HO of large gephyrocapsids (>5.5 µm; 1.26 Ma) and the HO of *Helicosphaera sellii* (1.34 Ma). In addition, *Reticulofenestra asanoi*, a common Pleistocene marker (0.84–1.14 Ma), and all large gephyrocapsids >5.5 µm (1.24–1.56 Ma) were missing from this section, suggesting a hiatus of at least 0.7 m.y.

Another hiatus was inferred between Samples 317-U1351B-16X-CC and 18X-CC (120.24–134.48 m), although the amount of time missing was not well constrained. This hiatus was evidenced by the absence of markers identifying the *Calcidiscus macintyrei* Zone and the abrupt disappearance of all *Gephyrocapsa* species below Sample 317-U1351B-16X-CC (i.e., there was no evidence of the downcore, large-to-small gradation associated with this genus in the early Pleistocene).

The Pliocene/Pleistocene boundary was identified between Samples 317-U1351B-18X-CC and 19X-CC (134.48–147.55 m) (Fig. F24). This boundary was also interpreted as unconformable, and planktonic foraminifers provided tentative evidence of a hiatus likely spanning the late Pliocene. The amount of time missing at this hiatus is uncertain.

Pliocene

A distinct increase in the amount of nannofossil reworking (mostly Miocene material) was evident between Cores 317-U1351B-20X-CC and 28X-CC (160.16–236.17 m). Bioevent marker species were poorly represented or absent, and samples were either barren or contained long-ranging taxa as well as reworked material. Benthic foraminifers suggest that deposition occurred in inner to middle shelf water depths, which is consistent with the low planktonic foraminiferal abundances typical of inner neritic environments. Calcareous nannoplankton prefer open oceanic conditions, and thus it is inferred that most of the nannofossil material in this interval is reworked. In addition, we inferred that standard zonal markers were inhibited by the influence of cold southern currents into the region because no low-latitude zonal markers were identified within this interval. Warm-water taxa including discoasters, ceratoliths, and amauroliths were absent, and only five Neogene sphenoliths were found.

The HOs of *Sphenolithus* spp. (3.45 Ma) and *Reticulofenestra pseudoumbilicus* (3.7 Ma) were identified between Samples 317-U1351B-28X-CC and 29X-CC (236.17–247.35 m). Their juxtaposition indicates the presence of a hiatus at this level. Below this hiatus, Samples 317-U1351B-29X-CC through 94X-CC (247.35–819.12 m) contained a substantial component of reworked late–early Miocene nannofossil taxa. Given the absence of standard Pliocene zonal markers, it was not possible to determine precise ages for this interval beyond a broad zonation.

Samples 317-U1351B-29X-CC through 78H-CC (247.35–678.99 m) contained late–middle Miocene reworked nannofossil material, whereas Samples 317-U1351B-78H-CC through 94X-CC (678.99–819.12 m) consisted of primarily middle–early Miocene and a minor component of Oligocene reworked material.

Miocene

Despite massive reworking of Miocene nannofossils in this part of the section, the presence of the short-ranging species *Scyphosphaera graphica* and *Scyphosphaera queenslandensis* in Sample 317-U1351B-95X-CC (822.69 m) indicates a late Miocene age for this sample. This is consistent with ages derived from other fossil groups. The Miocene/Pliocene boundary was constrained to the interval between Samples 317-U1351B-94X-CC and 95X-CC (819.12–822.69 m), which is consistent with findings from both planktonic and benthic foraminifers. Samples 317-U1351B-95X-CC through 116X-CC (822.69–1024.39 m) showed evidence of some in situ material within assemblages, including scyphosphaerids, *Sphenolithus neoabies* (one specimen in Sample 317-U1351B-111X-CC [976.66 m]), and abundant well-preserved coccospheres (delicate articulated nannoplankton skeletons). No definitive nannofossil age could be assigned to the basal cored sediments.

Planktonic foraminifers

Planktonic foraminiferal biostratigraphy of the cored Holocene to late Miocene section of Site U1351 was based on the shipboard study of core catcher samples from Holes U1351A and U1351B (Tables T6, T8, T9). Absolute ages assigned to biostratigraphic datums follow the references listed in Table T3 in the "Methods" chapter. See Tables T10 and T11 and Figure F25 for planktonic foraminiferal abundances and an interpretation of oceanicity.

Holocene

The base of the Holocene was not identified biostratigraphically but was tentatively correlated with a distinctive lithologic boundary at Section 317-U1351B-1H-2, 108 cm (2.58 m), where greenish gray marly sands overlie gray calcareous muds.

Pleistocene

Planktonic foraminiferal assemblages were well preserved in the cored Pleistocene sections of Holes U1351A and U1351B. Specimens, mostly small thin-walled forms, were common to abundant in the upper part of the Pleistocene between Samples 317-U1351A-1H-CC and 6H-CC (2.56–28.00 m) and 317-U1351B-1H-CC and 9H-CC (7.71–65.91 m), where they composed 9%–56% of the total foraminiferal assemblage. Deposition generally occurred under inner to outer neritic oceanic conditions, except in Samples 317-U1351B-6H-CC (39.27 m) and 9H-CC (65.91 m), where planktonic abundances indicate extraneritic oceanic conditions (Fig. F25). Planktonic abundances were <10% in the lower part of the Pleistocene section between Samples 317-U1351B-10H-CC and 18X-CC (69.83–134.48 m), indicating deposition under inner neritic and sometimes sheltered inner neritic oceanic conditions (Tables T10, T11).

Assemblages in the Pleistocene section were dominated by *Globigerina bulloides*, *Turborotalita* cf. *quinqueloba*, and other small globogerinid species.

Globoconella inflata, Neogloboquadrina pachyderma, Neogloboquadrina incompta, and *Orbulina universa* were also present in most of the section. Single specimens of the subtropical species *Globigerinoides ruber* and *Globigerinella aequilateralis* and a sinistrally coiled specimen of *Truncorotalia truncatulinoides* were also present in Sample 317-U1351B-4H-CC (28.17 m), the only sample in which these species were identified. The presence of *Tr. truncatulinoides* suggests that the uppermost part of the section is younger than 1.1 Ma (Table **T6**). Single specimens of *Zeaglobigerina* cf. *woodi* and *Zeaglobigerina woodi* in Samples 317-U1351B-19X-CC (147.55 m) and 21X-CC (168.48 m), respectively, mark the HO of the *Zg. woodi* group and indicate a minimum age of 2.7 Ma for the top of the cored Pliocene section. This suggests that the late Pliocene is missing, presumably at an unconformity between the Pliocene and Pleistocene.

Pliocene

Assemblages were generally well preserved in the middle Pliocene section of Hole U1351B, except in cemented horizons where tests were infilled with pyrite, glauconite, and sparry-calcite (Fig. **F26**). Planktonic foraminifers in this interval made up <6% of the total foraminiferal assemblage and included only small thin-walled forms typical of deposition under sheltered inner neritic oceanic conditions.

Middle Pliocene planktonic assemblages were dominated by *Globigerina bulloides* and other small *Globigerina* species. *Turborotalita* cf. *quinqueloba, Neogloboquadrina pachyderma, Nq. incompta*, and *Globoconella inflata* were also present, and *Globoconella puncticuloides* occurred sporadically below Sample 317-U1351B-20X-CC (160.16 m).

The preservation of planktonic foraminifers was good in the upper part of the Pliocene section of Hole U1351B, and moderately preserved, recrystallized, and pyrite-filled assemblages occurred in sandy horizons lower in the section. In the upper part of the section between Samples 317-U1351B-30X-CC and 69X-CC (255.06–591.90 m), planktonic foraminifers composed <18% of the total foraminiferal assemblage and included mostly small thin-walled forms, with an increasing number of thicker walled forms downcore. Deposition occurred generally under inner neritic and sheltered inner neritic oceanic conditions, except for Samples 317-U1351B-29X-CC (247.35 m), 30X-CC (255.06 m), and 55X-CC (486.50 m), which were deposited under outer neritic oceanic conditions. In the lowermost Pliocene section between Samples 317-U1351B-55X-CC and 94X-CC (486.50–819.12 m), planktonic abundances increased (Fig. **F25**) to a high of 54% at the base of

the section. The maximum size of planktonics also increased downhole, coincident with increased numbers of thicker walled forms.

Early Pliocene planktonic foraminiferal assemblages were dominated by *Globigerina bulloides* and other small globogerinids. *Neogloboquadrina pachyderma, Nq. incompta*, and *Turborotalita* cf. *quinqueloba* also occurred sporadically, with rare specimens of *Orbulina universa, Globigerinita glutinata*, and *Zeaglobigerina woodi* s.l. *Globoconella puncticuloides* and typical 3–3½-chambered specimens of *Gc. inflata* were also present in small numbers down to Samples 317-U1351B-43X-CC (372.13 m) and 44X-CC (382.57 m), respectively. Typical four-chambered populations of *Gc. puncticulata* s.s. were relatively common in the lowermost Pliocene section from Samples 317-U1351B-44X-CC through 94X-CC (382.57–819.12 m), immediately above the HO of *Globoconella sphericomiozea*, where 5% or more of fully grown specimens in populations of *Gc. puncticulata* and *Gc. sphericomiozea* had weak keels on the last formed chamber. In this region of the southwest Pacific, the HO of *Gc. puncticulata* s.s. is dated at ~4.3 Ma, and the HO of *Gc. sphericomiozea* is dated at 5.30 Ma (Cooper, 2004).

Miocene

The preservation of late Miocene planktonic foraminifers was generally moderate to poor. Foraminiferal tests were mostly recrystallized, and chambers were infilled with sparry-calcite (Fig. **F26**), especially in the early late Miocene interval from Samples 317-U1351B-114X-CC through 116X-CC (1005.34–1024.39 m), where zeolites were noted by the shipboard sedimentology team in interstitial cements. Planktonic abundances ranged from 17% to 89%, and planktonic specimens were often thick-walled and sometimes encrusted.

Late Miocene planktonic assemblages were dominated by *Globigerina*, including *Gg. bulloides*. Species of *Globoconella* useful for subdividing and dating the late Miocene were also common, and *Neogloboquadrina pachyderma, Hirsutella scitula, Orbulina universa,* and *Zeaglobigerina woodi* s.l. occurred sporadically in the section. The HO of *Globoconella conomiozea* s.s., where 95% or more of fully grown specimens in populations of *Gc. sphericomiozea* and *Gc. conomiozea* had keels, was constrained between Samples 317-U1351B-100X-CC and 101X-CC (877.62–882.55 m). Typical populations of *Gc. conomiozea* s.s. were present down to Sample 317-U1351B-113X-CC (998.34 m), immediately above the HOs of the early late Miocene species *Globoconella miotumida* and *Hirsutella panda* between Samples 317-U1351B-113X-CC and 114X-CC (998.34–1005.34 m) and the highest common

occurrence (HCO) of *Hirsutella panda* and the HO of *Paragloborotalia mayeri* s.l. within Samples 317-U1351B-114X-CC and 115X-CC (1005.34–1014.56 m). The juxtaposition of *Gc. conomiozea* in the sample above that in which these events occurred suggests a major unconformity with a minimum of 3.4 m.y. missing between Samples 317-U1351B-113X-CC and 114X-CC (998.34–1005.34 m). The planktonic foraminiferal assemblage in Sample 317-U1351B-116X-CC (1024.39 m) indicates a late Miocene age of 10.60–10.91 Ma at the bottom of the hole.

Benthic foraminifers

Benthic foraminifers (in the 150–1000 µm size fraction of washed samples) were examined in 114 core catcher samples from Hole U1351A and U1351B (Table **T12**). The preservation of benthic foraminifers was generally good to moderate in most samples, except in the lower part of the cored section between Samples 317-U1351B-90X-CC and 116X-CC (778.52–1024.39 m), where it was poor. The abundance of benthic foraminifers among a composite group of microfossils was dominant to abundant in the cored Holocene to upper Miocene section (see **"Biostratigraphy"** in the "Methods" chapter). Stratigraphic occurrences of age-diagnostic benthic foraminifers are shown in Table **T6.**

Holocene–Pleistocene

Benthic foraminifers were examined in six core catcher samples from Hole U1351A (Samples 317-U1351A-1H-CC through 6H-CC [2.56–28.00 m]) and 108 core catcher samples from Hole U1351B (Samples 317-U1351B-1H-CC through 116H-CC [7.71–1024.39 m]). Among the age-diagnostic benthic foraminifers, *Notorotalia zelandica* occurred abundantly throughout this hole, except in Sample 317-U1351A-3H-CC (18.15 m). *Notorotalia finlayi*, which is common today in shallow water depths of the New Zealand region, occurred only in Sample 317-U1351A-6H-CC (28.00 m), where it was rare. Only one possible reworked, broken specimen of *Bolivinita pliozea*, whose HO is associated with the mid-Pleistocene Transition (0.6 Ma) in New Zealand waters (e.g., Hayward, 2001), was found in the lowermost Sample 317-U1351A-6H-CC (28.00 m). A middle Pleistocene age (<0.6 Ma) was given to the bottom of Hole U1351A.

In Hole U1351B, the HO of the mid-Pleistocene marker species *Bolivinita pliozea* was observed between Samples 317-U1351B-7H-CC and 8H-CC (47.83–54.46 m). The LO of the extant taxon *Notorotalia zelandica* was noted between Samples 317-U1351B-23X-CC and 24X-CC (180.13–189.75 m)

and the HO of *Haeuslerella parri* was noted between Samples 317-U1351B-28X-CC and 29X-CC (236.17–247.35 m). Hornibrook et al. (1989) reported the appearance of *N. zelandica* in the late Pliocene at the base of the New Zealand Nukumaruan Stage (2.40 Ma) and the disappearance of *H. parri* in the early Pleistocene at the top of the Nukumaruan Stage (1.63 Ma).

Pliocene

The HO of *Notorotalia hurupiensis* was recognized between Samples 317-U1351B-33X-CC and 34X-CC (278.35–286.38 m). The LO of *Notorotalia finlayi* was observed between Samples 317-U1351B-57H-CC and 59H-CC (507.60–510.49 m). These datums are correlated with the base of the New Zealand Waipipian Stage (3.62 Ma). The HOs of *Notorotalia taranakia* and *Haeuslerella morgani* were identified between Samples 317-U1351B-83X-CC and 84X-CC (716.94–726.71 m), supporting an early Pliocene age (New Zealand Opotian Stage [3.62–5.30 Ma]) for this interval.

Miocene

Three benthic bioevents were noted in the late Miocene interval. The HO of *Texturalia miozea* was observed between Samples 317-U1351B-96X-CC and 97X-CC (832.15–847.79 m). This event is questionably dated as late Miocene (New Zealand upper Tongaporutuan Stage [6.67–8.95 Ma]). The LO of *Haeuslerella parri* was identified between Samples 317-U1351B-99X-CC and 100X-CC (861.39–877.62 m), and the LO of *Bolivinita pliozea* (including *Bolivinita* cf. *pliozea*) was recognized between Samples 317-U1351B-114X-CC and 115X-CC (1005.34–1014.56 m), New Zealand Kapitean and upper Tongaporutuan Stages, respectively.

Paleowater depths

Interpreted paleowater depths based on presence, absence, and frequency of key benthic foraminiferal species or genera are shown in Figure **F27.** Terminology for depth zones is given in Figure **F9** in the "Methods" chapter.

The most commonly occurring benthic group was the diverse *Notorotalia* group, which composed >30% of benthic assemblages in most of the cored sequence. The *Notorotalia* group includes *N. aucklandica*, *N. zelandica*, *N. finlayi*, *N. inornata*, *N. hornibrooki*, *N. hurupiensis*, *N. taranakia*, and *N. profunda*. Species abundances within this group varied in the studied section and provided valuable water depth information. Other ubiquitous taxa included *Nonionella flemingi*, *Astrononion* sp., *Anomalinoides sphericus*, shallow-water miliolids, and textularids (e.g., *Haeu-*

slerella). Uvigerinids, cassidulinids, and buliminids were generally less common.

Paleowater depths inferred from depth-restricted taxa suggest inner shelf and middle shelf environments for most of the Holocene–late Pleistocene interval in Hole U1351A, shallowing to subtidal in the lowermost part. The fauna is characterized by the inner to middle shelf species *Notorotalia zelandica*, *N. hornibrooki*, and *Quinqueloculina auberiana* in Samples 317-U1351A-1H-CC through 5H-CC (2.56–27.50 m). In Samples 317-U1351A-2H-CC (11.44 m) and 4H-CC (25.08 m), the middle to outer shelf indicator *Anomalinoides sphericus* was also abundant. Benthic faunas in Sample 317-U1351A-6H-CC were dominated by the estuarine to subtidal indicator *Elphidium charlottense* and associated *Notorotalia* and miliolids.

The Holocene–middle Pliocene section of Hole U1351B was dominated by taxa indicative of inner to middle shelf environments (Samples 317-U1351B-1H-CC through 30X-CC [7.71–255.06 m]), but inner or middle to outer shelf environments were occasionally noted in this interval. Taxa included inner to middle shelf species *Notorotalia zelandica*, *N. aucklandica*, *N. hornibrooki*, *Notorotalia depressa*, and *Quinqueloculina auberiana*. The latter taxon is occasionally associated with the estuarine to subtidal indicator *Elphidium charlottense* and the middle to outer shelf indicator *Anomalinoides sphericus*.

The late early Pliocene interval between Samples 317-U1351B-34X-CC and 65H-CC (286.39–563.80 m) contained abundant *Notorotalia hurupiensis* and the extant inner to middle shelf species *N. aucklandica*. *Anomalinoides sphericus* co-occurred with the above taxa in the lower part of the interval (Samples 317-U1351B-34X-CC through 43X-CC [286.39–372.13 m]). Thus, the paleowater depth for most of this section was estimated as inner to middle shelf and slightly deeper for the upper part of the section.

In the earliest Pliocene–late Miocene (Samples 317-U1351B-66X-CC through 116X-CC [564.07–1024.39 m]), the deepwater species *Notorotalia profunda* was dominant. This species occurred in association with *Notorotalia hurupiensis*, *Nonionella flemingi*, *Astrononion* sp., and other foraminifers common in bathyal depths, such as *Uvigerina* spp., *Pullenia* spp., and *Melonis* spp. Outer shelf to uppermost bathyal environments characterize the succession between Samples 317-U1351B-82X-CC and 116X-CC (707.27–1024.39 m), except in Sample 98X-CC (851.69 m) where there is an excursion to middle to outer shelf water depths.

The downhole transition from shelfal to bathyal faunas was poorly defined in terms of benthic assemblages but was inferred to occur between Samples 317-U1351B-69X-CC and 82X-CC (591.90–707.27 m).

Diatoms

All core catcher samples from the Holocene–late Pleistocene succession in Hole U1351A (Samples 317-U1351A-1H-CC through 6H-CC [2.56–28.00 m]) were examined for diatoms, but they were only found in Sample 317-U1351A-1H-CC (2.56 m) (Table T13). Diatoms were common and moderately preserved in this sample, and the assemblage was dominated by *Paralia sulcata* (99%), with minor *Thalassionema nitzschioides*, resting spores of *Chaetoceros* and *Hyalodiscus* sp. (living in today's coastal regions). A fragment of the freshwater and brackish water genus *Pinnularia*, which is presumed to have been transported from the mouth of a river, was also found in this sample.

Core catcher and calcareous concretion samples (124 in total) from Holocene–upper Miocene Hole U1351B sediments were examined for diatoms (Table T13). Although diatoms occurred in most samples, they were severely etched. Other samples were barren, most likely because of dissolution. An exception is Sample 317-U1351B-13H-CC (90.02 m), a hard silt taken from inside bivalve shells. Most of the preserved diatoms were fragments, but a biostratigraphically useful species, *Thalassiosira fasciculata* (HO = 0.56–0.61 Ma; LO = 4.30–4.69 Ma), was identified along with an extant cosmopolitan species, *Coscinodiscus radiatus*. No diatoms were found in any concretion sampled.

Macrofossils

Macrofossils were examined in cored sediments from all Site U1351 holes. Provisional identification, age, and habitat preferences are provided in Table T14.

Paleomagnetism

Paleomagnetic analyses at Site U1351 included routine measurement and partial demagnetization of natural remanent magnetization (NRM) of archive section halves and some discrete samples from the working halves of cores. Rock magnetic experiments were also performed on these discrete samples. All depths in this section are reported in m CSF-A.

Section-half measurements

Natural remanent magnetization

NRM was measured on all archive section halves from Holes U1351A and U1351B unless the core ma-

terial was too heavily disturbed by the drilling process. The record from Hole U1351A is similar to but much shorter than that from Hole U1351B and is therefore not presented in Figure **F28.** Magnetization intensities commonly ranged from 10^{-4} to 10^{-2} A/m, with anomalously high values (10^{-1} A/m) often observed at the tops of cores and occasionally at points within cores. High-intensity values at the tops of cores often correspond to high-susceptibility intervals of coarse and shelly sediments, interpreted as cave-in, which may contain rust from the drill pipe (Richter et al., 2007). On some occasions, intensity spikes within cores could be traced to blade fragments from core splitting or wires from loose microsphere bags (these wires were removed at subsequent sites). At other times, no obvious source of the high intensity was identified.

Alternating-field demagnetization

Archive section halves were routinely demagnetized with alternating fields at 10 and 20 mT steps to remove any unstable overprints from drilling and handling or natural viscous remanent magnetization (VRM) overprints in an attempt to isolate a stable characteristic remanence. The response to demagnetization varied throughout the core; however, on average, intensities were ~30% lower than NRM after the 20 mT step. The most systematic change in orientation with demagnetization was recorded in the uppermost 65 m of Hole U1351B (Fig. **F29**). The generally steep (~80°) positive inclinations of NRM became negative (about –60°) after 20 mT demagnetization. Other intervals (e.g., 150–170 m; Fig. **F30**) had very little variation in orientation with demagnetization. This lack of change, together with a bias toward northward declinations in the cores (which were not oriented below Core 317-U1351B-5H [32.39 m]), suggests a drilling overprint (such as that described by Richter et al., 2007) that is still stable at 20 mT. Nonmagnetic core barrels were used throughout APC coring to 94.7 m, and episodes of pervasive drilling overprints were recognized only below this depth.

In some intervals below 94.7 m, demagnetization caused variation in the orientation of the remanence, but a stable component could not be demonstrated. Higher levels of demagnetization of discrete specimens are required to determine whether these orientations are stable and characteristic.

Magnetic susceptibility

Magnetic susceptibility was measured on whole cores and archive section halves, as described in **"Physical properties."** Some correlation between magnetic susceptibility and NRM was observed in Hole U1351B (e.g., 150–175 m; Fig. **F30**), demonstrating that, at least in these intervals, ferromagnetic minerals contribute significantly to susceptibility.

Discrete measurements

A suite of measurements was applied to discrete samples to characterize the rock magnetic properties of the sediment. Reported intensities were derived from raw moments measured on the superconducting rock magnetometer (SRM) using a standard volume of 7 cm³ (see **"Paleomagnetism"** in the "Methods" chapter).

Thermal demagnetization of NRM

Magnetic iron sulfides were reported at nearby Site 1119 (Shipboard Scientific Party, 1999), and these were therefore expected in sediments cored at Site U1351. Because the coercivity spectra of these minerals normally overlap those of magnetite and other iron oxides, thermal demagnetization was attempted to test for the presence of magnetic iron sulfides, which have conspicuous unblocking temperatures of ~340°–360°C. Eight samples were thermally demagnetized, but the plastic cubes deformed upon heating to 140°C, and heating steps were discontinued. Susceptibility was monitored during thermal demagnetization by measuring each sample with a Kappabridge KLY 4S meter after remanence was measured. Susceptibility values ranged from 81×10^{-6} to 246×10^{-6} SI units. No significant changes in susceptibility were noted up to 140°C. Very little magnetization was lost by 140°C, and thus samples were further demagnetized using alternating fields up to 80 mT in the inline coils of the SRM.

Alternating-field demagnetization of NRM

A representative suite of samples was demagnetized in a stepwise fashion using alternating fields (5 mT steps up to 80 mT). Demagnetization data were noisy, and components were difficult to trace. However, most samples had an unstable subvertical positive inclination component that was removed by alternating fields of 15–25 mT and a second shallower, more stable component that tended toward the origin up to 50 mT. At higher peak fields, sample intensities increased, presumably through the acquisition of a gyro-remanent magnetization (GRM). The first component was interpreted as a subvertical result of viscous isothermal remanent magnetization (VIRM) drilling overprint and VRM natural overprint, and the second component was interpreted as the characteristic component, which confirms that in some cases the routine 20 mT demagnetization of

the archive section halves revealed the characteristic magnetization of the samples.

Isothermal remanent magnetization acquisition

Stepwise isothermal remanent magnetization (IRM; up to 1 T, followed by a backfield acquisition to the same field) was applied to seven samples to establish IRM saturation and coercivity of remanence (Fig. F31A). These acquisition curves show that saturation was reached between 300 and 400 mT for the majority of samples. Coercivity of remanence was typically 40–70 mT. These values are consistent with magnetite and/or iron sulfides as the remanence carriers.

Alternating-field demagnetization of IRM

The saturation IRM of the same seven samples was also demagnetized by alternating fields up to 80 mT (Fig. F31B, F31C). The resulting demagnetization curves show a distribution of mean destructive fields (MDF) from 25 to 65 mT (samples from 809 and 11 m, respectively), with most samples showing an MDF of 35–50 mT. Approximately 20% of IRM was demagnetized by the 20 mT step. A single sample (54 m) had an anhysteretic remanent magnetization imparted by a direct field of 0.05 mT in a 100 mT alternating field. This sample was then stepwise demagnetized with alternating fields, yielding a demagnetization spectrum similar to that of the IRM of the same sample (not shown).

Magnetostratigraphy

Because of low core recovery and a pervasive drilling overprint, it was not possible to construct an extensive magnetostratigraphy for Site U1351. However, some candidates for polarity reversals were identified in intervals with better core recovery, and these may be incorporated with other dating techniques to identify chrons from the geomagnetic polarity timescale (GPTS). The most compelling of these is the distinct change in demagnetization behavior across the unrecorded interval between 65.9 and 69.7 m (Fig. F29). This interval, composed of coarse shell hash interpreted as cave-in, was not measured in the SRM. The NRM of the overlying material had a positive inclination interpreted as an overprint, but demagnetization revealed a more stable negative (normal in the southern hemisphere) component. Below 69.7 m, intensity decreased with demagnetization, suggesting that an unstable component was still being removed. However, inclinations remained positive (reversed), which suggests that this boundary represents the first polarity change in Hole U1351B—from a long normal polarity zone interpreted as the Brunhes Chron to a reversed polarity interval interpreted as the Matuyama Chron or older. An interpretation of

this transition as the Brunhes/Matuyama boundary depends on how much time is represented by a potential unconformity between the two zones. Nannofossil evidence shows the HO of *Pseudoemiliania lacunosa* (0.44 Ma) between 65.96 and 70.98 m and the HO of *Gephyrocapsa* >5.5 μm (1.26 Ma) between 76.97 and 90.02 m.

Physical properties

The shipboard physical properties program at Site U1351 included nondestructive measurements of gamma ray attenuation (GRA) densitometer bulk density, magnetic susceptibility (loop sensor; MSL), natural gamma radiation (NGR), and *P*-wave velocity (measured with the *P*-wave logger [PWL]) on all whole-round core sections. Additionally, magnetic susceptibility (point sensor; MSP), discrete *P*-wave velocity (measured with *P*-wave bayonets [PWB] and the *P*-wave caliper [PWC]), spectrophotometry and colorimetry, moisture and density (MAD), and sediment strength were determined on working section halves from Holes U1351A and U1351B. Unless otherwise noted, all depths in this section are reported in m CSF-A.

All measurements were made on all APC cores from Holes U1351A and U1351B to 28.0 m (Section 317-U1351A-6H-2) and 512.4 m (Section 317-U1351B-59H-3), respectively. Continuous APC coring in Hole U1351B ended with Core 317-U1351B-13H (99.7 m). Below this depth, coring was accomplished predominantly with the XCB system, and only occasional APC cores were taken. Because of drilling disturbance associated with XCB coring and the slightly smaller diameter of the core relative to that of the core liner, whole-round magnetic susceptibility and *P*-wave measurements were degraded in quality for XCB cores. In general, physical property measurements of sections from Holes U1351A and U1351B correlate well. Whole-round and section-half core logging measurements below ~290 m in Hole U1351B were affected by poor core recovery.

Gamma ray attenuation bulk density

GRA bulk density was measured at 5 cm intervals (measurement time = 5 s). Raw data ranged from 0 to 2.3 g/cm³ (Fig. F32). After Gaussian low-pass filtering (50 passes), this range narrowed to 1.6–2.2 g/cm³ (Fig. F33). Cyclic variations in GRA density may reflect varying concentrations of sands and/or clays related to glacial–interglacial changes.

A comparison of GRA densitometer data with MAD data from samples in the uppermost 28 m of Holes U1351A and U1351B yields nearly identical results

(Fig. F34). One spurious MAD result was found in Hole U1351B, but otherwise the four data sets are remarkably consistent. Note that other spurious GRA densitometer results obtained at core section ends were removed from this plot. The remaining low values may be the result of incomplete filling of the core liner. Deeper in the hole (below ~400 m), GRA and MAD data diverge, with GRA data following the trend of MAD samples but yielding slightly lower values (Fig. F35A).

A comparison of bulk density measured with different methods and expanded to include downhole logging results (also using a GRA densitometer) from Hole U1351B is shown in Figure F35A. Significant parts of Hole U1351B were wider than 20 inches, suggesting less than ideal results for density and porosity downhole tools. Nevertheless, GRA bulk density from cores is consistently lower than density from downhole logging. Figure F36 illustrates two hole sections with fairly complete core recovery, one where the hole exceeded the caliper measurements (>19.5 inches) and one where the hole diameter was <19.5 inches.

In the narrow-diameter hole interval (~140–210 m), downhole logging and MAD data are nearly identical (Fig. F36A). The MAD outlier at 175 m is from a small concretion found in the core and represents a higher bulk density than the overall sediment at that depth. GRA density values are somewhat lower than both MAD and downhole logging data values. Variations related to coring disturbance are evidenced by the repeating pattern of GRA densitometer measurements, with relatively higher densities near the core base and lower values toward the top. The higher values are generally consistent with downhole logs and MAD measurements, whereas the lower values are not.

In the larger diameter hole interval (210–270 m), downhole logging again yielded the highest densities and the GRA densitometer gave the lowest estimates (Fig. F36B). Variations in bulk density are indicated by both MAD and GRA estimates from cores. However, GRA results again tended to be affected by the coring process in that densities were low at the top of each core and increased with depth. This is consistent with core compaction, which occurs as the core liners are progressively filled during the coring process. This trend was not seen in MAD data, nor was it observed in the downhole log.

MAD data are minimally affected by coring disturbance and are therefore generally more reliable than GRA density data from cores. MAD data usually have bulk density values very close to those of downhole density data (Fig. F36A). The discrepancy between values from MAD analyses and those from downhole logging (Fig. F36B) therefore points to the possibility that downhole density logs were affected by the large diameter of the hole.

Magnetic susceptibility

Magnetic susceptibility (MSL) was measured at 5 cm intervals (measurement time = 2 s). The raw data ranged from 3.5 to 134.5 instrument units in Hole U1351A and from 0 to 872.8 instrument units in Hole U1351B (Fig. F32). Note that extremely high or low values, interpreted as noise, are not shown. Extremely high values at the tops of core liners may be linked to caved shell-hash material. Contamination by caved sediments is also associated with high magnetic remanence values (see "Paleomagnetism"). Comparable low magnetic susceptibility was also obtained at Site 1119 (Shipboard Scientific Party, 1999) and potentially associated with voids. To help illustrate key trends, data were cleaned using a Gaussian low-pass filter (50 passes; Fig. F33).

Magnetic susceptibility (MSP) was measured at 5 cm intervals (measuring time = 1 s) (Fig. F32). Measurements were made on all section halves unless drilling or surface disruption precluded the collection of meaningful results. MSP data at Site U1351 correlate well with MSL data from whole-round core sections; this is most readily apparent in the uppermost 180 m of Hole U1351B (Figs. F37, F38). Again, extreme low and high values are not plotted. Filtered data (using the same 50-pass Gaussian low-pass filter applied to MSL data) are plotted for Hole U1351B in Figures F33 and F38.

MSP and MSL measurements are clearly cyclical in the uppermost ~180 m of Hole U1351B, particularly in the uppermost 80 m where core recovery was most complete (Figs. F37, F38). This cyclicity is similar to that noted in magnetic susceptibility and NGR data from Site 1119 (Shipboard Scientific Party, 1999). At Site 1119, NGR cycles were interpreted as glacial–interglacial cycles (Carter and Gammon, 2004). In Hole U1351B, magnetic susceptibility shows a degree of correlation with NGR and GRA bulk density, most noticeably in the raw (unfiltered) data of the uppermost 180 m (Fig. F37).

Natural gamma radiation

NGR was measured with the Natural Gamma Radiation Logger (NGRL) on all core sections at 10 cm intervals. Measured values ranged from 5 to 75 counts per second (cps), with higher values associated with muddy lithologies and lower values associated with sands. A marked cyclicity is apparent in the uppermost 75 m, where four (not necessarily contiguous)

cycles occur. At greater depths, poor recovery precluded cycle recognition (Figs. **F32, F33**).

Where they overlap in coverage, NGRL measurements correspond moderately well with those from the downhole triple combo gamma ray tool, as do measurements made through the drill pipe down to 90 m WSF. The downhole record displays gamma cyclicity down to ~220 m WSF, which is therefore the probable base of the interval of marked sand/mud cyclicity that characterizes the upper part of Hole U1351B (see **"Downhole logging"**).

The uppermost 20 m of the NGRL record displays a cyclical pattern similar to that of marine isotope Stages (MIS) 1–6, as documented previously at nearby Site 1119 (Shipboard Scientific Party, 1999) (Fig. **F39**); however, below this depth, the NGR pattern becomes irregular and is difficult to match with earlier parts of the oxygen isotope curve. Carter and Gammon (2004) have shown the inverted NGR record to be a close proxy for MIS in offshore eastern South Island to at least 2.4 Ma. Although the record from Hole U1351B may seem to display an out-of-pattern sharp gamma low near the inferred time of peak MIS 6 cooling, Carter et al. (2004) interpreted a similar peak at Site 1119 as representing the passage of the Subtropical Front over the site.

Assigning ages of 127 ka to the MIS 5e peak and 12 ka to the inferred latest Pleistocene point (where NGR suddenly decreases from ~58 to 20 cps) allows a provisional timescale to be derived for the uppermost 25 m of Hole U1351B (Fig. **F39**). In turn, this age model suggests that an almost 3 m thick section of Holocene age may occur at the top of the core. If these correlations are correct, the MIS 1–5 glacial–interglacial cycle is 16 m thick in Hole U1351B compared with 46 m thick at Site 1119, indicating that over this part of the record Hole U1351B has a sedimentation rate about one-third that of Site 1119.

Below 22 m (i.e., below MIS 6), the lack of age control and the almost certain occurrence of other significant unconformities make it impractical to use the NGR record to contribute to age control.

P-wave velocities

P-wave velocity measurements were recorded nearly continuously on sections from Holes U1351A and U1351B at 5 cm intervals using the PWL on the Whole-Round Multisensor Logger. *P*-wave velocities were also measured on section halves using the PWC and PWB (Fig. **F40**). In a Cartesian coordinate system, the PWC measures *P*-wave velocity vertically to the sectional plane of the working half (*x*-axis), whereas the PWB measures the cross section (*y*-axis) and long axis (*z*-axis) of the core.

Unfortunately, all three measuring tools yielded poor results below ~22.5 m in both holes because of signal attenuation and sediment cracking caused by high gas content. Below 512 m, sediment disturbance related to XCB coring was too great for any signal to be generated. PWL, PWC, and PWB data from the uppermost 25 m in Holes U1351A and U1351B are presented in Figure **F40.** Poor results for *z*-axis *P*-wave velocity are not shown.

PWL data from both holes and discrete *P*-wave velocity from Hole U1351B are positively correlated. Within the uppermost ~22.5 m, the values range from 1411 to 1751 m/s. In the uppermost ~2.0 m, *P*-wave velocity decreases slightly downhole (from 1580 to 1530 m/s). Below this depth, *P*-wave velocity increases gradually downhole (from 1530 to 1650 m/s), matching the increase in bulk density indicated by MAD results. Discrete *P*-wave (*x*- and *y*-axis) velocity data from Hole U1351A are more scattered but show the same trend.

Spectrophotometry and colorimetry

Spectrophotometric measurements and associated colorimetric calculations were made on section halves at 5 cm intervals at the same positions as MSP measurements. Color data were recorded as L*, a*, and b* variations. L* values in particular show clear long-term trends in Hole U1351B (Fig. **F41**). Similar but less pronounced trends are also observable in b* data. Variations in a* are less pronounced than those in b* or L*. Variations in b* correlate with similar variations in magnetic susceptibility, particularly in the uppermost ~80 m of the hole (Fig. **F42**), which suggests that the lithologic/mineralogic controls on b* may be the same or at least similar to those that control magnetic susceptibility. A noticeable departure from this covariant relationship occurs between ~28 and ~35 m, an interval corresponding broadly to a sand-rich interval (Fig. **F42**). Within this interval, L*, a*, and b* values fluctuate more markedly and do not correlate well with magnetic susceptibility.

Moisture and density

MAD measurements were made on approximately one sample per section throughout Holes U1351A and U1351B (Fig. **F43**). Extra measurements were taken for occasional variations in facies. Measurements were coordinated with smear slide samples. Two cemented nodules at 175 and 976 m were sampled and measured, with the former having the lowest porosity measured in the core (15.2%) and the latter having a relatively low porosity (28.7%).

High variability typical of these properties was observed in the shallowest cores, followed by some

reduction in variation with depth. The sampling method was tested in one case because of a fortuitous error. Samples were collected using a syringe as a miniature piston corer to minimize the compaction of samples during acquisition. Because of a sampling error, two adjacent samples were taken in Hole U1351B. One was compacted by the syringe by ~20%, whereas the other was obtained in the usual manner. The differences in calculated bulk density, grain density, porosity, and void ratio between the two samples vary between 0.9% and 1.9%, confirming that the MAD method is not sensitive to the sampling procedure and is insensitive to fabric disturbance as long as no water is lost in the process. However, a total analysis error of at least 1%–2% should be assumed.

Curve fitting revealed a subtle burial effect in Hole U1351B (Fig. **F43**). Statistically, bulk density had the poorest relationship with depth and increased at a rate of <0.1 g/cm^3/km. The decrease in porosity with depth fits an exponential compaction curve:

$$\rho_b = 2.01 + 0.09z \qquad (R = 0.28),$$

$$\rho_g = 2.83 + 0.10z \qquad (R = 0.40),$$

$$\phi = 45e^{-(z/5.168)} \qquad (R = 0.51),$$

$$v = 0.83e^{-(z/2.93)} \qquad (R = 0.52),$$

where

  ρ_b = bulk density in g/cm^3,
  ρ_g = grain density,
  ϕ = porosity in percent,
  v = void ratio, and
  z = depth in kilometers.

The overall uniform nature of the sediments at Site U1351 is ideal for using downhole logging methods to determine porosity. However, the diameter of Hole U1351B was often too large for reliable porosity results from downhole logging (Fig. **F35B, F35C**). Despite this limitation, the general log porosity trend compares well with that seen in MAD data. Low porosity values calculated from downhole log density (Fig. **F35B**) are consistent with MAD porosities and higher GRA densities (Fig. **F35A**). This is shown clearly in the expanded view of the 140–260 m interval (Fig. **F44**). Interestingly, where the hole was wide, neutron porosity downhole log values are entirely consistent with MAD porosities, whereas neutron porosities are somewhat higher where the hole was relatively narrow. The highest porosity values seen in the logs (below 600 m; Fig. **F35B**) are most likely artifacts of hole-width issues

related to sands in the formation that were partially washed out by the coring process. However, many of the more moderate high-porosity intervals do not correspond to recovered cores and, as such, may correspond to high porosity in unconsolidated sands and/or gravels.

Sediment strength

Sediment strength measurements were conducted on working section halves from Holes U1351A and U1351B using automated vane shear (AVS) and fall cone penetrometer (FCP) testing systems (Fig. **F45**). A comparison of both measurement methods is shown in the cross-plot in Figure **F45E**.

Shear strength indicates that sediments range from very soft (0–20 kN/m^2) to very stiff (150–300 kN/m^2). Vane shear and fall cone shear strength correlate well in very soft and soft sediments, but AVS values are about three times lower in firm to very stiff sediments (standard deviation = 20.8 kN/m^2) than FCP values (standard deviation = 68.9 kN/m^2). These findings suggest that the applicability of vane shear in firm to very stiff sediments is limited and the vane shear test underestimates the strength of stiffer sediments. Overall, vane shear and fall cone strength data from Holes U1351A and U1351B correlate positively (Fig. **F45A–F45D**). Between 0 and ~250 m, shear strength increases slightly, indicating a change from very soft to firm sediments. Intervals with very poor core recovery (~250–730 m and ~810 m to hole bottom) have distinctly lower strength values, which may be associated with the disadvantageous sediment properties that led to the poor core recovery. Between ~730 and ~810 m, sediment shear strength increases from firm to stiff. In the uppermost 50 m, shear strength correlates well with cycles seen in magnetic susceptibility, GRA density, and NGR, supporting the interpretation that these fluctuations represent prominent changes in the sedimentary regime reflecting glacial and interglacial climate.

Geochemistry and microbiology

Organic geochemistry

Shipboard organic geochemical studies of cores from Site U1351 included monitoring hydrocarbon gases, carbonate carbon, total organic carbon (TOC), total sulfur (TS), and total nitrogen (TN) and characterizing organic matter by pyrolysis assay. The procedures used in these studies are summarized in **"Geochemistry and microbiology"** in the "Methods" chapter. All depths in this section are reported in CSF-A.

Volatile gases

All cores recovered at Site U1351 were monitored for gaseous hydrocarbons using the headspace (HS) gas technique, and, where possible, core gas voids were analyzed using the vacuum syringe (VAC) technique (Tables T15, T16; Figs. F46, F47).

Sediment gas content is below detection levels in the uppermost three cores from Hole U1351A. Methane is first detectable at 19.7 m in Hole U1351A and at 18.2 m in Hole U1351B. The dissolved methane gradient (equivalent to 0.17 mM/m) from 18 to 40 m projects to 17.4 m as the division between diagenetic zones, characterized by sulfate reduction above and methane generation below.

Headspace methane content generally increases to a maximum of 22,660 ppmv at 117 m and then decreases downhole. Headspace methane content represents residual gas in cores, with some gas having been lost during core retrieval and sampling. Ethane is present in all cores in which gas was detected, but propane is present only in cores below 750 m (Fig. F46). One section (317-U1351B-106X-3; 931 m) contains a trace of ethene, but no propene was detected in any cores (Table T15). The composition of the gas, as expressed by the C_1/C_2 ratio (Fig. F46), shows the expected gradual increase in relative ethane content with increasing depth and temperature. However, C_1/C_2 ratios are unusually low for sediments with such shallow depths of burial and are difficult to reconcile with prevailing sediment temperatures at the present time. The relatively high content of ethane at this site could reflect greater subsurface loss of methane (by intense anaerobic methane oxidation at the sulfate–methane transition), perhaps enhanced by the numerous episodes of shelf emergence during periods of lower sea level. However, the presence of ethane in headspace samples at levels of 10–20 ppm immediately beneath the sulfate reduction zone is unusual in sediments recovered during ODP or IODP expeditions, indicating that the sediments have a history of higher temperatures. A series of unconformities in the uppermost 250 m of sediment suggests some removal of sediment (see "Lithostratigraphy"), which, combined with a history of exposure to warmer seafloor temperatures, could account for the apparently anomalous ethane contents.

The C_1/C_2 results of the six core void gases (Fig. F46) are generally parallel with headspace gas data but are offset to higher values because more C_1 was retained during core retrieval and sampling. Core void gases also contain detectable proportions of wet gas components, including propane, butanes, pentanes, and hexanes, in addition to a trace of ethene (but no pro-

pene) in two samples (Table T16). In the two deepest cores sampled for core void gas analysis, including the core with the highest hydrocarbon abundance (Section 317-U1351B-93X-6 [810.6 m]) (Table T16), a marked depletion of $n\text{-}C_4$ and $n\text{-}C_5$ relative to branched $i\text{-}C_4$ and $i\text{-}C_5$ (Fig. F47) could be interpreted as a partial removal of normal alkanes by biodegradation but more likely reflects the presence of labile hydrocarbon precursors such as isoprene or terpene moieties.

Carbon and elemental analyses

Inorganic carbon (IC), total carbon (TC), total organic carbon by difference (TOC_{DIFF}), TN, and TS were analyzed in 132 sediment samples from 0 to 1014 m (Table T17; Fig. F48). Table T17 also shows TOC_{SRA}, which is derived directly from the source rock analyzer (SRA), whereas TOC_{DIFF} is derived from the difference between TC (measured on the elemental analyzer) and IC (measured by coulometry).

Carbonate content fluctuates between 0.6 and 62.4 wt%, with high carbonate samples concentrated in the uppermost 72 m and scattered high carbonate samples at 144, 172, and 251 m (Table T17). TOC_{DIFF} fluctuates between 0.1 and 1.3 wt% but is mostly <0.5 wt% and averages 0.27 wt%. TOC_{DIFF} is systematically lower than the organic carbon determination given by the SRA (TOC_{SRA}). TOC_{SRA} ranges from 0.3 to 1.5 wt% and averages 0.87 wt% (see "Total organic carbon measurement").

TN and TS vary considerably with depth (Fig. F49). TN is significantly higher in the uppermost 165 m (0.4–0.8 wt%, but with wide scatter), whereas TN values cluster tightly between 0.25 and 0.35 wt% at greater depths. The higher nitrogen content in Hole U1351A and at the top of Hole U1351B corresponds to a zone where TS varies widely from near zero to 0.6 wt%. Below 200 m, sulfur content is never less than 0.2 wt% (average = ~0.45 wt%) and in some samples is >0.8 wt% (Fig. F49D). TOC_{DIFF}/TN and TOC_{DIFF}/TS ratios are less variable, with TOC_{DIFF}/TN ratios clustering at ~1 ± 0.5 and TOC_{DIFF}/TS generally clustering between 0.5 and 1, except in the upper section (above 200 m), where values vary widely. TOC_{DIFF}/TN and TOC_{DIFF}/TS values seem somewhat low, but this may be partially due to using TOC_{DIFF} to calculate the ratios.

Organic matter pyrolysis

Samples from Holes U1351A and U1351B were characterized by SRA pyrolysis (Table T18; Figs. F50, F51). S_1, S_2, and S_3 vary most in the uppermost 200 m, mirroring elemental analysis data, which also

show more variable and higher weight percent N values in this zone (Fig. F49C). Organic matter is dominantly of terrestrial or degraded marine origin, based on predominantly low hydrogen indexes (most samples = <70 mg/g; all samples = <150 mg/g). Again, higher quality organic matter is indicated in the top part of Hole U1351B and in Hole U1351A, with all of the highest hydrogen indexes being in samples shallower than 100 m (Fig. F51A). Oxygen indexes are also more scattered in the uppermost 200 m, suggesting that greater oxygen-containing functional groups may be attached to the kerogen, which is consistent with the low amount of diagenetic alteration of organic matter expected in this zone.

A modified van Krevelen diagram of hydrogen index versus oxygen index (Fig. F52) shows that the sediments dominantly contain Type IV organic matter (no oil-generative potential; dominated by inertinitic macerals), typical of relatively poorly preserved terrestrial organic matter. These results are consistent with data from smear slides, which indicate that little marine organic matter is present and that the visible kerogen comprises plant cells and poorly preserved pollen (see "Lithostratigraphy" and "Biostratigraphy").

T_{max} averages 415° ± 15°C. No consistent trend with depth is visible (Fig. F51C). Some samples have a greater proportion of volatile hydrocarbons (S_1) relative to S_2, resulting in higher production indexes. This is likely due to better preservation of lipids in these particular sediments rather than to the generation of free hydrocarbons, which would not be measurable at the low thermal maturities estimated for this sedimentary succession (maximum temperature near total depth [~1000 m] is probably only 45°–55°C, based on a typical geothermal gradient of 35°–45°C/km for this region) (Sykes and Funnel, 2002; Reyes, 2007).

Total organic carbon measurement

Sediments at Site U1351 were measured for TOC using two completely independent methods:

1. TOC_{SRA} is derived directly from the SRA as the sum of pyrolysis carbon (0.83 × [S_1 + S_2]/10) and residual carbon (S_4/10). The S_4 parameter is the oxidizable (at 580°C) residual carbon remaining after pyrolysis. This technique has the advantage of being derived directly during an analytical run on one instrument.

2. TOC_{DIFF} is derived from the difference between TC (measured on the elemental analyzer) and IC (measured by coulometry). This technique has the advantage of being derived partly from the traditional elemental analysis approach but the

disadvantage of relying on two separate instruments, because carbon associated with carbonate content must be subtracted from TC.

The cross-plot of TC from the elemental analyzer and TC from the SRA and coulometer demonstrates that there is a good correlation (R^2 = 0.95) and that the SRA gives consistently higher values than the elemental analyzer (Fig. F53). The difference is mostly ~40% ± 10%. The calibration method using a 3.1 wt% TOC standard for the SRA may have led to an overestimation of TOC in these organically lean sediments, but it is also possible that the elemental analyzer understated TOC. Inaccuracies in carbonate content or wt% TC measurements are responsible for the apparent negative TOC_{DIFF} values (Table T17).

Preliminary interpretation of organic matter

TOC values are low for typical coastal sediments, regardless of the TOC method considered, likely because of the poor preservation of terrestrially derived organic matter in both carbonate- and siliciclastic-rich sediments that were exposed to extensive bioturbation and sediment reworking. The dilution of organic matter by high sedimentation rates may also be a factor in the low TOC. There is no correlation between carbonate content and TOC_{SRA} (Fig. F54). Samples with high TOC_{SRA} (>1 wt%) have carbonate contents between <1 and >40 wt%, whereas organically lean samples can be either rich or poor in carbonate, which is suggestive of a primary preservation control on organic matter rather than depositional facies. Low TOC contents and the SRA data indicate that Site U1351 sediments contain predominantly terrestrial organic matter and suggest that marine productivity was low. In this respect, this Canterbury Basin shelf site contrasts strongly with New Jersey shelf sites (e.g., ODP Site 902 [Shipboard Scientific Party, 1994] and ODP Sites 1071 and 1072 [Austin, Christie-Blick, Malone, et al., 1998]), which contain high amounts of marine algal–derived organic matter.

Inorganic geochemistry

Forty-nine interstitial water samples (Tables T19, T20) from Site U1351 were collected and analyzed. Eleven samples were taken from Hole U1351A, which was cored to 28 m and dedicated largely to chemistry and microbiological sampling. The intended sampling frequency for Hole U1351B was approximately one sample per core to ~270 m and one sample every other core below that, but actual sample spacing was highly dependent on irregular core recovery. Results from Holes U1351A and U1351B are plotted together in Figures F55, F56, F57, F58, and F59.

Salinity, chloride, and pH

The salinities of interstitial water samples primarily range from 3.1 to 3.4 (Fig. F55D), with the two shallowest samples (at 1.1 and 3.8 m) having somewhat higher salinities (3.8 and 3.5, respectively). Chloride increases steadily downhole in the uppermost 80 m from a near-surface value of 545 mM to a maximum of 612 mM at 52 m (Fig. F55A). Below this depth, chloride fluctuates, decreasing to near-seawater values at 240 m and below and irregularly increasing to 570–572 mM in the less frequently sampled intervals below 400 m. Below 920 m, chloride rises slightly.

pH values measured on pore water samples generally vary between 7.3 and 7.5, a somewhat lower range than that observed in typical or deeper water ODP/IODP core samples (Fig. F56C).

Alkalinity, sulfate, ammonium, phosphate, and dissolved silica

The measured alkalinity of interstitial water samples increases immediately beneath the seafloor, reaching a maximum of 10.1 mM at 16.3 m (Fig. F57A). Alkalinity then decreases steadily throughout the rest of the cored section, reaching 1.2–1.3 mM in the interval from 350 m to total depth in Hole U1351B. The alkalinity increase is mirrored by a decrease in sulfate from 28 mM at 1.1 m to 0.31 mM at 16.3 m (Fig. F57B), defining a sulfate reduction zone. Sulfate remains at or near zero throughout the rest of Hole U1351B, with departures from zero probably representing seawater contamination in the cores.

Ammonium initially increases downhole from near zero at the sediment/water interface to relatively low concentrations (2–3 mM) and then remains relatively constant (Fig. F58C). Phosphate initially increases (from 1.9 to 8.6 µM) in the sulfate reduction zone and then rapidly drops off to essentially zero. Silica initially increases from approximate seawater values to a peak of ~750 µM at 60 m and then decreases to values mostly between 200 and 400 µM throughout the rest of Hole U1351B (Fig. F58B).

Calcium, magnesium, and strontium

Calcium and magnesium both initially decrease in the sulfate reduction zone (Fig. F56), probably in relation to the buildup of dissolved bicarbonate and the precipitation of authigenic carbonate. Below the sulfate reduction zone (0–16 m), calcium increases slightly and magnesium decreases or is relatively constant to ~200 m. Below this depth, magnesium decreases again to ~20 mM and remains constant throughout the remainder of Hole U1351B. In contrast, calcium rapidly increases from 16 mM at 200 m to >30 mM below 220 m (Fig. F56D). The Mg/Ca ratio

decreases correspondingly. Thereafter, calcium remains relatively constant, decreasing in the middle of the section with poor recovery, before increasing again to >45 mM in the deepest sample (989.75 m). Strontium increases throughout the sulfate reduction zone, stays constant to ~200 m, and then increases steadily to ~800 m, where it reaches a peak of 2.1 mM (Fig. F56A). The Sr/Ca ratio decreases sharply at ~200 m and also declines significantly below ~800 m.

Sodium, potassium, barium, boron, silicon, and lithium

Sodium increases to ~12% above seawater values in the uppermost 50 m and then fluctuates before decreasing below seawater values at ~200 m (Fig. F59B). At ~250 m and below, sodium levels out at values ~8% lower than seawater.

Potassium decreases markedly (from 11 to 2 mM) in the uppermost 250 m and then varies between 2 and 4 mM in the lower 750 m (Fig. F59C).

Barium peaks at 23 µM at 6.8 m before decreasing rapidly to ~3 µM at 16 m (Fig. F59D). Thereafter, the profile is relatively constant to 620 m before decreasing to 1 µM at 760 m. In the deepest section of Hole U1351B, barium increases again from 1 to 6.1 µM.

Boron increases rapidly in the sulfate reduction zone and then increases gradually downhole to ~200 m (Fig. F59E). From 200 to 230 m, boron rapidly increases in concentration again. Below 230 m, boron fluctuates mainly between 3 and 5 mM.

Silicon has a maximum value of 756 µM at 10 m and gradually decreases to ~400 µM below ~200 m (Fig. F58D).

Lithium is low from the surface to 150 m and then increases slowly to 200 m, below which it rapidly increases between 200 and 330 m (Fig. F59A). Below this abrupt increase, lithium remains relatively constant before gradually increasing between 750 m and the bottom of the hole. Some of the inductively coupled plasma–atomic emission spectroscopy data for the sample at 555 m may be spurious (boron, strontium, silicon, and lithium).

Preliminary interpretation of diagenesis

Figure F60 is a combined depth plot of methane, alkalinity, sulfate, calcium, magnesium, phosphate, silica, and barium in the uppermost 100 m of Holes U1351A and U1351B. This plot emphasizes the almost exact synchronicity of some of the microbially mediated biogeochemical changes at Site U1351. The increase in alkalinity represents dissolved bicarbonate generated during sulfate reduction. The alkalinity increase, when corrected for the amount of

carbonate precipitation represented by the decrease in calcium and magnesium, just balances the millimolar amount of sulfate removed (Table T21). This approximate 1:1 proportion of bicarbonate added and sulfate removed is consistent with sulfate reduction being driven primarily by the anaerobic oxidation of methane. Methane only appears below 17 m (Fig. F60). The relatively low maximum concentrations of ammonium (3 mM) and phosphate (9 µM) at Site U1351 are also consistent with methane oxidation. Oxidation of marine organic matter during sulfate reduction could potentially produce up to 8 mM of ammonium and 500 µM of phosphate during the reduction of 28 mM of sulfate. Methane oxidation generates no ammonium or phosphate and is thus consistent with the observed low concentrations of these ions.

The increase in dissolved silica throughout the sulfate reduction zone also reflects the decomposition of organic matter, although an increase in silica can also be influenced by the dissolution of diatoms. Changes in calcium and magnesium with depth to 17 m (Fig. F61) probably reflect the precipitation and dissolution of carbonates and/or cation exchange with clay minerals. Both cations decrease rapidly during sulfate reduction, probably because of the formation of isotopically light (from methane oxidation) carbonate. However, little dolomite was observed by XRD analysis of these sediments, so an additional reason for the magnesium trend is possible. Moreover, the increase in ammonium could potentially expel cations from exchangeable positions in clay minerals (Gieskes, 1983). Ammonium ions are known to compete with cations for exchange sites at mineral surfaces (von Breymann et al., 1990). Changes in the concentration of ammonium might lead to other changes in the adsorbed ion fractions.

The downhole decrease in potassium appears to be unrelated to sulfate reduction because the decrease extends considerably farther from the surface to ~150 m (Fig. F59C). Glauconite becomes abundant between 125 and 350 m (see "Lithostratigraphy"), and this may well explain the decrease in potassium in the interstitial waters. A similar but less well defined decrease in sodium (Fig. F59B) extends to ~250 m, and this could also be partly related to glauconite.

Beneath the zone of sulfate reduction, calcium increases, whereas magnesium is relatively constant to ~200 m (Fig. F61). Below 200 m, calcium increases from 16 to 40 mM, whereas magnesium drops from 30 to 20 mM and chloride also decreases. This may represent the dissolution of biogenic calcite with some reprecipitation of diagenetic carbonate. Similar deflections are evident in the depth profiles of lithium, strontium, and boron, although the profiles of

other minor and major elements do not show deflections at 200 m. The lack of a consistent swing in all analytes may suggest that the increases in calcium, lithium, and boron are not due to an influx of basinal brine. The abrupt changes between 200 and 230 m could be due to a major change in lithology or an unconformity that promotes these changes in diagenetic processes.

The increase in calcium, lithium, and barium in the interstitial waters deeper in Hole U1351B (>850 m) may also be related to similar diagenetic processes caused by a lithostratigraphic break (Figs. F56, F59). Chloride, salinity, and silica also increase slightly in this depth interval (Figs. F55, F58), whereas strontium decreases (Fig. F56A). Below 800 m, the dominant lithology changes from muddy sand to sandy mud, with occasional mud intervals (see "Lithostratigraphy"). However, XRD data show little mineralogical variation across this zone, although there is a slight increase in mica content in smear slides below 800 m. Specifically, there is no evidence at present for the dissolution of barite or lithium-rich micas that might explain this significant shift in interstitial water composition. The increase in lithium below 850 m also does not correspond to the more subtle increases in silica and silicon, which occur deeper (Fig. F58B, F58D). Therefore, lithium enrichment is probably not from the transformation of biogenic opal; rather, it may reflect ion-exchange or desorption reactions in which lithium that is adsorbed onto marine sediments becomes incorporated into authigenic clays.

In Holes U1351A and U1351B, boron enrichment is pronounced, having values as high as 11 times that of seawater, with two remarkable increases in the sulfate reduction zone and at ~200–230 m. Boron is usually enriched in marine sediments because it has a great affinity for clay minerals (Hingston, 1964). The deeper boron increase is possibly related to the diagenetic opal-A/opal-CT transition. A smaller fraction of boron may also be associated with bacterial degradation of organic matter.

Microbiology

Microbiological shipboard investigations included testing samples for contamination and performing total cell counts.

Sample collection

At this site, 194 samples were collected for microbiological investigations. These were divided in the cold room into three groups for (1) determining the abundance, identity, and distribution of microbial groups (84 samples); (2) determining intact polar lipid concentrations, types, and stable carbon iso-

tope compositions (26 samples); and (3) conducting contamination tests (84 samples). The sampling strategy is described in **"Geochemistry and microbiology"** in the "Methods" chapter (see Fig. **F10** in the "Methods" chapter).

Contamination tracer tests

In order to reveal the extent to which seawater or individual prokaryotic cells penetrated a sediment sample during drilling operations, a particulate tracer (submicron microspheres) and a water-soluble chemical tracer (PFT) were used. Water-soluble and particulate tracer tests have been successfully employed during other ODP/IODP expeditions (e.g., ODP Legs 185 and 201 and IODP Expedition 301) because the tracers are chemically inert and can be detected with high sensitivity (Smith et al., 2000; House et al., 2003; Expedition 301 Scientists, 2005). After core retrieval and the cutting of the 9.5 m core into six 1.5 m sections, 3 cm^3 samples for PFT measurement were immediately taken from the section ends adjacent to the whole-round samples selected for microbiological analysis (see **"Geochemistry and microbiology"** in the "Methods" chapter and Fig. **F10** in the "Methods" chapter). Samples for PFT analysis were not taken from the actual whole-round samples because we assumed that flushing the samples with nitrogen in the glove box would remove a large quantity of PFT.

Water-soluble tracer

A calibration curve for the PFT analysis could not be achieved despite several attempts. No consistent set of tests on the samples could be performed because relatively high peaks were observed in the same retention time period as the expected PFT peak when a blank run was analyzed. Additionally, peaks located close to the expected retention time of PFT were sometimes present in the chromatograms of the few samples that were analyzed.

Particulate tracer

The number of fluorescent microspheres (2×10^{11}/ 20 mL bag) deployed is equivalent to the number of prokaryotes in ~400 L of seawater (assuming 5×10^8 bacteria/L). Fluorescent beads were successfully deployed in all cores sampled at Site U1351 except Section 317-U1351A-1H-1, whose microsphere bag broke on the catwalk after the core had been retrieved. Beads were detected on the outside of all cores from which samples were taken except Section 317-U1351A-2H-3 (Table **T22**). Nevertheless, their deployment was not homogeneous along the core liner. Consequently, microsphere concentrations may temporarily exceed the natural seawater concentrations of prokaryotes in some locations but be absent elsewhere. No difference in microsphere deployment was found between APC and XCB coring. There was a difference in microsphere concentrations of about three orders of magnitude between the outside and the inside part of the cores. Beads were absent from the center of most cores. Between 10 and 100 beads/cm^3 were detected in only 6 of the 21 whole rounds collected at this site, which indicates potential contamination of samples with a maximum of 100 prokaryotes/cm^3 (Section 317-U1351B-25X-1; Table **T22**). Therefore, the beads are at best a semiquantitative measure of contamination. The presence of multiple microspheres is a strong indication that contamination by microbe-sized particles has occurred, but their absence cannot confirm that a sample is uncontaminated. At this site, microspheres in the outer part of the sediments were not detected in only one sample (Table **T22**). Consequently, additional samples were taken from the drilling fluid to screen potential contaminants and compare them with the phylotypes found in the potentially contaminated samples.

Total cell counts

For prokaryotic cell enumeration, 1 cm^3 plugs were taken from whole-round microbial characterization samples at 21 depths (between 1.4 and 52.1 m in Hole U1351A [12 samples] and between 117.3 and 989.9 m in Hole U1351B [9 samples]). Prokaryotes were present at all 21 depths, with the exception of two samples (Sections 317-U1351A-31X-3 [261.1 m] and 92X-1 [930.9 m]) in which no cells were detected (Fig. **F62**). The greatest abundance of cells was found in the near-surface sample (Section 317-U1351A-1H-1 [1.4–1.5 m]), which contains 1.08×10^8 cells/cm^3; the lowest number of cells (1.34×10^5 cells/cm^3) was found at 930.9 m (Section 317-U1351B-106X-2), a decrease in cell density of a factor of 800. Generally, the total number of cells decreases rapidly with depth in the upper layers of sediment (uppermost 4 m). This depth profile follows the same trend observed at other ODP sites (Parkes et al., 2000). However, the absolute numbers of prokaryotes are lower than the average numbers for all previously examined sites, particularly below 4 m (Fig. **F62**). These results might be related to the detection limit, which is ultimately controlled by counting statistics. In practice, variability in the blanks (arising from the presence of cells resulting from contamination of reagents and during handling) can actually determine the detection limit (in this case the detection limit is 33 cells/filter membrane). If the number of cells counted in the blank is negligible, then the

detection limit is estimated to be the number of cells in a sample required for one cell to be detected with a specified probability (Kallmeyer et al., 2008; Morono et al., 2009). For 2×10^{-4} cm³ of sediment applied to the filter and 200 fields of view counted at 63× and 100× magnification, between 6.02×10^5 and 1.5×10^6 cells/cm³, respectively, must be present in the original sample for one cell to be detected with 95% probability. Treating samples with 1% hydrofluoric acid solution reduced much of the autofluorescence of the filters and allowed the counting of larger amounts of sediment. However, a detection limit <6.02×10^5 cells/cm³ could only be achieved by counting a larger number of fields of view, which was not possible on board ship. Therefore, we decided to count some of the samples with values below detection limit on shore (Fig. **F62**).

Heat flow

Geothermal gradient

Temperature measurements were conducted using the APCT-3 during APC coring in Hole U1351A and the SET tool during XCB coring in Hole U1351B. However, it was not possible to obtain the geothermal gradient. Five temperature measurements were taken in total (Fig. **F63;** Table **T23**). The one APCT-3 measurement yielded a reliable temperature of 11.61°C at 25.1 m CSF-A (unless otherwise noted, all depths in this section are reported in CSF-A) in Hole U1351A. The four trials with the SET tool in Hole U1351B failed because the conductive cooling time after the tool penetrated the sediment was too short (<300 s) to generate reliable fitting curves (Fig. **F63A**). This could have resulted from tool movement caused by ship heave and/or severely disturbed sediments falling around the SET tool tip from the top of the core during measurement. Nevertheless, all five temperature measurements were used to estimate the geothermal gradient. The fitting line to temperature versus depth data is (Fig. **F63B**)

$$T(z) = 0.0141 \times z + 10.209 \qquad (R^2 = 0.6537),$$

where $T(z)$ is in situ temperature at depth z (m CSF-A). The estimated geothermal gradient is therefore 14.1°C/km, which is much lower than the 40°–50°C/km gradient obtained from the nearby exploration well Clipper-1 (Reyes, 2007). The geothermal gradient at Site U1351 is thus likely underestimated because (1) Site U1351 is only ~15 km distant from Clipper-1, (2) sediment as thick as several kilometers at both sites prohibits local fluid circulation in the absence of conduits, and

(3) the geothermal gradient at Clipper-1 was measured in a deep hole (up to 4.7 km below seafloor), so it would not have been affected by seasonal variations in bottom water temperature. For reference, the geothermal gradients at nearby ODP Sites 1120, 1124, and 1125 are 57.4°, 52.1°, and 64.9°C/km, respectively (Carter, McCave, Richter, Carter, et al., 2000).

Thermal conductivity

Thermal conductivity was measured in available whole-round core sections from Holes U1351A and U1351B. The TK04 system was employed using the full-space needle probe method. Measurement frequency was usually once per section with one measuring cycle at each point. This included 19 points (0.3–27.9 m) in Hole U1351A and 212 points (0.7–1004.9 m) in Hole U1351B. Ideally, measurements were to be conducted in the major lithology of each section measured. However, it was difficult to recognize the lithology of whole rounds through the core liner, so the middle of the section was chosen as a measurement point unless a void or crack was observed. Few lithologic variations occurred in each section at Site U1351, so this sampling procedure was appropriate. Probe V10701 was used, and heating power was kept to ~3 W.

Thermal conductivity data were screened when (1) measurements did not satisfy criteria suggested by the TK04 manufacturer because of poor contact between the probe and materials, (2) thermal conductivity values were close to that of water (0.6 W/[m·K]) because of sediment dilution during coring, or (3) measurements were taken in unsuitable lithologies such as shell hash. Thermal conductivity versus depth data from Holes U1351A and U1351B are consistent (Fig. **F64A**). The laboratory-measured thermal conductivity range is 0.962–2.233 W/(m·K) (average = 1.474 W/[m·K]) (Table **T24**). These values are higher than those observed at Site 1119 (Shipboard Scientific Party, 1999), although thermal conductivity data from Site 1119 were collected over a shorter depth interval (<130 meters below seafloor [mbsf]). These high conductivities may be due to high concentrations of quartz (6.5–12.5 W/[m·K]) in the fine-grained sediment, including the clay-sized fraction (see **"Lithostratigraphy"**) and/or carbonate cementation (0.5–4.4 W/[m·K]).

Based on depth (m CSF-A), a bulk density of 2.01 g/cm³ from MAD results (see **"Physical properties"**), and the estimated geothermal gradient, correction for in situ conditions yielded a thermal conductivity range of 0.959–2.215 W/(m·K)

(average = 1.467 W/[m·K]). This calculated in situ thermal conductivity value differs from laboratory measurements by less than ±2.2%.

Despite significant scattering, thermal conductivity generally increases linearly with depth. In particular, decreasing porosity and increasing bulk density in the uppermost 35 m may control the rapid increase in thermal conductivity. Thermal conductivity values reach a local maximum followed by a relatively sudden drop of ~15% at 35 m, where porosity and bulk density do not show such fluctuation. The cause of these variations in thermal conductivity is unclear. Significant scatter in thermal conductivity below ~90 m might be a result of locally cemented sediments with higher thermal conductivities and/or reduced thermal conductivity caused by XCB drilling disturbance.

Despite fluctuations in the topmost portion of the cored interval, data corrected to in situ conditions can be represented by the following linear fit (Fig. **F64A**):

$$\lambda(z) = 1.3704 + 0.0003 \times z,$$

where z is depth (m CSF-A).

Thermal conductivity at Site U1351 varies negatively with porosity and positively with bulk density (Fig. **F64B, F64C**), as expected. Variation in terms of lithology could not be detected.

Bullard plot

Thermal resistance is derived based on the relationship of thermal conductivity with depth:

$$\Omega(z) = [\ln(1.3704 + 0.0003 \times z) - \ln(1.3704)]/0.0003.$$

Following the Bullard approach by assuming conductive heat flow, a linear fit of temperature versus thermal resistance is expected (Fig. **F65**):

$$T(z) = 10.176 + 0.0201 \times \Omega(z) \quad (R^2 = 0.6516).$$

This yields a heat flow of 20.1 mW/m² at Site U1351, which is about one-third that estimated at the Clipper-1 well when adopting the same thermal conductivity as Site U1351. Care should be taken when using the above-estimated geothermal gradient and/or heat flow values because of the poor temperature data.

Downhole logging

Operations

Two holes were logged at Site U1351. Hole U1351B was logged after the completion of coring, whereas Hole U1351C was drilled as a dedicated logging hole in order to increase the chances of obtaining high-quality logs and a vertical seismic profile (VSP) at this site.

Hole U1351B

Logging operations in Hole U1351B began by conditioning the hole for logging immediately after coring was completed at 1616 h on 24 November 2009 (all times are local ship time, UTC + 13 h) to a total depth of 1163.3 m DRF (1030.6 m DSF). After the hole was swept with 50 bbl of high-viscosity mud and displaced with 420 bbl of logging gel, the bit was raised to the logging depth of 215 m DRF (81 m DSF). Rig up of the triple combo tool string (natural gamma ray, bulk density, electrical resistivity, and porosity) began at 2245 h, and the tool string was run into the hole (RIH) at 0015 h on 25 November. While the tool string was being lowered at a speed of 3500–4000 ft/h, gamma ray and resistivity data were recorded from the seafloor to a few meters above the total depth of 1163 m WRF, where a first logging pass was started at 0135 h. This repeat pass was completed at 0203 h (1023 m WRF), and the tool string was run back down to total depth for the full pass, which started at 0225 h at a speed of 900 ft/h. At 0540 h (258 m WRF), the caliper was closed for reentry into the pipe, and the pass was completed at 0615 h when the seafloor was identified by a drop in the gamma ray log at 132 m WRF. The tool string was back on deck at 0630 h and rigged down at 0730 h.

By 0830 h, the FMS-sonic tool string had been rigged up and RIH at a speed of 1500 ft/h to record sonic velocity on the way down. After a difficult exit from the drill pipe, the tool string met an obstruction at 618 m WRF, and after several attempts to go deeper we concluded that the borehole was rapidly deteriorating. At 1050 h, we decided to begin logging up with both the FMS and sonic tools from the deepest depth reached (620 m WRF) at a speed of 1200 ft/h. Because of the apparent collapse of the hole, no second pass was attempted, and the FMS calipers were closed at 255 m WRF before the top of the tool string was pulled into the pipe. Data acquisition concluded at 1200 h, when the sonic log identified the bottom of the drill string. The tool string was back at the surface at 1215 h and rigged down completely at 1315 h. The initial logging plan included a VSP; however, because of the poor hole condition, this was postponed until the next hole, and the rig floor was cleared to resume drilling operations.

Hole U1351C

Hole U1351C was drilled without coring as a dedicated logging hole in order to provide the best possible

conditions for acquiring a complete set of high-quality logging data at Site U1351. The hole was drilled with a 9⅞ inch tricone bit to a total depth of 1100 m DRF (966 m DSF), which was reached at 1815 h on 27 November. After circulating seawater and sweeping the hole with 50 bbl of high-viscosity mud, the bit was released, the hole was displaced with logging gel, and the bit was raised to the logging depth of 218 m DRF (84 m DSF). Rig-up of the triple combo tool string started at 0350 h on 28 November, and the tool string was RIH at 0500 h. At 0515 h, the recording of gamma ray and resistivity logs was initiated as the tools were lowered downhole at a speed of 1500 ft/h. At 0700 h, with the bottom of the tool string at 934 m WRF, the readings of wireline surface tension dropped, but tool head tension remained normal. To restore surface tension, the wireline had to be reeled in to a reading of 915 m WRF. This indicated that the wireline had been spooled over while the tool was not moving. The normal head tension and zero-acceleration of the tool suggested that some section of the upper hole had collapsed and fallen in on the wireline and that the tool string was being held underneath. After several attempts to move up and down, pulling several times up to the limit of the wireline before trying to slack off and apply moderate tension in the hope of wiggling the tool free, we decided that the only way to recover the tool was to go down with the pipe to clear the obstruction and release the tool. The wireline was cut and held from the surface with an assemblage of T-bars. The drill string was lowered around the wireline and trapped tool string, one stand at a time, while circulating in an attempt to clear the obstruction. After a ~36 h effort, the entire tool string was brought to the surface at 1830 h on 29 November, showing only damage to the wireline immediately above the tool, likely from the process of trying to bring the tool inside the pipe. At this point, the logging tools were laid down, and full circulation and rotation capability were restored to the drill string, which was then tripped back to the surface after cementing and abandoning Hole U1351C. As a result, the only logs recorded in Hole U1351C were the resistivity and gamma ray measurements made on the way downhole.

Data quality

Figures **F66, F67,** and **F18** show a summary of the main logging data recorded in Hole U1351B. These data were converted from the original field records to depth below seafloor and processed to match depths between different logging runs. The resulting depth scale is WMSF (see **"Downhole logging"** in the "Methods" chapter).

The first indicators of the overall quality of the logs are the size and shape of the borehole measured by the calipers. The hole size measured by the Hostile Environment Litho-Density Sonde (HLDS) caliper during the triple combo run and by the FMS arms are shown in the left-hand columns of Figures **F66** and **F67,** respectively. Both sets of calipers show that the hole diameter is almost uniformly larger than 18.5 inches (>46 cm) above 500 m WMSF, suggesting that none of the tools were able to make good contact with the formation above this depth and that density and porosity data in particular should be used with caution. Below 500 m WMSF, the hole is apparently less enlarged, but it becomes very irregular. Many anomalously low density readings below 600 m WMSF are likely indicative of multiple narrow washouts that significantly affect the quality of the density readings.

The quality of the logs can also be assessed by comparing log data with measurements made on cores from the same hole. Figure **F66** shows a comparison of gamma ray and density logs with NGR and GRA bulk density track data and with MAD measurements made on cores recovered from Hole U1351B (see **"Physical properties"** for description of core measurements). The different sets of measurements generally agree well, even in the upper half of the hole where the calipers indicate an enlarged borehole. Because of the in situ nature of the density log, its values should be equal to or slightly higher than measurements made on the recovered core. The fact that this is verified over most of the interval logged is one more indication that, with the exceptions of the obvious anomalies in the deeper section of the hole, the density log was not seriously affected by the hole conditions and should provide reliable constraints for the generation of a synthetic seismogram and detailed seismic–well correlations.

The very good agreement shown in Figure **F19** between the logs recorded in Holes U1351B and U1351C shows that the gamma ray and resistivity logs were not significantly affected by the enlarged hole in the upper part of Hole U1351B. None of the low gamma ray and resistivity peaks below 620 m WMSF in Hole U1351B are matched in Hole U1351C, suggesting that they result from the irregular hole in the deeper section of Hole U1351B. Although the logging tool string could not go deeper than 770 m WMSF in Hole U1351C, the overall good agreement between the two holes above that depth suggests that similar low gamma ray and resistivity peaks at greater depths in Hole U1351B are also the result of irregular hole size.

The high coherence in sonic waveforms indicated by distinct red areas in the V_P and V_S tracks in Figure

F67 suggests that, despite the enlarged hole, the Dipole Sonic Imager was able to capture the compressional and flexural wave arrivals and should provide reliable compressional and shear velocity values. However, in some intervals the automatic labeling of the wave arrivals (black curve) failed to recognize the compressional wave and selected the stronger but slower "mud" arrival instead. This is particularly clear between ~165 and 210 m WMSF, where the high velocity in the sandy intervals is shown by coherence peaks for velocity values >2000 m/s, whereas the arrival automatically labeled corresponds to velocities near ~1500 m/s (i.e., the velocity of sound in the borehole fluid). Additional postcruise processing will be required to correct these profiles and will also likely reduce the variability of V_P and V_S in some intervals.

Logging stratigraphy

The combined analysis of gamma ray, resistivity, density, and velocity logs allows for the identification of several logging units defined by characteristic trends. Because of the uniformity of the sediments at this site (see **"Lithostratigraphy"**), these units are mostly defined by subtle changes in trends and correlations rather than by indications of significant changes in the formation. The downhole logs were used to define three logging units.

Logging Unit 1 (83–260 m WMSF) is characterized by relatively high amplitude variations in gamma ray values, generally increasing with depth. The low peaks in gamma ray in this unit between ~170 and 210 m WMSF correspond to intervals with high resistivity and sonic velocity values, which are likely sand-rich layers consistent with the poor core recovery in this interval. The overall logging signature of this unit is indicative of alternating sand-rich and clay-rich beds. One of the most striking features in this unit is a 7 m thick layer between ~248 and 255 m WMSF with the highest uranium readings in the interval logged (Fig. **F18**), associated with low gamma ray counts and high resistivity, density, and sonic velocity. This layer coincides generally with Core 317-U1351B-30X, where the lithologic observations that potentially explain these log values are the occurrence of calcareous concretions and glauconitic sandy mud.

Logging Unit 2 (260–510 m WMSF) is defined by low-amplitude variability and decreasing trends with depth in gamma ray and resistivity. Three distinct intervals of increasing-upward gamma ray within this unit suggest fining-upward, transgressive subunits. Caliper readings consistently larger than 18.5 inches in Units 1 and 2 show that the formation has little cohesion.

The top of logging Unit 3 (510–1032 m WMSF) is defined by a significant increase in gamma ray, which is accompanied by increases in density and resistivity. Below a ~50 m thick interval with high gamma ray, density, and resistivity values, the logs are variable within this unit and without clear trends. Resistivity increases slightly with depth, whereas natural radioactivity generally decreases downhole. Logging Unit 3 corresponds to an interval where the borehole diameter is slightly smaller (12–18 inches) than in the upper units, suggesting more consolidated or cohesive sediments.

Core-log correlation

Although the full integration of coring and logging data will be the object of various postcruise efforts, some preliminary correlations can be made at this stage to illustrate the complementary nature of these data sets.

Gamma ray logs through the pipe

Natural gamma ray values were logged through the drill pipe in Holes U1351B and U1351C. Gamma ray measurements are highly attenuated when the tool is inside the BHA and the drill pipe (above 81 and 84 m WSF in Holes U1351B and U1351C, respectively). Although the signal was attenuated by a factor of about four, the correlation between gamma ray from logs and NGR from cores is still very good (Fig. **F68**). Gamma ray from Hole U1351C has a closer fit with core data, suggesting a less enlarged borehole than Hole U1351B. Sandy layers of meter- and submeter-scale thickness described in the cored interval of Hole U1351B correspond to low peaks in the gamma ray log, suggesting that even an attenuated gamma ray signal can be used as a proxy for lithology. Two additional peaks (at ~68 and ~80 m WSF) in the gamma ray log may indicate the presence of sand layers that were not recovered in cores.

Formation MicroScanner images

When drilling with low recovery, FMS images can be used to recognize features in the cores that help identify similar features in the images recorded in intervals without recovery. Some of the lithologies recovered at Site U1351 with recognizable signatures in the FMS images are shown in Figure **F69.** The fine sand layers inferred from the FMS images in Figure **F69A** were not recovered but present the same character as thicker sand layers that were recovered deeper in the hole. The authigenic carbonates observed in Section 317-U1351B-27X-4 can be seen in Figure **F69B** as bright, sharp layers, as well as more subtle resistive features distributed along the image, whereas the shell-rich intervals distributed in Section

317-U1351B-28X-2 appear as more dispersed, bright resistive patterns in Figure F69C.

Stratigraphic correlation

Holes U1351A and U1351B were drilled ~20 m from each other, with Hole U1351A being dedicated to whole-round sampling for geochemical analysis. The drilling of two holes at Site U1351 provides an opportunity for stratigraphic correlation and the possible construction of a spliced stratigraphic record with a common core composite depth below seafloor (CCSF) depth scale (see "Stratigraphic correlation" in the "Methods" chapter). Magnetic susceptibility (MSL), NGR, color, and GRA bulk density data were all used in the analysis of Site U1351 holes. Analysis of the physical property records reveals very few unambiguous tie points that could be used to correlate the two holes. Equally, the short length of Hole U1351A and the reasonable depth match between the few correlative features that could be unambiguously assigned in each hole obviated the need for detailed composite record construction and splicing in Correlator. On the basis of the magnetic susceptibility record and lithostratigraphic observations, the two holes can be tied at the base of a sandy unit at ~15.7 m in both holes (Fig. F6).

References

Abbott, S.T., and Carter, R.M., 1999. Stratigraphy of the Castlecliffian type section: 10 mid-Pleistocene sequences from the Wanganui coast, New Zealand. *N. Z. J. Geol. Geophys.,* 42:91–111. http://www.royalsociety.org.nz/publications/journals/nzjg/1999/008/

Abbott, S.T., Naish, T.R., Carter, R.M., and Pillans, B.J., 2005. Sequence stratigraphy of the Nukumaruan stratotype (Pliocene–Pleistocene, c. 2.08–1.63 Ma), Wanganui Basin, New Zealand. *J. R. Soc. N. Z.,* 35(1–2):123–150. doi:10.1080/03014223.2005.9517779

Austin, J.A., Jr., Christie-Blick, N., Malone, M.J., et al., 1998. *Proc. ODP, Init. Repts.,* 174A: College Station, TX (Ocean Drilling Program). doi:10.2973/odp.proc.ir.174a.1998

Bentley, S.J., Sheremet, A., and Jaeger, J.M., 2006. Event sedimentation, bioturbation, and preserved sedimentary fabric: field and model comparisons in three contrasting marine settings. *Cont. Shelf Res.,* 26(17–18):2108–2124. doi:10.1016/j.csr.2006.07.003

Carter, R.M., 2007. The role of intermediate-depth currents in continental shelf-slope accretion: Canterbury Drifts, SW Pacific Ocean. *In* Viana, A.R., and Rebesco, M. (Eds.), *Economic and Paleoceanographic Significance of Contourite Deposits.* Geol. Soc. Spec. Publ., 276(1):129–154. doi:10.1144/GSL.SP.2007.276.01.07

Carter, R.M., and Gammon, P., 2004. New Zealand maritime glaciation: millennial-scale southern climate change since 3.9 Ma. *Science,* 304(5677):1659–1662. doi:10.1126/science.1093726

Carter, R.M., Gammon, P.R., and Millwood, L., 2004. Glacial–interglacial (MIS 1–10) migrations of the subtropical front across ODP Site 1119, Canterbury Bight, Southwest Pacific Ocean. *Mar. Geol.,* 205(1–4):29–58. doi:10.1016/S0025-3227(04)00017-9

Carter, R.M., McCave, I.N., Richter, C., Carter, L., et al., 2000. *Proc. ODP, Init. Repts.,* 181: College Station, TX (Ocean Drilling Program). doi:10.2973/odp.proc.ir.181.2000

Clifton, H.E., 2006. A reexamination of facies models for clastic shorelines. *In* Posamentier, H.W., and Walker, R.A. (Eds.), *Facies Models Revisited.* Spec. Publ.—SEPM (Soc. Sediment. Geol.), 84:294–337.

Cooper, R.A., 2004. *The New Zealand Geological Timescale.* Inst. Geol. Nucl. Sci. Monogr., 22.

Doveton, J.H., 1994. Geologic log interpretation. *SEPM Short Course,* 29:33–36.

Expedition 301 Scientists, 2005. Methods. *In* Fisher, A.T., Urabe, T., Klaus, A., and the Expedition 301 Scientists, *Proc. IODP,* 301: College Station, TX (Integrated Ocean Drilling Program Management International, Inc.). doi:10.2204/iodp.proc.301.105.2005

Field, B.D., and Browne, G.H., 1989. *Cretaceous and Cenozoic Sedimentary Basins and Geological Evolution of Canterbury Region, South Island, New Zealand.* N. Z. Geol. Surv., Basin Stud., 2.

Gieskes, J.M., 1983. The chemistry of interstitial waters of deep sea sediments: interpretation of deep sea drilling data. *In* Riley, J.P., and Chester, R. (Eds.), *Chemical Oceanography* (Vol. 8): London (Academic), 221–269.

Hayward, B.W., 2001. Global deep-sea extinctions during the Pleistocene ice ages. *Geology,* 29(7):599–602. doi:10.1130/0091-7613(2001)029<0599:GDSEDT>2.0.CO;2

Hingston, F.J., 1964. Reactions between boron and clays. *Aust. J. Soil Res.,* 2(1):83–95. doi:10.1071/SR9640083

Hornibrook, N. de B., Brazier, R.C., and Strong, C.P., 1989. Manual of New Zealand Permian to Pleistocene foraminiferal biostratigraphy. *Paleontol. Bull.,* 56.

House, C.H., Cragg, B.A., Teske, A., and the Leg 201 Scientific Party, 2003. Drilling contamination tests during ODP Leg 201 using chemical and particulate tracers. *In* D'Hondt, S.L., Jørgensen, B.B., Miller, D.J., et al., *Proc. ODP, Init. Repts.,* 201: College Station, TX (Ocean Drilling Program), 1–19. doi:10.2973/odp.proc.ir.201.102.2003

Kallmeyer, J., Smith, D.C., Spivack, A.J., and D'Hondt, S., 2008. New cell extraction procedure applied to deep subsurface sediments. *Limnol. Oceanogr.: Methods,* 6:236–245. http://www.aslo.org/lomethods/free/2008/0236.pdf

Lourens, L.J., Hilgen, F.J., Shackleton, N.J., Laskar, J., and Wilson, D., 2004. The Neogene period. *In* Gradstein, F.M., Ogg, J.G., and Smith, A.G. (Eds.), *A Geological Time*

Scale 2004. Cambridge (Cambridge Univ. Press), 409–440.

Lu, H., and Fulthorpe, C.S., 2004. Controls on sequence stratigraphy of a middle Miocene–Holocene, current-swept, passive margin: offshore Canterbury Basin, New Zealand. *Geol. Soc. Am. Bull.,* 116(11):1345–1366. doi:10.1130/B2525401.1

Lu, H., Fulthorpe, C.S., and Mann, P., 2003. Three-dimensional architecture of shelf-building sediment drifts in the offshore Canterbury Basin, New Zealand. *Mar. Geol.,* 193(1–2):19–47. doi:10.1016/S0025-3227(02)00612-6

Lu, H., Fulthorpe, C.S., Mann, P., and Kominz, M., 2005. Miocene–Recent tectonic and climate controls on sediment supply and sequence stratigraphy: Canterbury Basin, New Zealand. *Basin Res.,* 17(2):311–328.

Morono, Y., Terada, T., Masui, N., and Inagaki, F., 2009. Discriminative detection and enumeration of microbial life in marine subsurface sediments. *ISME J.,* 3(5):503–511. doi:10.1038/ismej.2009.1

Naish, T.R., Wehland, F., Wilson, G.S., Browne, G.H., Cook, R.A., Morgans, H.E.G., Rosenberg, M., King, P.R., Smale, D., Nelson, C.S., Kamp, P.J.J., and Ricketts, B., 2005. An integrated sequence stratigraphic, palaeoenvironmental, and chronostratigraphic analysis of the Tangahoe Formation, southern Taranaki coast, with implications for mid-Pliocene (c. 3.4–3.0 Ma) glacio-eustatic sea level changes. *J. R. Soc. N. Z.,* 35(1–2):151–196. http://www.royalsociety.org.nz/publications/journals/nzjr/2005/006/

Parkes, R.J., Cragg, B.A., and Wellsbury, P., 2000. Recent studies on bacterial populations and processes in subseafloor sediments: a review. *Hydrogeol. J.,* 8(1):11–28. doi:10.1007/PL00010971

Posamentier, H.W., Jervey, M.T., and Vail, P.R., 1988. Eustatic controls on clastic deposition, I. Conceptual framework. *In* Wilgus, C.K., Hastings, B.S., Ross, C.A., Posamentier, H.W., Van Wagoner, J., and Kendall, C.G.St.C. (Eds.), *Sea-Level Changes: An Integrated Approach.* Spec. Publ.—Soc. Econ. Paleontol. Mineral., 42:109–124.

Reyes, A.G., 2007. Abandoned oil and gas wells: a reconnaissance study of an unconventional geothermal resource. *GNS Sci. Rep.,* 2007/23.

Richter, C., Acton, G., Endris, C., and Radsted, M., 2007. Handbook for shipboard paleomagnetists. *ODP Tech. Note,* 34. doi:10.2973/odp.tn.34.2007

Saul, G., Naish, T.R., Abbott, S.T., and Carter, R.M., 1999. Sedimentary cyclicity in the marine Pliocene–Pleistocene of the Wanganui Basin (New Zealand): sequence stratigraphic motifs characteristic of the past 2.5 m.y.

Geol. Soc. Am. Bull., 111(4):524–537. doi:10.1130/0016-7606(1999)111<0524:SCITMP>2.3.CO;2

Shipboard Scientific Party, 1994. Site 902. *In* Mountain, G.S., Miller, K.G., Blum, P., et al., *Proc. ODP, Init. Repts.,* 150: College Station, TX (Ocean Drilling Program), 63–127. doi:10.2973/odp.proc.ir.150.106.1994

Shipboard Scientific Party, 1999. Site 1119: drift accretion on Canterbury Slope. *In* Carter, R.M., McCave, I.N., Richter, C., Carter, L., et al., *Proc. ODP, Init. Repts.,* 181: College Station, TX (Ocean Drilling Program), 1–112. doi:10.2973/odp.proc.ir.181.103.2000

Smith, D.C., Spivack, A.J., Fisk, M.R., Haveman, S.A., Staudigel, H., and the Leg 185 Shipboard Scientific Party, 2000. Methods for quantifying potential microbial contamination during deep ocean coring. *ODP Tech. Note,* 28. doi:10.2973/odp.tn.28.2000

Suter, J.R., 2006. Facies models revisited: clastic shelves. *In* Posamentier, H.W., and Walker, R.A. (Eds.), *Facies Models Revisited.* Spec. Publ.—SEPM (Soc. Sediment. Geol.), 84:339–397.

Sykes, R., and Funnel, R.H., 2002. Petroleum source rock potential and generation history in the offshore Canterbury Basin. *Min. Econ. Dev. N. Z. Pet. Rep.,* PR2707.

Vail, P.R., Audemard, F., Bowman, S.A., Eisner, P.N., and Perez-Cruz, G., 1991. The stratigraphic signatures of tectonics, eustasy, and sedimentology—an overview. *In* Einsele, G., Ricken, W., and Seilacher, A. (Eds.), *Cycles and Events in Stratigraphy:* Berlin (Springer), 617–659.

von Breymann, M.T., Collier, R., and Suess, E., 1990. Magnesium adsorption and ion exchange in marine sediments: a multicomponent model. *Geochim. Cosmochim. Acta,* 54(12):3295–3313. doi:10.1016/0016-7037(90)90286-T

Wheatcroft, R.A., Sommerfield, C.K., Drake, D.E., Borgeld, J.C., and Nittrouer, C.A., 1997. Rapid and widespread dispersal of flood sediment on the northern California margin. *Geology,* 25(2):163–166. doi:10.1130/0091-7613(1997)025<0163:RAWDOF>2.3.CO;2

Wheatcroft, R.A., Stevens, A.W., Hunt, L.M., and Milligan, T.G., 2006. The large-scale distribution and internal geometry of the fall 2000 Po River flood deposit: evidence from digital X-radiography. *Cont. Shelf Res.,* 26(4):499–516. doi:10.1016/j.csr.2006.01.002

Zielinski, U., and Gersonde, R., 2002. Plio–Pleistocene diatom biostratigraphy from ODP Leg 177, Atlantic sector of the Southern Ocean. *Mar. Micropaleontol.,* 45:225–268. doi:10.1016/S0377-8398(02)00031-2

Figure F1. A. Dip Profile EW00-01-66 showing Site U1351. Proposed alternate Site CB-03A is also shown. **B.** Crossing strike Profile CB-82-25. Red = actual penetration, yellow = proposed penetration. CDP = common depth point. MP = Marshall Paraconformity.
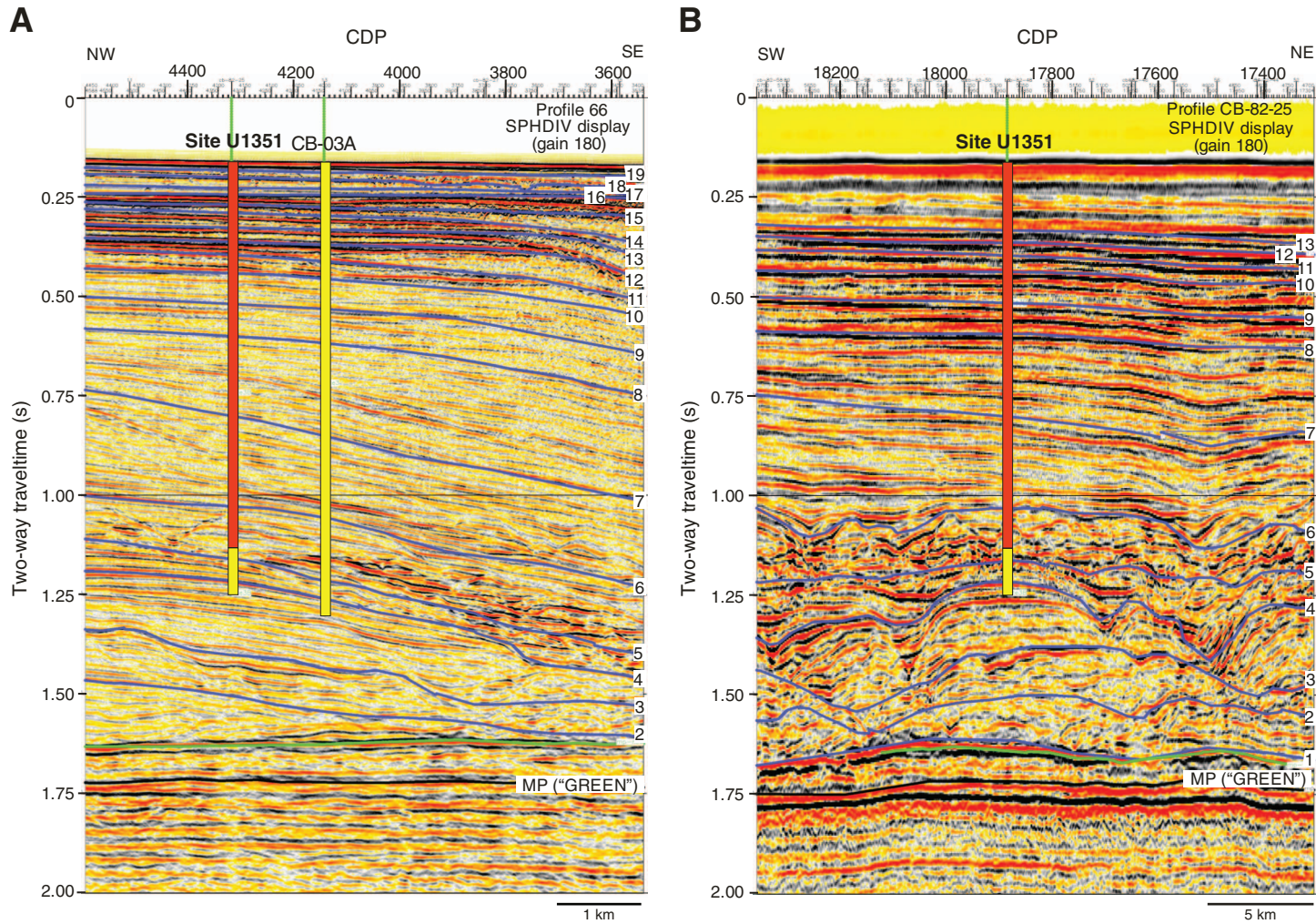
Figure F2. Map of drilled and proposed Expedition 317 sites, together with EW00-01 high-resolution (frequencies up to 300 Hz) multichannel seismic (MCS) grid (thick straight lines), low-resolution CB-82 commercial MCS grid (thin straight lines), exploration wells Clipper and Resolution, and Ocean Drilling Program (ODP) Site 1119. The EW00-01 survey was designed to provide improved vertical resolution (~5 m in the upper 1 s) to enhance our ability to define high-frequency sedimentary sequences. Also shown is the distribution of seismically resolvable sediment drifts D1–D11, along with D8 and D9 subdrifts. Blue curved lines = crests of drift mounds, dashed blue lines = drifts identified on CB-82 profiles. Dip Profiles EW00-01-66, EW00-01-60, EW00-01-01, EW00-01-07a, and CB-82-25 are also labeled.
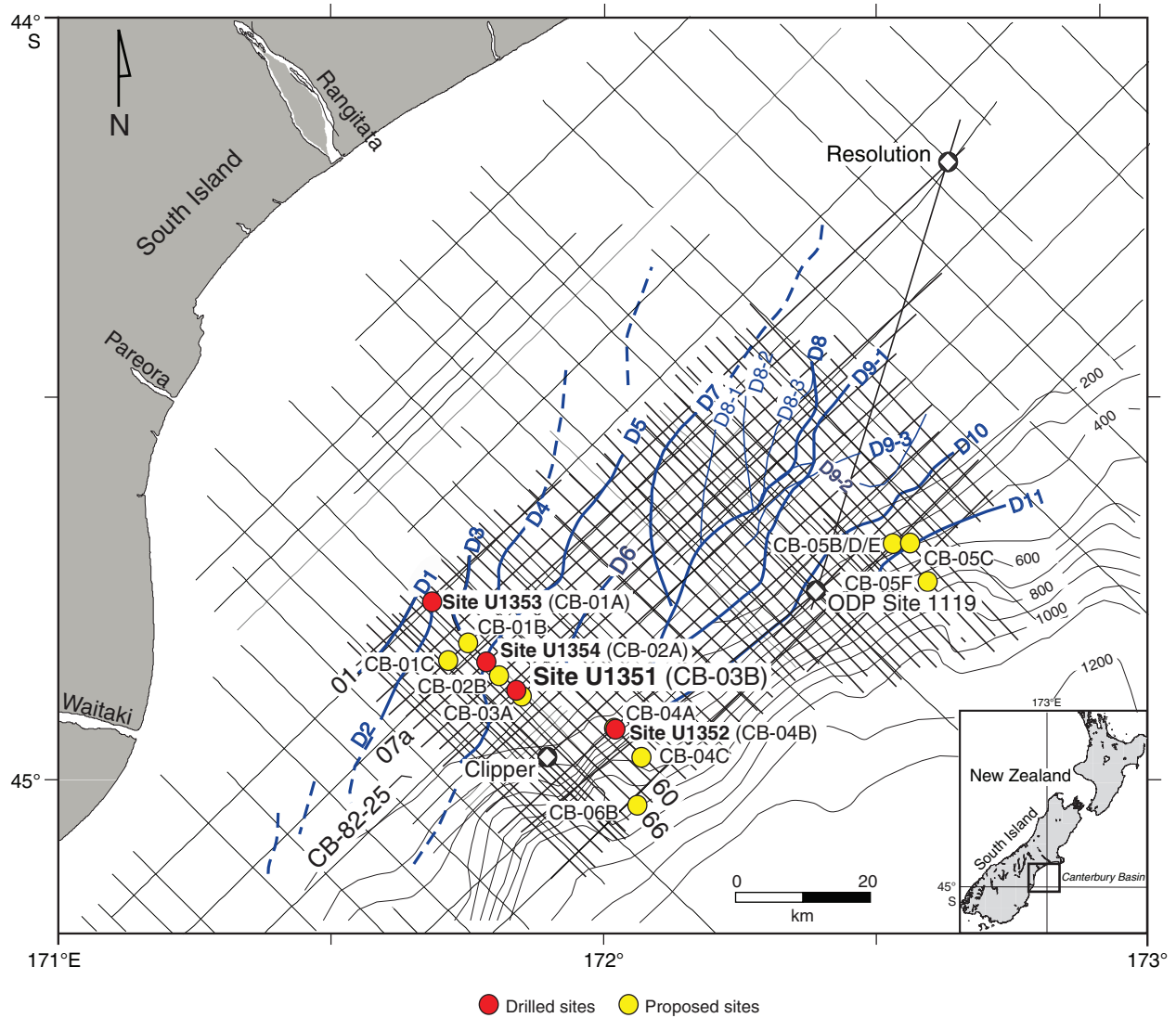
Figure F3. Summary of core recovery, lithology, lithologic units, unit descriptions, physical property data, and gamma ray data from downhole logging, Hole U1351B. NGR = natural gamma radiation. Gray shaded box in Lith. unit column shows potential boundary area. Downhole logging data are plotted on the WMSF depth scale.
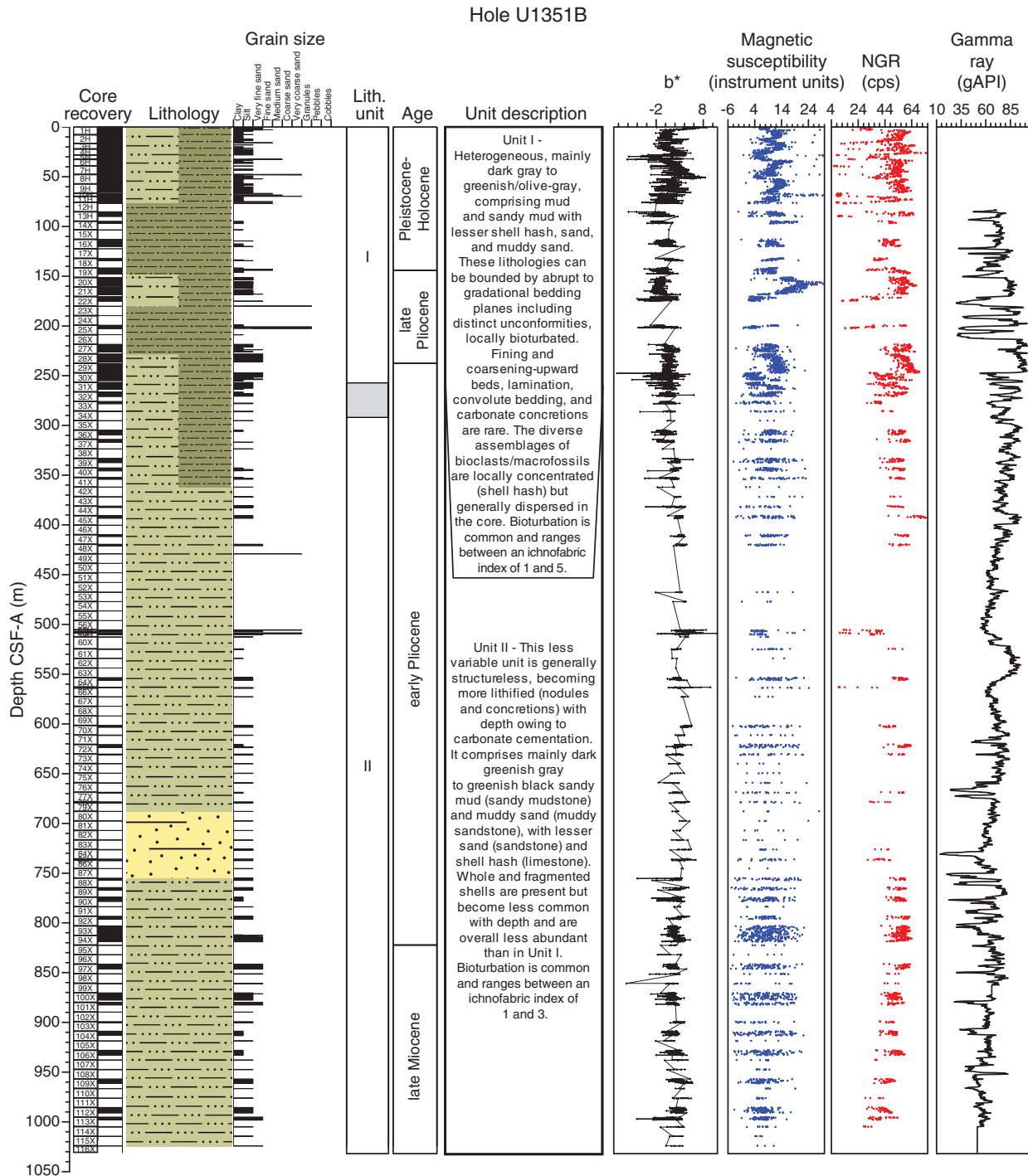
Figure F4. Histogram of core recovery and lithology shown as a proportion of the recovered interval (lithology [%] × recovery [%]/100) in Hole U1351B. Depth scale in CSF-A (m) is variable, but for graphical purposes each core is depicted by an equally thick horizontal bar.
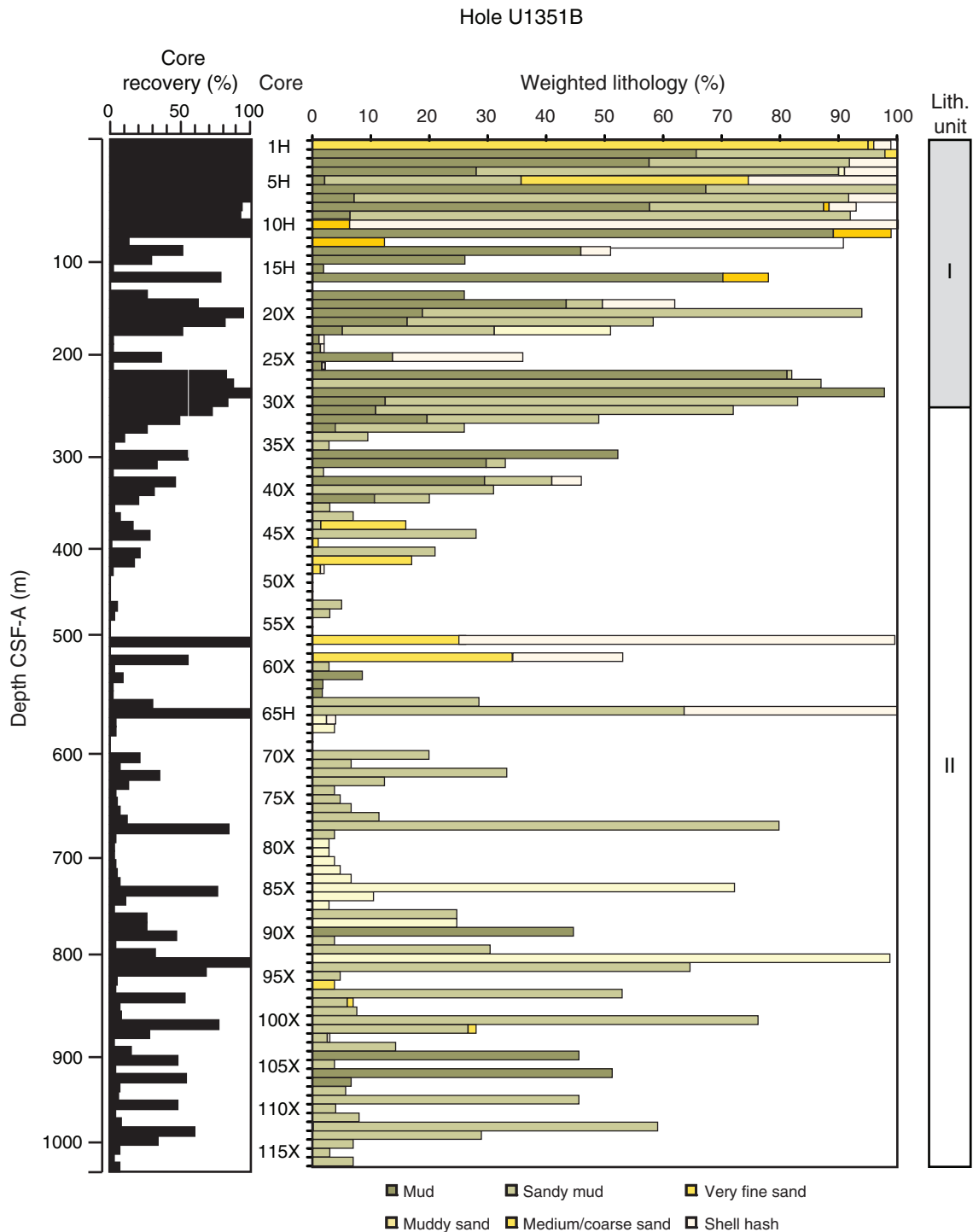
Figure F5. Comparison of standard gamma ray log to core recovery in the uppermost 350 m of Hole U1351B, illustrating alternative Unit I/II boundaries. Core recovery and a boundary option located in a recovered core (Option B; Section 317-U1351B-31X-4) are displayed on the left. Four other boundary options (all of which fall within nonrecovered intervals) based on changes in the gamma ray log are also shown: Option A (gap between Cores 317-U1351B-29X and 30X), Option C (gap between Cores 317-U1351B-31X and 32X), Option D (gap between Cores 317-U1351B-33X and 34X), and Option E (gap between Cores 317-U1351B-35X and 36X). Core photographs illustrate lithologic changes across each proposed boundary. The range of options is shaded in gray. Dashed lines correlate depths of each option in the core and in the gamma ray log.

Figure F6. Lithostratigraphic correlation between Cores 317-U1351A-1H through 6H and 317-U1351B-1H through 5H. Lithologic surfaces U1351A-S1/U1351B-S1 and U1351A-S2/U1351B-S2 are connected with dashed lines labeled S1 and S2 (see Table **T4**). Geochemical and microbiological sampling horizons are shown for Hole U1351A. S1 is the base of a Type 1 facies assemblage. The sand placed below S2 in Hole U1351A is the top of a Type 2 facies assemblage. A similar sand is placed above S2 in Hole U1351B. However, there was some uncertainty in the location of this surface in both holes, as represented by the question marks, and the precise S2 surface may not have been recovered in Hole U1351A.

Figure F7. Core photographs showing correlative intervals, including lithologic surfaces U1351A-S1 and U1351B-S1 (labeled S1), between Cores 317-U1351A-3H and 317-U1351B-2H (see also Fig. F6). Red arrows = large burrows infilled with coarse materials from the overlying beds. Some of these burrows are continuous for 15 cm.
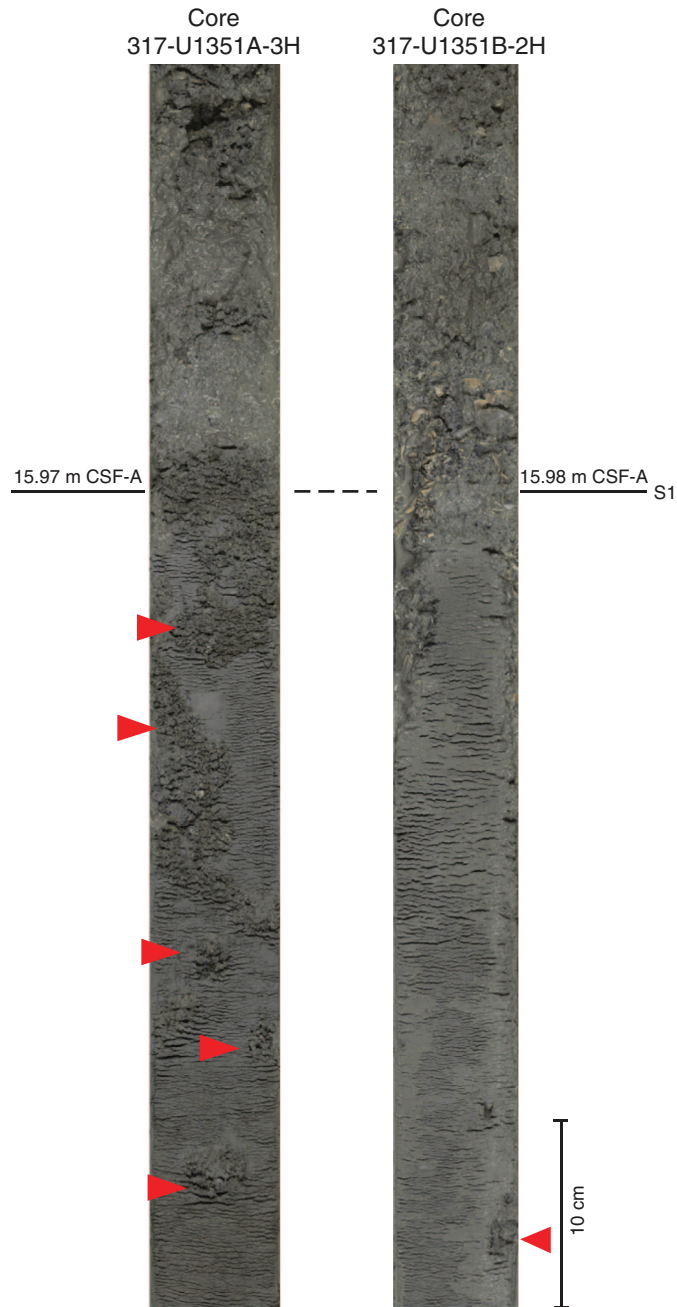
Figure F8. Core photograph of a slumped deposit (interval 317-U1351A-4H-2, 52–105 cm). Soft-sediment deformation is clearly shown by the isoclinal and recumbent folds, highlighted by the light-to-dark color variability within the mud lithology.
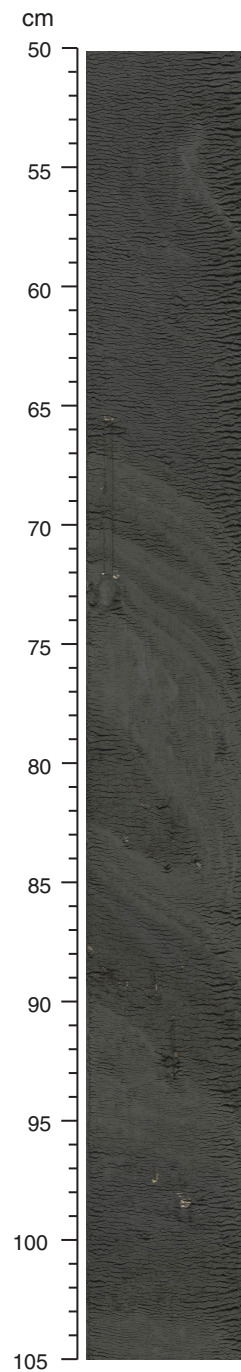
Figure F9. Core photographs of biscuiting structures in (**A**) Unit I (interval 317-U1351B-20X-6, 136–148 cm) and (**B**) Unit II (interval 317-U1351B-94X-3, 129–142 cm). **C.** Photograph of core section in B taken after the core surface was cleaned with a glass slide.
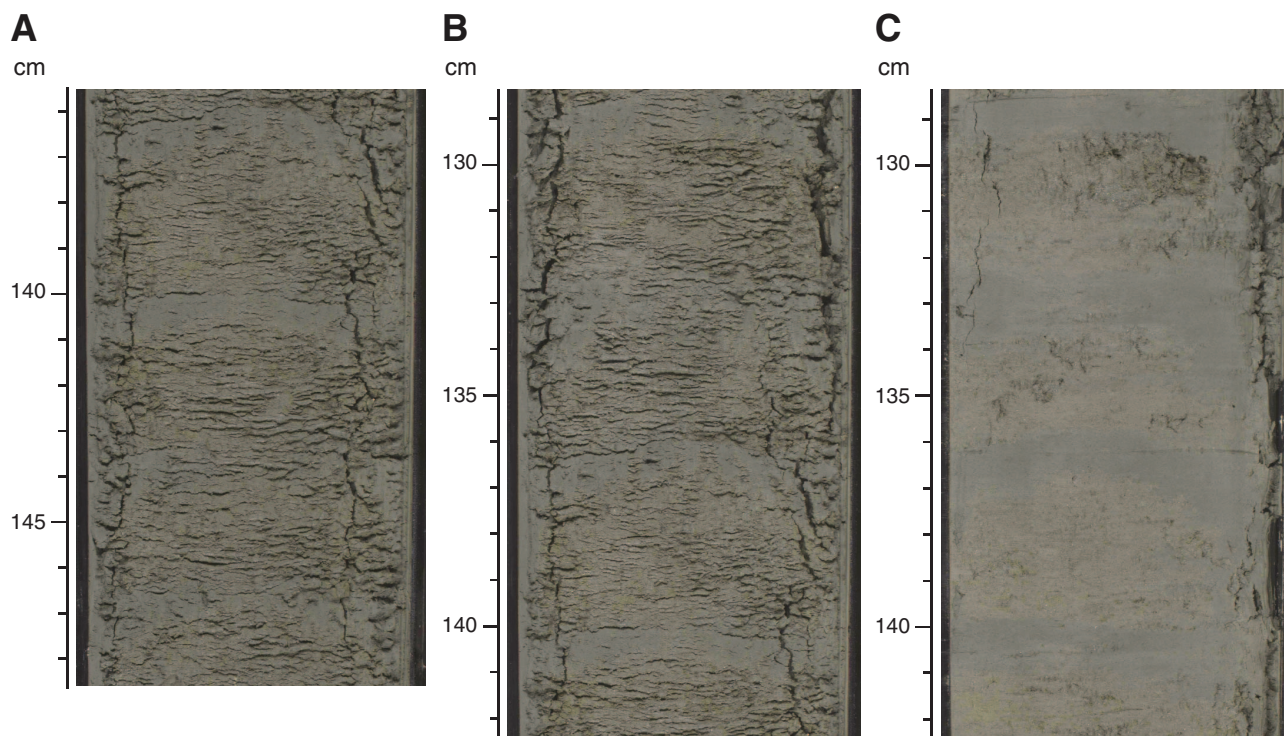
Figure F10. Core photographs of downhole cave-in. **A.** Shell hash (interval 317-U1351B-65H-1, 0–39 cm). **B.** Possible in situ shell hash (interval 317-U1351B-10H-2, 0–29 cm). Note the presence of finer (in situ) sediment at top of section. This shell hash is also found deeper in Section 2 and thus probably does not represent cave-in. **C.** Distinct sand horizon (interval 317-U1351B-85X-1, 0–26 cm), likely representing cave-in.
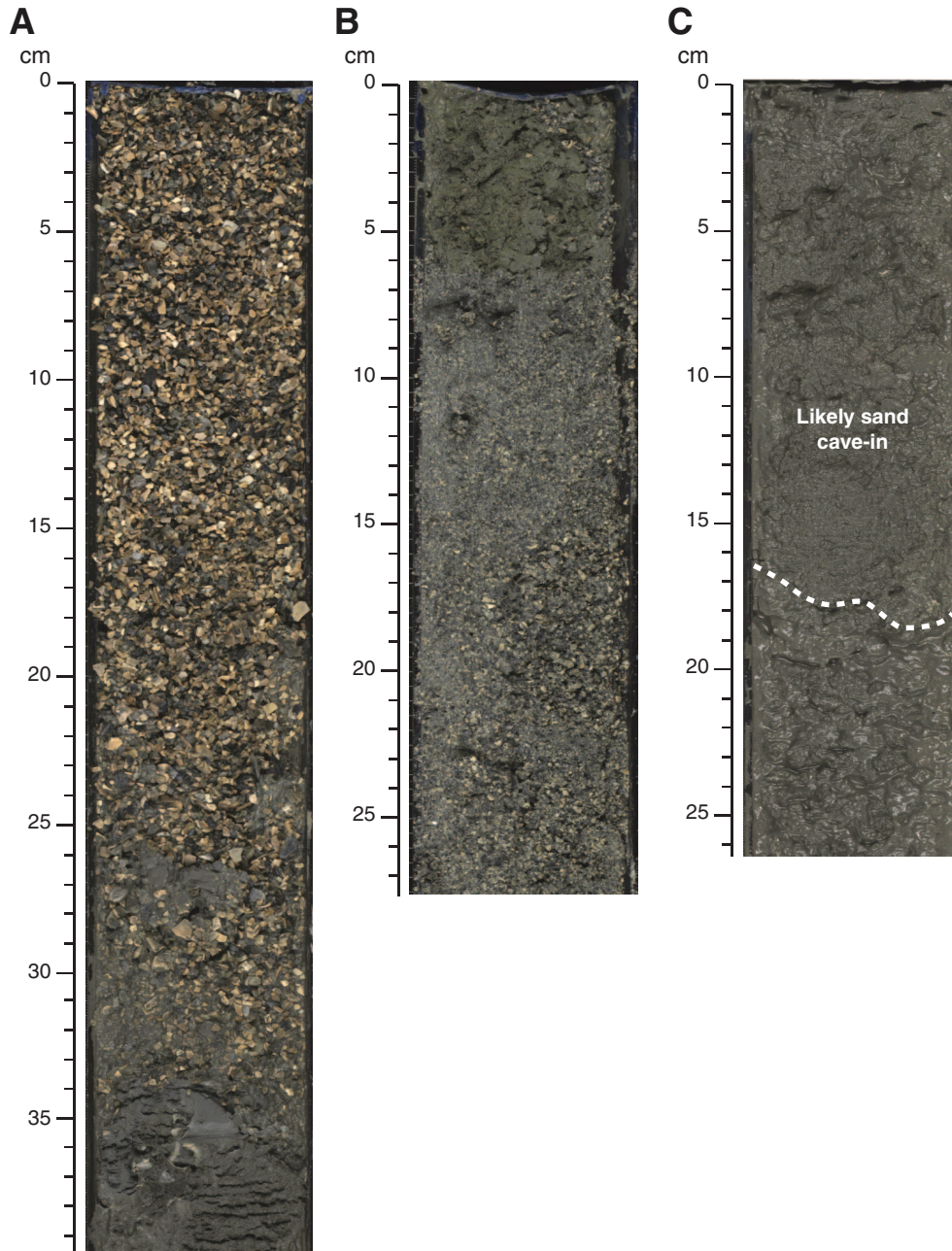
Figure F11. Core photographs of Unit I lithologies in Section 317-U1351A-3H-3, including lithologic surface U1351A-S1, which is a sharp contact separating muddy shelly sand above (10–74 cm) from mud beneath. This surface is extensively bioturbated and possibly represents seismic sequence boundary U19.
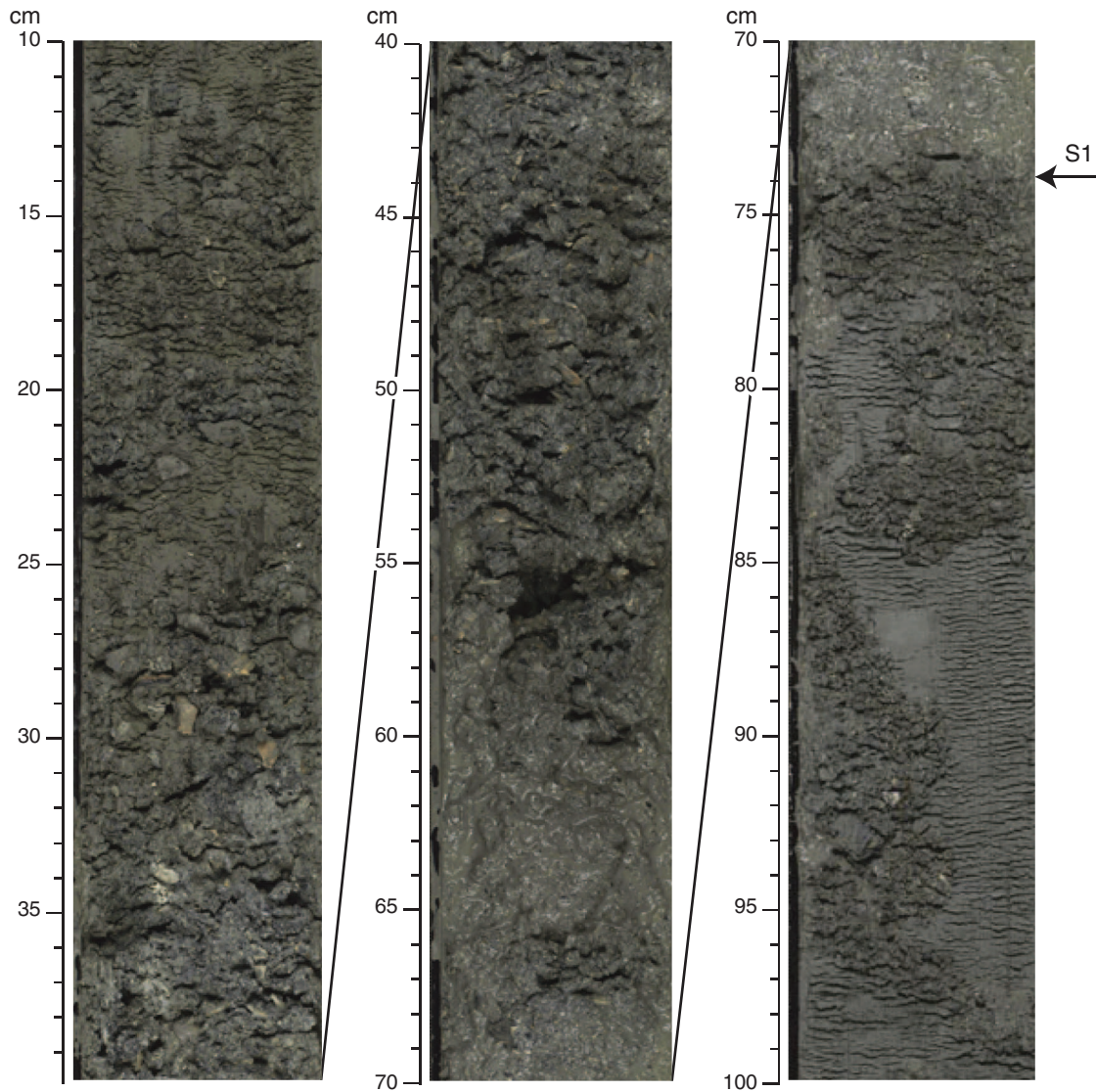
Figure F12. Core photographs of lithologies associated with lithologic surfaces in Unit I. **A.** Intervals 317-U1351B-5H-1, 113–135 cm; 5H-2, 120–145 cm; and 5H-3, 0–20 cm. The depth of the sand bed base (surface U1351B-S2) correlates with the predicted depth of seismic sequence boundary U18. **B.** Interval 317-U1351B-19X-2, 80–110 cm. A sharp, heavily bioturbated contact separates the shell bed above from the clayey mud beneath. This surface (U1351B-S6) is near the predicted depth of U13.
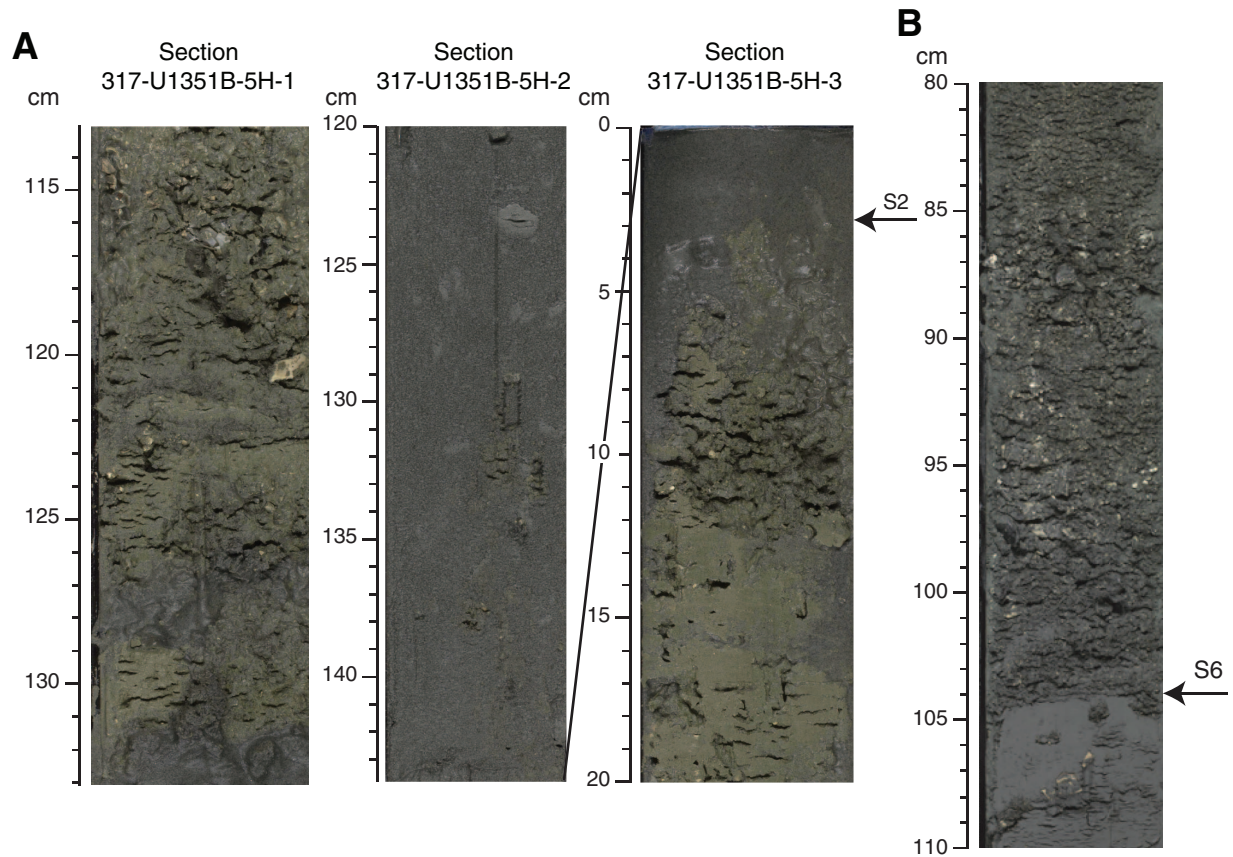
Figure F13. Close-up core photographs of Unit I lithologies. **A.** Shelly mud bed (interval 317-U1351B-30X-5, 30–60 cm). **B.** Mud (interval 317-U1351B-19X-3, 40–65 cm). **C.** Color-banded light gray to gray mud (interval 317-U1351B-20X-9, 73–113 cm).
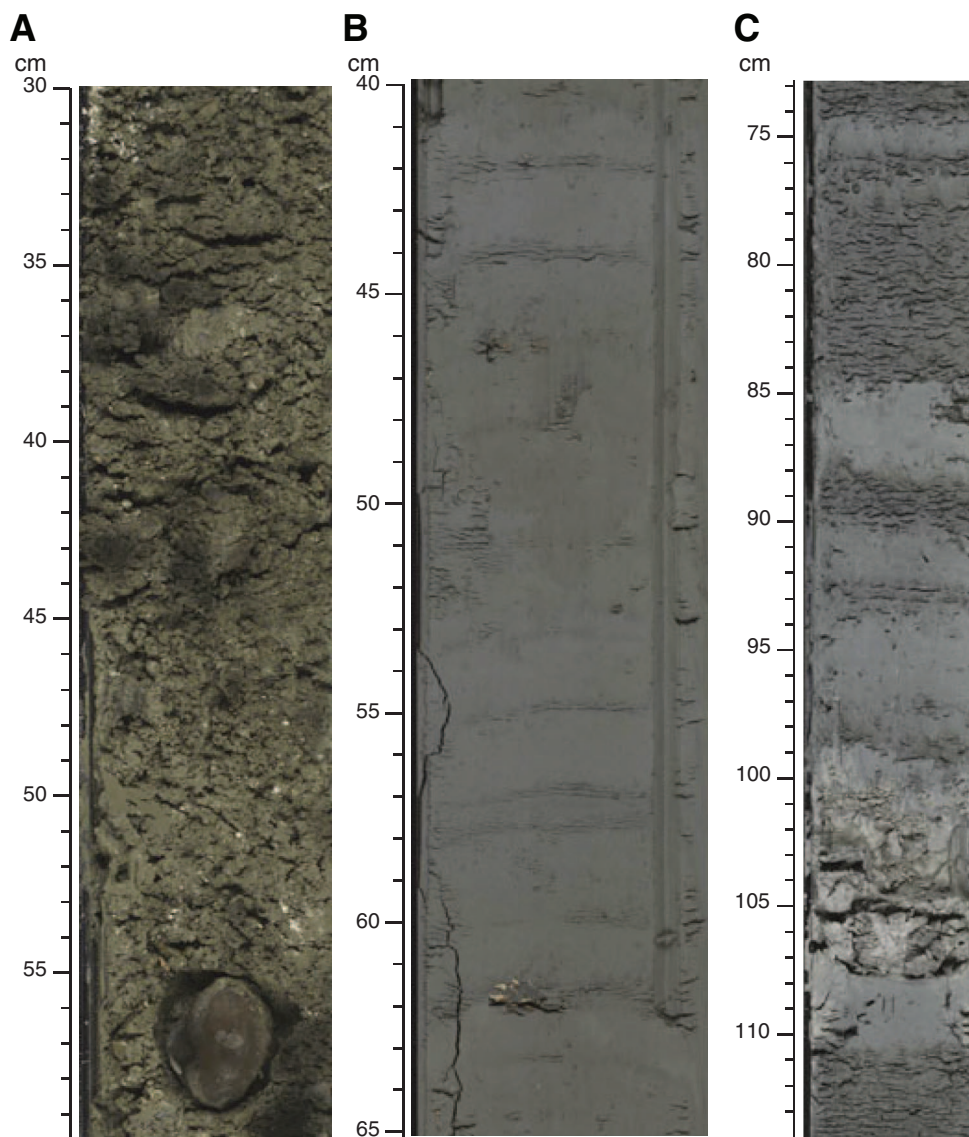
Figure F14. Photomicrographs of smear slide mineralogy. **A.** Foraminifers infilled with pyrite, grains of quartz/feldspar, green biotite, and a small round calcareous spicule (right) in a muddy matrix (Sample 317-U1351A-3H-1, 30 cm). **B.** Calcareous sponge spicules (three pointed), pyrite-filled foraminifers, biotite, and amphibole (Sample 317-U1351A-4H-4, 40 cm). **C.** Amphibole and plagioclase grains among quartz/feldspar, rock fragments, and altered grains (Sample 317-U1351B-5H-2, 100 cm). **D.** Low-grade metamorphic and other rock fragments (center) (Sample 317-U1351B-5H-2, 100 cm). **E.** Similar view as C (rotated counterclockwise relative to view in C) but with nicols crossed. **F.** Same view as D but with nicols crossed.
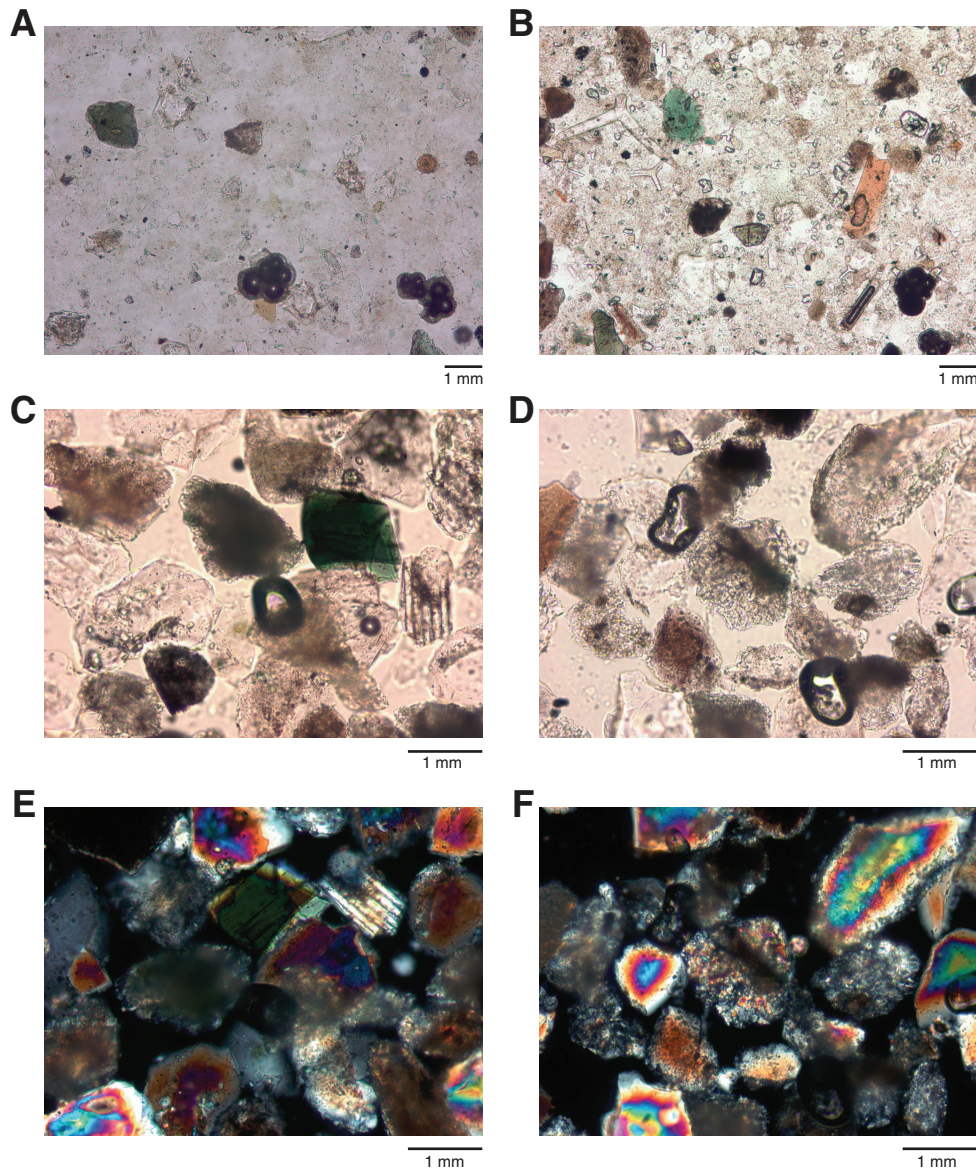
Figure F15. Core photographs and thin section photomicrographs of glauconitic limestone beds. **A.** Section 317-U1351B-19X-CC (top depth = 147.23 m). **B.** Section 317-U1351B-22X-CC (top depth = 174.90 m). **C.** Thin section of Sample 317-U1351B-19X-CC, 25–27 cm, showing glauconite infilling fossil void spaces. **D.** Thin section of Sample 317-U1351B-19X-CC, 25–27 cm, showing glauconite alteration of echinoderm plate and sparry calcite infilling a foraminifer. **E.** Thin section of Sample 317-U1351B-22X-CC, 21–23 cm, showing glauconite infilling borings on an eroded shell fragment.
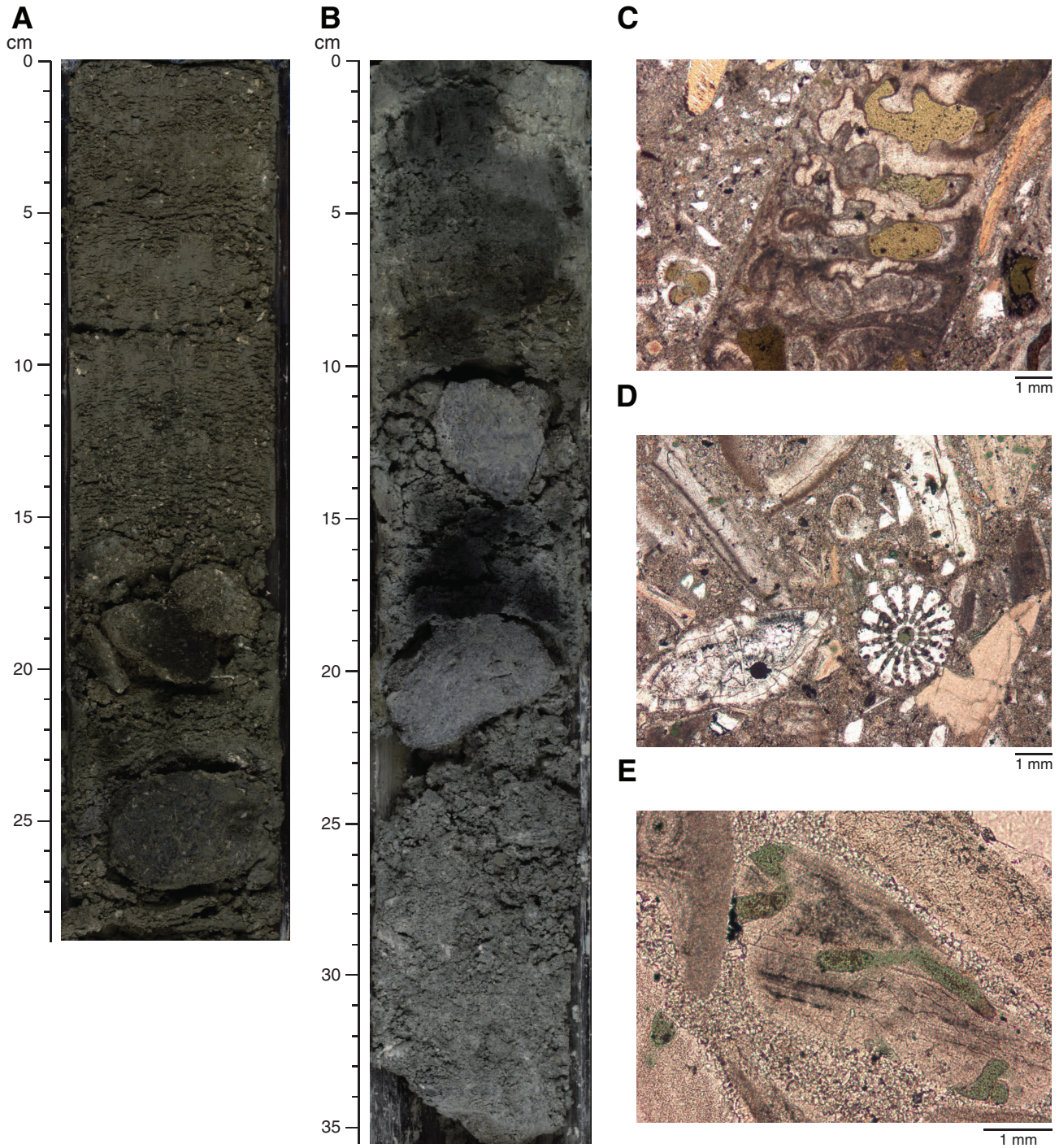
Figure F16. Summary of some shipboard analyses for Hole U1351B showing a graphical depiction of recovered core, magnetic susceptibility, gamma ray logging data, the distribution of facies assemblages, lithologic surfaces identified in the cores, and seismic sequence boundaries (the latter after Lu and Fulthorpe, 2004). Downhole logging data are plotted on the WMSF depth scale. **A.** 0–150 m CSF-A. (**Continued on next page.**)
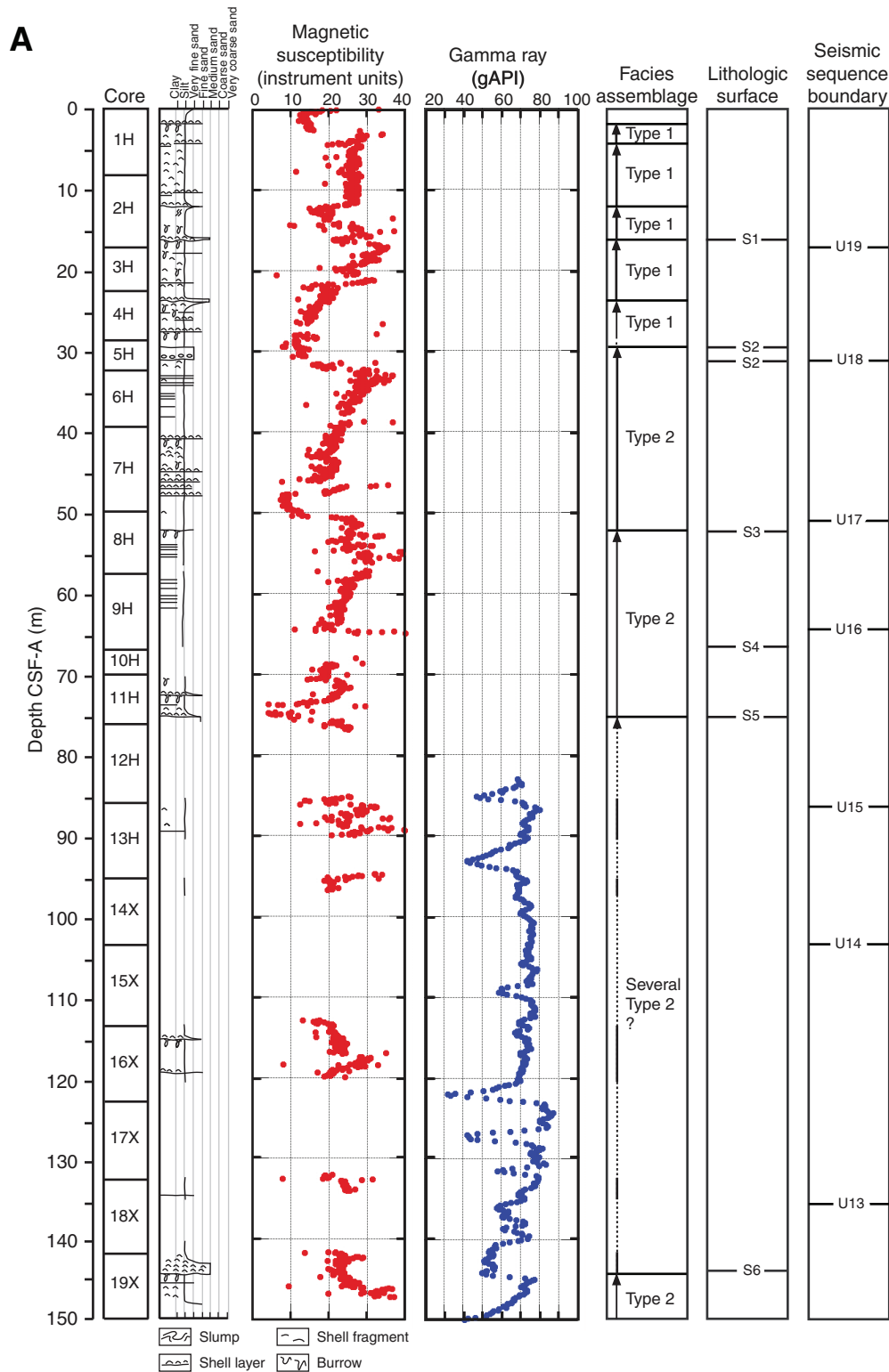
Figure F16 (continued). B. 150–300 m CSF-A.
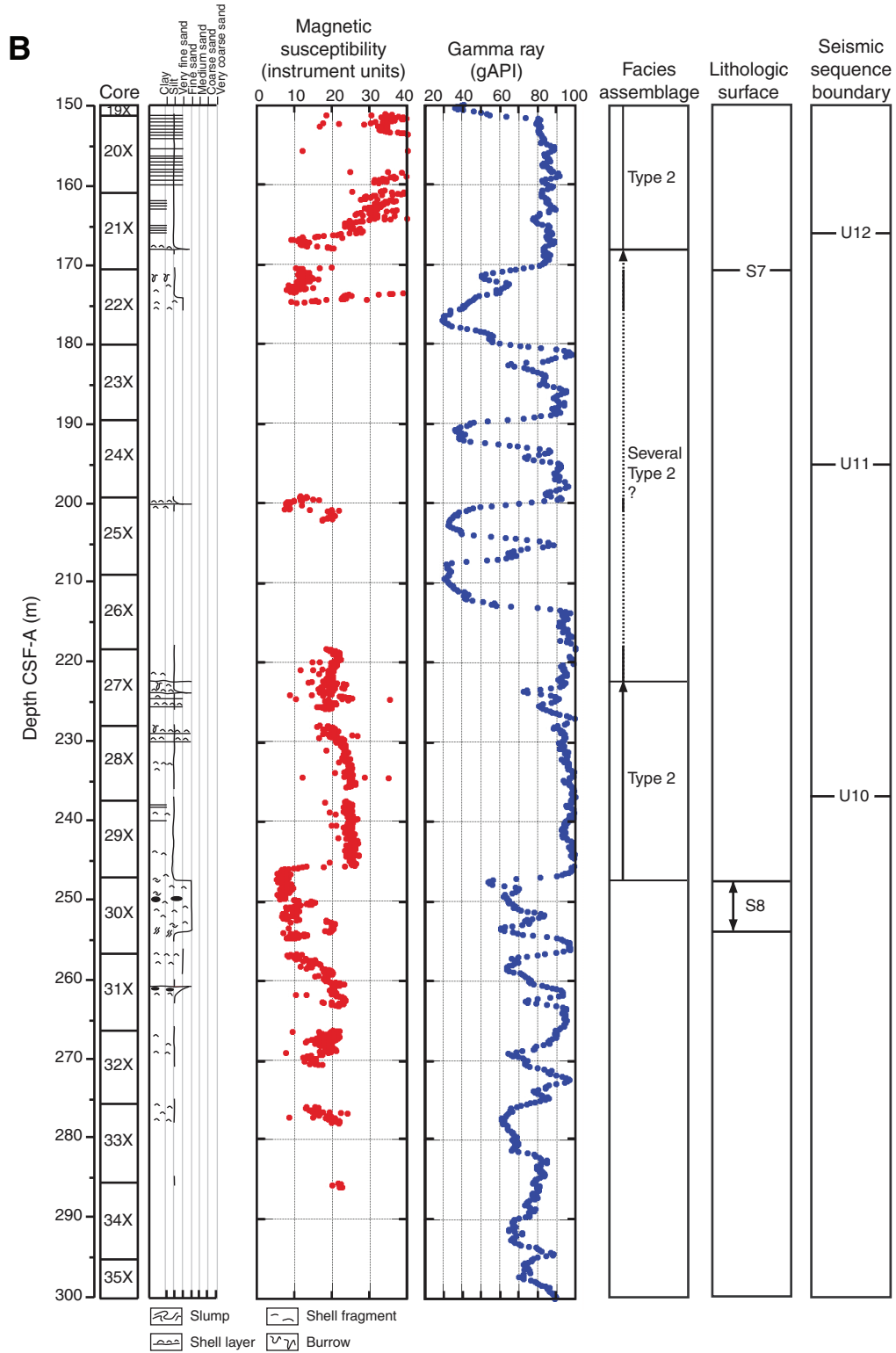
Figure F17. Schematic model of the repetitive facies assemblages that characterize lithologic Unit I. The Type 2 facies assemblage is composed of greenish gray shelly bioturbated mud with a sharp lower contact, followed by a transition uphole into dark gray micaceous very fine sandy mud with color banding and alternations of sand and mud showing upward coarsening. The Type 1 facies assemblage is the basal part of the Type 2 assemblage.
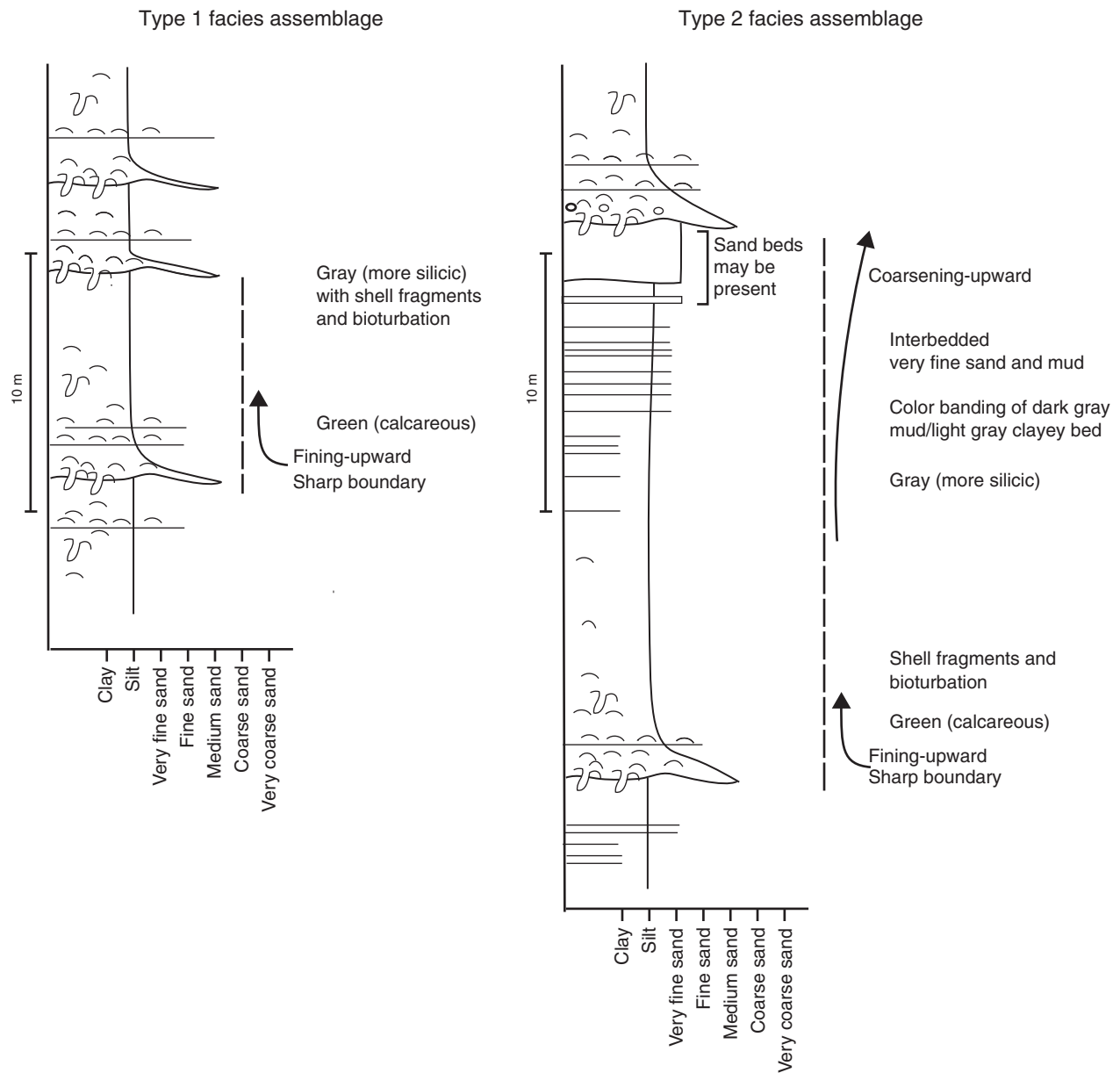
Figure F18. Summary of spectral natural gamma ray measurements from downhole logging in Hole U1351B. SGR = standard gamma ray, CGR = computed gamma ray (gamma ray without uranium contribution). Both the SGR (higher values) and CGR (lower values) curves are plotted in green. The area between the two curves, also colored in green, shows the contribution of uranium, a common indicator of organic content. For details, see **"Downhole logging."**
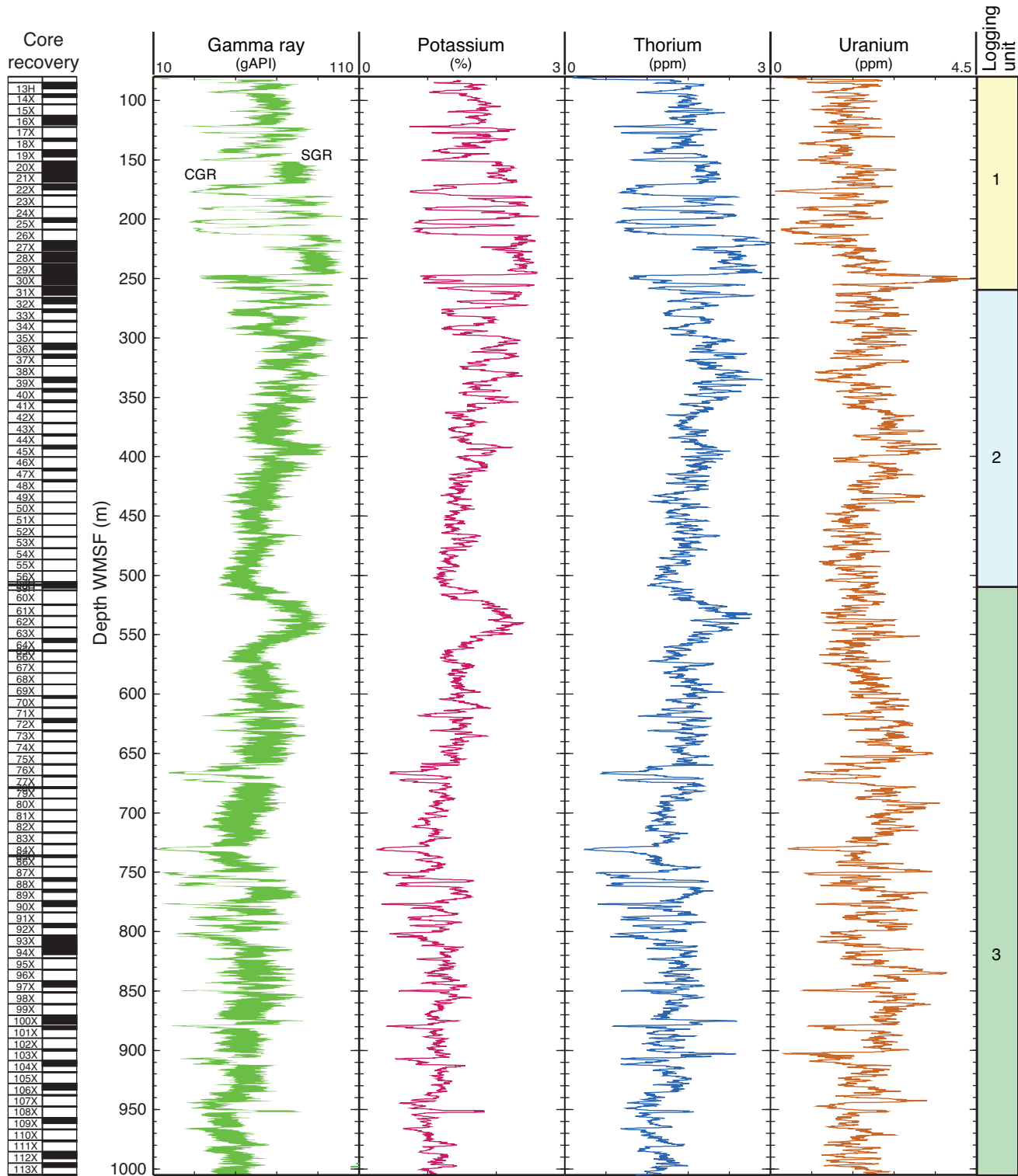
Figure F19. Comparison of logging data recorded in Holes U1351B and U1351C. Because data from Hole U1351C were recorded while the tool was being lowered, the only reliable measurements in this hole are from gamma ray, gamma ray spectroscopy, and resistivity logs. For details, see "Downhole logging."
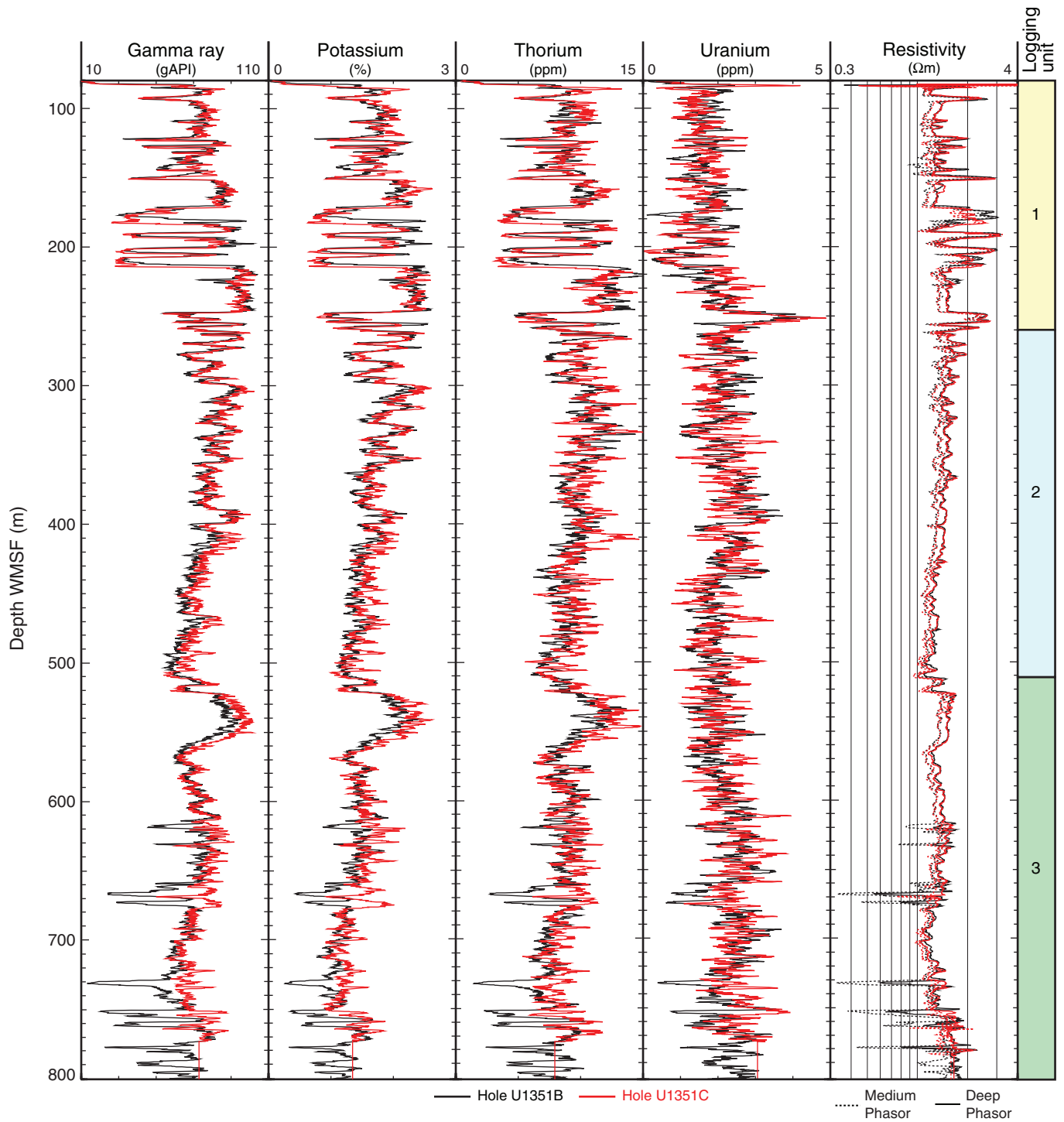
Figure F20. Core photographs of Unit II lithologies. **A.** Mud with common shell fragments (interval 317-U1351B-39X-3, 70–90 cm). **B.** Muddy very fine sand (interval 317-U1351B-88X-1, 70–90 cm). **C.** Calcareous sandy mud (interval 317-U1351B-104X-2, 70–90 cm).
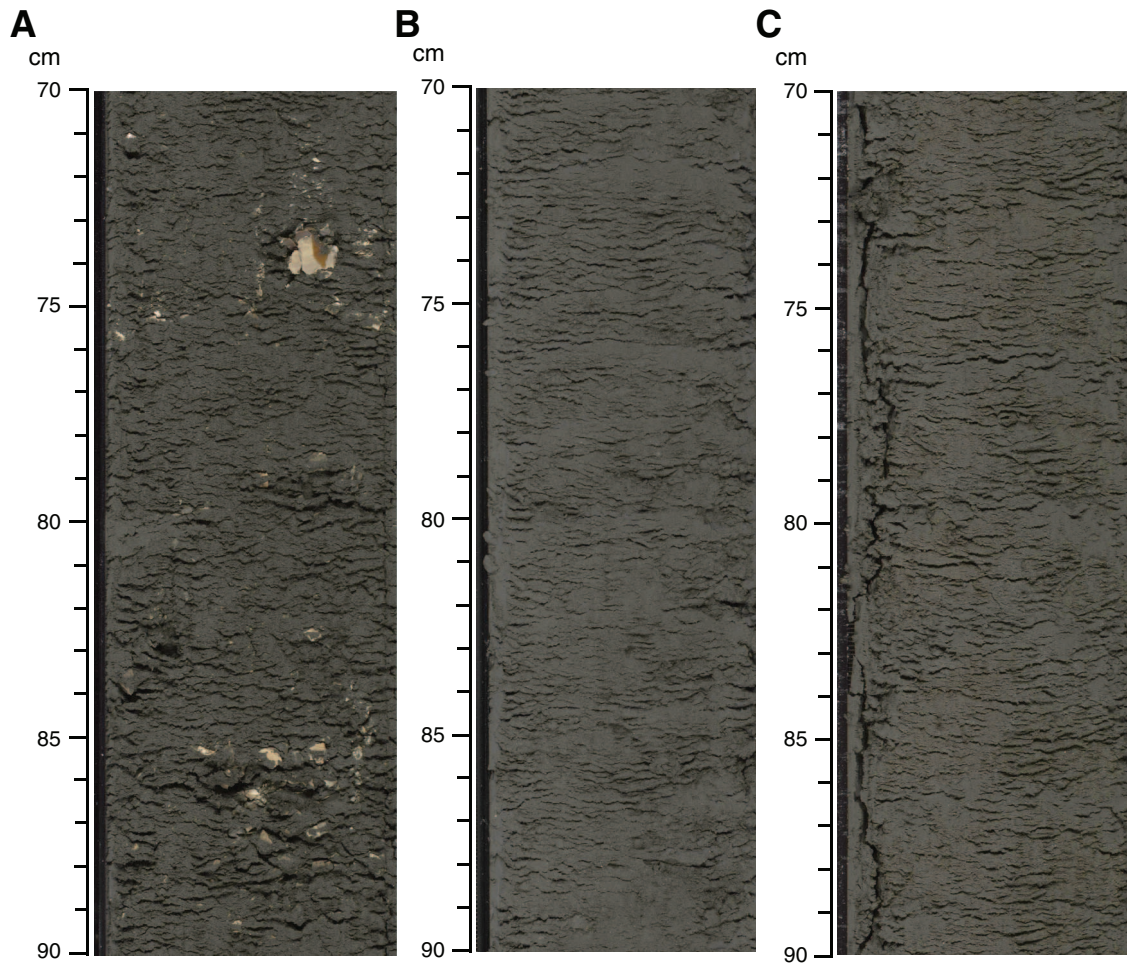
Figure F21. Core photographs of induration and cementation in Hole U1351B. **A.** Calcareous cementation in host sediment (interval 317-U1351B-90X-3, 66–80 cm). **B.** Incipient nodule formation in host sediment (interval 317-U1351B-100X-5, 37–45 cm). **C.** Calcareous nodule in host sediment (interval 317-U1351B-100X-3, 12–18 cm). **D.** Calcareous concretion in host sediment (interval 317-U1351B-96X-CC, 0–15 cm). **E.** Drilling-induced induration (interval 317-U1351B-89X-CC, 24–31 cm). **F.** Extreme drilling-induced induration resulting from drilling compaction (interval 317-U1351B-112X-CC, 20–35 cm). The dark coloration at the base of the photograph is the result of sediment heating induced by drilling.
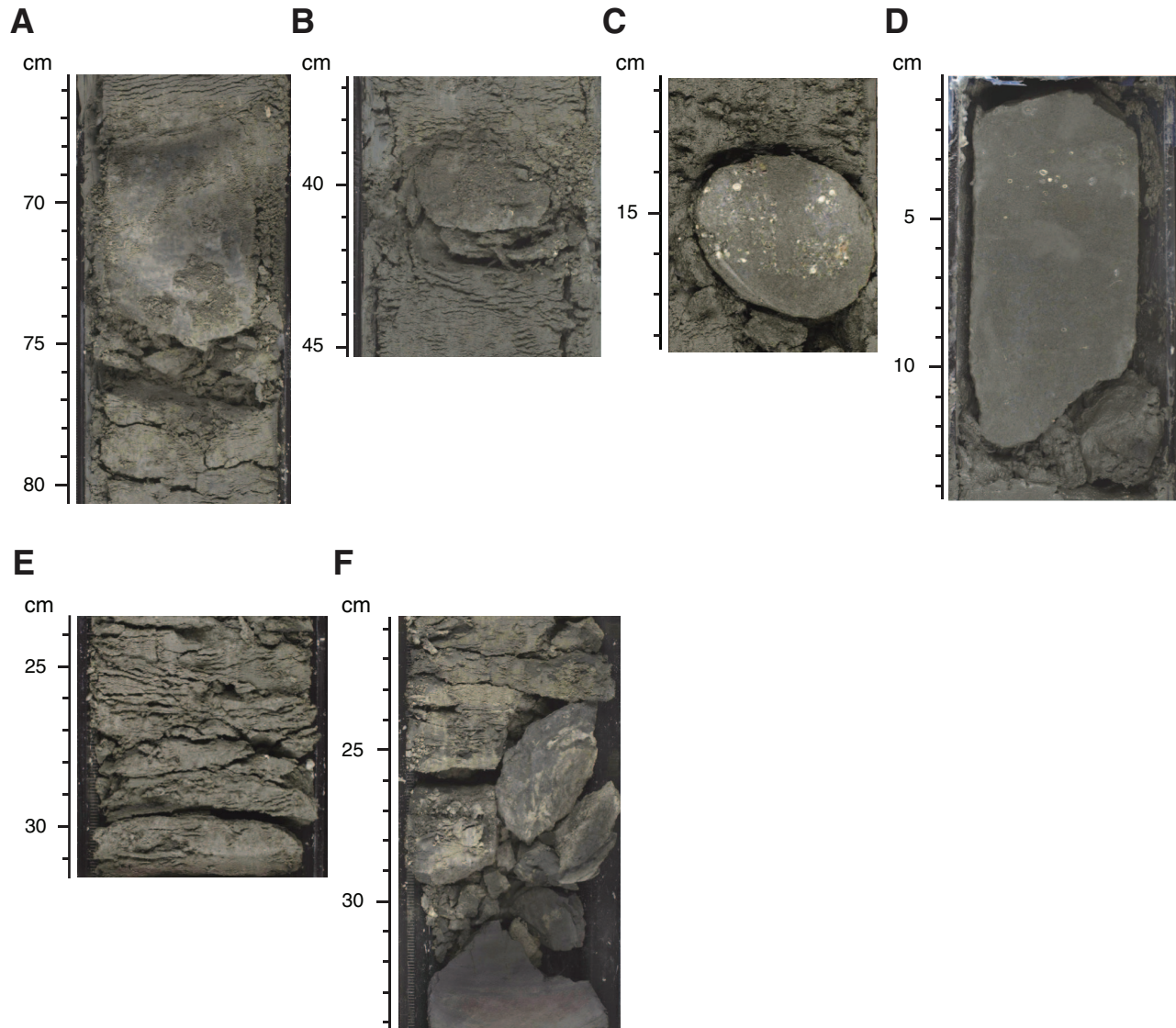
Figure F22. Plots of relative maximum peak intensity in XRD analyses of common minerals, Holes U1351A and U1351B.
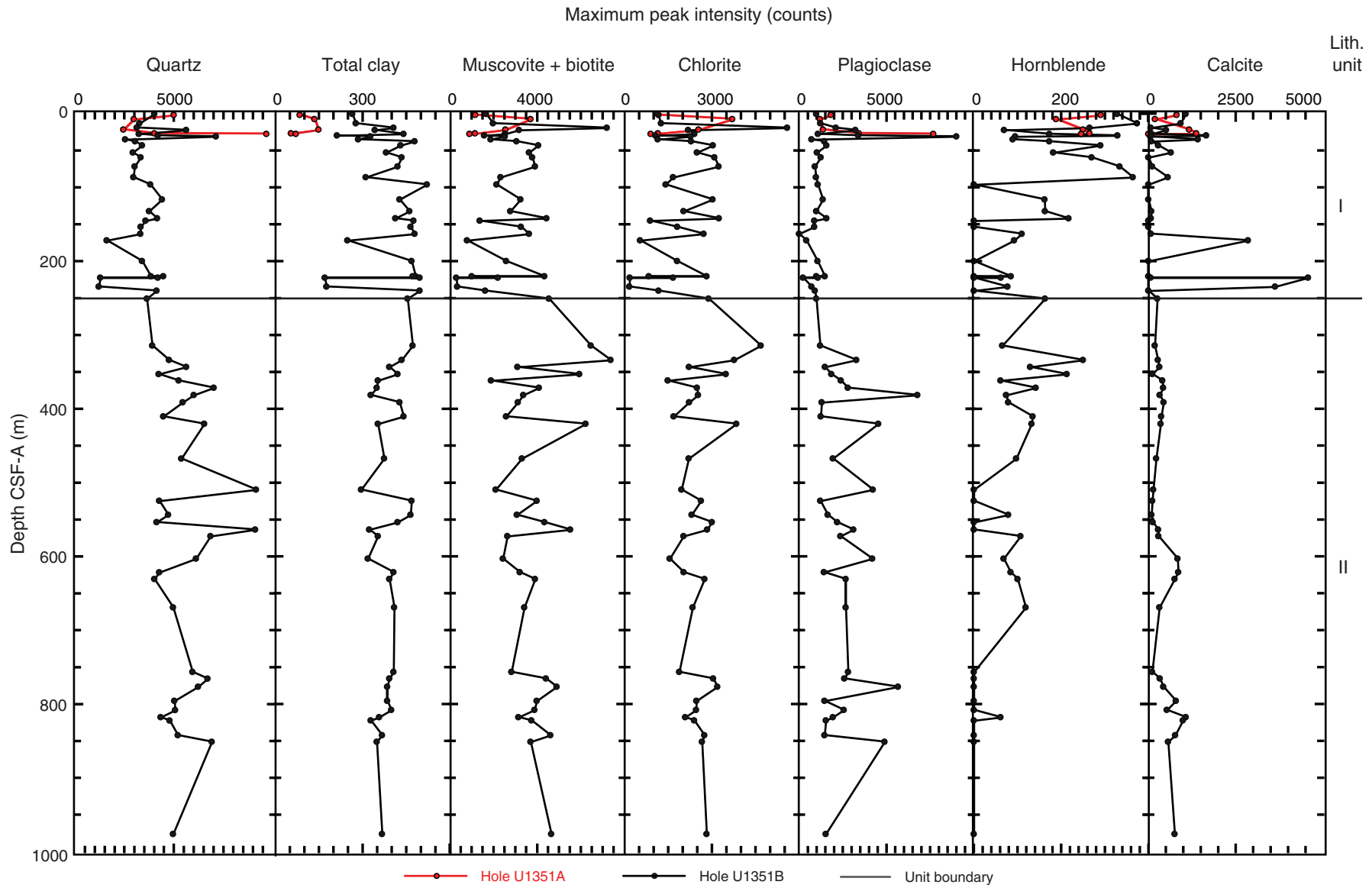
Figure F23. Plots of mineral concentration estimates based on smear slide data from Holes U1351A (open symbols) and U1351B (solid symbols). CaCO$_3$ estimates are plotted against data from coulometry analyses for comparison. Solid line = Unit I/II boundary.
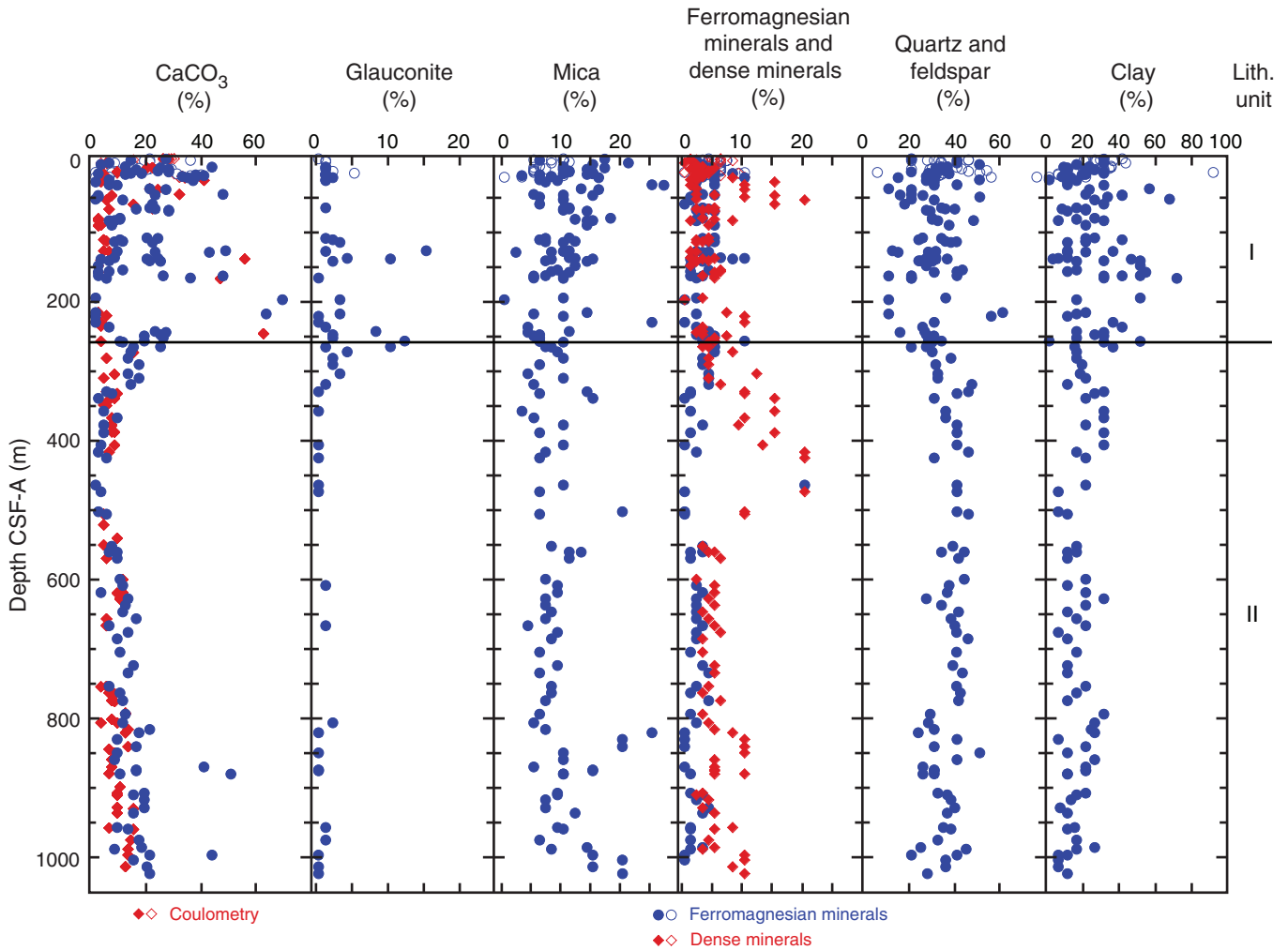
Figure F24. Core recovery, epochs, calcareous nannofossil (NN) zones, and New Zealand (NZ) stage correlation for planktonic foraminifers (PF) and benthic foraminifers (BF), Site U1351. Solid wavy lines = hiatuses between biozones, dashed wavy lines = hiatuses within biozones. See Figure F5 in the "Methods" chapter for NZ stage abbreviations.
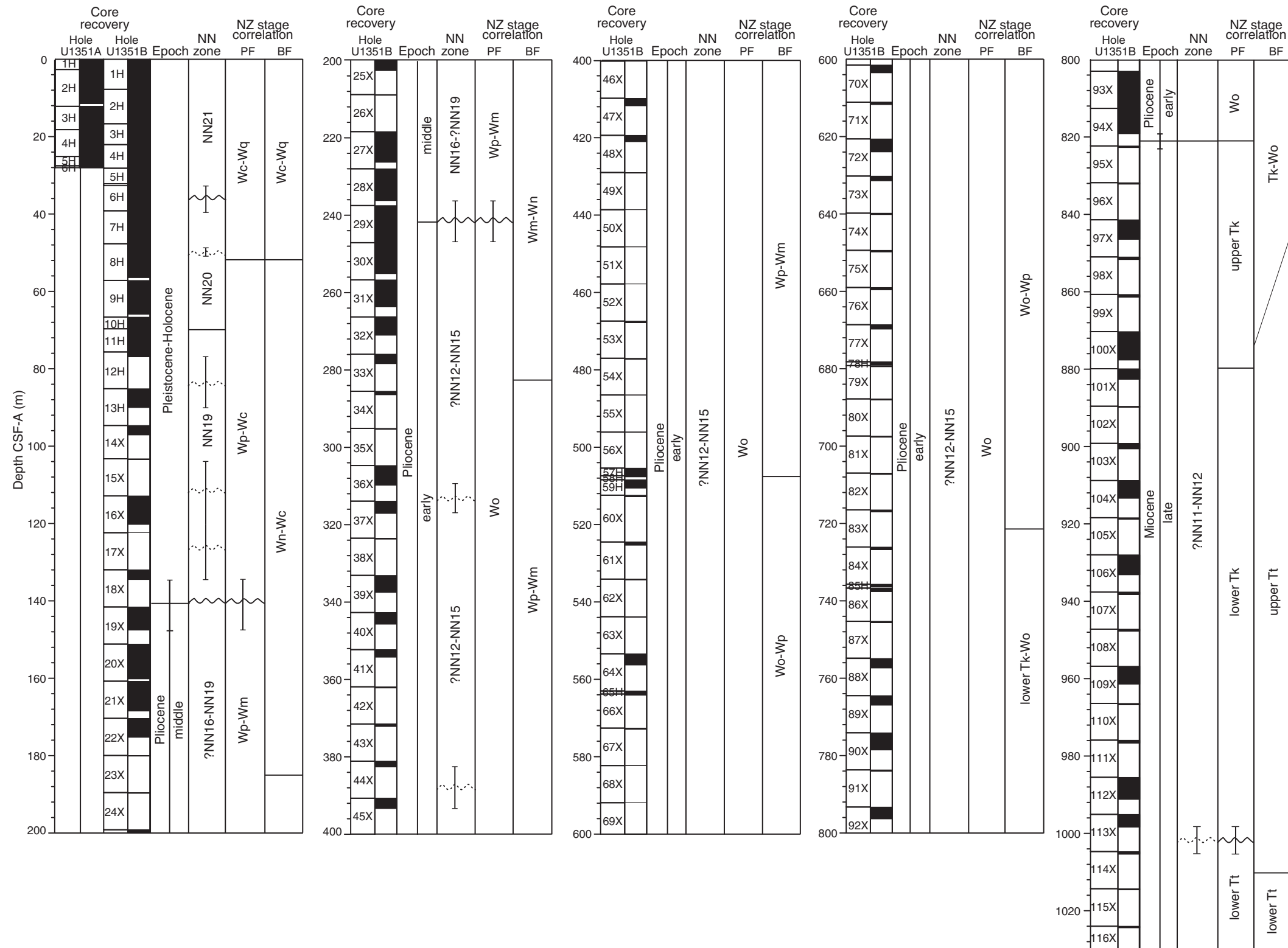
Figure F25. Plot of planktonic foraminiferal abundance relative to total foraminifers and oceanicity, Hole U1351B. See Figure F7 in the "Methods" chapter. For NZ stage abbreviations, see Figure F5 in the "Methods" chapter.
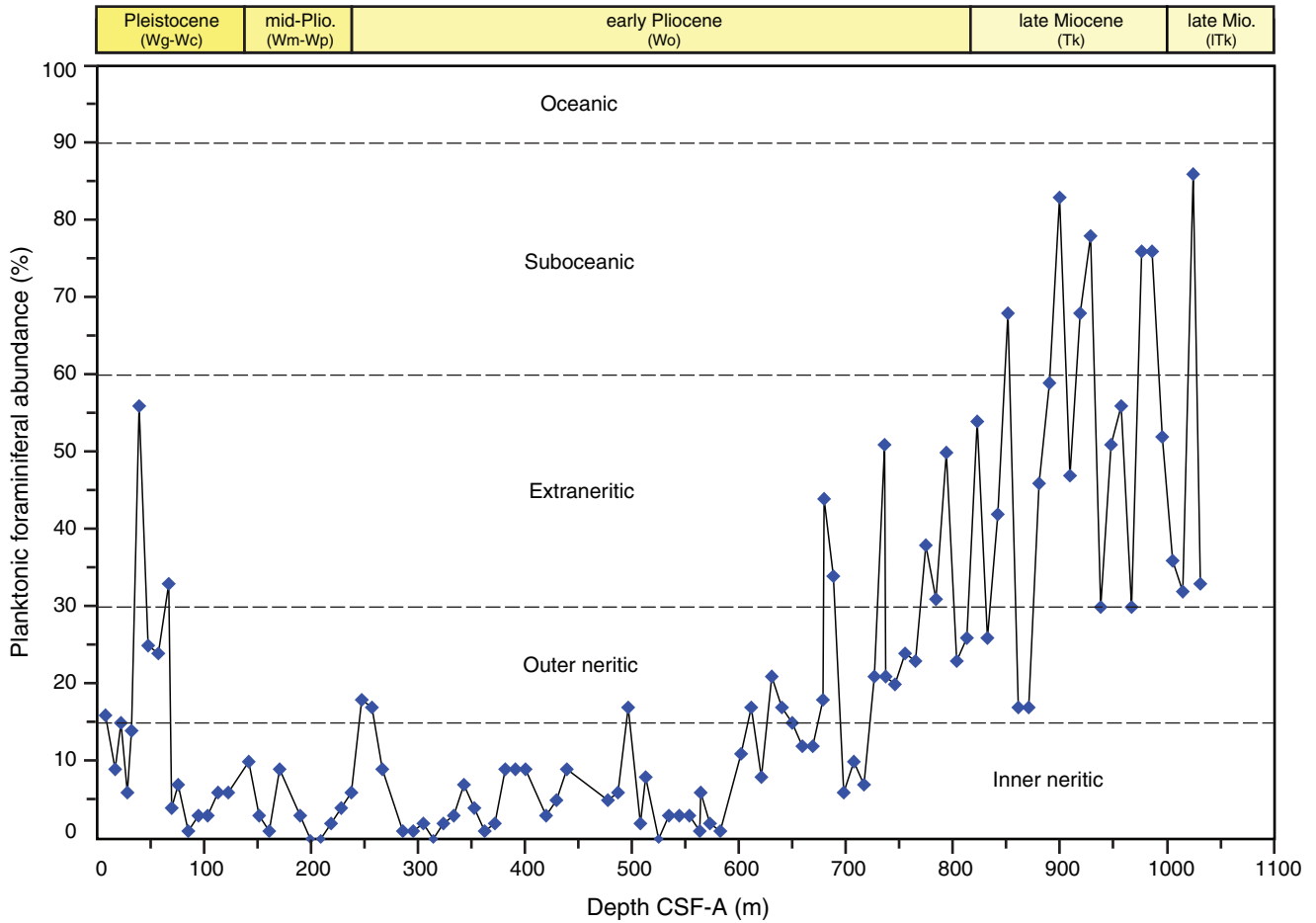
Figure F26. Thin section photomicrographs of (**A**) sparry calcite and (**B**) glauconite-infilled benthic foraminifers in a limestone nodule (Sample 317-U1351B-19X-CC [147.55 m]).

200 µm

200 µm
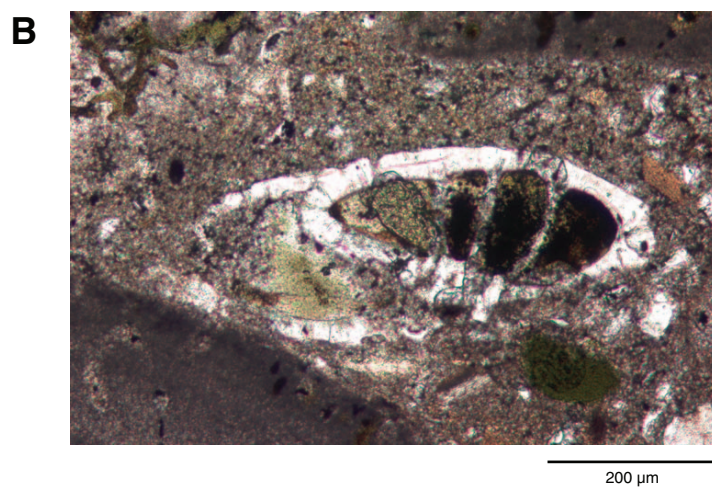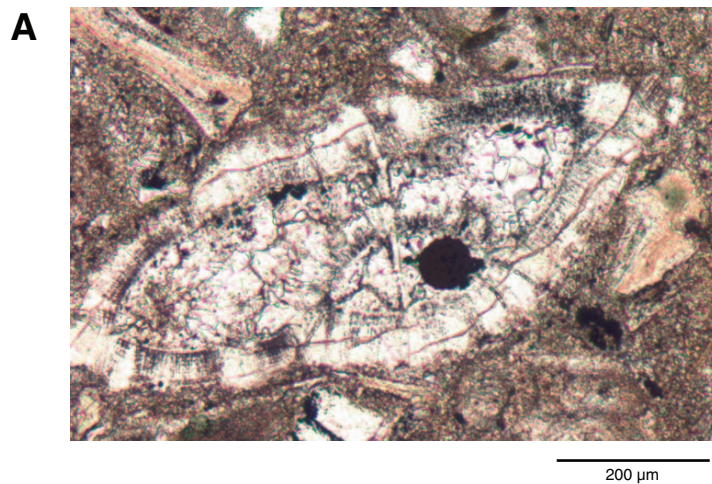
Figure F27. Paleodepth interpretation based on benthic foraminiferal assemblages, Site U1351. For NZ stage abbreviations, see Figure **F5** in the "Methods" chapter.
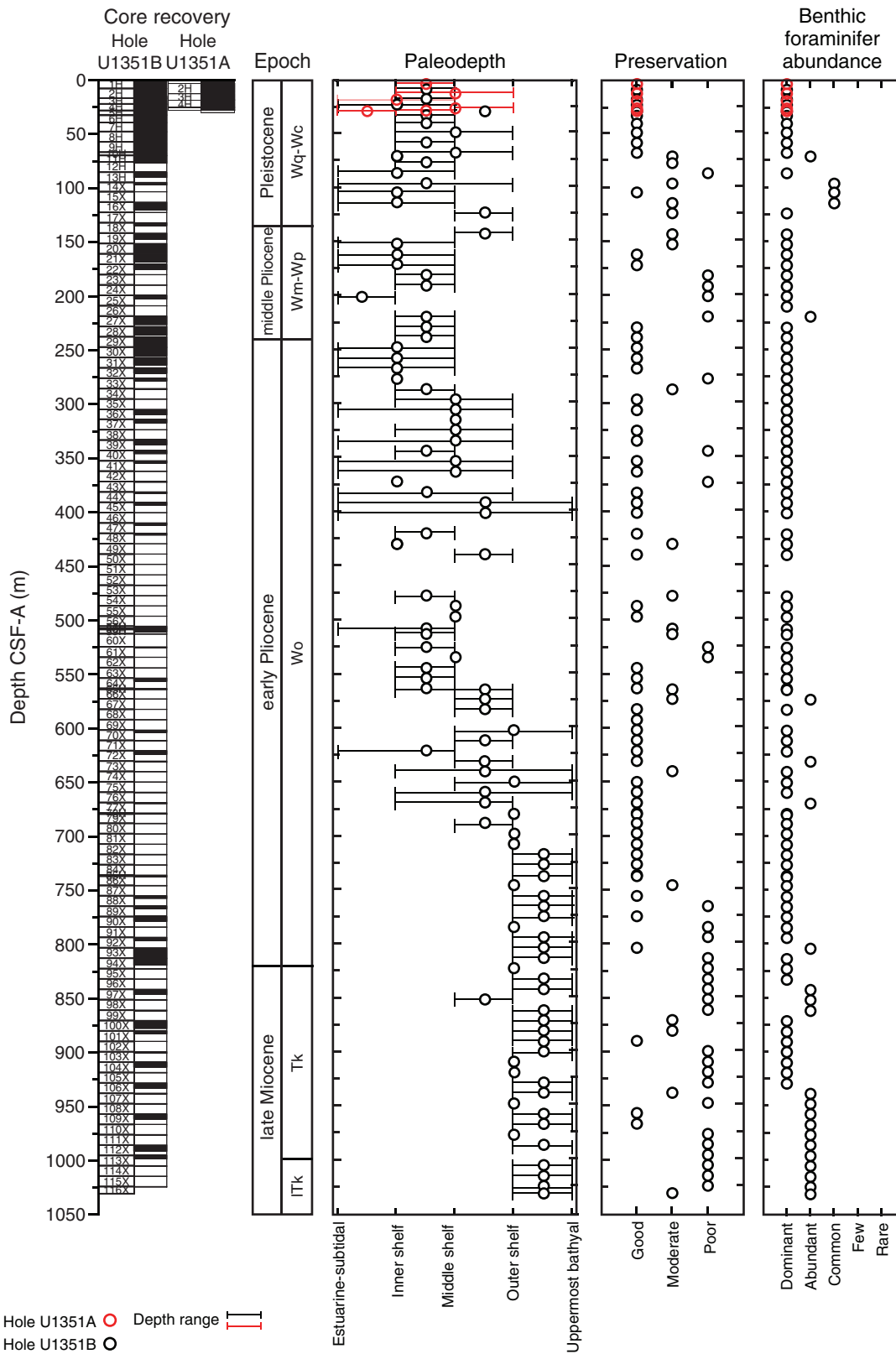
Figure F28. Natural remanent magnetization (NRM) paleomagnetic record for Hole U1351B.
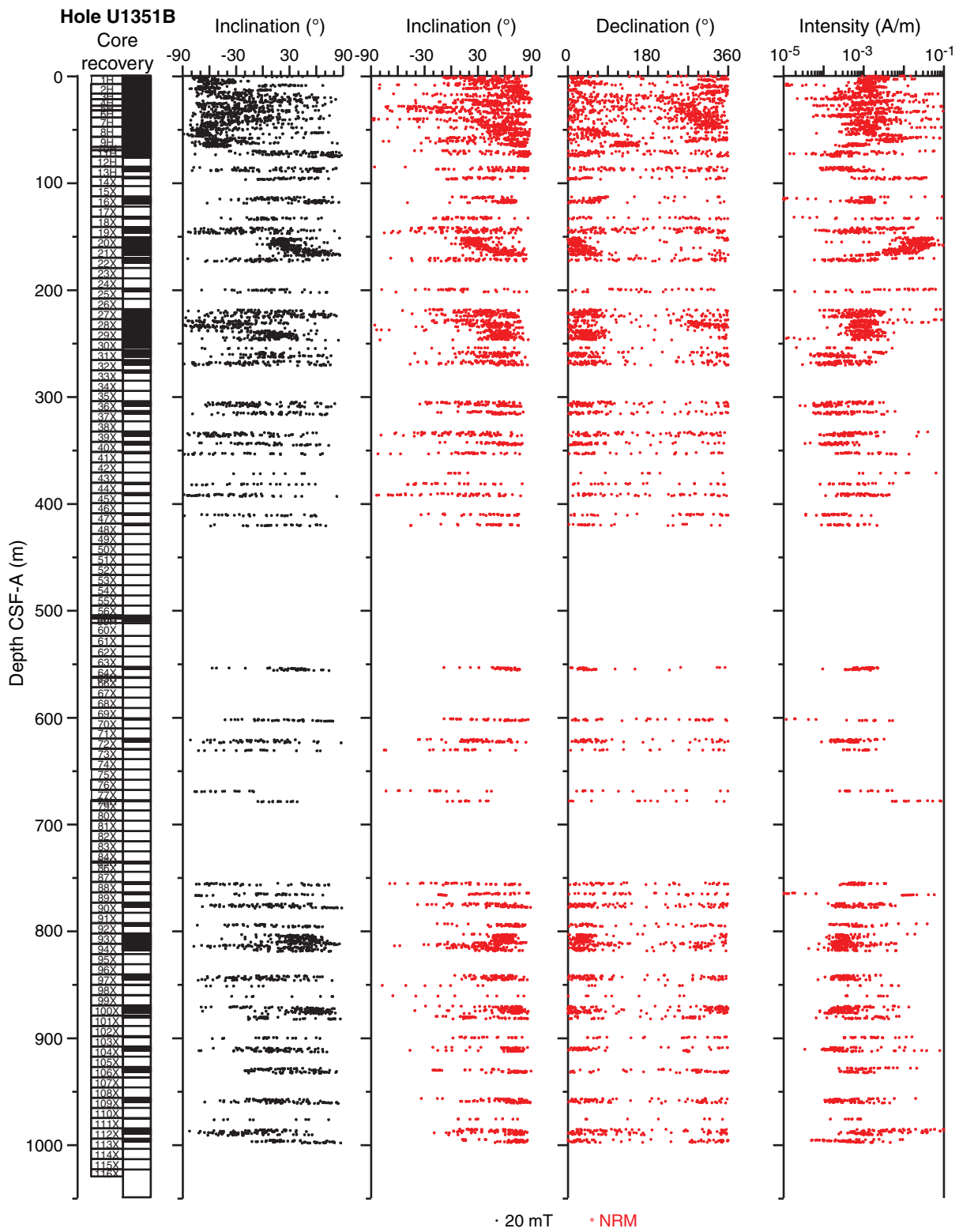
Figure F29. Natural remanent magnetization (NRM) paleomagnetic record of the 0–100 m depth interval in Hole U1351B. Magnetic susceptibility is also shown.
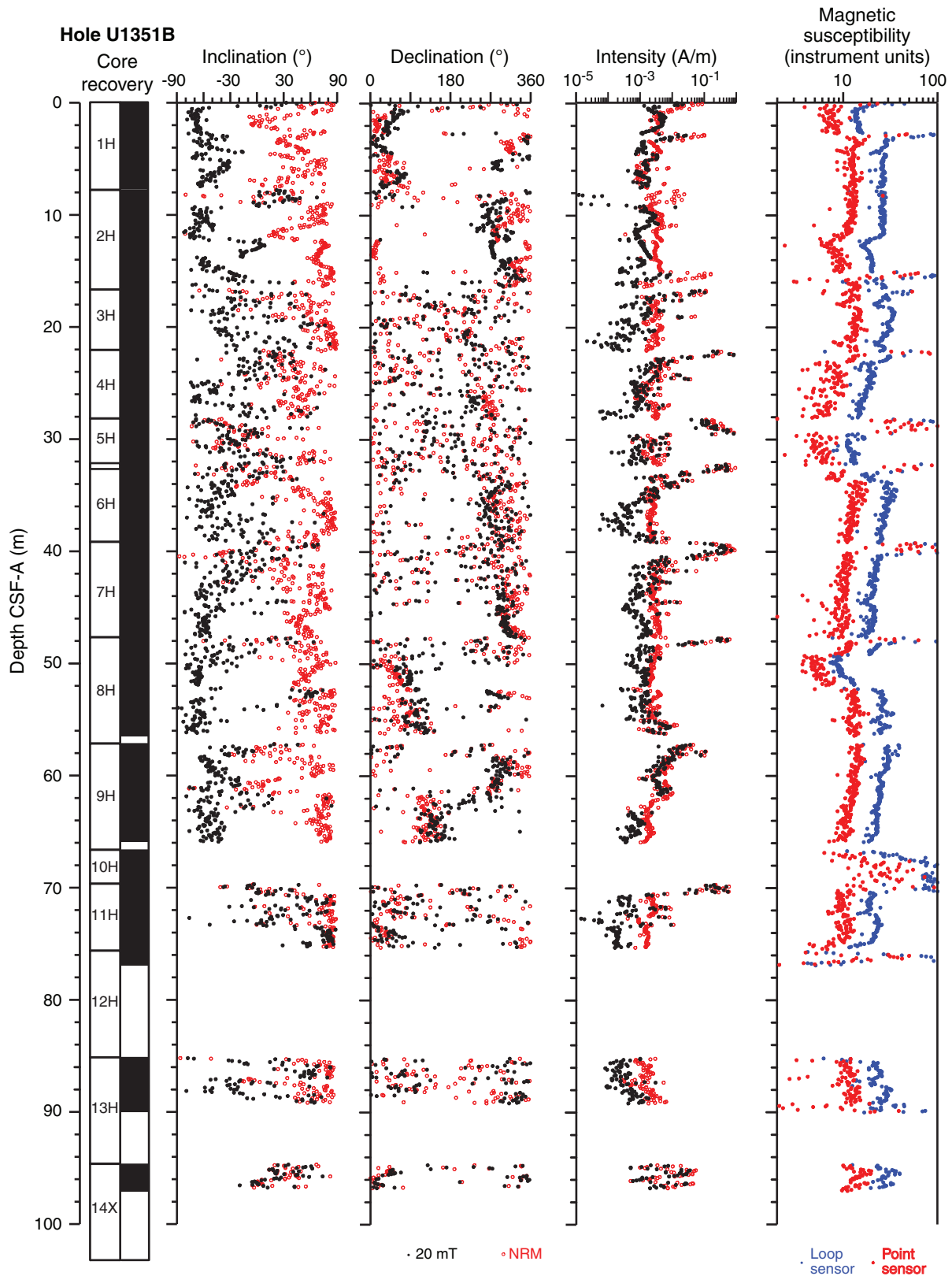
Figure F30. Natural remanent magnetization (NRM) paleomagnetic record of the 110–275 m depth interval in Hole U1351B. Magnetic susceptibility is also shown.
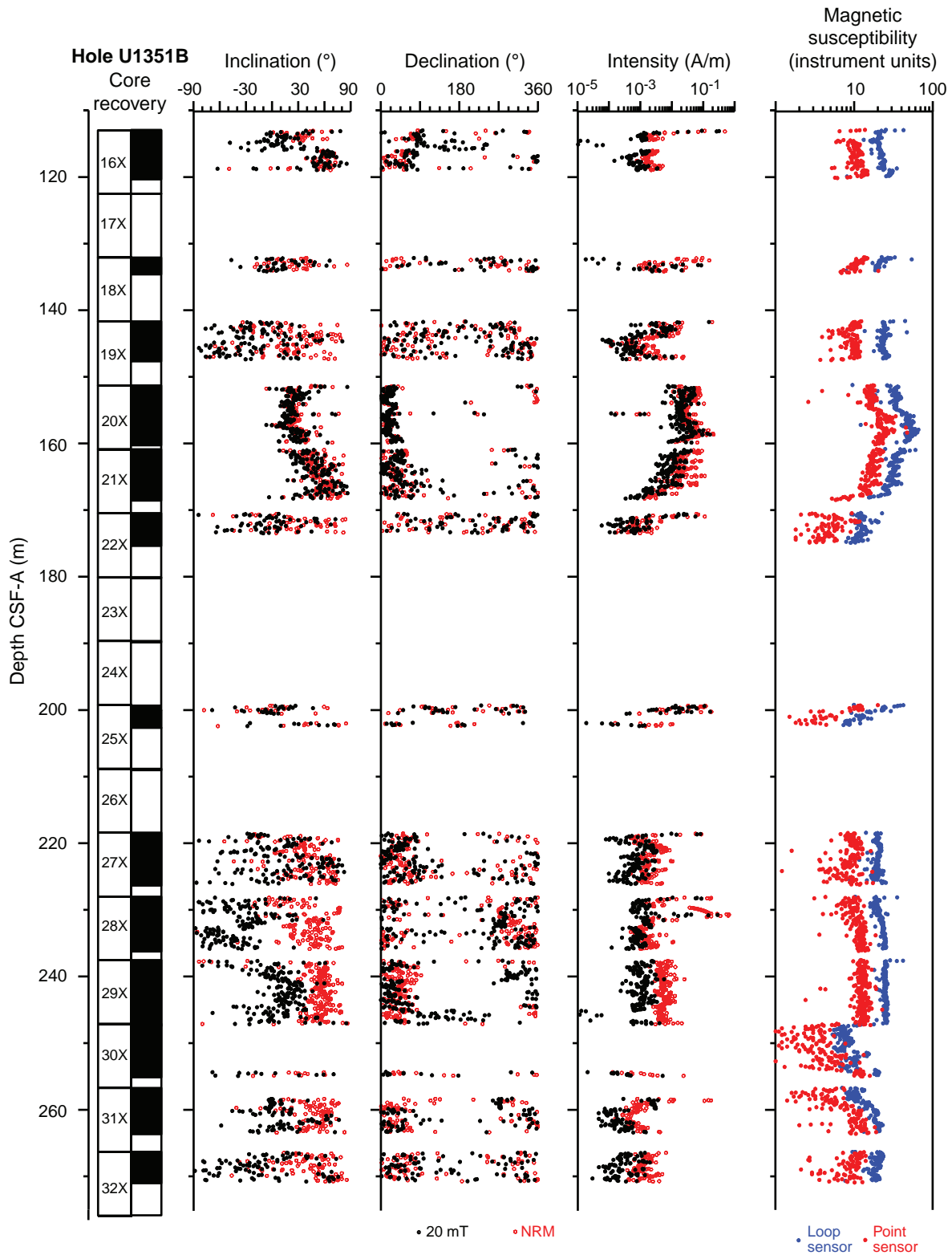
Figure F31. A. Isothermal remanent magnetization (IRM) and backfield acquisition curves for seven discrete samples from Hole U1351B. Samples reach saturation between 300 and 400 mT, and coercivity of remanence (B_{cr}) ranges between 32 and 85 mT. **B.** Alternating-field demagnetization of IRM of the same seven samples. **C.** Same as B, but intensities are normalized to saturation IRM for each sample.
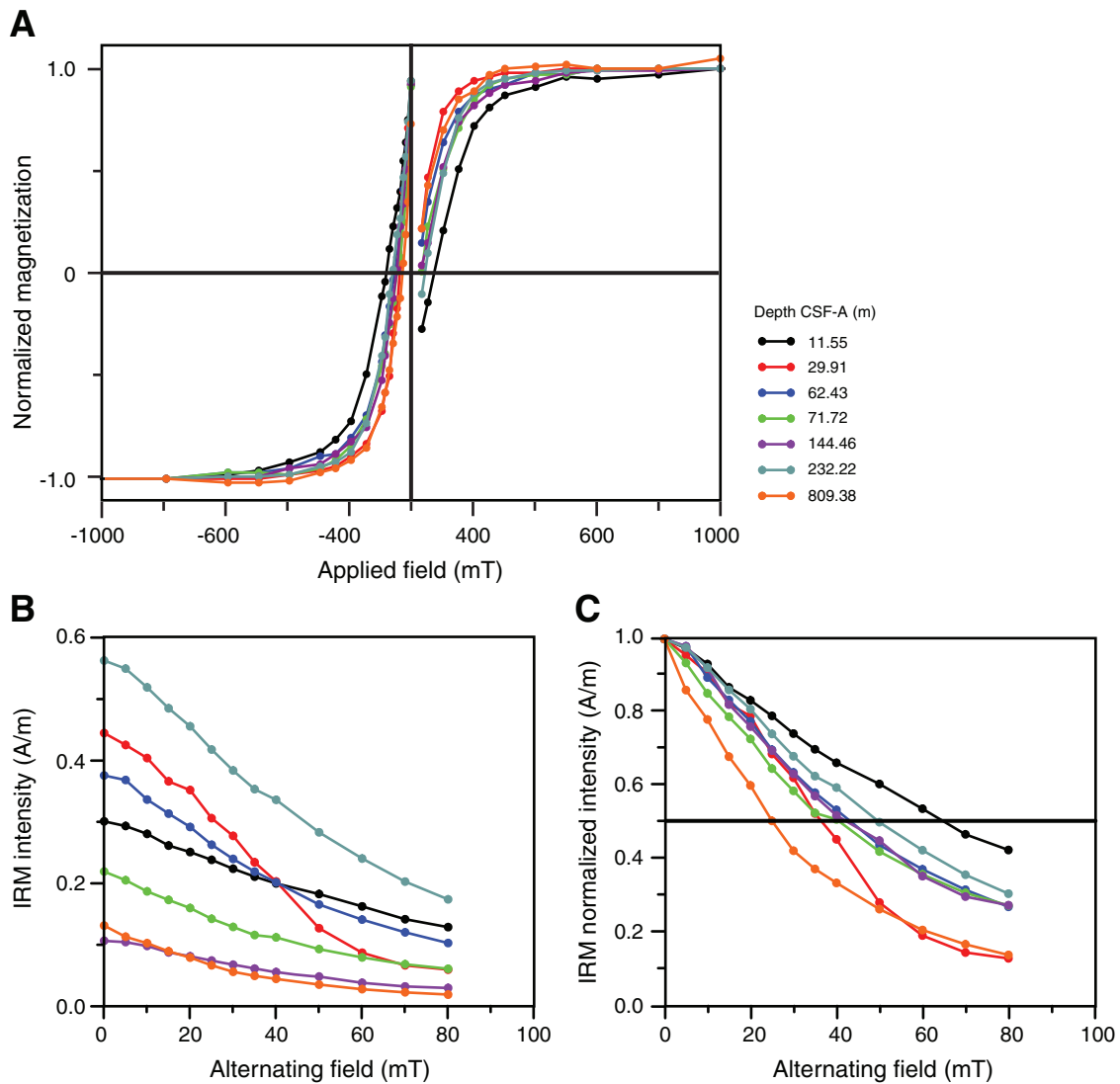
Figure F32. Raw data for magnetic susceptibility (loop and point sensors), natural gamma radiation (NGR), gamma ray attenuation (GRA) bulk density, and color reflectance parameter b*, Hole U1351B.
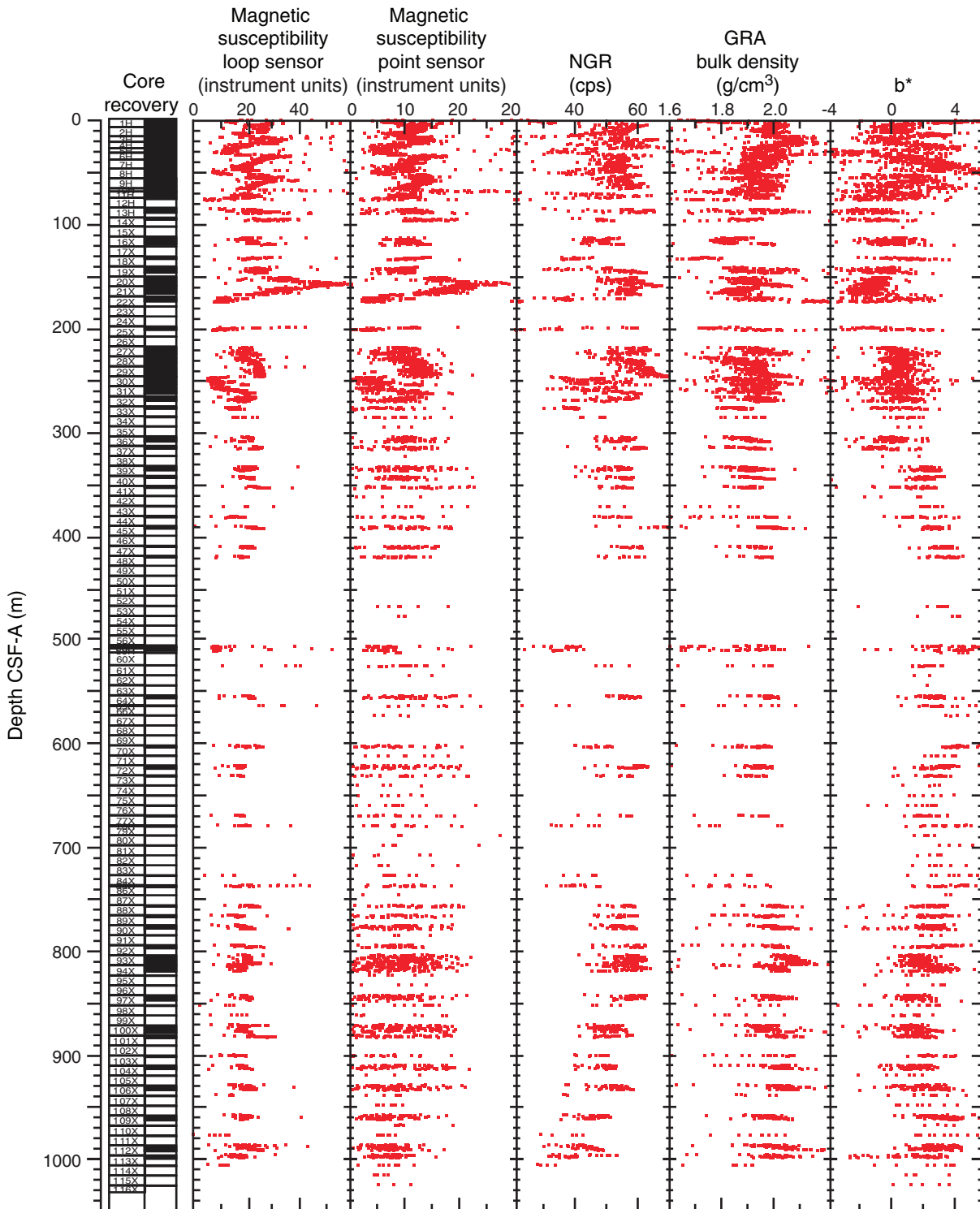
Figure F33. Gaussian low-pass filtered data (50 passes) for magnetic susceptibility (loop and point sensors), natural gamma radiation (NGR), gamma ray attenuation (GRA) bulk density, and color reflectance parameter b*, Hole U1351B.
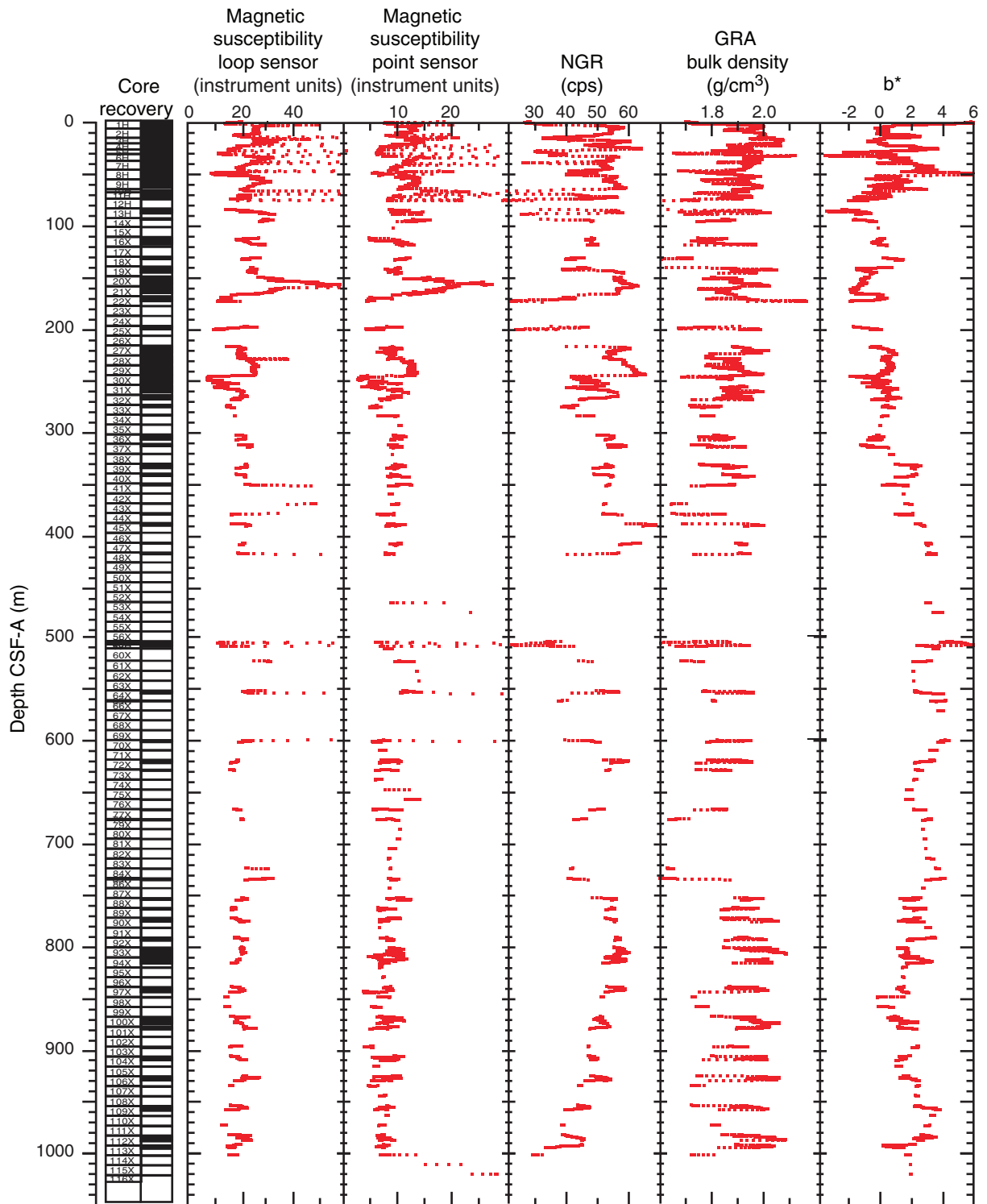
Figure F34. Comparison of bulk density measurements, Holes U1351A (black) and U1351B (red). Circles = moisture and density results, lines = GRA bulk density.
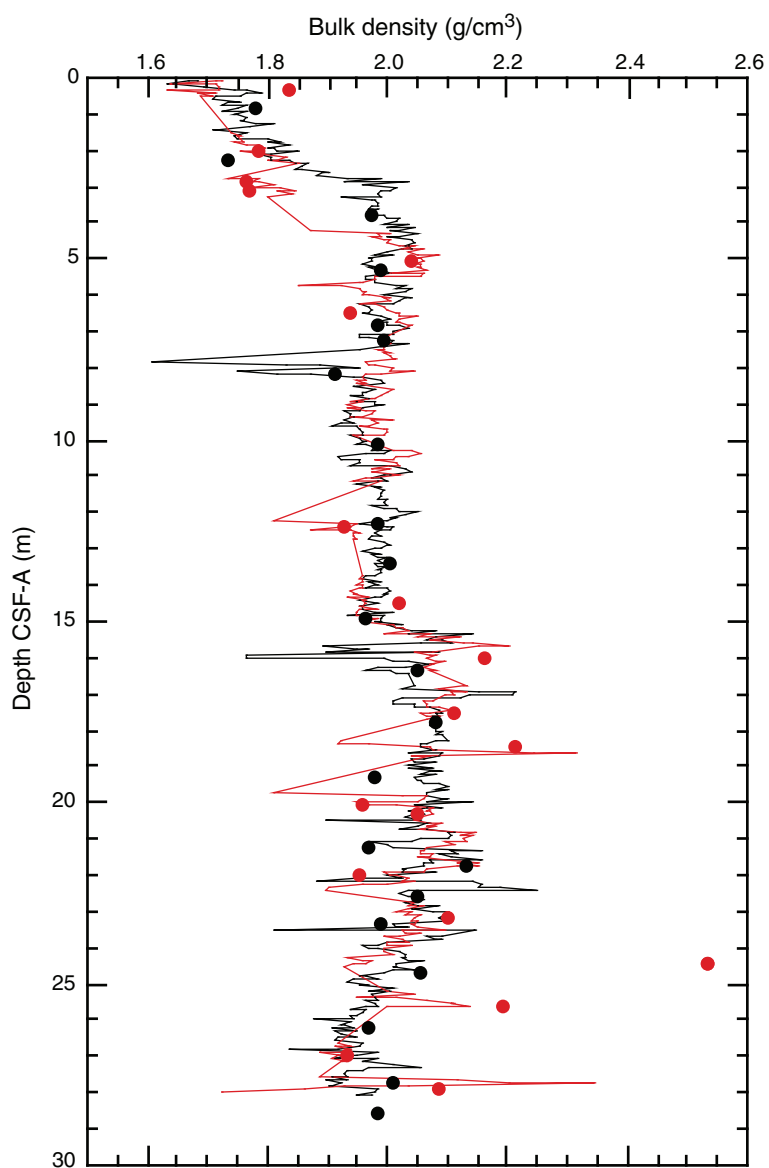
Figure F35. A. Comparison of GRA bulk density (red), density from downhole logs (black), and MAD bulk density (blue), Hole U1351B. Data points affected at the ends of core sections are removed from GRA bulk density data. **B.** Comparison of MAD porosity (blue), neutron porosity from downhole logs (green), and porosity from downhole density logs (black), Hole U1351B. **C.** Hole size, based on caliper measurements during downhole logging, plotted to aid interpretation of downhole logging results. Depth (m) refers to CSF-A for MAD and GRA core data and to WMSF for downhole logging data.
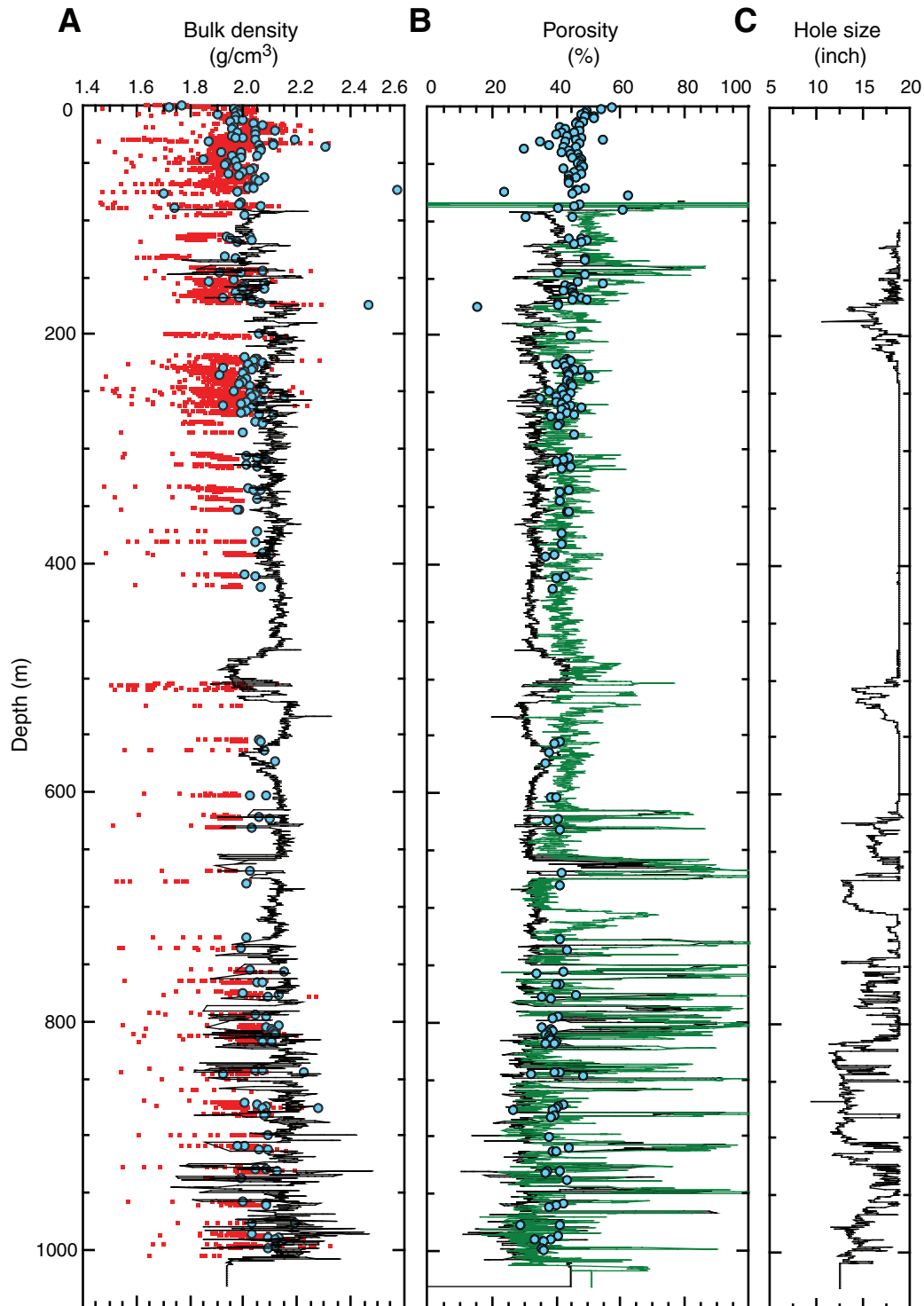
Figure F36. Detailed comparison of bulk density results shown in Figure **F35** for (**A**) 140–210 m, where hole size was <20 inches (based on downhole logs), and (**B**) 210–270 m, where hole size was >20 inches (based on downhole logs). Red = GRA bulk density, black = density from downhole logs, blue = MAD bulk density. Depth (m) refers to CSF-A for MAD results and to WMSF for downhole logging data.
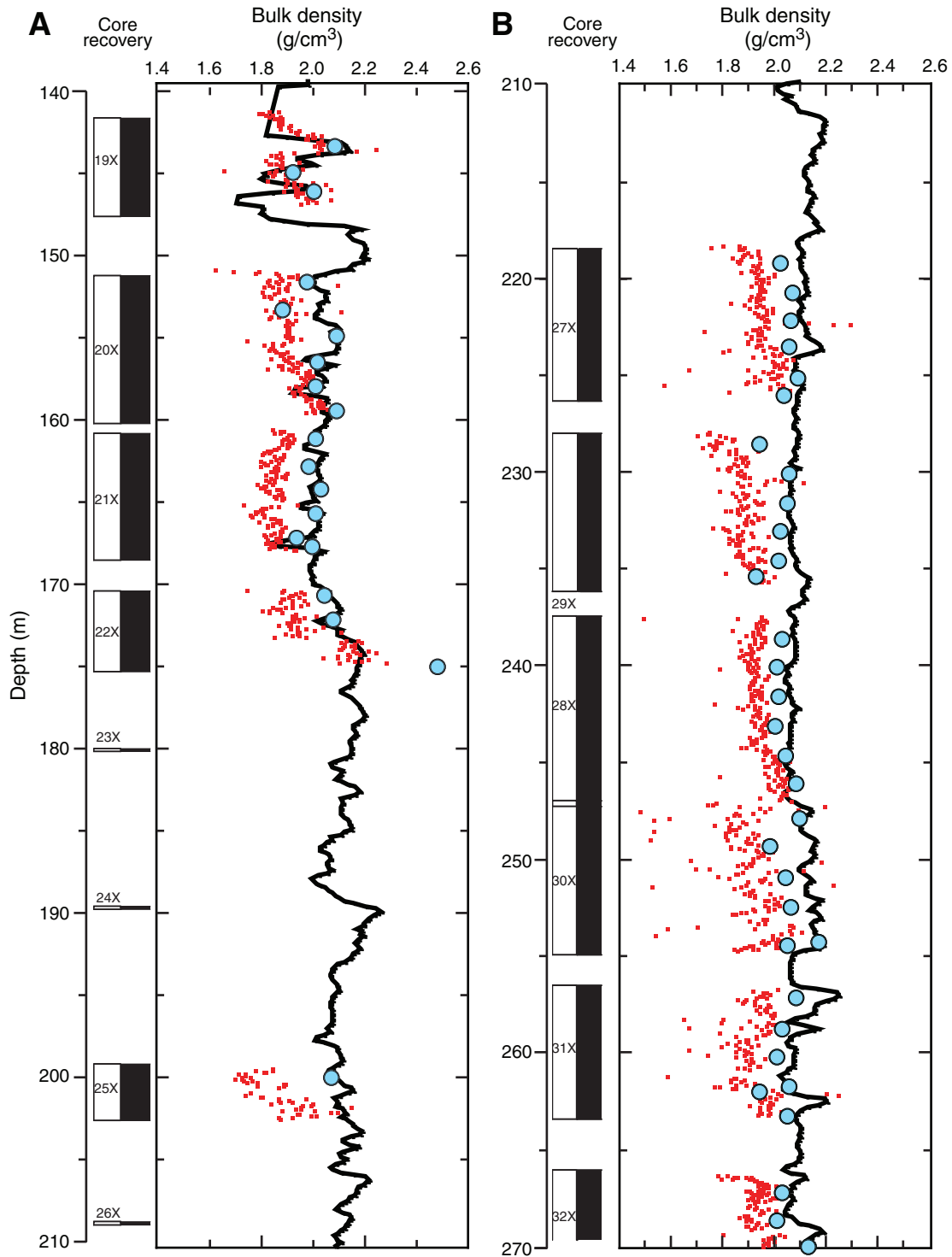
Figure F37. Raw data for magnetic susceptibility (loop and point sensors), natural gamma radiation (NGR), gamma ray attenuation (GRA) bulk density, and color reflectance parameter b*, uppermost 180 m of Hole U1351B.
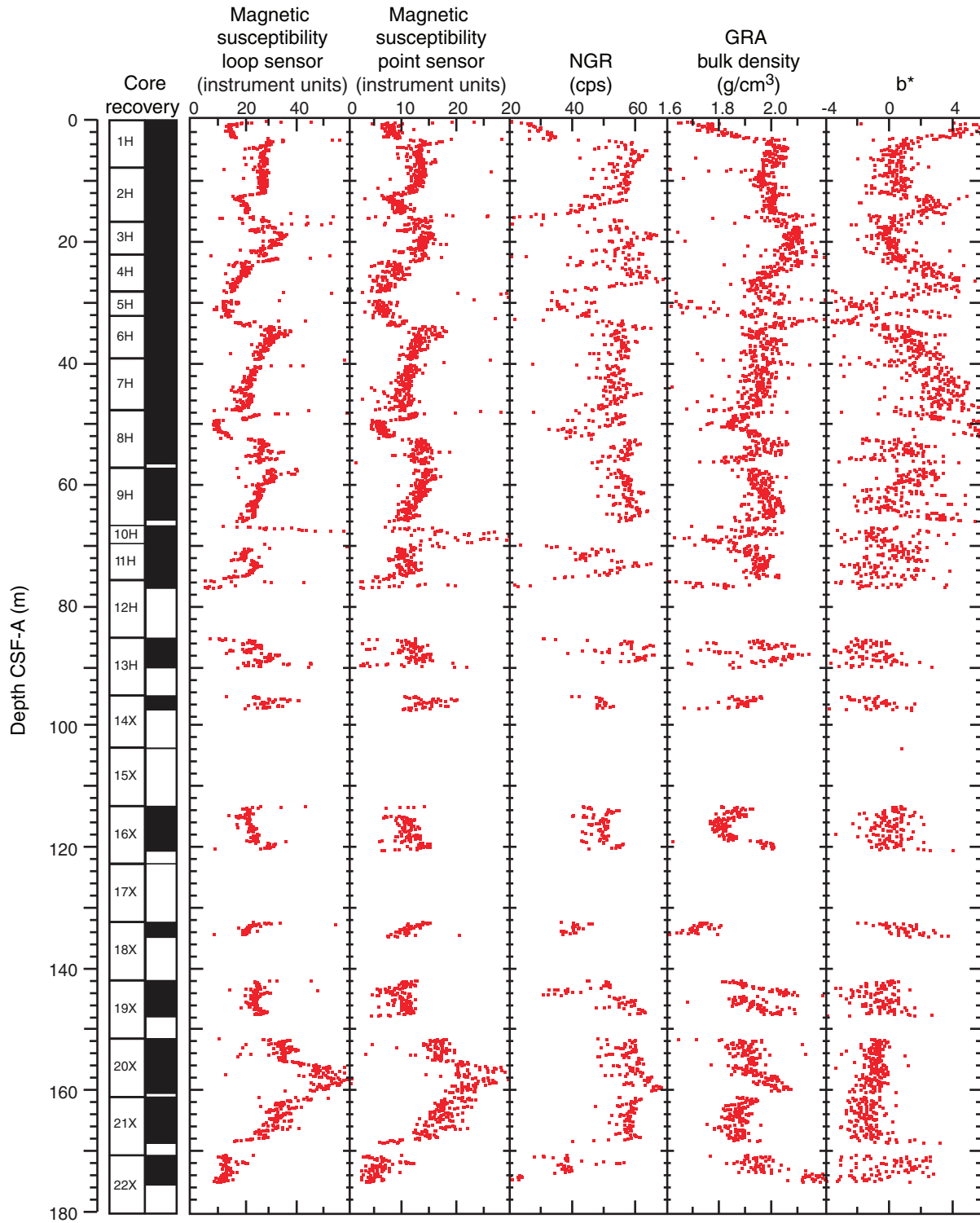
Figure F38. Gaussian low-pass filtered data (50 passes) for magnetic susceptibility (loop and point sensors), natural gamma radiation (NGR), gamma ray attenuation (GRA) bulk density, and color reflectance parameter b*, uppermost 180 m of Hole U1351B.
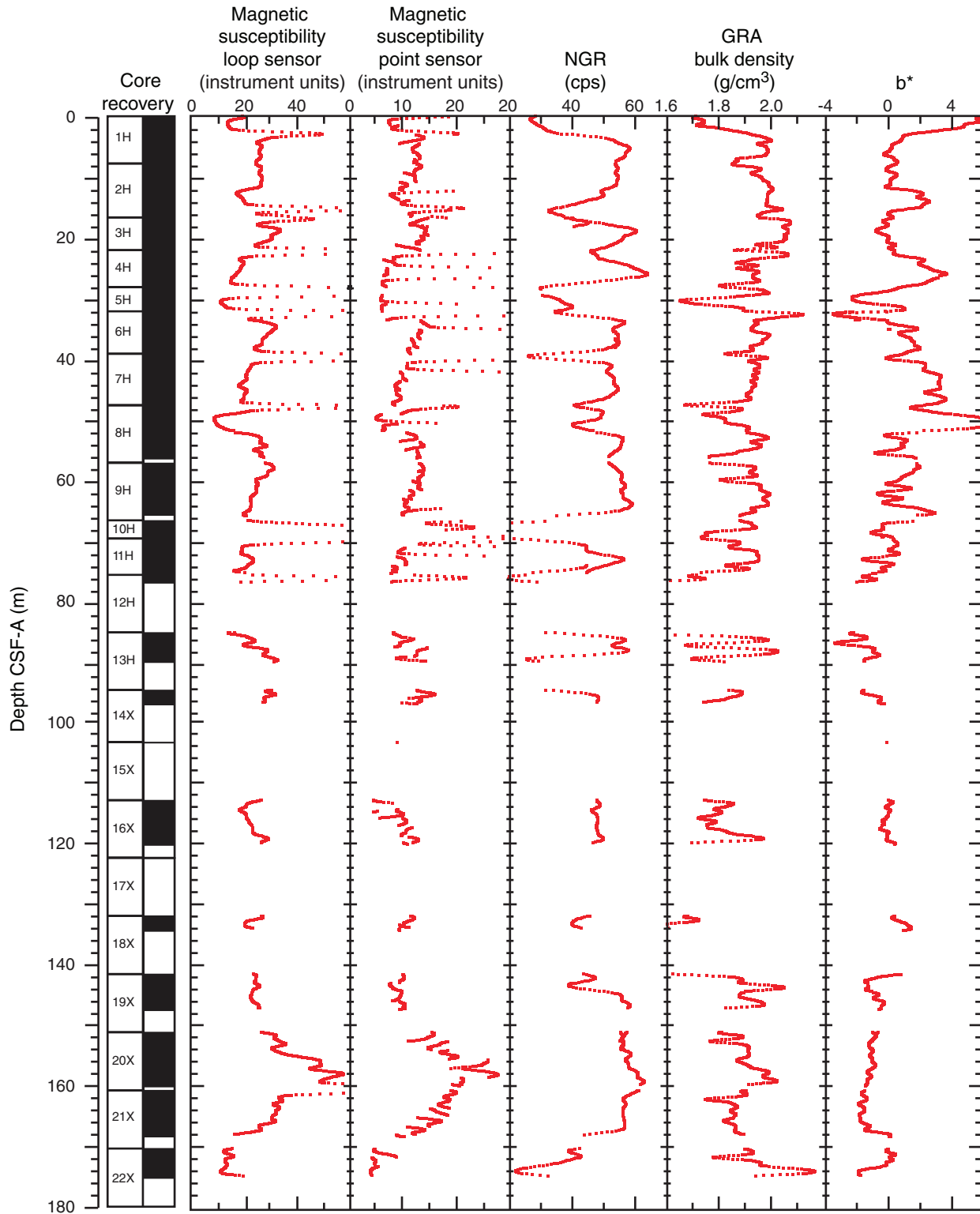
Figure F39. Natural gamma radiation (NGR) core data for the inferred youngest climatic cycle in Hole U1351B (~170 ka; marine isotope Stages [MIS] 1–6) compared with a similar record from Ocean Drilling Program (ODP) Hole 1119C (after Carter et al., 2004), plotted against (A, C) depth and (B, D) age model, respectively. NGR values are plotted on an inverted scale to aid in recognition of the climatic pattern. Selected isotope stages are labeled.
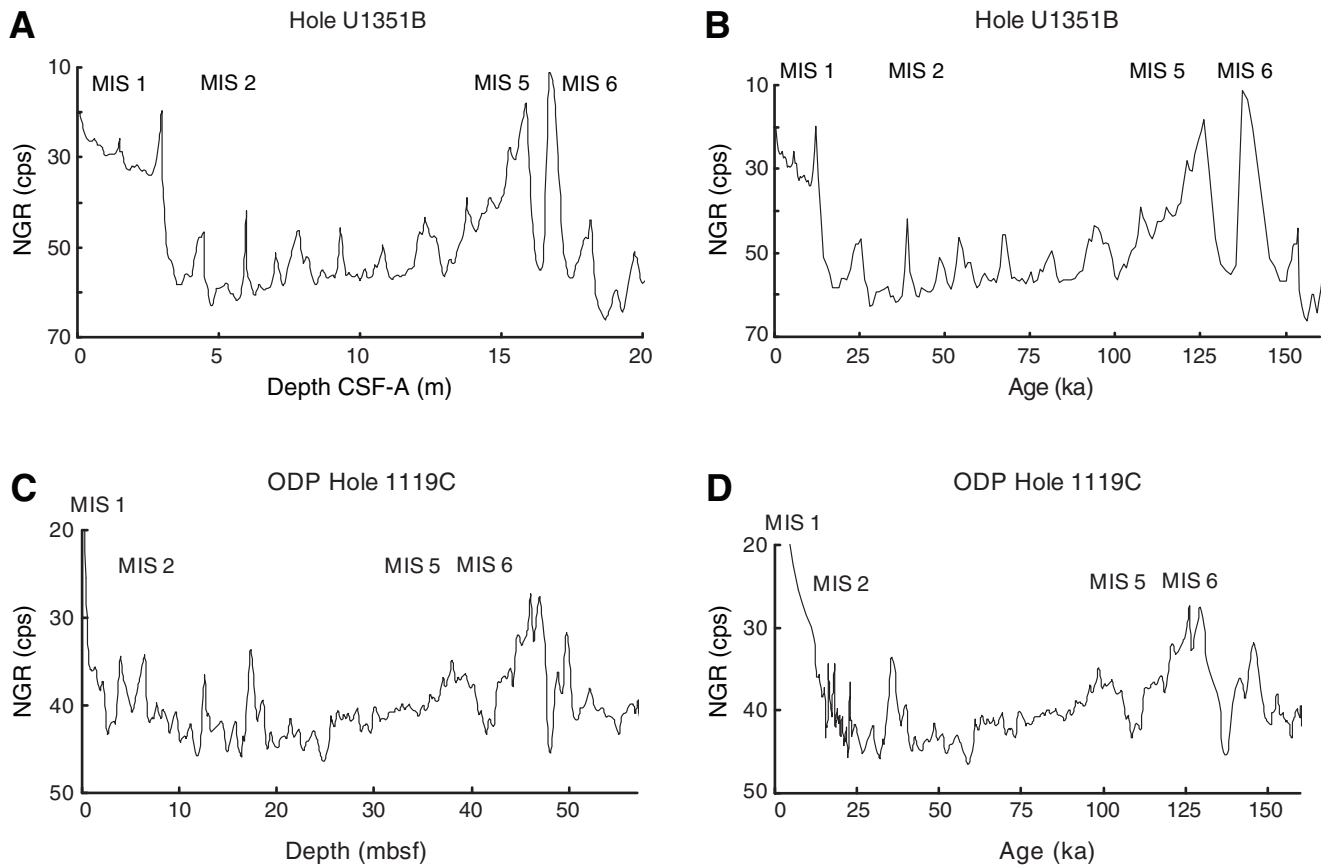
Figure F40. Comparison of (**A, C**) whole-round and (**B, D**) section-half *P*-wave velocities (*x*- and *y*-axis) in the uppermost 25 m of Holes U1351A and U1351B. PWL = *P*-wave logger, PWC = *P*-wave caliper, PWB = *P*-wave bayonets.
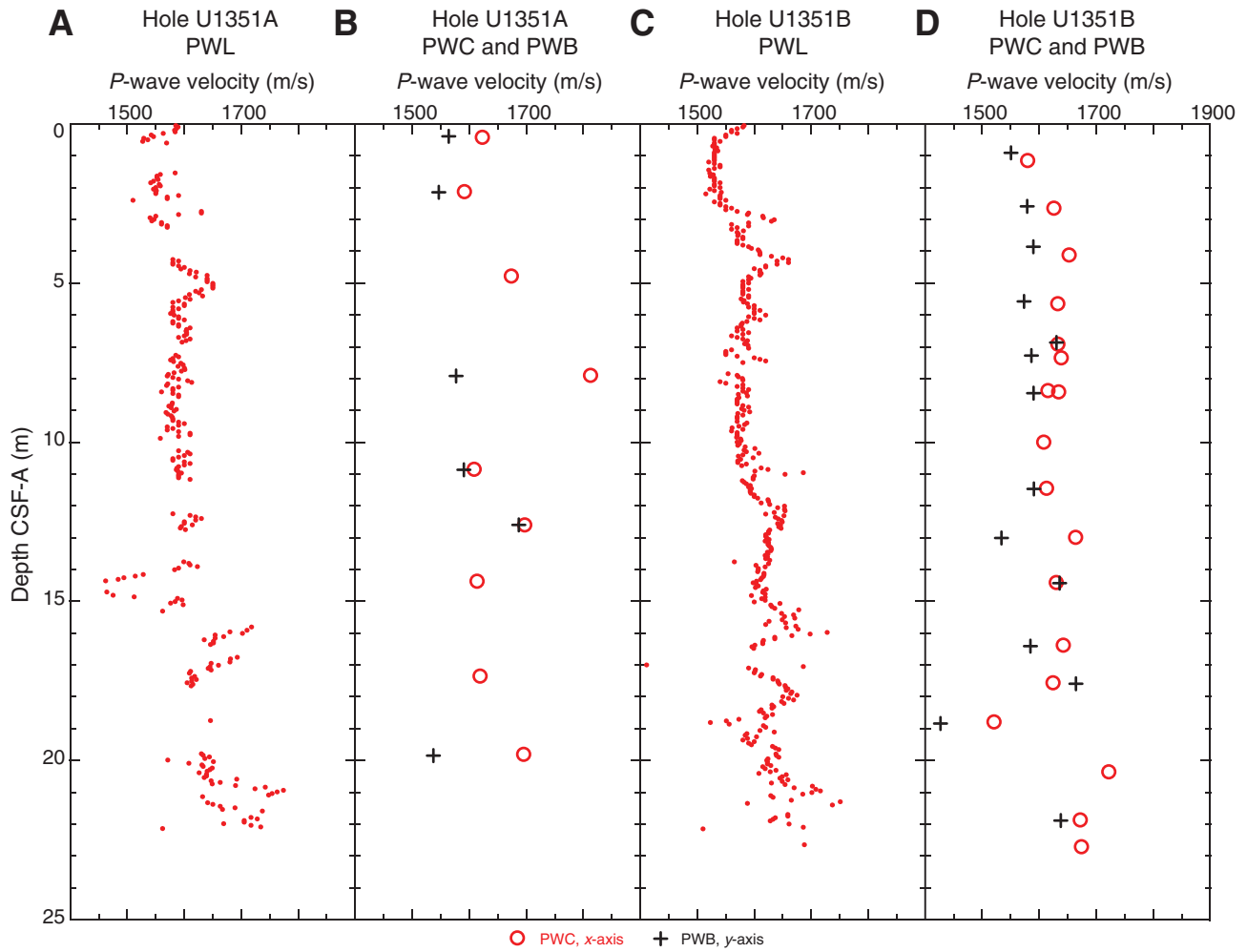
Figure F41. Magnetic susceptibility (point sensor) and colorimetry data, Hole U1351B. Only values <50 instrument units are plotted for magnetic susceptibility (see "Magnetic susceptibility").
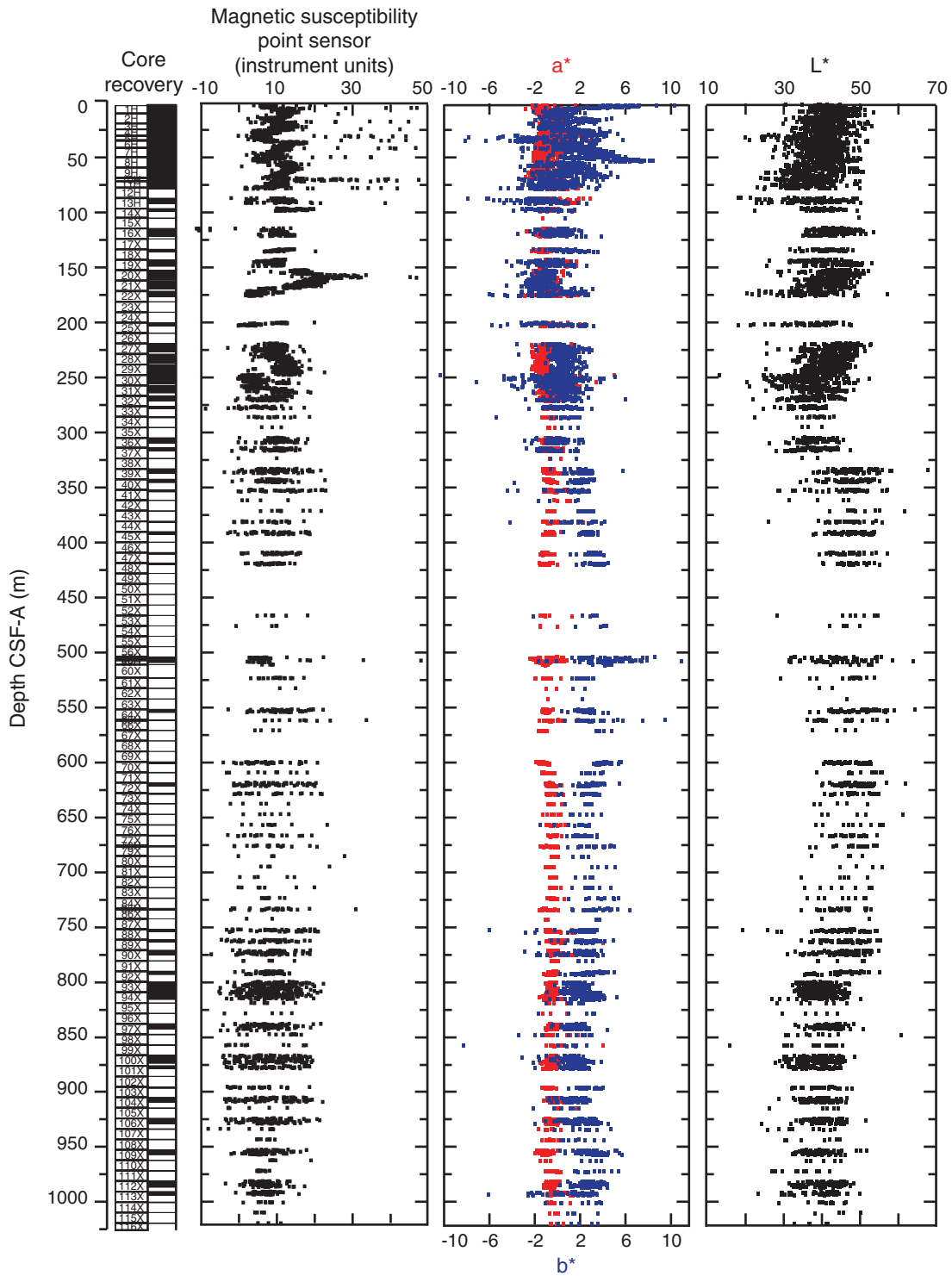
Figure F42. Magnetic susceptibility (point sensor) and colorimetry data for the uppermost 80 m of Hole U1351B. Only values <25 instrument units are plotted for magnetic susceptibility (see **"Magnetic suscepti-bility"**).
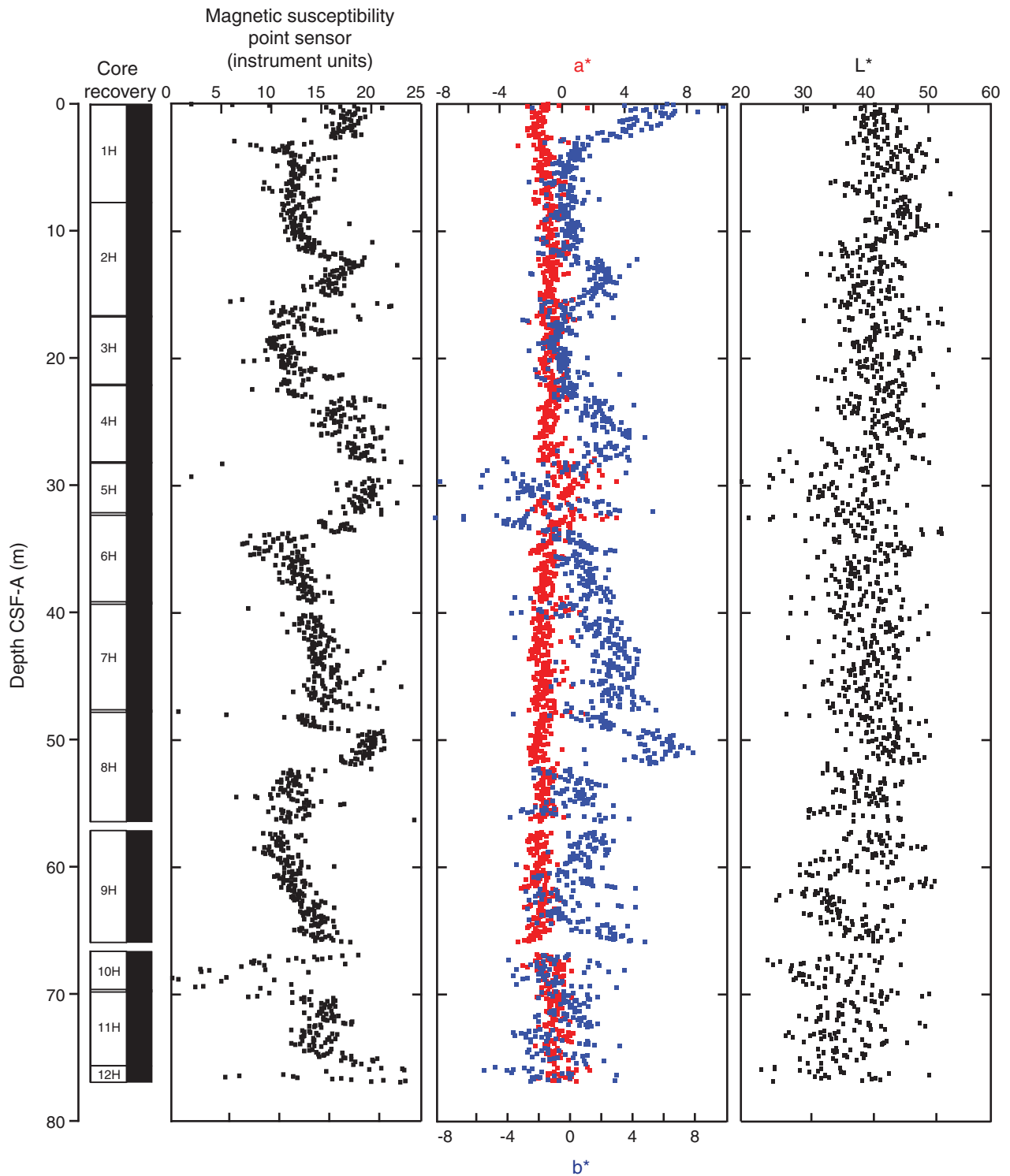
Figure F43. Bulk density, grain density, porosity, and void ratio results for (**A**) Hole U1351A and (**B**) Hole U1351B. Note that vertical scales differ for A and B. Red line = simple relations derived as a function of depth in Hole U1351B. Porosity and void ratio yielded slightly higher correlation with an exponential relationship, whereas bulk and grain density relationships are straight lines.
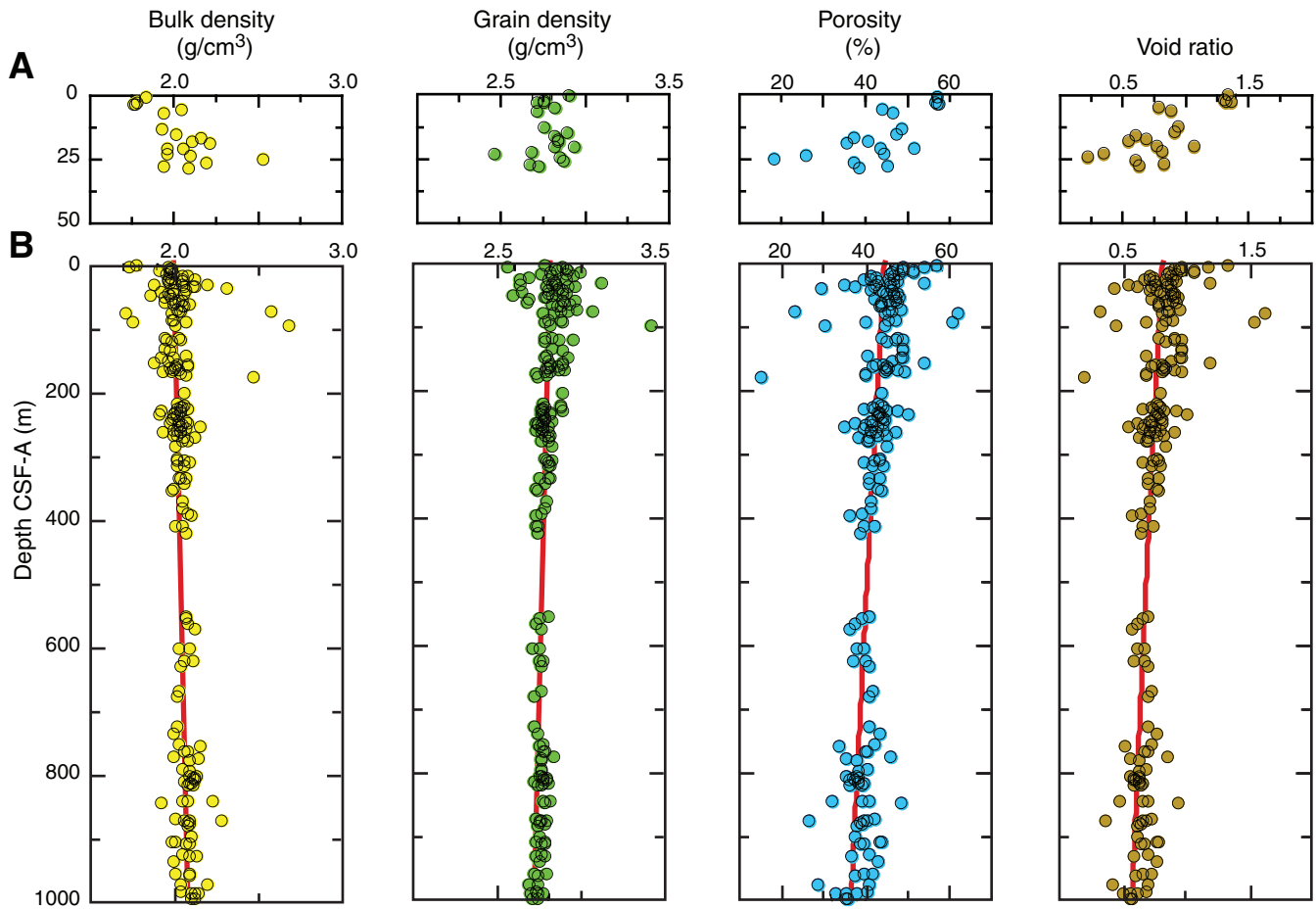
Figure F44. Detailed comparison of porosity results shown in Figure **F35** for (**A**) 140–210 m, where hole size was <20 inches (based on downhole logs), and (**B**) 210–270 m, where hole size was >20 inches (based on downhole logs). Black = porosity derived from downhole density log, green = neutron porosity from downhole logs, blue = MAD porosity. Depth (m) refers to CSF-A for MAD results and to WMSF for downhole logging data.
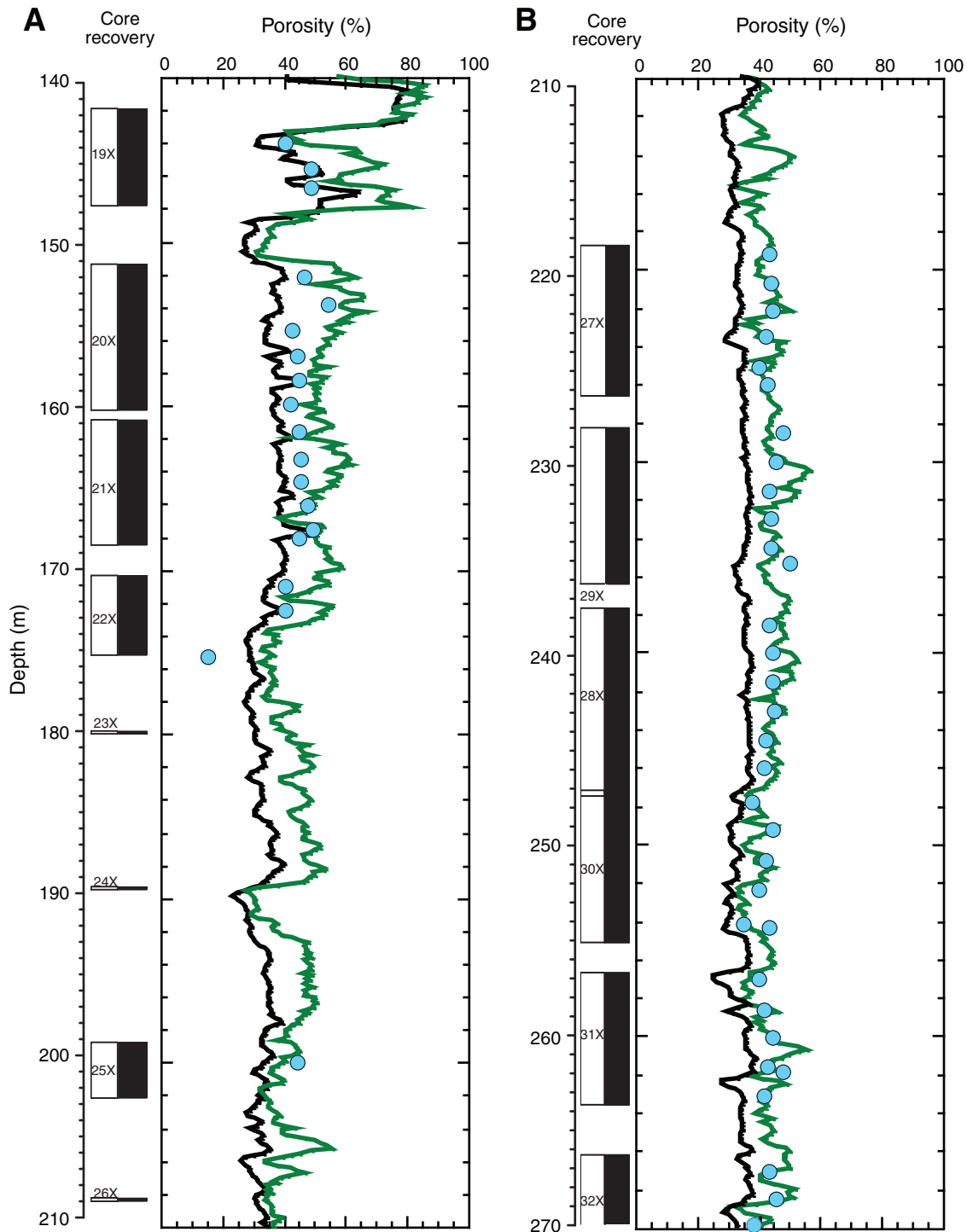
Figure F45. (**A**) Vane shear and (**B**) fall cone penetrometer sediment strength, Hole U1351B; (**C**) vane shear and (**D**) fall cone penetrometer data, uppermost 30 m of Holes U1351A and U1351B; and (**E**) cross-plot of vane shear and fall cone penetrometer data, Holes U1351A and U1351B.
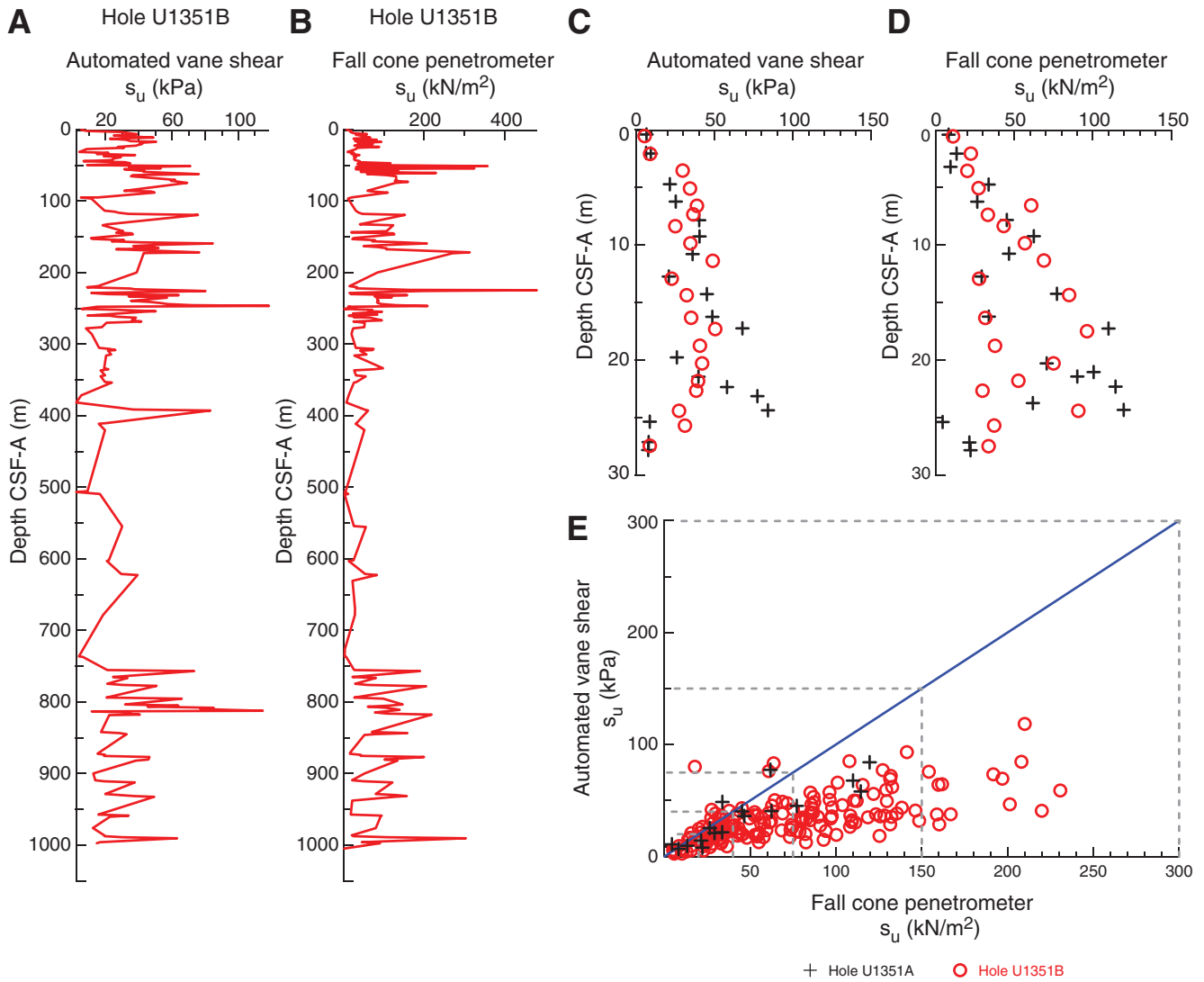
Figure F46. Plots of gas concentrations and composition vs. depth, Holes U1351A (open symbols) and U1351B (solid symbols). **A, D.** Methane (C_1), ethane (C_2), and propane (C_3) in headspace (HS) gas. **B, E.** C_1, C_2, and C_3 from core voids sampled by syringe (VAC). **C, F.** C_1/C_2 gas ratio from both HS and VAC. Bottom panels show total depth; top panels show uppermost 100 m.
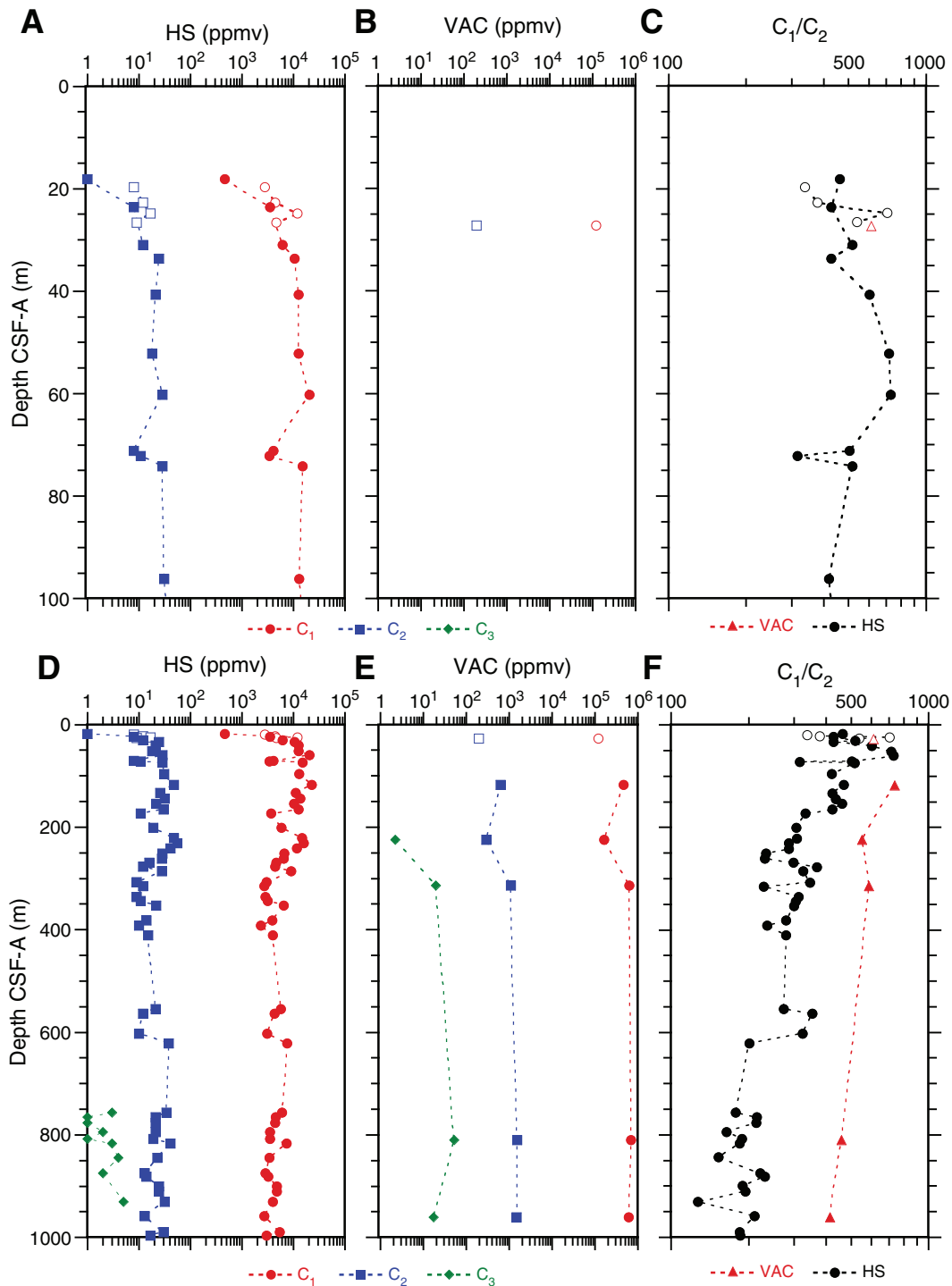
Figure F47. Plots of concentrations of methane (C_1), ethane (C_2), propane (C_3), butanes (n-C_4 = n-butane; i-C_4 = iso-butane), pentanes (n-C_5 = n-pentane; i-C_5 = iso-pentane), and hexanes (n-C_6 = n-hexane) for the six gases from core voids from Holes U1351A and U1351B. br-C_6 = the peak eluting before n-C_6, which may include up to five branched C_6 alkane isomers.
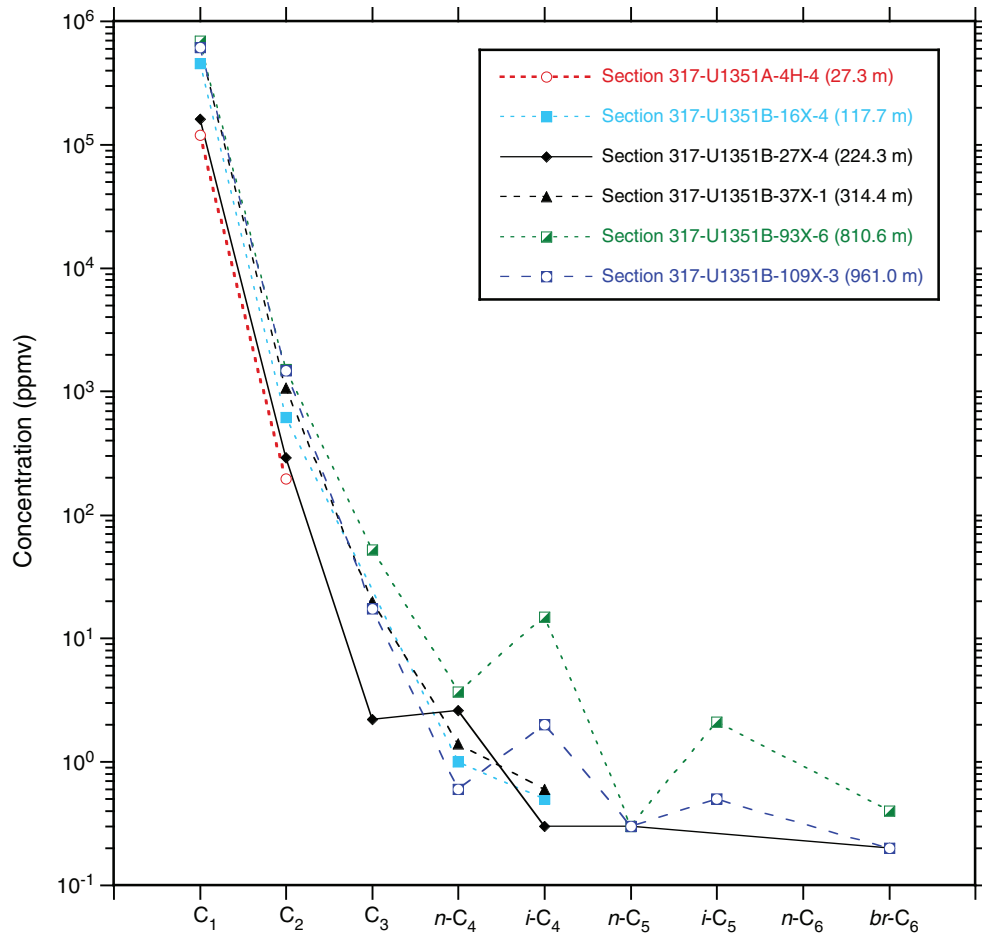
Figure F48. Plots of carbon variation vs. depth, Holes U1351A (red) and U1351B (black). **A.** Carbonate carbon (as $CaCO_3$). **B.** Total carbon. **C.** Total organic carbon by difference (TOC_{DIFF}). **D.** Total organic carbon from the source rock analyzer (TOC_{SRA}).
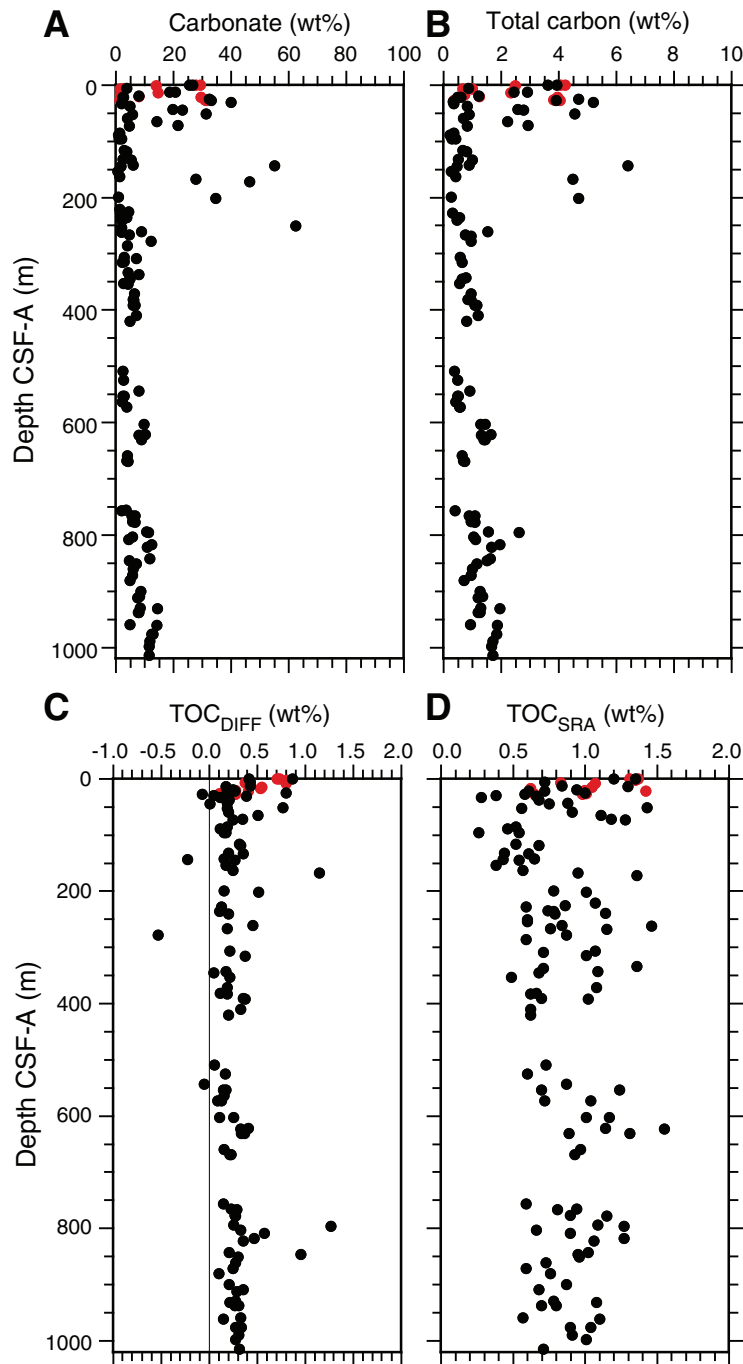
Figure F49. Plots of sediment elemental concentrations vs. depth, Holes U1351A (red) and U1351B (black). **A.** Ratio of total organic carbon by difference (TOC_{DIFF}) to total nitrogen. **B.** Ratio of TOC_{DIFF} to total sulfur. **C.** Total nitrogen. **D.** Total sulfur.
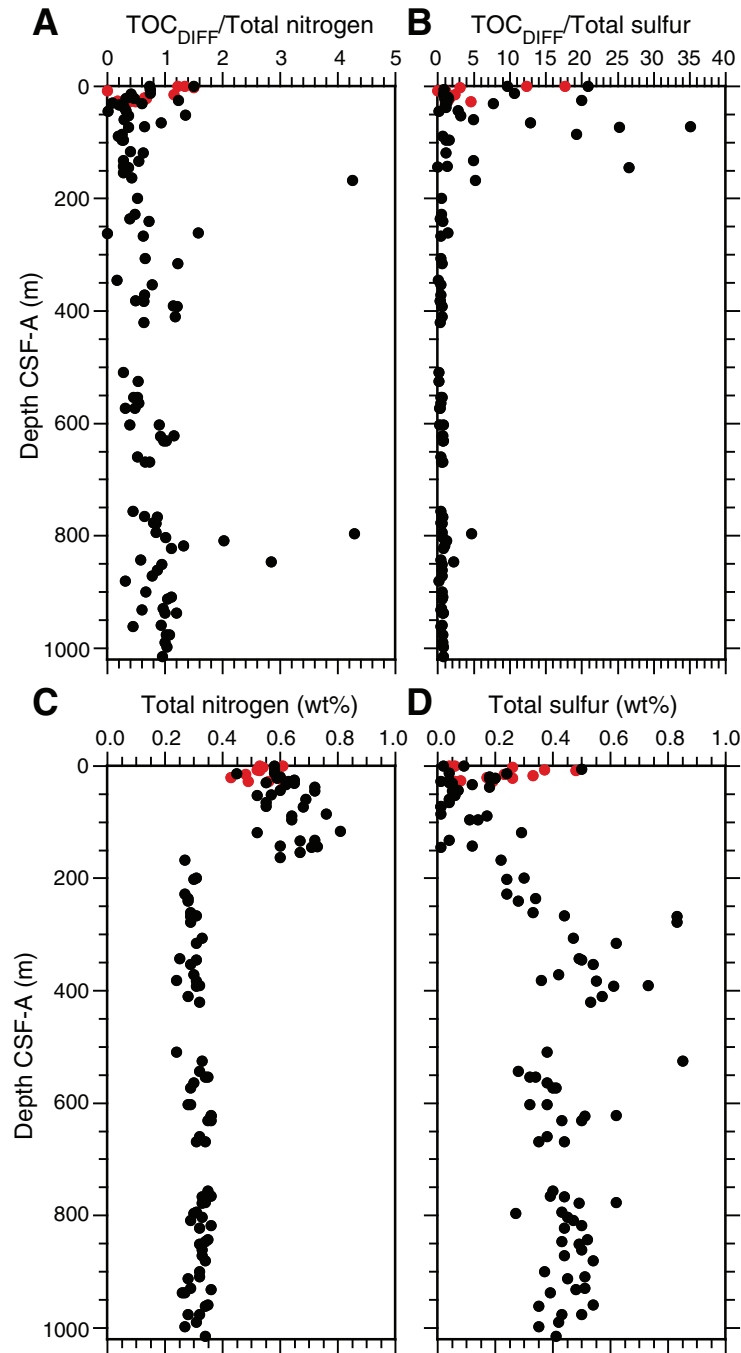
Figure F50. Plots of source rock analyzer data vs. depth, Holes U1351A (red) and U1351B (black). Sed = sediment. **A.** Volatile hydrocarbons (S_1). **B.** Pyrolyzable kerogen (S_2). **C.** Oxidized kerogen (S_3) at <390°C. **D.** Pyrolysis carbon (PC).
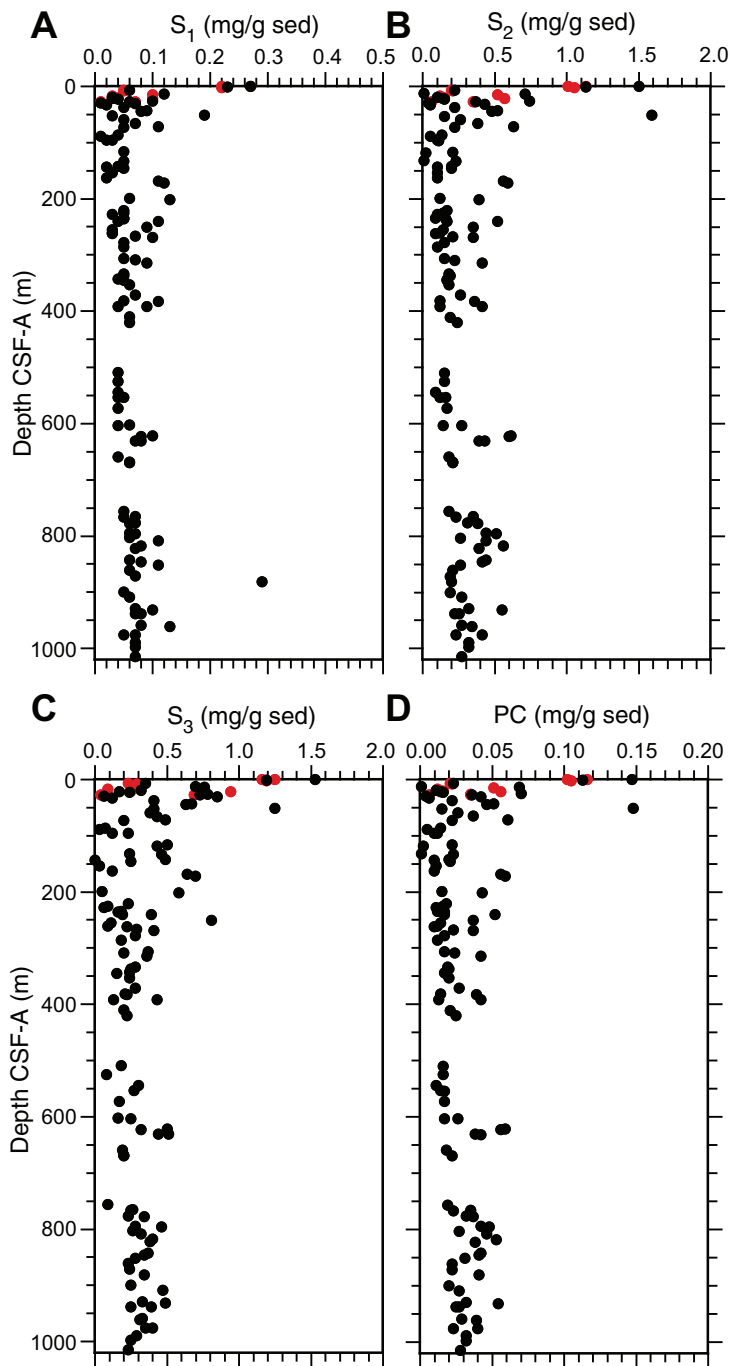
Figure F51. Plots of source rock analyzer (SRA) parameters vs. depth, Holes U1351A (red) and U1351B (black).
A. Hydrogen index. **B.** Oxygen index. **C.** Pyrolysis temperature of maximum hydrocarbon yield from S_2 (T_{max}).
D. Production index. HC = hydrocarbons, TOC = total organic carbon from SRA.
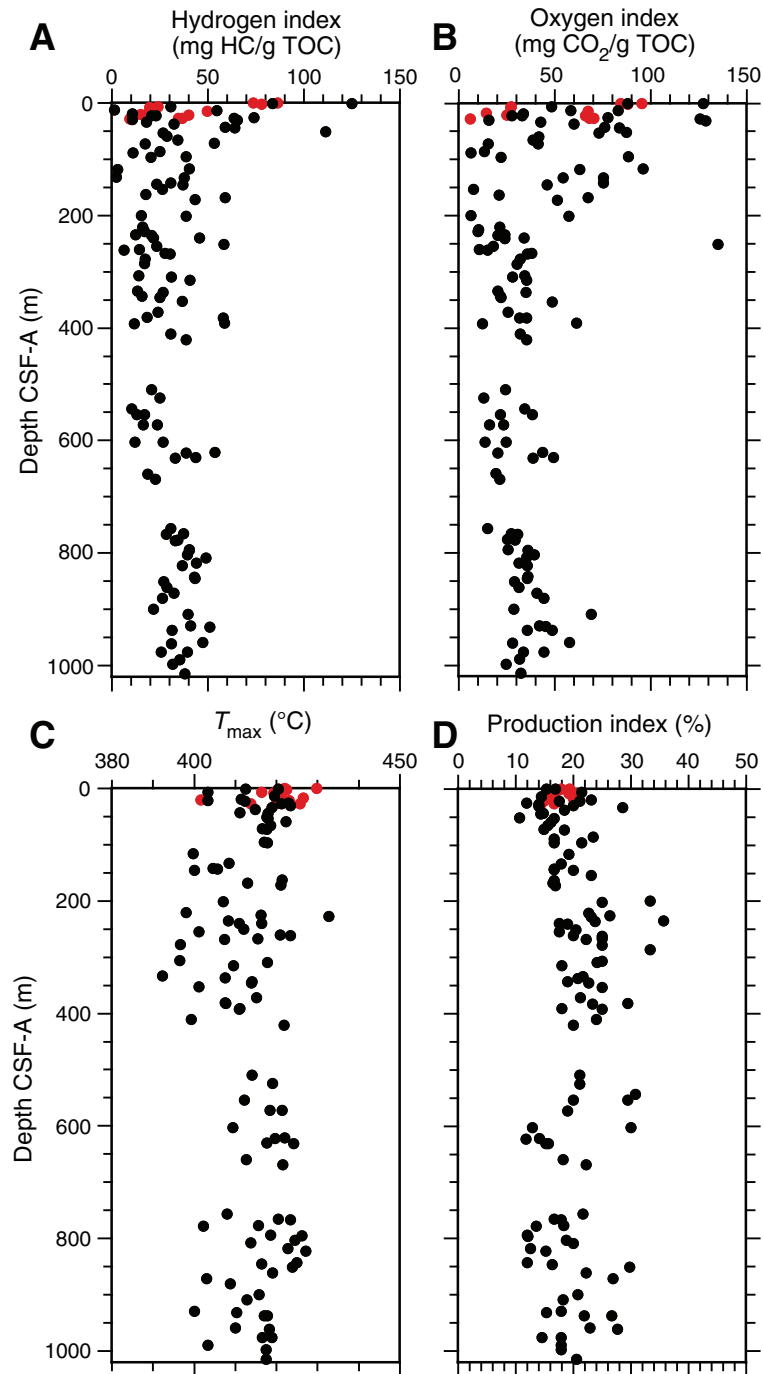
Figure F52. Modified and enlarged van Krevelen diagram based on a cross-plot of hydrogen index vs. oxygen index, showing trend lines for kerogen Types III and IV, Holes U1351A (red) and U1351B (black). Trend lines are not shown for kerogen Types I and II. TOC = total organic carbon from SRA.
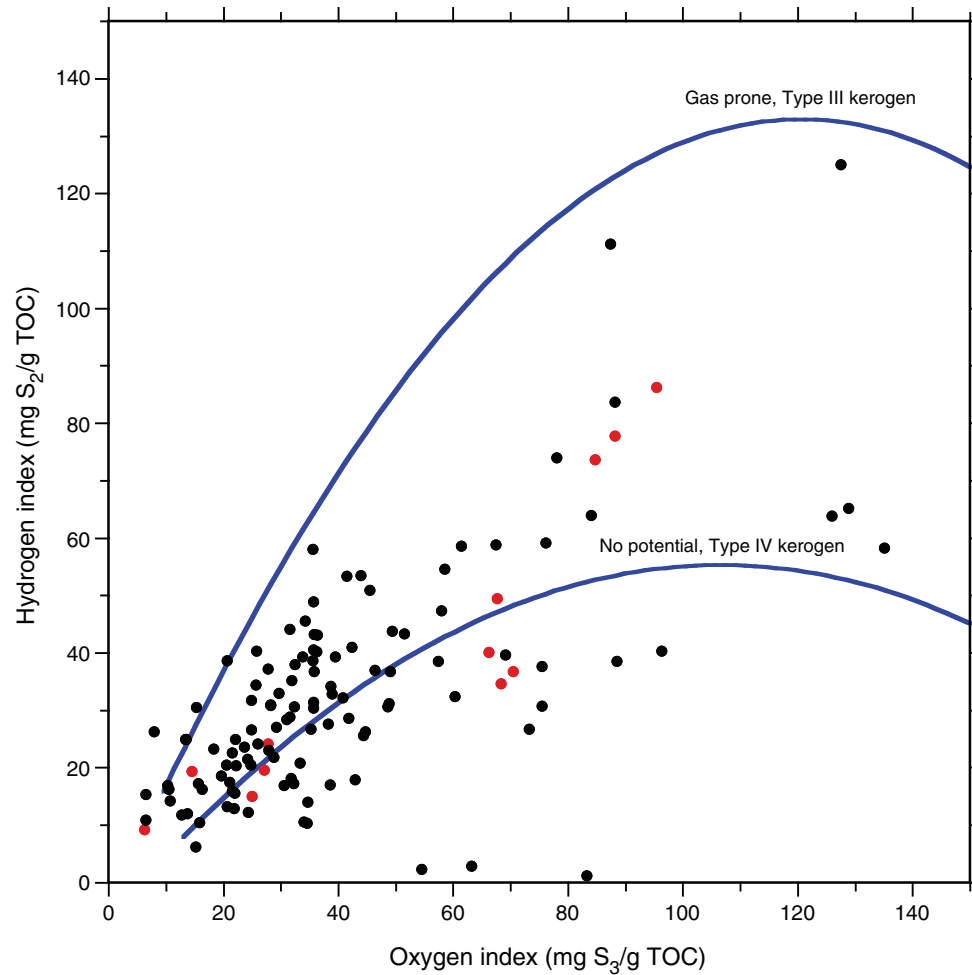
Figure F53. Cross-plot of total carbon measured using two approaches: (1) direct measurement with the CHNS elemental analyzer and (2) the sum of inorganic carbon measured by the coulometer (IC_{COUL}) and total organic carbon measured by the source rock analyzer (TOC_{SRA}). Black line = 1:1 line, dashed red line = correlation line for all data.
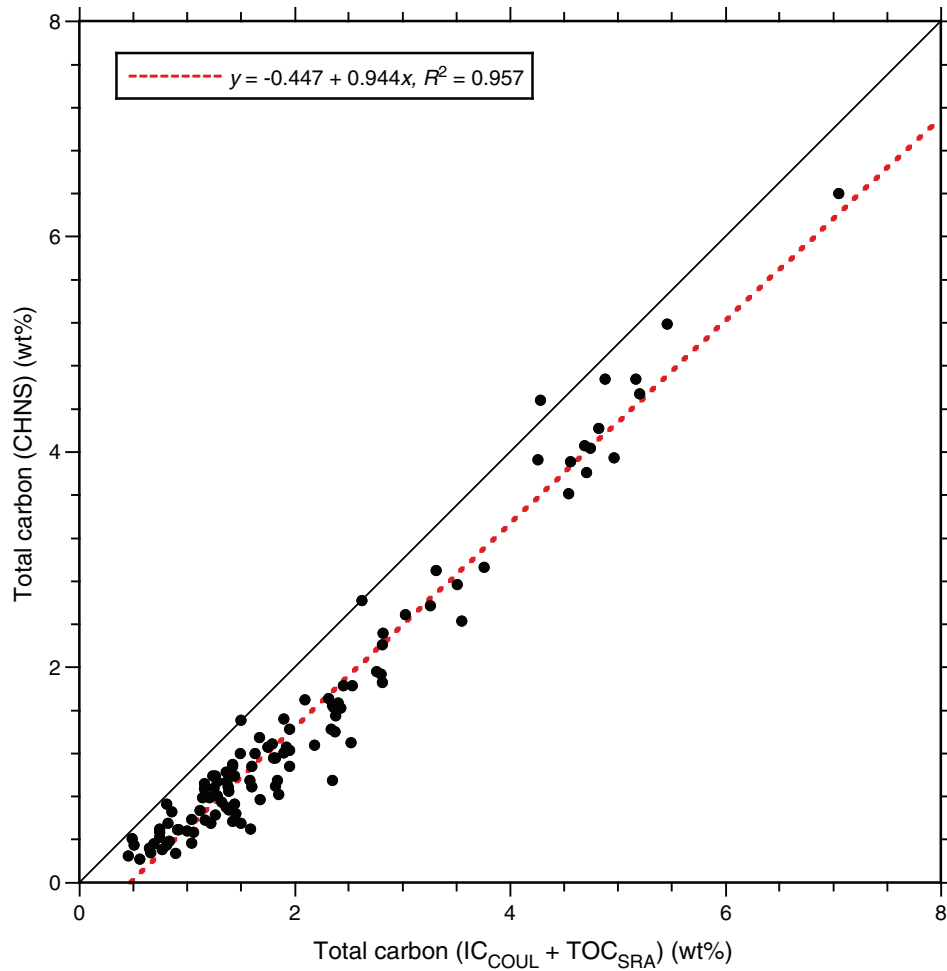
Figure F54. Cross-plot of total carbonate content vs. total organic carbon from the source rock analyzer (TOC$_{SRA}$), Holes U1351A (red) and U1351B (black).
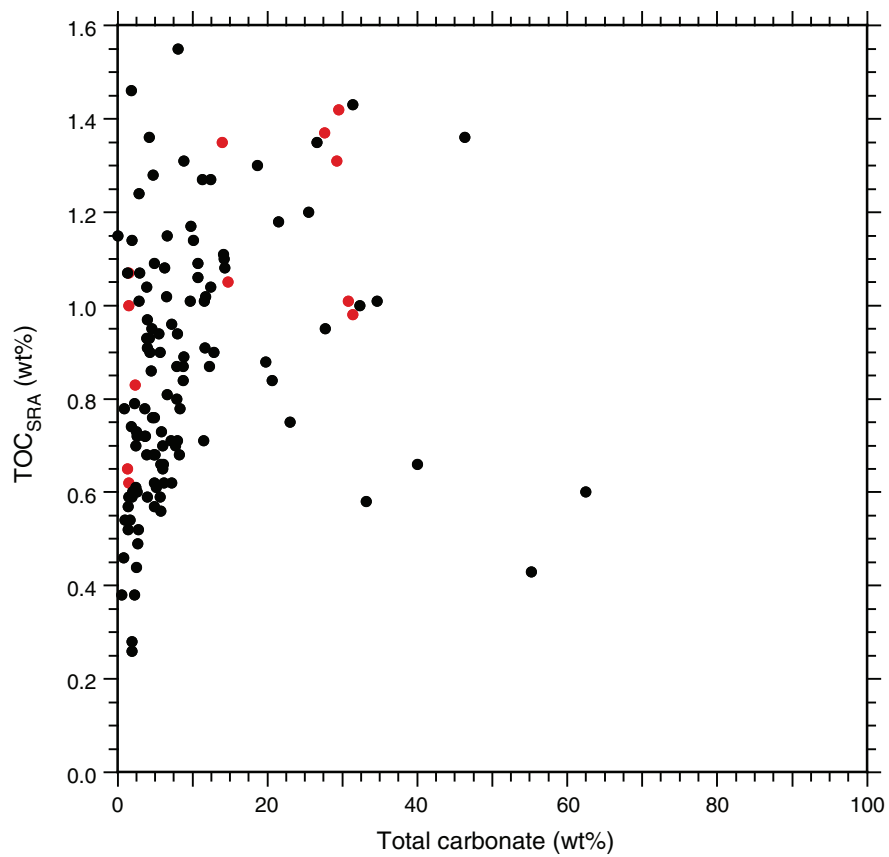
Figure F55. Plots of ionic constituents of interstitial water vs. depth, Holes U1351A (red) and U1351B (black). **A, C.** Chloride. **B, D.** Salinity. Bottom panels show total depth; top panels show uppermost 100 m. SW = IAPSO seawater values.
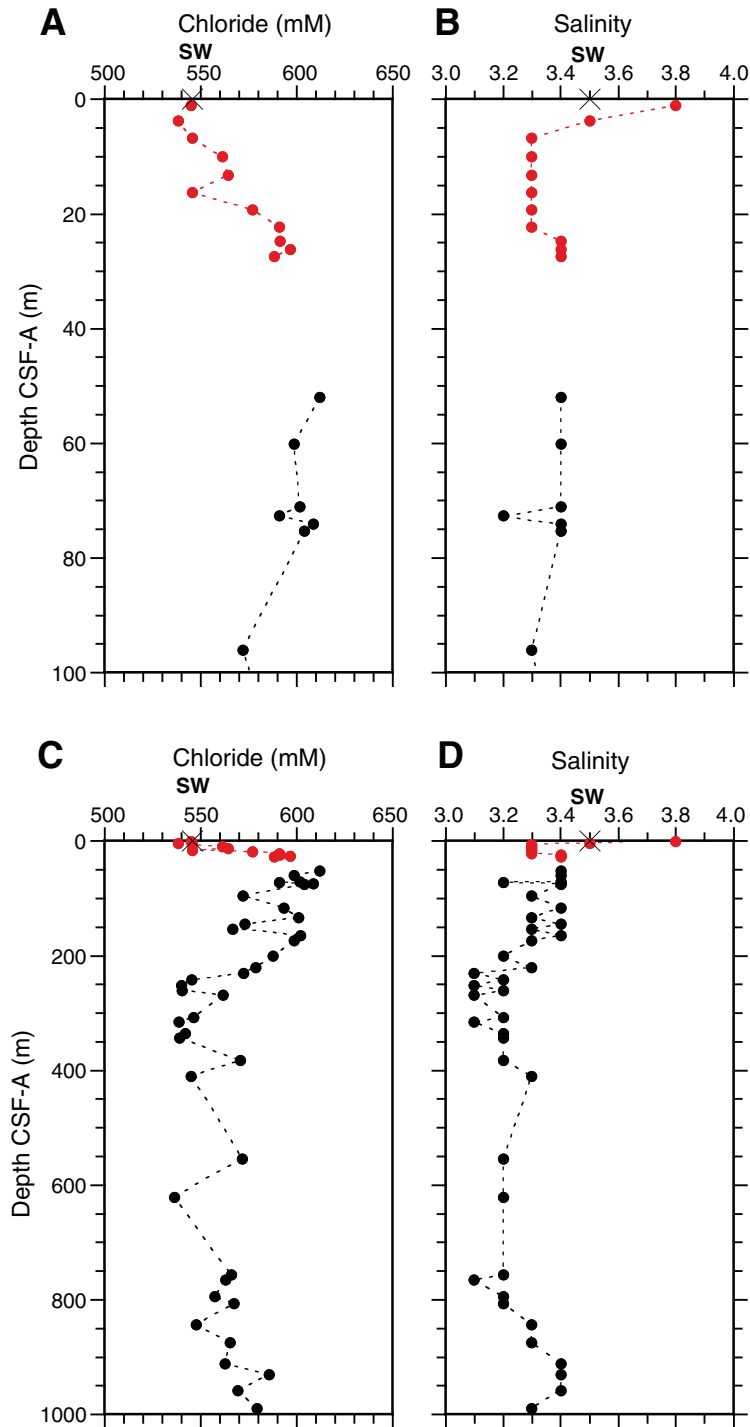
Figure F56. Plots of ionic constituents of interstitial water vs. depth, Holes U1351A (red) and U1351B (black). **A.** Strontium. **B.** Strontium/calcium ratio. **C.** pH. **D.** Calcium. **E.** Magnesium. **F.** Magnesium/calcium ratio. SW = IAPSO seawater values.
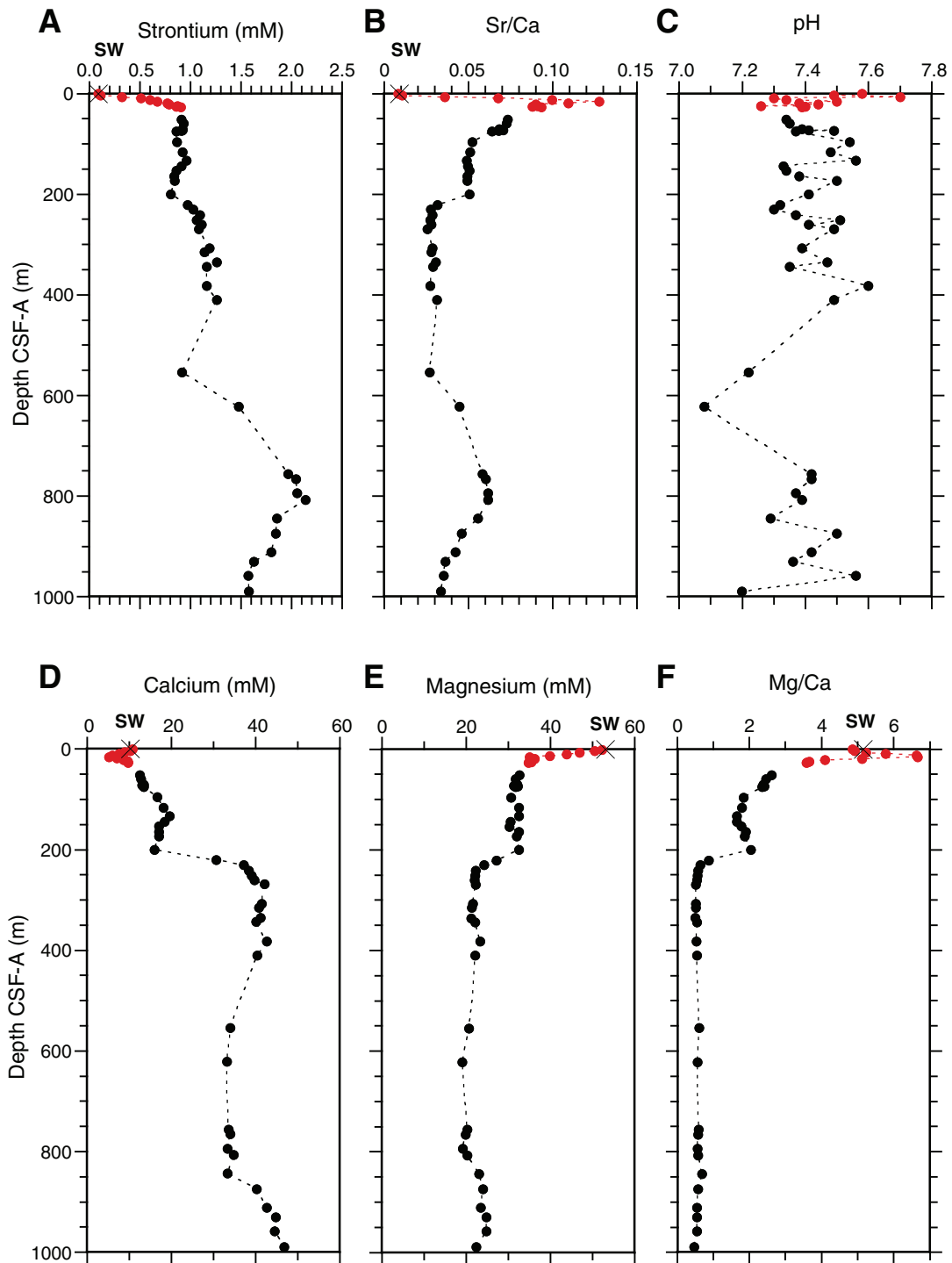
Figure F57. Plots of ionic constituents of interstitial water vs. depth, Holes U1351A (red) and U1351B (black). **A, C.** Alkalinity. **B, D.** Sulfate. Bottom panels show total depth; top panels show uppermost 100 m. SW = IAPSO seawater values.
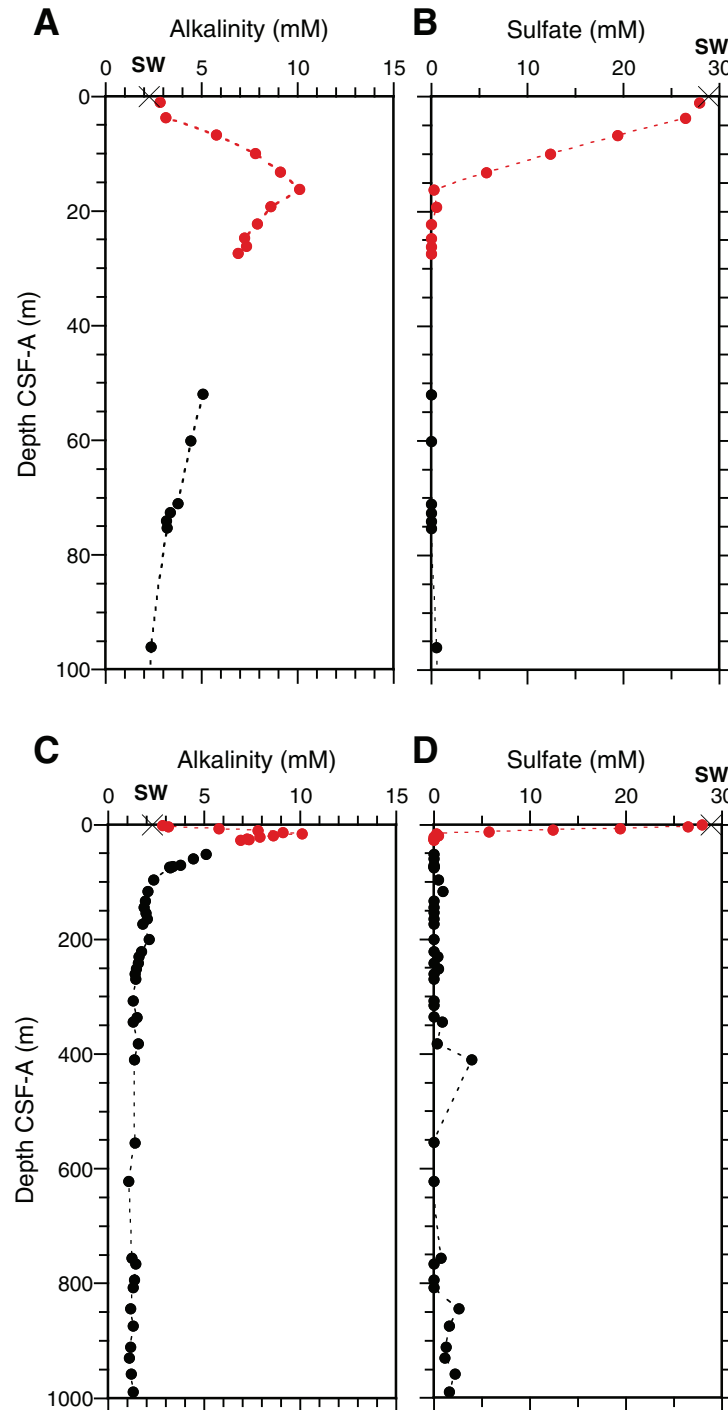
Figure F58. Plots of ionic constituents of interstitial water vs. depth, Holes U1351A (red) and U1351B (black). **A.** Phosphate. **B.** Dissolved silica. **C.** Ammonium. **D.** Silicon from inductively coupled plasma spectroscopy (ICP). SW = IAPSO seawater values.
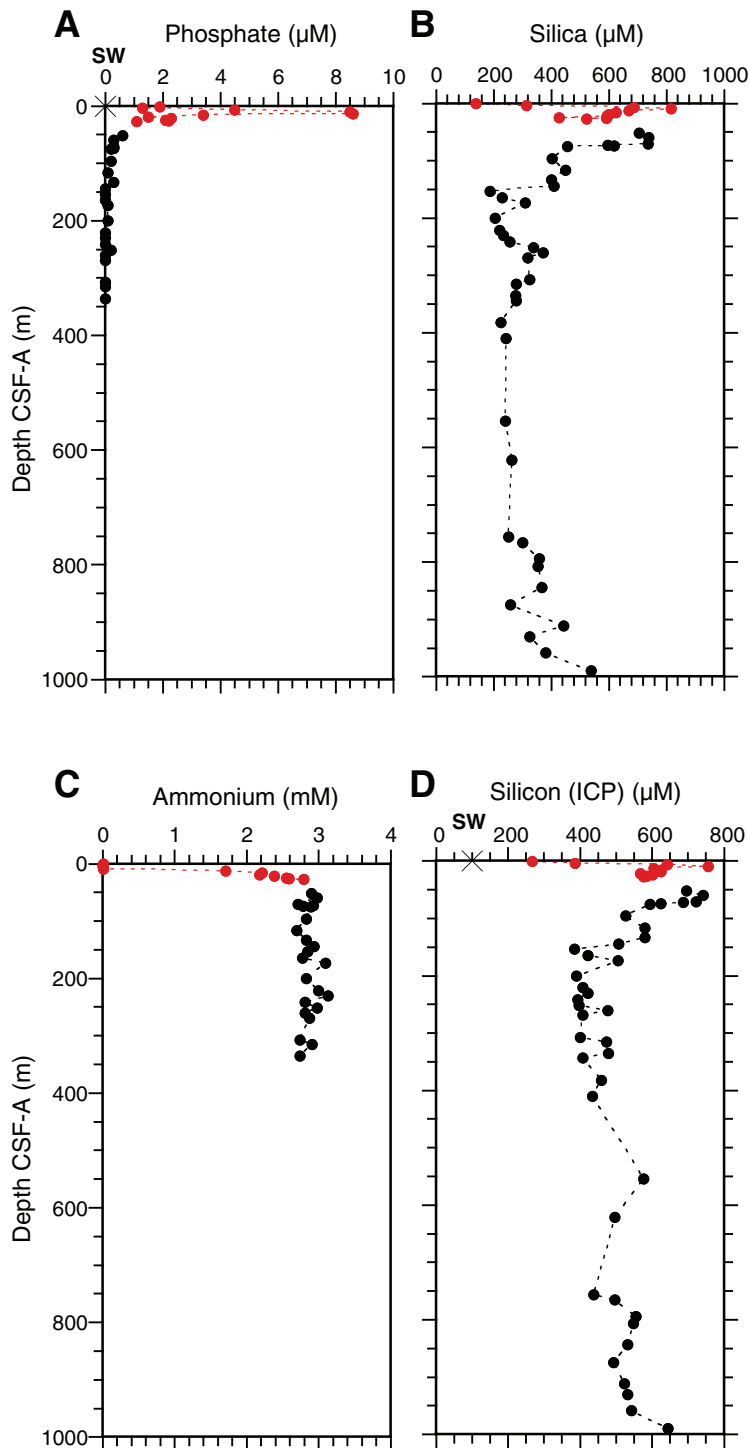
Figure F59. Plots of ionic constituents of interstitial water vs. depth, Holes U1351A (red) and U1351B (black). **A.** Lithium. **B.** Sodium. **C.** Potassium. **D.** Barium. **E.** Boron. SW = IAPSO seawater values.
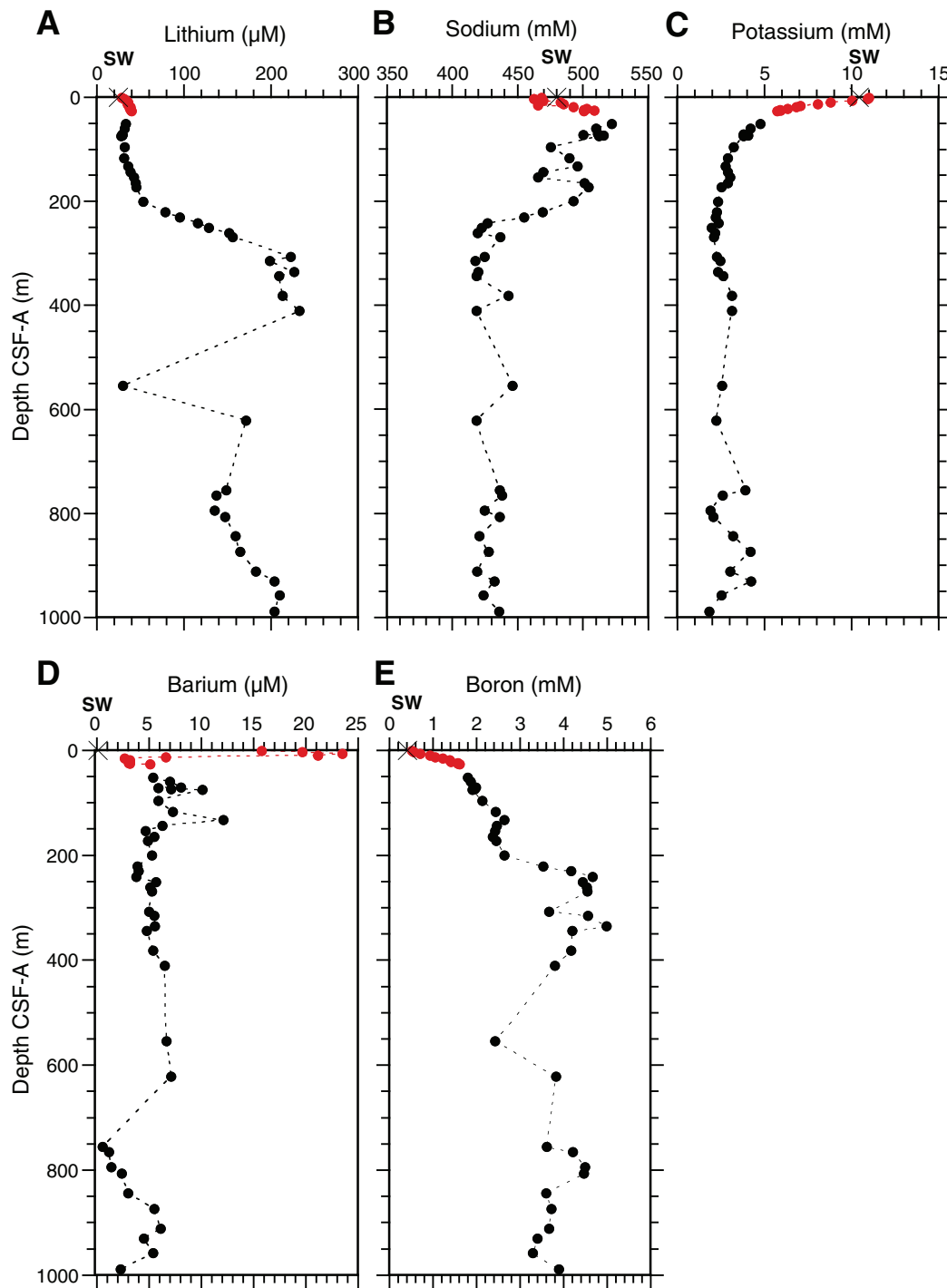
Figure F60. Uppermost 100 m depth profiles for Holes U1351A (open symbols) and U1351B (solid symbols). Blue shading = sulfate–methane transition zone. **A.** Methane, alkalinity, sulfate, calcium, and magnesium. **B.** Phosphate. **C.** Dissolved silica. **D.** Barium.
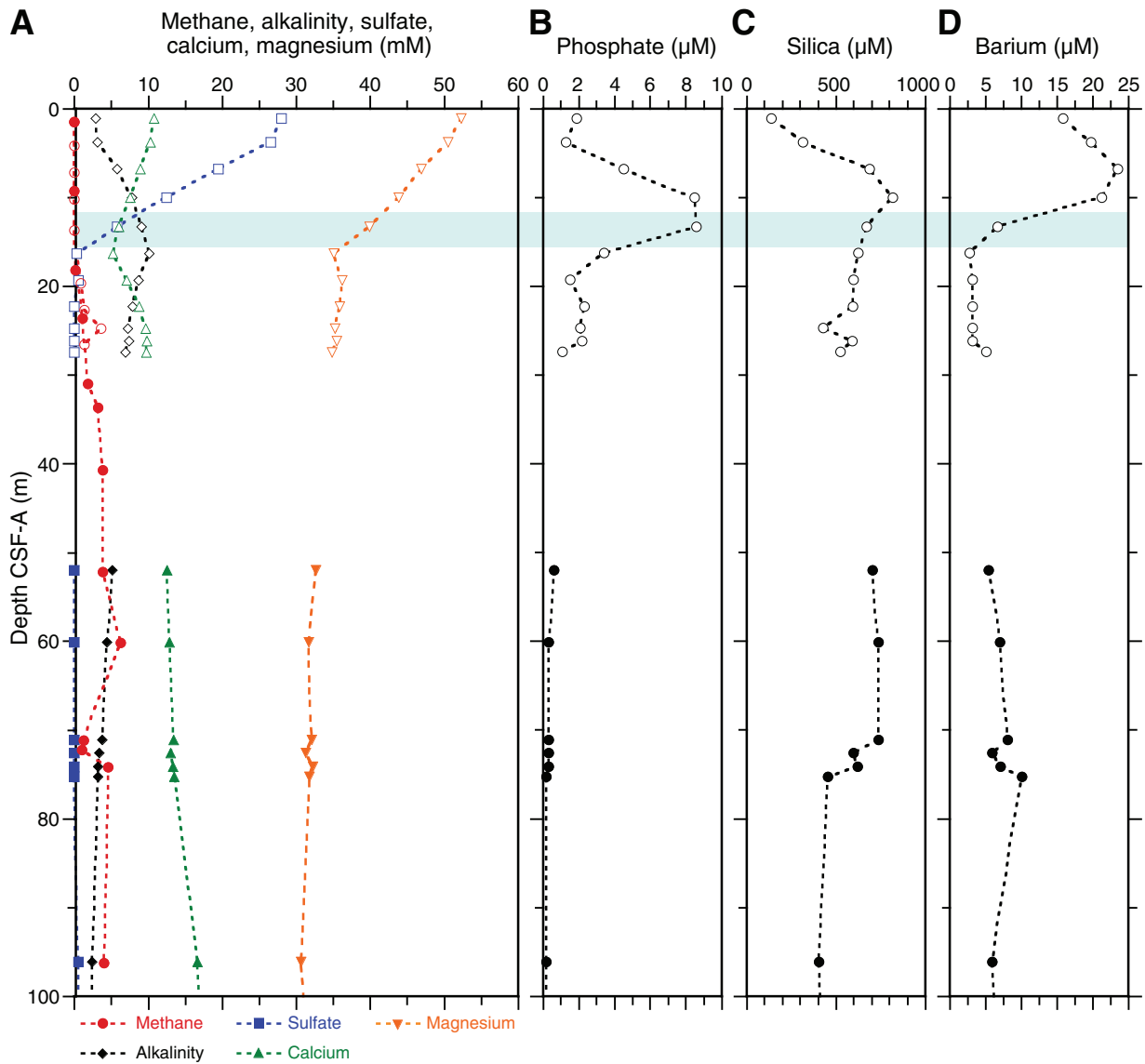
Figure F61. Uppermost 300 m depth profiles for Holes U1351A (open symbols) and U1351B (solid symbols). **A.** Potassium, calcium, magnesium, and sodium. **B.** Lithium. **C.** Strontium. **D.** Boron. Blue shading = zone of diagenetic changes.
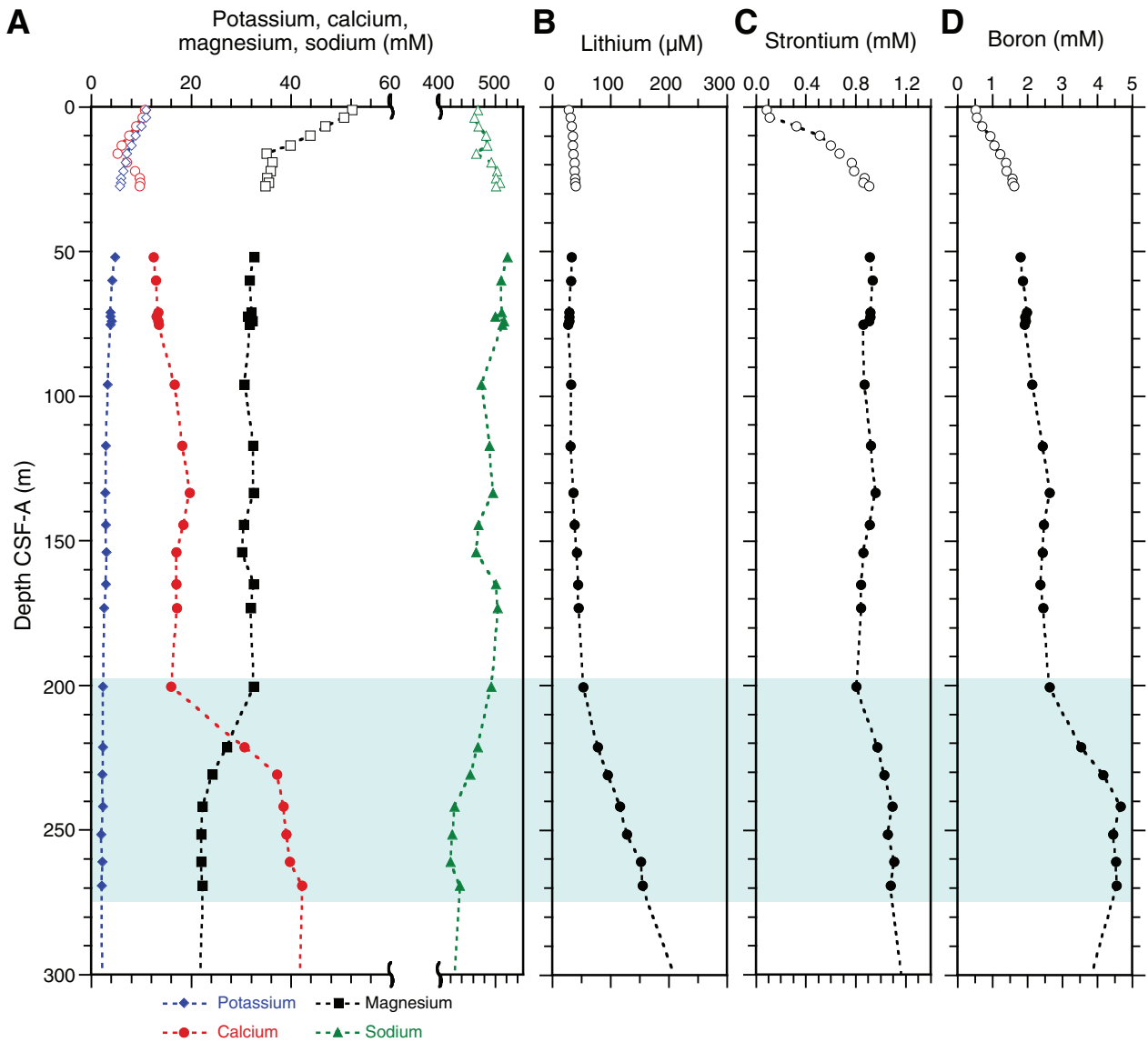
Figure F62. Plots of variation in total prokaryotic cells counted by SYBR Green staining vs. depth, Site U1351. **A.** Total cells/cm^3 on a linear scale. **B.** Total cells/cm^3 on a logarithmic scale (blue circles and line) and total prokaryotic cell range distribution for previously examined sites (red dashed lines; from Parkes et al., 2000).
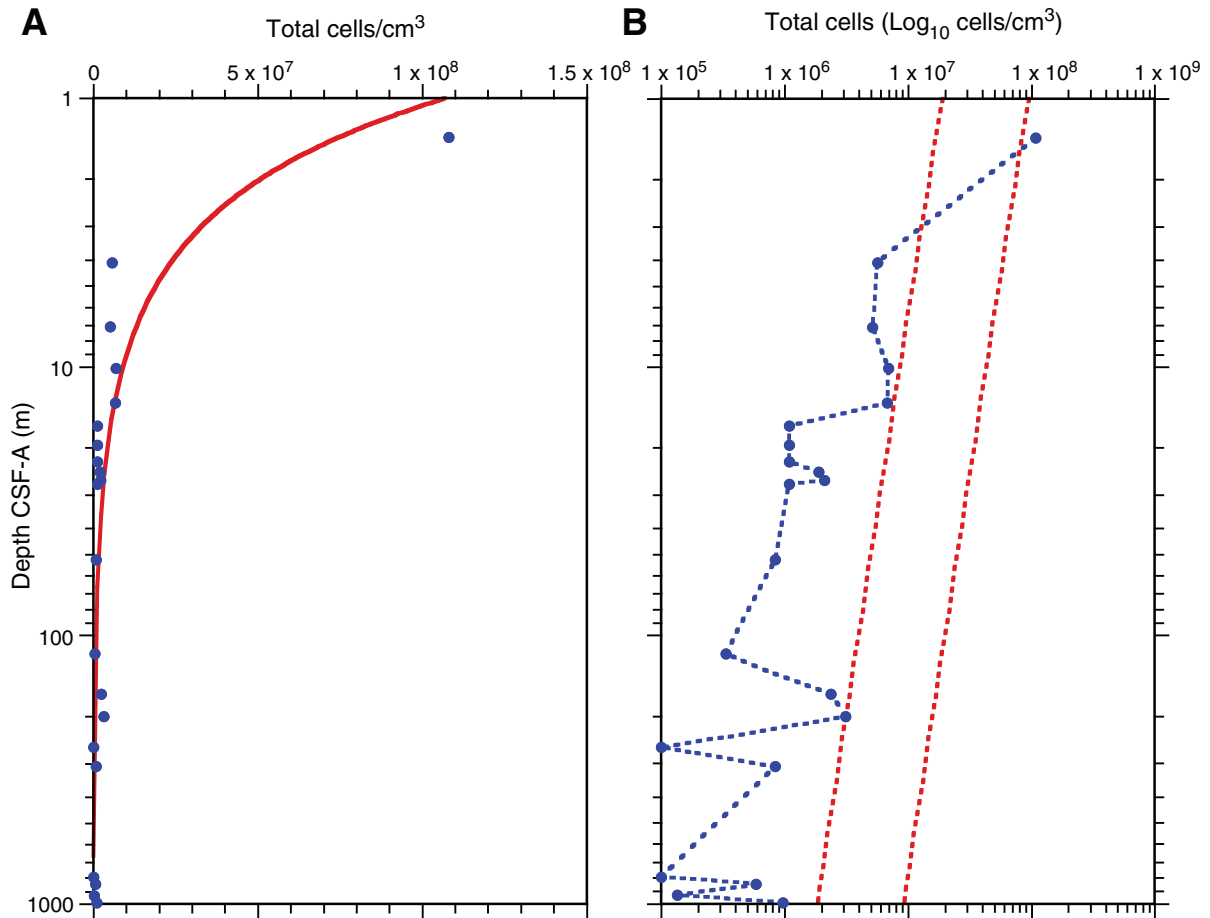
Figure F63. A. Temperature data for Site U1351. An exponential decrease in temperature is expected for the time interval shown and used to estimate ambient temperature. This decrease is only evident for measurements in Core 317-U1351A-4H. Temperature fluctuations in subsequent cores render these data unreliable. However, data from the time interval t_i to t_f (triangles and squares, respectively) were used. See Table **T23** for these values. **B.** Resulting geothermal gradient (14.1°C/km). Solid circle = only reliable temperature measurement.
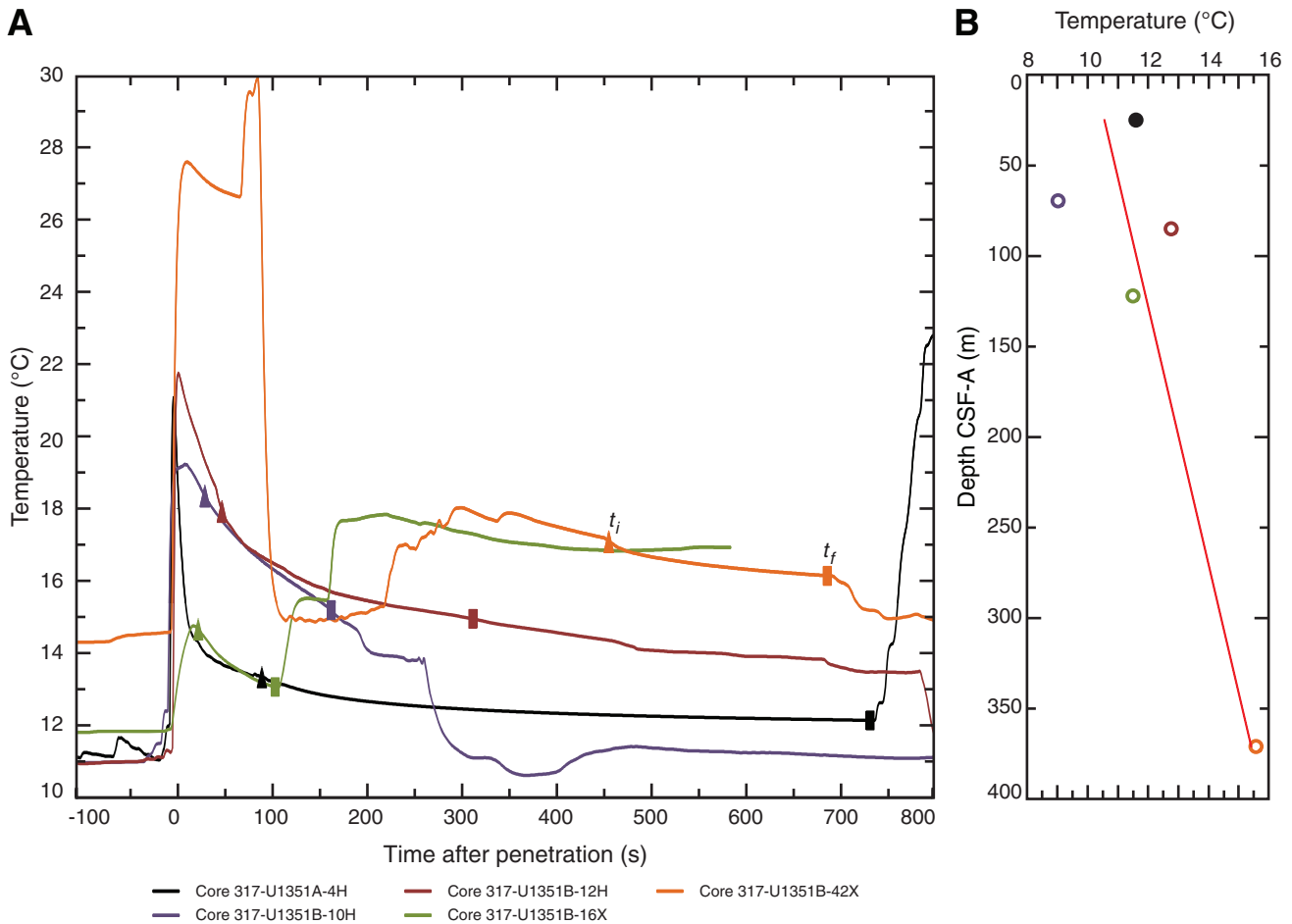
Figure F64. Thermal conductivity for Site U1351 vs. (**A**) depth, (**B**) porosity, and (**C**) bulk density. Thermal conductivity measurements from Holes U1351A and U1351B were used to determine relationship between thermal conductivity and depth. A linear fit represents increasing thermal conductivity with depth despite variability in the topmost portion. Thermal conductivity exhibits a negative relationship with porosity and a positive relationship with bulk density. However, variation with lithology was not detected.
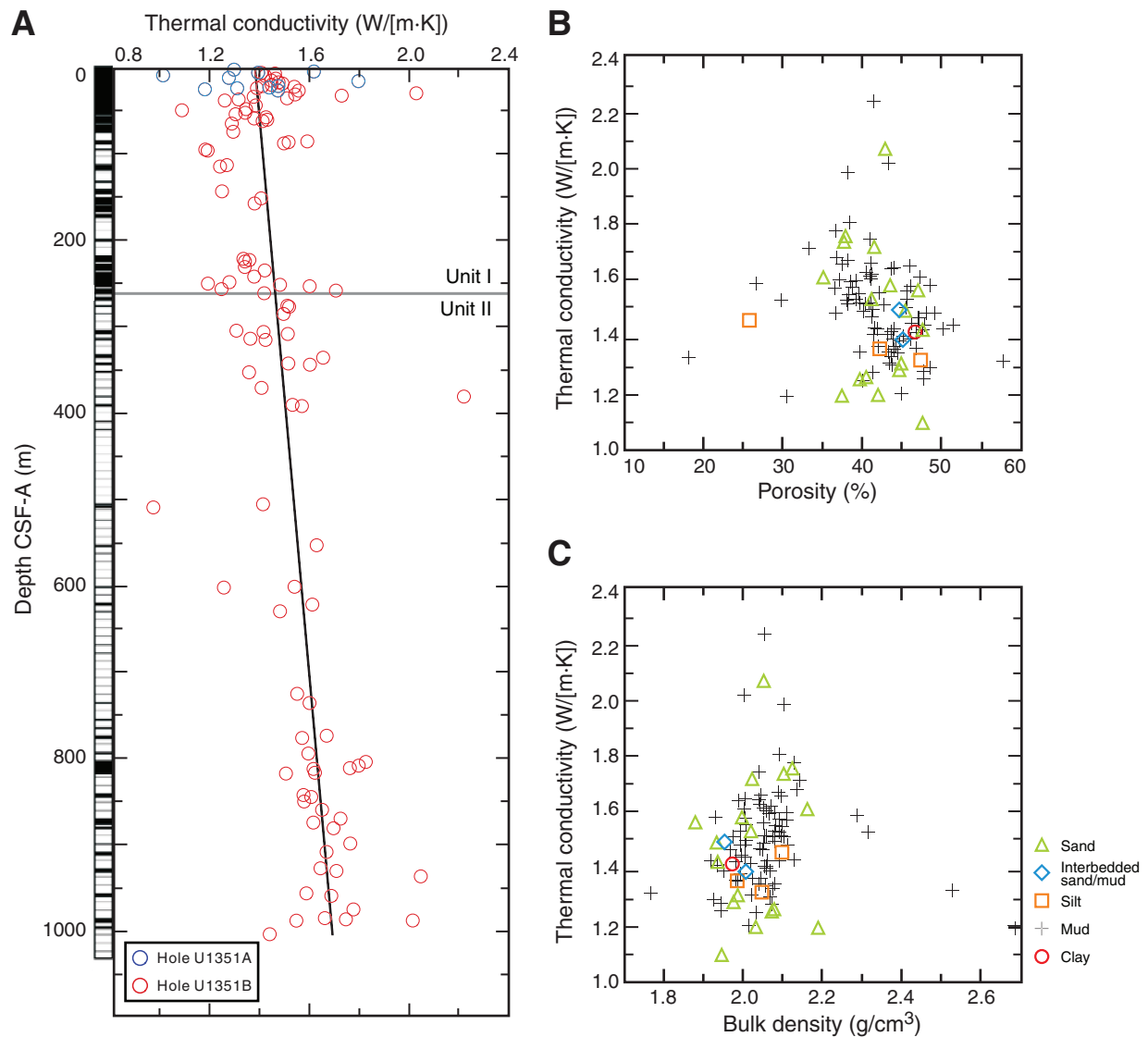
Figure F65. Bullard plot for Site U1351. Thermal resistance is derived from the linearly increasing trend of thermal conductivity with depth. Estimated heat flow is 20.1 mW/m². Solid circle = only reliable data point.
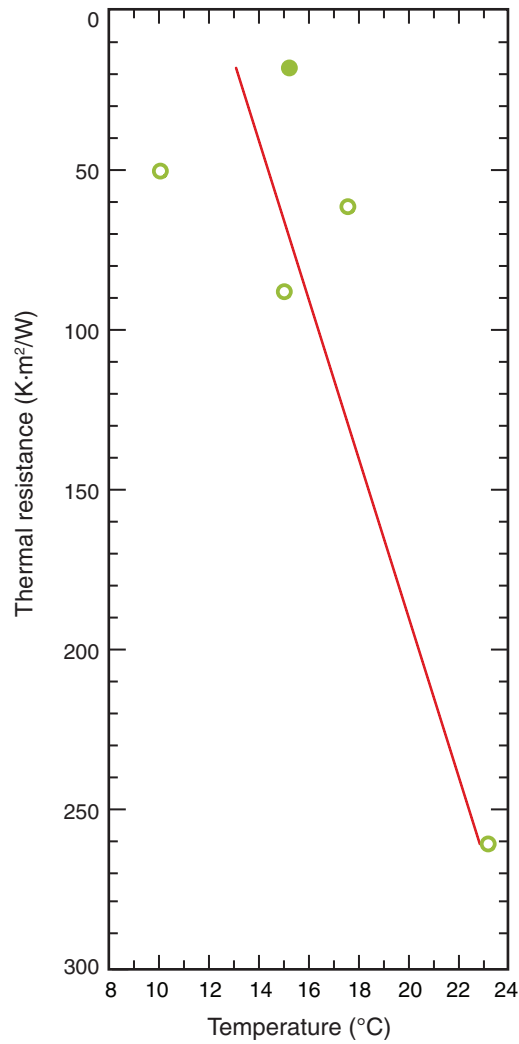
Figure F66. Summary of logs recorded by the triple combination tool string in Hole U1351B and comparison to physical property data measured on recovered cores. HLDS = Hostile Environment Litho-Density Sonde, NGR = natural gamma radiation core measurements, MAD = moisture and density core data, GRA = gamma ray attenuation bulk density core measurements, IDPH = phasor deep induction log, IMPH = phasor medium induction log.
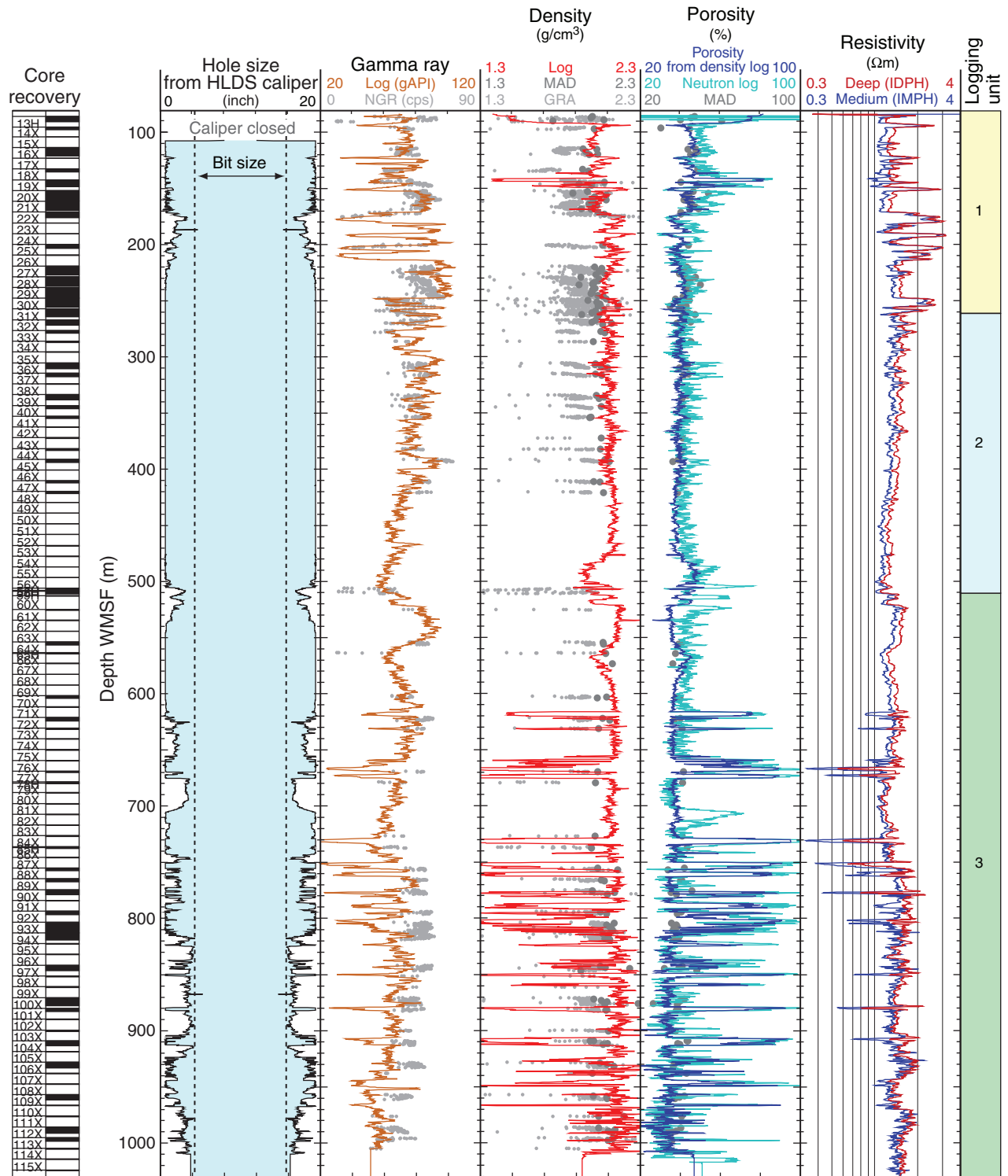
Figure F67. Summary of logs recorded by the Formation MicroScanner (FMS)-sonic tool string in Hole U1351B. Hole size was calculated by the two orthogonal calipers of the FMS (C1 and C2). In the gamma ray track, gamma ray recorded in Pass 2 with the FMS-sonic tool string is compared to gamma recorded with the triple combination (TC) tool string in the same hole. Sonic waveform (WF) amplitude is shown as an indicator of the quality of the data. High waveform coherence, shown in red in the two velocity tracks, is a measure of the reliability of the slowness/time coherence algorithm used to derive compressional (V_P) and shear (V_S) velocities from the monopole and lower dipole sonic waveforms, respectively.
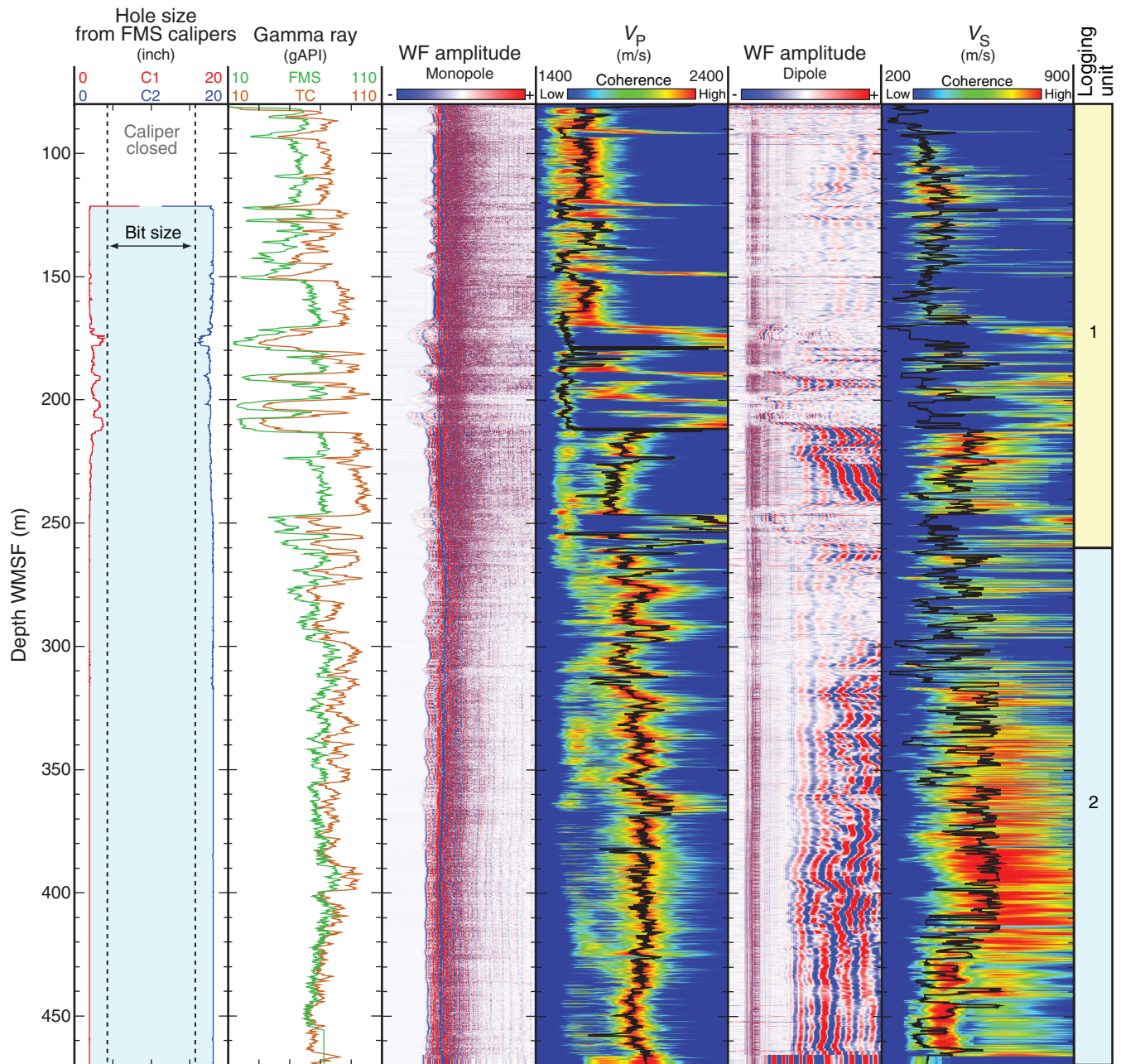
Figure F68. Comparison of gamma ray logs recorded through the drill pipe in Holes U1351B and U1351C and gamma ray track data from Hole U1351B cores. NGR = natural gamma radiation track measurements. Sand layers described in cores (red arrows) correspond to low peaks in gamma ray logs, indicating a gamma ray response to lithology despite signal attenuation by the drill pipe. Additional sand layers may be present (red arrows with question mark) in the uppermost 84 m, even where not recovered by coring.
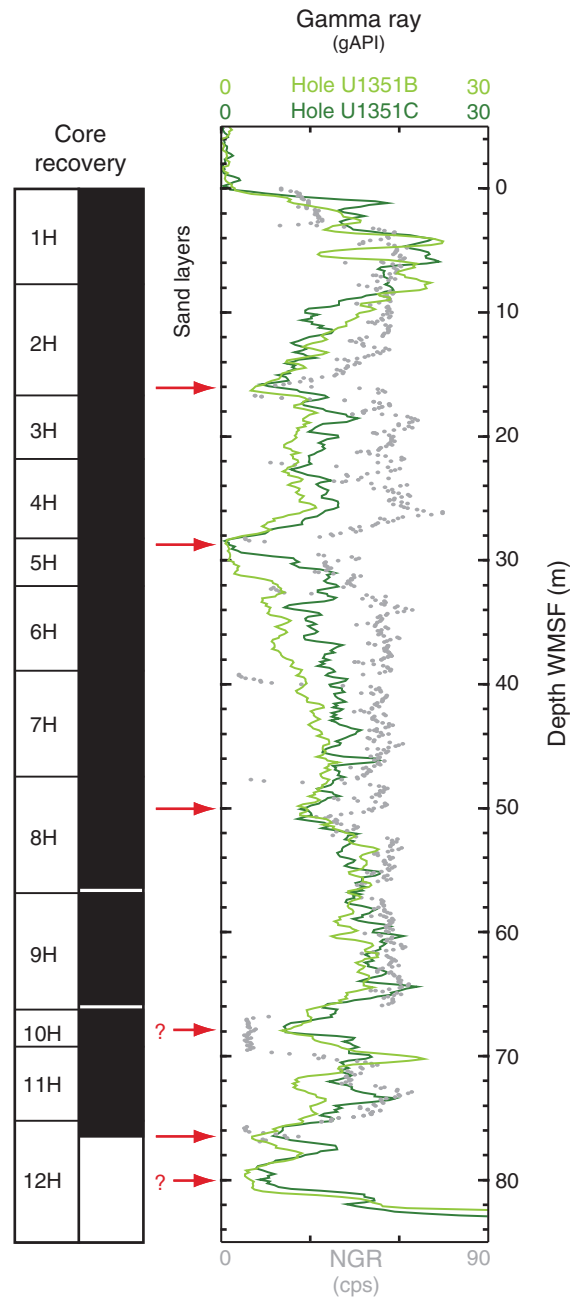
Figure F69. FMS images and associated core photographs that are representative of some lithologies in Hole U1351B. **A.** Fine sand layers not re-covered during coring. **B.** Authigenic carbonates (Section 317-U1351B-27X-4). **C.** Shell-rich layers (Section 317-U1351B-28X-2). The sand layers, carbonates, and shelly layers generated higher resistivity, apparent as brighter colors in the FMS images. See **"Downhole logging"** for details.
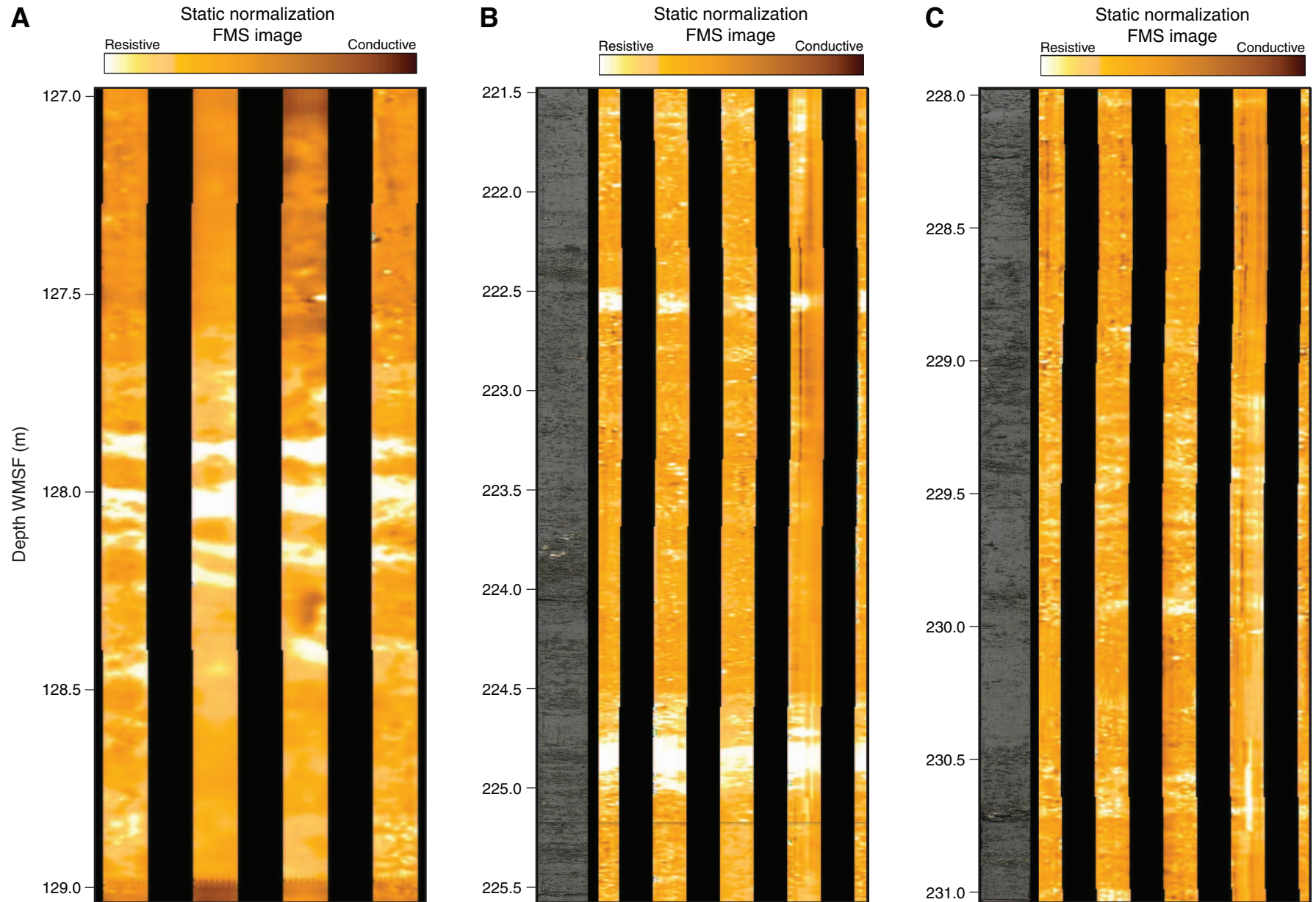
Table T1. Coring summary, Site U1351. (**See table notes.**) (**Continued on next two pages.**)

Hole U1351A
Latitude: 44°53.0307′S
Longitude: 171°50.4037′E
Time on hole (d): 0.58 (18 Nov, 0931 h–2330 h)
Seafloor (drill pipe measurement from rig floor, m DRF): 133.3 (APC mudline)
Distance between rig floor and sea level (m): 11.0
Water depth (drill pipe measurement from sea level, m): 122.3
Total depth (drill pipe measurement from rig floor, m DRF): 161.3
Total penetration (m DSF): 28.0
Total length of cored section (m): 28.0
Total core recovered (m): 27.3
Core recovery (%): 98
Total number of cores: 6

Hole U1351B
Latitude: 44°53.0422′S
Longitude: 171°50.4065′E
Time on hole (d): 6.77 (18 Nov, 2330 h–25 Nov, 1800 h)
Seafloor (drill pipe measurement from rig floor, m DRF): 132.7 (APC mudline)
Distance between rig floor and sea level (m): 11.0
Water depth (drill pipe measurement from sea level, m): 121.7
Total depth (drill pipe measurement from rig floor, m DRF): 1163.3
Total penetration (m DSF): 1030.6
Total length of cored section (m): 1030.6
Total core recovered (m): 304.5
Core recovery (%): 30
Total number of cores: 116

Hole U1351C
Latitude: 44°53.0572′S
Longitude: 171°50.4057′E
Time on hole (d): 4.33 (25 Nov, 1800 h–30 Nov, 0200 h)
Seafloor (drill pipe measurement from rig floor, m DRF): 132.7 (by proxy, Hole U1351B)
Distance between rig floor and sea level (m): 11.0
Water depth (drill pipe measurement from sea level, m): 121.7
Total depth (drill pipe measurement from rig floor, m DRF): 1100.0
Total penetration (m DSF): 967.3
Total length of cored section (m): 0.00
Total core recovered (m): 0.0
Core recovery (%): 0.0
Total number of cores: 0

Core	Date (2009)	UTC (h)	Top of cored interval (m DSF)	Bottom of cored interval (m DSF)	Interval advanced (m)	Top of recovered core (m CSF-A)	Bottom of recovered core (m CSF-A)	Length of core recovered (m)	Recovery (%)
317-U1351A-									
1H	18 Nov	0435	0.0	2.7	2.7	0.0	2.61	2.61	97
2H	18 Nov	0530	2.7	12.2	9.5	2.7	11.49	8.79	93
3H	18 Nov	0630	12.2	18.2	6.0	12.2	18.20	6.00	100
4H	18 Nov	0740	18.2	25.1	6.9	18.2	25.13	6.93	100
5H	18 Nov	0845	25.1	27.5	2.4	25.1	27.55	2.45	102
6H	18 Nov	0950	27.5	28.0	0.5	27.5	28.05	0.55	110
			Advanced total:		28.0			27.33	98
			Total interval cored:		28.0				
317-U1351B-									
1H	18 Nov	0200	0.0	7.8	7.8	0.0	7.76	7.76	99
2H	18 Nov	0310	7.8	16.7	8.9	7.8	16.78	8.98	101
3H	18 Nov	0420	16.7	22.1	5.4	16.7	22.16	5.46	101
4H	18 Nov	0535	22.1	28.2	6.1	22.1	28.22	6.12	100
5H	18 Nov	0645	28.2	32.2	4.0	28.2	32.39	4.19	105
6H	18 Nov	0810	32.2	39.2	7.0	32.2	39.32	7.12	102
7H	18 Nov	1420	39.2	47.7	8.5	39.2	47.88	8.68	102
8H	18 Nov	1530	47.7	57.2	9.5	47.7	56.51	8.81	93
9H	18 Nov	1615	57.2	66.7	9.5	57.2	65.96	8.76	92
10H	18 Nov	1715	66.7	69.7	3.0	66.7	69.88	3.18	106
11H	18 Nov	1855	69.7	75.7	6.0	69.7	75.62	5.92	99
12H	18 Nov	2020	75.7	85.2	9.5	75.7	76.97	1.27	13
13H	18 Nov	2135	85.2	94.7	9.5	85.2	90.07	4.87	51
14X	19 Nov	0130	94.7	103.3	8.6	94.7	97.16	2.46	29
15X	19 Nov	0210	103.3	112.9	9.6	103.3	103.47	0.17	2
16X	19 Nov	0255	112.9	122.4	9.5	112.9	120.29	7.39	78

Table T1 (continued). ()

Core	Date (2009)	UTC (h)	Top of cored interval (m DSF)	Bottom of cored interval (m DSF)	Interval advanced (m)	Top of recovered core (m CSF-A)	Bottom of recovered core (m CSF-A)	Length of core recovered (m)	Recovery (%)
17X	19 Nov	0505	122.4	132.0	9.6	122.4	122.4	0.00	0
18X	19 Nov	0550	132.0	141.6	9.6	132.0	134.53	2.53	26
19X	19 Nov	0640	141.6	151.2	9.6	141.6	147.6	6.00	62
20X	19 Nov	0740	151.2	160.8	9.6	151.2	160.21	9.01	94
21X	19 Nov	0830	160.8	170.4	9.6	160.8	168.53	7.73	81
22X	19 Nov	0910	170.4	180.0	9.6	170.4	175.32	4.92	51
23X	19 Nov	1030	180.0	189.6	9.6	180.0	180.17	0.17	2
24X	19 Nov	1115	189.6	199.2	9.6	189.6	189.79	0.19	2
25X	19 Nov	1200	199.2	208.8	9.6	199.2	202.64	3.44	36
26X	19 Nov	1240	208.8	218.4	9.6	208.8	209.01	0.21	2
27X	19 Nov	1320	218.4	228.0	9.6	218.4	226.32	7.92	82
28X	19 Nov	1415	228.0	237.5	9.5	228.0	236.22	8.22	87
29X	19 Nov	1500	237.5	247.1	9.6	237.5	247.40	9.90	103
30X	19 Nov	1540	247.1	256.7	9.6	247.1	255.11	8.01	83
31X	19 Nov	1630	256.7	266.3	9.6	256.7	263.66	6.96	72
32X	19 Nov	1700	266.3	275.9	9.6	266.3	271.02	4.72	49
33X	19 Nov	1750	275.9	285.5	9.6	275.9	278.39	2.49	26
34X	19 Nov	1835	285.5	295.1	9.6	285.5	286.43	0.93	10
35X	19 Nov	1920	295.1	304.7	9.6	295.1	295.36	0.26	3
36X	19 Nov	2010	304.7	313.9	9.2	304.7	309.79	5.09	55
37X	19 Nov	2050	313.9	323.5	9.6	313.9	317.09	3.19	33
38X	19 Nov	2140	323.5	333.1	9.6	323.5	323.74	0.24	2
39X	19 Nov	2220	333.1	342.7	9.6	333.1	337.49	4.39	46
40X	19 Nov	2320	342.7	352.3	9.6	342.7	345.72	3.02	31
41X	19 Nov	2355	352.3	361.9	9.6	352.3	354.25	1.95	20
42X	20 Nov	0045	361.9	371.5	9.6	361.9	362.20	0.30	3
43X	20 Nov	0245	371.5	381.1	9.6	371.5	372.18	0.68	7
44X	20 Nov	0355	381.1	390.7	9.6	381.1	382.62	1.52	16
45X	20 Nov	0525	390.7	400.2	9.5	390.7	393.39	2.69	28
46X	20 Nov	0630	400.2	409.8	9.6	400.2	400.25	0.05	1
47X	20 Nov	0715	409.8	419.4	9.6	409.8	411.77	1.97	21
48X	20 Nov	0755	419.4	429.0	9.6	419.4	421.04	1.64	17
49X	20 Nov	0830	429.0	438.6	9.6	429.0	429.17	0.17	2
50X	20 Nov	0935	438.6	448.2	9.6	438.6	438.60	0.00	0
51X	20 Nov	1010	448.2	457.8	9.6	448.2	448.20	0.00	0
52X	20 Nov	1045	457.8	467.4	9.6	457.8	457.80	0.00	0
53X	20 Nov	1140	467.4	477.0	9.6	467.4	467.84	0.44	5
54X	20 Nov	1245	477.0	486.5	9.5	477.0	477.29	0.29	3
55X	20 Nov	1345	486.5	496.1	9.6	486.5	486.51	0.01	0
56X	20 Nov	1435	496.1	505.4	9.3	496.1	496.10	0.00	0
57H	20 Nov	2020	505.4	507.4	2.0	505.4	507.67	2.27	114
58H	20 Nov	2110	507.4	508.4	1.0	507.4	507.40	0.00	0
59H	20 Nov	2200	508.4	512.4	4.0	508.4	510.59	2.19	55
60X	20 Nov	2350	512.4	524.5	12.1	512.4	512.81	0.41	3
61X	21 Nov	0150	524.5	534.1	9.6	524.5	525.34	0.84	9
62X	21 Nov	0245	534.1	543.8	9.7	534.1	534.33	0.23	2
63X	21 Nov	0400	543.8	553.4	9.6	543.8	543.97	0.17	2
64X	21 Nov	0520	553.4	563.0	9.6	553.4	556.32	2.92	30
65H	21 Nov	0550	563.0	563.8	0.8	563.0	563.85	0.85	106
66X	21 Nov	0650	563.8	572.6	8.8	563.8	564.12	0.32	4
67X	21 Nov	0740	572.6	582.3	9.7	572.6	572.95	0.35	4
68X	21 Nov	0845	582.3	591.9	9.6	582.3	582.30	0.00	0
69X	21 Nov	0940	591.9	601.5	9.6	591.9	591.93	0.03	0
70X	21 Nov	1145	601.5	611.1	9.6	601.5	603.54	2.04	21
71X	21 Nov	1235	611.1	620.6	9.5	611.1	611.74	0.64	7
72X	21 Nov	1335	620.6	630.2	9.6	620.6	623.97	3.37	35
73X	21 Nov	1430	630.2	639.8	9.6	630.2	631.46	1.26	13
74X	21 Nov	1520	639.8	649.4	9.6	639.8	640.17	0.37	4
75X	21 Nov	1610	649.4	659.0	9.6	649.4	649.84	0.44	5
76X	21 Nov	1740	659.0	668.6	9.6	659.0	659.63	0.63	7
77X	21 Nov	1840	668.6	678.2	9.6	668.6	669.77	1.17	12
78H	21 Nov	1905	678.2	679.2	1.0	678.2	679.04	0.84	84
79X	21 Nov	2000	679.2	687.8	8.6	679.2	679.51	0.31	4
80X	21 Nov	2050	687.8	697.4	9.6	687.8	688.11	0.31	3
81X	21 Nov	2130	697.4	707.0	9.6	697.4	697.72	0.32	3
82X	21 Nov	2240	707.0	716.5	9.5	707.0	707.35	0.35	4
83X	21 Nov	2345	716.5	726.1	9.6	716.5	716.99	0.49	5
84X	22 Nov	0045	726.1	735.7	9.6	726.1	726.76	0.66	7

Table T1 (continued).

Core	Date (2009)	UTC (h)	Top of cored interval (m DSF)	Bottom of cored interval (m DSF)	Interval advanced (m)	Top of recovered core (m CSF-A)	Bottom of recovered core (m CSF-A)	Length of core recovered (m)	Recovery (%)
85H	22 Nov	0125	735.7	736.7	1.0	735.7	736.46	0.76	76
86X	22 Nov	0345	736.7	745.3	8.6	736.7	737.64	0.94	11
87X	22 Nov	0445	745.3	754.9	9.6	745.3	745.63	0.33	3
88X	22 Nov	0600	754.9	764.5	9.6	754.9	757.38	2.48	26
89X	22 Nov	0735	764.5	774.1	9.6	764.5	766.99	2.49	26
90X	22 Nov	0855	774.1	783.7	9.6	774.1	778.57	4.47	47
91X	22 Nov	1105	783.7	793.3	9.6	783.7	784.09	0.39	4
92X	22 Nov	1205	793.3	803.0	9.7	793.3	796.38	3.08	32
93X	22 Nov	1300	803.0	812.6	9.6	803.0	812.94	9.94	104
94X	22 Nov	1355	812.6	822.3	9.7	812.6	819.17	6.57	68
95X	22 Nov	1455	822.3	831.8	9.5	822.3	822.74	0.44	5
96X	22 Nov	1555	831.8	841.4	9.6	831.8	832.20	0.40	4
97X	22 Nov	1730	841.4	851.0	9.6	841.4	846.48	5.08	53
98X	22 Nov	1915	851.0	860.7	9.7	851.0	851.69	0.69	7
99X	22 Nov	2010	860.7	870.3	9.6	860.7	861.44	0.74	8
100X	22 Nov	2115	870.3	879.9	9.6	870.3	877.68	7.38	77
101X	22 Nov	2200	879.9	889.6	9.7	879.9	882.61	2.71	28
102X	23 Nov	0000	889.6	899.2	9.6	889.6	889.86	0.26	3
103X	23 Nov	0135	899.2	908.8	9.6	899.2	900.64	1.44	15
104X	23 Nov	0230	908.8	918.4	9.6	908.8	913.40	4.60	48
105X	23 Nov	0350	918.4	928.0	9.6	918.4	918.82	0.42	4
106X	23 Nov	0525	928.0	937.6	9.6	928.0	933.19	5.19	54
107X	23 Nov	0830	937.6	947.2	9.6	937.6	938.27	0.67	7
108X	23 Nov	1000	947.2	956.8	9.6	947.2	947.75	0.55	6
109X	23 Nov	1140	956.8	966.4	9.6	956.8	961.45	4.65	48
110X	23 Nov	1305	966.4	975.9	9.5	966.4	966.79	0.39	4
111X	23 Nov	1445	975.9	985.5	9.6	975.9	976.71	0.81	8
112X	23 Nov	1700	985.5	995.1	9.6	985.5	991.23	5.73	60
113X	23 Nov	1915	995.1	1004.7	9.6	995.1	998.40	3.30	34
114X	23 Nov	2025	1004.7	1014.3	9.6	1004.7	1005.40	0.70	7
115X	23 Nov	2155	1014.3	1024.0	9.7	1014.3	1014.61	0.31	3
116X	24 Nov	0315	1024.0	1030.6	6.6	1024.0	1024.44	0.44	7
			Advanced total:	1030.6				304.52	30
			Total interval cored:	1030.6					
317-U1351C-									
1D	27 Nov	0042		***** Drilled from 0.0 to 967.3 m *****					
			Advanced total:	0.0				0.00	0
			Total interval cored:	967.3					

Notes: APC = advanced piston corer. DRF = drilling depth below rig floor, DSF = drilling depth below seafloor, CSF-A = core depth below seafloor. UTC = Universal Time Coordinated.

Table T2. Lithostratigraphic summary, Site U1351. (**See table note.**)

Lith. unit	Age	Interval	Depth (m)	Lithologies (decreasing order of importance)
I	Holocene–Pleistocene to early Pliocene	317- U1351A-1H through 6H U1351B-1H through transition zone	0–28.1 0–262*	Mud, sandy mud, shell hash, sand, muddy sand
I/II	early Pliocene	U1351B-29X-CC, 33 cm, to 36X-1, 0 cm	247–300	Transition zone
II	early Pliocene to late Miocene	Transition zone to U1351B-116X-CC, 44 cm	262*–1024.4	Sandy mud, muddy sand, mud, sand (sandstone), shell hash (limestone)

Note: * = tentative; see options in text.

Table T3. Cemented intervals, Hole U1351B. (**See table note.**)

Core, section, interval (cm)	Top depth CSF-A (m)	Type of hard surface	Correlation with physical property data	Major lithology	Core recovery (%)
317-U1351B-					
9H-3, 73–120	57.2	Cemented beds	No data	Sandy mud	92
19X-CC, 17–29	141.6	Nodule/concretion	Yes	Mud	62
20X-1, 86–92	151.2	Nodule/concretion	Yes	Mud	94
20X-2, 100–106	151.2	Nodule/concretion	Yes	Mud	94
20X-4, 130–132	151.2	Nodule/concretion	Yes	Mud	94
30X-1, 20–40	247.1	Nodule/concretion	Yes	Fine muddy sand	83
30X-1, 56–58	247.1	Nodule/concretion	Yes	Fine muddy sand	83
30X-3, 5–10	247.1	Nodule/concretion	Yes	Fine muddy sand	83
30X-3, 20–25	247.1	Nodule/concretion	Yes	Fine muddy sand	83
30X-5, 75–80	247.1	Nodule/concretion	Yes	Fine muddy sand	83
31X-2, 23–25	256.7	Nodule/concretion	Yes	Mud	72
33X-3, 30–35 (base of CC)	275.9	Cemented bed	Yes	Sandy mud	26
34X-CC, 16–21	285.5	Cemented bed	Yes	Very fine sandy mud	10
34X-CC, 28–29	285.5	Cemented bed	Yes	Very fine sandy mud	10
44X-1, 1–5	381.1	Cemented bed	Yes	Muddy very fine sand	16
44X-1, 65–68	381.1	Cemented bed	Yes	Muddy very fine sand	16
46X-CC, 0–5 (base of CC)	400.2	Cemented bed	Yes	Sandstone	1
49X-CC, 8–10 (base of CC)	429.0	Cemented bed	Yes	Sand	2
60X-CC, 28–31 (base of CC)	512.4	Cemented bed	Yes	Very fine sandy mud	3
61X-CC, 14–16	524.5	Cemented bed	Yes	Mud	9
61X-CC, 22–36	524.5	Cemented bed	Yes	Mud	9
62X-CC, 11–16 (base of CC)	534.1	Cemented bed	No	Mud	2
77X-2, 8–31	668.6	Cemented bed	Yes	Very fine sandy mud	7
87X-CC, 18–22 (base of CC)	745.3	Cemented bed	Yes	Very fine sandy mud	3
88X-CC, 22–33 (base of CC)	754.9	Cemented bed	Yes	Very fine sandy mud	26
89X-CC, 26–31 (base of CC)	764.5	Cemented bed	Yes	Very fine sandy mud	26
92X-CC, 4–8 (base of CC)	793.3	Cemented bed	Yes	Very fine sandy mud	32
93X-6, 134–150	803.0	Cemented bed	Yes	Very fine sandy mud	104
93X-CC, 31–37 (base of CC)	803.0	Cemented bed	Yes	Very fine sandy mud	104
96X-CC, 0–12	831.8	Nodule/concretion (TS)	Yes	Very fine sandy mud	4
98X-CC, 25–32 (base of CC)	851.0	Nodule/concretion (TS)	Yes	Very fine sandy mud	7
99X-1, 0–2	860.7	Nodule/concretion	Yes	Very fine sandy mud	8
100X-3, 15–17	870.3	Nodule/concretion	Yes	Sandy mud	77
100X-3, 70–75	870.3	Nodule/concretion	Yes	Sandy mud	77
100X-4, 90–93	870.3	Nodule/concretion	Yes	Sandy mud	77
100X-5, 45–50	870.3	Nodule/concretion	Yes	Sandy mud	77
101X-2, 29–33	879.9	Nodule/concretion	Yes	Very fine sandy mud	28
102X-CC, 3–7	889.6	Nodule/concretion	No	Very fine sandy mud	3
104X-CC, 38–39 (base of CC)	908.8	Cemented bed	Yes	Very fine sandy mud	48
105X-CC, 33–36 (base of CC)	918.4	Cemented bed	Yes	Very fine sandy mud	4
106X-4, 14–16	928.0	Cemented bed	Yes	Silty mud	54
107X-CC, 30–32 (base of CC)	937.6	Cemented bed	Yes	Very fine sandy mud	7
108X-CC, 35–48 (base of CC)	947.2	Cemented bed	Yes	Very fine sandy mud	6
109X-CC, 27–29 (base of CC)	956.8	Cemented bed	Yes	Very fine sandy mud	48
110X-CC, 27–29 (base of CC)	966.4	Cemented bed	Yes	Very fine sandy mud	4
111X-CC, 28–32 (base of CC)	975.9	Cemented bed (TS)	Yes	Very fine sandy mud	8
112X-CC, 24–32 (base of CC)	985.5	Cemented bed (TS)	Yes	Very fine sandy mud	60
113X-1, 100–115	995.1	Nodule/concretion (TS)	Yes	Very fine sandy mud	34
113X-2, 8–13	995.1	Nodule/concretion	Yes	Very fine sandy mud	34
113X-2, 45–53	995.1	Nodule/concretion	Yes	Very fine sandy mud	34
113X-2, 75–78	995.1	Nodule/concretion	Yes	Very fine sandy mud	34
113X-2, 130–135	995.1	Nodule/concretion	Yes	Very fine sandy mud	34
113X-CC, 12–16	995.1	Nodule/concretion	Yes	Very fine sandy mud	34
114X-CC, 23–31 (base of CC)	1004.7	Cemented bed	No data	Very fine sandy mud	7
115X-CC, 18–26 (base of CC)	1014.3	Cemented bed	No data	Very fine sandy mud	3
116X-CC, 21–37 (base of CC)	1024.0	Cemented bed	No data	Very fine sandy mud	7

Note: TS = thin section.

Table T4. Lithologic surfaces and their interpretation, Site U1351. (**See table note.**)

Lithologic surface	Hole, core, section, interval (cm)	Depth CSF-A (m)	Overlying lithology	Nature of significant surface	Seismic sequence boundary	Predicted depth (m)	Preliminary biostratigraphy (Ma)
	317-						
U1351A-S1	U1351A-3H-3, 74	15.93	Shelly	Sharp basal contact	U19	17	<0.29 (CN); possibly <0.1 (CN)
U1351B-S1	U1351B-2H-6, 68	15.98	Shelly	Sharp basal contact			
U1351B-S2	U1351A-6H-1, 26	27.76	Shelly sand	Sharp basal contact	U18	31	<0.29 (CN); possibly <0.1 (CN)
U1351B-S2	U1351B-5H-3, 3	31.00	Sand	Sharp basal contact			
U1351B-S3	U1351B-8H-4, 5	52.25	Muddy gravely sand	Sharp basal contact; burrows beneath	U17	51	0.29 (CN)–0.44 (CN)
U1351B-S4	U1351B-10H-2, 45	67.27	Sandy shelly mud	Gradational contact separating sandy, shelly muds above from shelly sands beneath; possible cave-in	U16	64	0.44 (CN)–1.01 (CN)
U1351B-S5	U1351B-12H-1, 122	76.92	Muddy, shelly sand	Burrowed; incomplete recovery	U15	86	1.34–1.69 (CN)
U1351B-S6	U1351B-19X-2, 104	144.14	Shelly sand	Sharp basal contact	U13	135	Pleistocene/Pliocene boundary sediments above 1.69–1.81; below ?>2.7 (PF)
U1351B-S7	U1351B-22X-1, 102	171.42	Shelly sandy mud	Sharp basal contact; burrowed clays beneath	U12	166	?>2.7 (PF)
U1351B-S8	U1351B-30X-5, 80	253.90	Shelly sand	Well-preserved shells and fragments in a muddy sand matrix; sharp burrowed contact	U10	237	3.7 (CN)–4.3 (PF)

Note: CN = calcareous nannofossil, PF = planktonic foraminifer.

Table T5. Preliminary lithostratigraphic/chronostratigraphic correlation. (**See table note.**)

Lithologic surface	Seismic sequence boundary	Preliminary biostratigraphic age (Ma)
S1	U19	<0.29 (CN); possibly <0.1 (CN)
S2	U18	<0.29 (CN); possibly <0.1 (CN)
S3	U17	0.29–0.44 (CN)
S4	U16	0.44–1.01 (CN)
S5	U15	0.44–0.01 (CN); below >1.34 (CN)
	U14	1.34–1.7
S6	U13	Pleistocene/Pliocene boundary sediments; above 1.69–1.81; below >2.7 (PF)
S7	U12	2.45–3.04 (PF)
	U11	>2.7 (PF)
S8	U10	3.7–4.3 (PF)

Note: CN = calcareous nannofossil, PF = planktonic foraminifer.

Table T6. Microfossil bioevents, Site U1351. (**See table notes.**)

Core, section, interval (cm) Top	Bottom	Microfossil	Bioevents, unconformities, and epoch boundaries	Age (Ma)	Depth CSF-A (m) Top	Bottom	Midpoint	±	Comments
317-U1351A- 1H-CC	317-U1351A- 5H-CC	CN	In *Emiliania huxleyi* Zone (NN21a)	<0.29	2.56	28.00			Well defined
317-U1351B- 4H-CC	317-U1351B- 4H-CC	PF	Contains *Truncorotalia truncatulinoides*	0–1.1 (± 0.1)	28.17	28.17	28.17		
5H-CC	6H-CC	CN	LO *Emiliania huxleyi* (NN21 base)	0.29 (± 0.03)	32.34	39.27	35.81	3.46	UC below this event
7H-CC	8H-CC	BF	HO *Bolivinita pliozea*	0.60 (± 0.2)	47.83	56.46	52.15	4.32	
9H-CC	11H-1,128	CN	HO *Pseudoemiliania lacunosa* (NN20 base)	0.44 (± 0.01)	65.91	70.98	68.45	2.54	
11H-CC	12H-CC	CN	LO *Gephyrocapsa omega*	1.01 (± 0.3)	75.57	76.92	76.25	0.67	Poorly defined
12H-CC	13H-CC	CN	HO *Gephyrocapsa* >5.5 µm	1.26 (± 0.01)	76.92	90.02	83.47	6.55	UC above this event
12H-CC	13H-CC	CN	HO *Helicosphaera sellii*	1.34 (± 0.01)	76.92	90.02	83.47	6.55	UC above this event
15X-CC	16X-2, 6–7	CN	LO *Gephyrocapsa* >4 µm	1.69 (± 0.05)	103.42	114.46	108.95	5.52	UC below this event?
18X-CC	19X-CC		Pliocene/Pleistocene boundary	1.81	134.48	147.55	141.02	6.54	
19X-CC	20X-CC	PF	HO *Zeaglobigerina* cf. *woodi* (one specimen)	2.7 (± 0.3)	147.55	160.16	153.86	6.30	Very poorly defined
20X-CC	21X-CC	PF	HO *Zeaglobigerina woodi*	2.7 (± 0.3)	160.16	168.48	164.32	4.16	Poorly defined
23X-CC	24X-CC	BF	LO *Notorotalia zelandica*	2.4 (± 0.5)	180.13	189.75	184.94	4.81	
26X-CC	27X-CC	PF	HO *Globoconella puncticuloides*	1.5 (± 0.3)	208.96	226.27	217.62	8.66	Poorly defined & dated
28X-CC	28X-CC	PF	Within upper *Truncorotalia crassaformis* dextral coiling zone	2.45–3.04 (± 0.02)	236.17	236.17	236.17		Poorly defined
28X-CC	29X-CC	BF	HO *Haeuslerella parri*	1.63 (± 0.5)	236.17	247.35	241.76	5.59	
28X-CC	29X-CC	CN	HO *Sphenolithus* spp.	3.54 (± 0.1)	236.17	247.35	241.76	5.59	UC above this event?
28X-CC	29X-CC	CN	HO *Reticulofenestra pseudoumbilicus* (8–10 µm)	3.7 (± 0.05)	236.17	247.35	241.76	5.59	UC above this event?
33X-CC	34X-CC	BF	HO *Notorotalia hurupiensis*	3.6 (± 0.5)	278.35	286.39	282.37	4.01	
39X-CC	40X-CC	PF	Lowest *Globoconella inflata* s.s. population	<4.3 (± 0.3)	337.45	345.68	341.57	4.12	Reliable
40X-CC	41X-CC	PF	HO *Globoconella puncticulata* s.l.	?4.3 (± 0.3)	345.68	354.21	349.95	4.26	Poorly defined
44X-CC	45X-CC	CN	Lowest *Helicosphaera sellii* (above NN12)	<5.33	382.57	393.34	387.96	5.38	
44X-CC	45X-CC	PF	Highest *Globoconella puncticulata* s.s. population	4.3 (± 0.3)	382.57	393.34	387.96	5.38	Reliable
45X-CC	46X-CC	PF	LO *Globoconella puncticuloides*	4.3 (± 0.3)	393.34	411.72	402.53	9.19	Poorly defined
57H-CC	59H-CC	BF	LO *Notorotalia finlayi*	3.6 (± 0.5)	507.60	510.49	509.05	1.44	
83X-CC	84X-CC	BF	HO *Haeuslerella morgani*	5.3 (± 0.1)	716.94	726.71	721.83	4.85	
94X-CC	95X-CC	PF	LO *Globoconella puncticulata* s.s.	5.3 (± 0.1)	819.12	822.69	820.91	1.79	Population, well defined
94X-CC	95X-CC		Miocene/Pliocene boundary	5.33	819.12	822.69	820.91	1.79	
94X-CC	95X-CC	PF	HO *Globoconella sphericomiozea* s.s.	5.3 (± 0.1)	819.12	822.69	820.91	1.79	Population, well defined
94X-CC	95X-CC	CN	Contains *Scyphosphaera graphica*; *Scyphosphaera queenslandensis*		819.12	822.69	820.91	1.79	late Miocene markers
96X-CC	97X-CC	BF	HO *Textularia miozea*	6.67 (± 0.5)	832.15	847.79	839.97	7.82	
99X-CC	100X-CC	BF	LO *Haeuslerella parri*	5.3 (± 0.1)	861.39	877.62	869.51	8.12	
100X-CC	101X-CC	PF	LO *Globoconella sphericomiozea* s.s.	5.6 (± 0.1)	877.62	882.55	880.09	2.46	Population, well defined
100X-CC	101X-CC	PF	HO *Globoconella conomiozea* s.s.	5.6 (± 0.1)	877.62	882.55	880.09	2.46	Population, well defined
110X-CC	111X-CC	CN	Contains *Sphenolithus neoabies*	<12	966.74	976.66	971.70	4.96	
113X-CC	114X-CC	PF	Lowest *Globoconella conomiozea* s.s. intra-late Miocene unconformity	<7.07 (± 0.1)	998.34	1005.34	1001.84	3.50	Immediately above UC
113X-CC	114X-CC	PF	Highest *Globoconella miotumida* s.s.	>7.07 (± 0.1)	998.34	1005.34	1001.84	3.50	Immediately below UC
113X-CC	114X-CC	PF	Highest *Hirsutella panda*	>10.50 (± 0.05)	998.34	1005.34	1001.84	3.50	Immediately below UC
114X-CC	115X-CC	BF	Lowest *Bolivinita pliozea*	<8.95	1005.34	1014.56	1009.95	4.61	
114X-CC	115X-CC	PF	HO *Paragloborotalia mayeri* s.l.	10.56 (± 0.1)	1005.34	1014.56	1009.95	4.61	Poorly defined
114X-CC	115X-CC	PF	*Hirsutella panda* acme zone	10.64–10.91 (± 0.02)	1005.34	1014.56	1009.95	4.61	Upper or lower *Hr. panda* acme zone?
115X-CC	116X-CC	PF	late Miocene assemblage, above KCZ	<10.91	1014.56	1024.39			Well constrained

Notes: CN = calcareous nannofossil, PF = planktonic foraminifer, BF = benthic foraminifer. LO = lowest occurrence, HO = highest occurrence. KCZ = Kaiti Coiling Zone. UC = unconformity. This table is also available in **ASCII.**

Table T7. Calcareous nannofossil abundance, preservation, and distribution, Site U1351. This table is available in an **oversized format.**

Table T8. Planktonic foraminifer abundance, preservation, and distribution, Hole U1351A. (**See table notes.**)

Core, section	Top depth CSF-A (m)	Epoch	NZ stage	Abundance	Preservation	Planktonic foraminifer (%)	Planktonic foraminifers																																		Miscellaneous									Comments
							Globigerina spp.	*Globigerina bulloides*	*Globigerina eamesi*	*Globigerina falconensis*	*Globigerinella* sp.	*Globigerinella aequilateralis*	*Globigerinita glutinata*	*Globigerinoides ruber*	*Globigerinopsis obesa*	*Globoconella conomiozea*	*Globoconella explicationis*	*Globoconella inflata*	*Globoconella miotumida*	*Globoconella puncticulata*	*Globoconella puncticuloides*	*Globoconella sphericomiozea*	*Hirsutella scitula*	*Hirsutella panda*	*Neogloboquadrina dutertrei*	*Neogloboquadrina incompta*	*Neogloboquadrina pachyderma*	*Orbulina universa*	*Paragloborotalia mayeri* s.l.	*Tenuitella* sp.	*Truncorotalia crassaformis*	*Truncorotalia juanai*	*Turborotalita quinqueloba*	*Truncorotalia truncatulinoides*	*Zeaglobigerina* sp.	*Zeaglobigerina druryi*	*Zeaglobigerina woodi*	Echinoid plate fragments	Echinoid spines	Fish teeth	Ostracods	Shell fragments	Micro-mollusks	Barnacle fragments	Bryozoan fragments	
317-U1351A-																																															
1H-CC	2.56			A	G	13	X										X										X							cf.					F			F	A			
2H-CC	11.44			A	G	17	X	X		X							?																	cf.								A	A	A		
3H-CC	18.15	Pleistocene	Wq	A	G	26	X	X									?																	cf.									A			
4H-CC	25.08			A	G	29	X	X			X						X											X	X					cf.					F				A			
5H-CC	27.50			A	G	8	X	X									X											X	X					cf.	X				F			F	A			
6H-CC	28.00			A	G	24	X										X										X							cf.					R			R				

Notes: Abundance: A = abundant, C = common, F = few, R = rare, X = present, ? = questionable presence. Preservation: G = good. For NZ stage abbreviations, see Figure **F5** in the "Methods" chapter. This table is also available in **ASCII.**

Table T9. Planktonic foraminifer abundance, preservation, and distribution, Hole U1351B. This table is available in an **oversized format.**

Table T10. Planktonic foraminiferal summary, Hole U1351A. (**See table note.**)

Core, section	Top depth CSF-A (m)	Interpreted age	NN zone	NZ stage correlation	NZ stage	Age (Ma)	Planktonic foraminifer (%)	Oceanicity	Key species and comments
317-U1351A-									
1H-CC	2.56				Wq–uWo	0–4.3	13	Inner neritic	*Globoconella inflata*
2H-CC	11.44				Wq–uWo	0–4.3	17	Outer neritic	*Globoconella inflata*
3H-CC	18.15		NN21	Haweran	Wq–uWo	0–4.3	26		*Globoconella inflata?*
4H-CC	25.08	Pleistocene		(Wq)	Wq–uWo	0–4.3	29		*Globoconella inflata?*
5H-CC	27.50				Wq–uWc	0–1.1	8	Inner neritic	*Truncorotalia truncatulinoides,* cold-water assemblage
6H-CC	28.00				Wq–uWo	0–4.3	24	Outer neritic	*Globoconella inflata*

Note: For New Zealand (NZ) stage abbreviations, see Figure **F5** in the "Methods" chapter. This table is also available in **ASCII.**

Table T11. Planktonic foraminiferal summary, Hole U1351B. This table is available in an **oversized format.**

Table T12. Benthic foraminifer abundance, preservation, and distribution, Site U1351. This table is available in an **oversized format.**

Table T13. Diatom abundance, preservation, and distribution, Site U1351. (**See table notes.**) (**Continued on next two pages.**)

Core, section, interval (cm)	Top depth CSF-A (m)	Group abundance	Preservation	*Coscinodiscus radiatus*	*Hyalodiscus* sp.	*Paralia sulcata*	*Pinnularia* sp.	*Thalassiosira fasciculata*	*Triceratium* sp.	*Chaetoceros* resting spores	Comments
317-U1351A-											
1H-CC	2.56	C	M		R	A	R	R	R	R	Coastal, near estuary?
2H-CC	11.44	B	—								
3H-CC	18.15	B	—								
4H-CC	25.08	B	—								
5H-CC	27.50	B	—								
6H-CC	28.00	B	—								
317-U1351B-											
1H-CC	7.71	B	—								
2H-CC	16.66	B	—								
3H-CC	22.29	B	—								
4H-CC	28.17	B	—								
5H-CC	32.34	B	—								
6H-CC	39.27	B	—								
7H-CC	47.83	B	—								
8H-CC	56.46	B	—								
9H-CC	65.91	B	—								
10H-CC	69.83	B	—								
11H-CC	75.57	B	—								
12H-CC	76.92	B	—								
13H-CC	90.02	R	P	R				R			Diatoms rarely occur and only in hard silt inlying bivalves dissolved by HCl and sieved by mesh from 125 to 20 µm.
14X-CC	97.11	B	—								
15X-CC	103.42	B	—								
16X-CC	120.24	B	—								
18X-CC	134.48	B	—								
19X-CC	147.55	B	—								
20X-CC	160.16	B	—								
21X-CC	168.48	B	—								
22X-CC	175.27	B	—								
23X-CC	180.13	B	—								
24X-CC	189.75	B	—								
25X-CC	202.59	B	—								
26X-CC	208.96	B	—								
27X-CC	226.27	B	—								
28X-CC	236.17	B	—								
29X-CC	247.35	B	—								
30X-CC	255.06	B	—								
31X-CC	263.61	B	—								
32X-CC	270.97	B	—								
33X-CC	278.35	B	—								
34X-CC	286.39	B	—								
35X-CC	295.32	B	—								
36X-CC	309.75	B	—								
37X-CC	317.05	B	—								
38X-CC	323.70	B	—								
39X-CC	337.45	B	—								
40X-CC	345.68	B	—								
41X-CC	354.21	B	—								
42X-CC	362.15	B	—								
43X-CC	372.13	B	—								
44X-CC	382.57	B	—								
44X-1, 3–8	381.13	B	—								Calcareous concretion
44X-1, 67–69	381.77	B	—								Calcareous concretion
45X-CC	393.34	B	—								
46X-CC	400.24	B	—								Sediment with calcareous concretion
47X-CC	411.72	B	—								

Table T13 (continued). (Continued on next page.)

Core, section, interval (cm)	Top depth CSF-A (m)	Group abundance	Preservation	*Coscinodiscus radiatus*	*Hyalodiscus sp.*	*Paralia sulcata*	*Pinnularia sp.*	*Thalassiosira fasciculata*	*Triceratium sp.*	*Chaetoceros resting spores*	Comments
48X-CC	421.03	B	—								Sediment with calcareous concretion
49X-CC	429.14	B	—								
53X-CC	467.79	B	—								
54X-CC	477.24	B	—								
55X-CC	486.50	B	—								
57H-CC	507.60	B	—								
59H-CC	510.49	B	—								
60X-CC	512.76	B	—								Calcareous concretion
61X-CC	525.29	B	—								Calcareous concretion
62X-CC	534.28	B	—								Calcareous concretion
63X-CC	543.92	B	—								
64X-CC	556.27	B	—								
65H-CC	563.80	B	—								
66X-CC	564.07	B	—								
67X-CC	572.90	B	—								
69X-CC	591.90	B	—								
70X-CC	603.49	B	—								
71X-CC	611.69	B	—								
72X-CC	623.60	B	—								
73X-CC	631.41	B	—								
74X-CC	640.12	B	—								
75X-CC	649.79	B	—								
76X-CC	659.58	B	—								
77X-CC	669.72	B	—								
78H-CC	678.99	B	—								
79X-CC	679.46	B	—								
80X-CC	688.06	B	—								
81X-CC	697.67	B	—								
82X-CC	707.27	B	—								
83X-CC	716.94	B	—								
84X-CC	726.71	B	—								
85H-CC	736.41	B	—								
86X-CC	737.59	B	—								Sediment with calcareous concretion
87X-CC	745.30	B	—								
88X-CC	757.33	B	—								
89X-CC	766.94	B	—								
90X-CC	778.52	B	—								
91X-CC	784.04	B	—								Sediment with calcareous concretion
92X-CC	796.33	B	—								
93X-CC	812.51	B	—								
94X-CC	819.12	B	—								
95X-CC	822.69	B	—								
96X-CC	832.15	B	—								
97X-CC	847.79	B	—								Sediment with calcareous concretion
98X-CC	851.64	B	—								Sediment with calcareous concretion
99X-CC	861.39	B	—								
100X-1, 122–123	871.52	B	—								Calcareous concretion
100X-3, 71–72	874.01	B	—								Calcareous concretion
100X-5, 39–41	876.69	B	—								Calcareous concretion
100X-CC	877.62	B	—								
101X-CC	882.55	B	—								
102X-CC	889.81	B	—								
103X-CC	900.59	B	—								
104X-CC	913.35	B	—								
105X-CC	918.77	B	—								
106X-CC	933.14	B	—								
107X-CC	938.22	B	—								
108X-CC	938.22	B	—								
109X-CC	947.70	B	—								
110X-CC	961.40	B	—								
111X-CC	966.74	B	—								
112X-CC	976.66	B	—								

Table T13 (continued).

Core, section, interval (cm)	Top depth CSF-A (m)	Group abundance	Preservation	*Coscinodiscus radiatus*	*Hyalodiscus* sp.	*Paralia sulcata*	*Pinnularia* sp.	*Thalassiosira fasciculata*	*Triceratium* sp.	*Chaetoceros* resting spores	Comments
113X-CC	991.18	B	—								
114X-CC	998.34	B	—								
115X-CC	1005.34	B	—								
116X-CC	1014.56	B	—								
117X-CC	1024.39	B	—								

Notes: Abundance: A = abundant, C = common, R = rare, B = barren. Preservation: M = moderate, P = poor, — = no data. This table is also available in **ASCII.**

Table T14. Invertebrate macrofossils. This table is available in an **oversized format.**

Table T15. Headspace gas composition from sediments, Site U1351. (**See table note.**)

Core, section, interval (cm)	Depth CSF-A (m)	C_1 (ppmv)	C_2 (ppmv)	$C_{2=}$ (ppmv)	C_3 (ppmv)	C_1 (mM)	C_1/C_2
317-U1351A-							
1H-2, 0	1.50	0	0.0	0	0	0.00	ND
2H-2, 0	4.20	0	0.0	0	0	0.00	ND
2H-4, 0	7.20	0	0.0	0	0	0.00	ND
2H-6, 0	10.20	0	0.0	0	0	0.00	ND
3H-2, 0	13.70	0	0.0	0	0	0.00	ND
4H-2, 0	19.70	2,837	8.0	0	0	0.86	338
4H-4, 0	22.70	4,495	12.0	0	0	1.36	378
4H-5, 145	24.80	12,003	17.0	0	0	3.62	706
5H-2, 0	26.60	4,629	9.0	0	0	1.40	538
317-U1351B-							
1H-2, 0	1.50	0	0.0	0	0	0.00	ND
2H-2, 0	9.30	0	0.0	0	0	0.00	ND
3H-2, 0	18.20	463	1.0	0	0	0.14	463
4H-2, 0	23.60	3,555	8.0	0	0	1.07	428
5H-3, 0	31.00	6,210	12.0	0	0	1.87	518
6H-2, 0	33.70	10,516	25.0	0	0	3.17	427
7H-2, 0	40.70	12,716	21.0	0	0	3.84	603
8H-2, 0	52.20	12,816	18.0	0	0	3.87	716
9H-3, 0	60.20	20,816	29.0	0	0	6.28	730
11H-2, 0	71.20	4,135	8.0	0	0	1.25	504
11H-3, 0	72.20	3,446	11.0	0	0	1.04	316
11H-4, 0	74.20	15,203	29.0	0	0	4.59	517
14X-2, 0	96.20	13,181	31.0	0	0	3.98	420
16X-4, 0	117.40	22,660	48.0	0	0	ND	468
18X-2, 0	133.50	11,057	26.0	0	0	ND	422
19X-3, 0	144.60	13,815	32.0	0	0	ND	437
20X-3, 0	154.20	10,217	22.0	0	0	ND	462
21X-4, 0	165.30	12,667	30.0	0	0	ND	422
22X-3, 0	173.40	3,698	11.0	0	0	ND	333
25X-2, 0	200.70	5,869	19.0	0	0	ND	306
27X-3, 0	221.40	14,768	48.0	0	0	ND	308
28X-3, 0	231.00	15,939	56.0	0	0	ND	286
29X-4, 0	242.00	11,714	41.0	0	0	ND	286
30X-4, 0	251.60	6,704	29.0	0	0	ND	234
31X-4, 0	261.20	6,520	28.0	0	0	ND	231
32X-3, 0	269.30	4,677	16.0	0	0	ND	298
33X-2, 0	277.40	4,430	12.0	0	0	ND	369
34X-1, 51	286.00	9,033	28.0	0	0	ND	325
36X-3, 0	307.70	3,017	9.0	0	0	ND	347
37X-2, 0	315.40	2,706	12.0	0	0	ND	229
39X-3, 0	336.20	2,900	9.0	0	0	ND	312
40X-2, 0	344.30	3,227	11.0	0	0	ND	304
41X-2, 0	353.30	6,574	22.0	0	0	ND	300
44X-1, 116	382.30	3,878	14.0	0	0	ND	279
45X-2, 0	392.20	2,360	10.0	0	0	ND	236
47X-2, 0	410.80	4,055	15.0	0	0	ND	280
64x-2, 0	554.90	5,692	21.0	0	0	ND	274
65H-1, 52	563.52	4,369	12.0	0	0	ND	353
70X-2, 0	602.80	3,117	10.0	0	0	ND	324
72X-1, 130	621.90	7,652	38.0	0	0	ND	201
88X-2, 0	756.40	6,102	34.0	0	2.6	ND	178
89X-2, 0	766.00	4,562	21.0	0	1.3	ND	215
90X-3, 0	777.10	4,431	21.0	0	0.9	ND	214
92X-2, 0	794.80	3,510	21.0	0	2.0	ND	164
93X-4, 0	807.50	3,513	19.0	0	1.1	ND	188
94X-4, 0	817.10	7,434	41.0	0	2.7	ND	184
97X-3, 0	844.40	3,453	23.0	0	3.7	ND	153
100X-4, 0	874.80	2,861	13.0	0	1.7	ND	222
101X-2, 0	881.40	3,296	14.0	0	0	ND	231
103X-1, 101	900.21	4,777	25.0	0	0	ND	189
104X-2, 0	910.30	4,810	25.0	0	0	ND	194
106X-3, 0	931.00	4,034	32.0	1.05	4.6	ND	127
109X-2, 0	958.30	2,716	13.0	0	0	ND	211
112X-4, 0	990.00	5,480	30.0	0	0	ND	184
113X-2, 0	996.60	3,052	17.0	0	0	ND	185

Note: ND = not determined.

Table T16. Core void gas composition, Site U1351. (**See table notes.**)

Core, section, interval (cm)	Depth CSF-A (m)	C_1 (ppmv)	C_2 (ppmv)	$C_{2=}$ (ppmv)	C_3 (ppmv)	n-C_4 (ppmv)	i-C_4 (ppmv)	n-C_5 (ppmv)	i-C_5 (ppmv)	n-C_6 (ppmv)	br-C_6 (ppmv)	C_1/C_2	n-$C_4/(i$-$C_4 + n$-$C_4)$ (%)	n-$C_5/(i$-$C_5 + n$-$C_5)$ (%)
317-U1351A-														
4H-4, 66	27.30	119,449	195	0.0	0.0	ND	ND	ND	ND	ND	ND	612	ND	ND
317-U1351B-														
16X-4, 34	117.74	454,356	616	0.0	0.0	1.0	0.5	0.0	0.0	0.0	0.0	737	66.1	ND
27X-4, 140	224.30	160,675	291	0.0	2.2	2.6	0.3	0.3	0.0	0.0	0.2	551	89.0	ND
37X-1, 48	314.38	632,762	1,076	0.0	19.8	1.4	0.6	0.0	0.0	0.0	0.0	588	71.2	ND
93X-6, 8	810.60	691,745	1,509	1.1	52.0	3.7	14.9	0.3	2.1	0.0	0.4	458	19.8	11.4
109X-3, 119	961.00	609,849	1,474	1.6	17.4	0.6	2.0	0.3	0.5	0.0	0.2	414	24.8	35.3

Notes: C_1–C_3 analyzed on GC3. C_1 and C_4–C_6 analyzed on natural gas analyzer and normalized to methane from GC3 analysis. br-C_6 is the peak eluting before n-C_6, which may include as many as five branched C_6 alkane isomers. ND = not determined.

Table T17. Carbon, nitrogen, and sulfur analyses of sediments, Site U1351. (See table notes.) (Continued on next two pages.)

Core, section, interval (cm)	Depth CSF-A (m)	IC (wt%)	CaCO₃ (wt%)	TC (wt%)	TN (wt%)	TS (wt%)	TOC_DIFF (wt%)	TOC_SRA (wt%)	TOC_DIFF/TN	TOC_DIFF/TS
317-U1351A-										
1H-1, 11	0.11	3.51	29.3	4.22	0.530	0.040	0.71	1.31	1.34	17.67
1H-1, 25	0.25	3.32	27.7	4.06	0.610	0.060	0.74	1.37	1.22	12.32
1H-2, 43	1.92	1.68	14.0	2.49	0.540	0.260	0.81	1.35	1.50	3.11
2H-3, 98	6.68	0.29	2.4	0.67	0.520	0.370	0.38	0.83	0.74	1.03
2H-4, 50	7.70	0.19	1.6	0.99	0.530	0.480	0.80	1.07	ND	ND
3H-2, 77	14.47	1.77	14.8	2.32	0.480	0.230	0.55	1.05	1.15	2.39
3H-4, 56	17.26	0.19	1.6	0.73	ND	0.330	0.54	0.62	ND	1.64
4H-2, 127	20.97	0.95	7.9	1.23	0.430	0.170	0.28	1.00	0.64	1.63
4H-3, 76	21.96	3.54	29.5	3.95	0.600	0.260	0.41	1.42	0.68	1.58
5H-2, 34	26.94	3.70	30.8	3.81	0.610	0.080	0.11	1.01	0.18	1.38
5H-2, 54	27.14	3.76	31.4	4.04	0.560	0.060	0.28	0.98	0.49	4.59
6H-1 35	27.85	0.16	1.3	0.35	0.490	0.190	0.19	0.65	0.39	1.02
317-U1351B-										
1H-1, 50	0.50	3.06	25.5	3.93	0.580	0.090	0.87	1.20	1.50	9.66
1H-1, 78	0.78	3.19	26.6	3.61	0.580	0.020	0.42	1.35	0.73	20.89
1H-5, 41	6.41	0.44	3.7	0.87	0.580	0.500	0.43	0.72	0.74	0.85
2H-4, 69	12.99	2.47	20.6	2.90	0.580	0.040	0.43	0.84	0.74	10.66
2H-4, 101	13.31	2.25	18.7	2.43	0.450	0.240	0.18	1.30	0.41	0.76
3H-2, 101	19.22	0.96	8.0	1.21	0.600	0.180	0.25	0.94	0.42	1.40
3H-4, 88	22.08	0.30	2.5	0.49	0.590	0.200	0.19	0.61	0.32	0.95
4H-1, 40	22.50	0.32	2.6	0.59	0.590	0.180	0.27	0.72	0.46	1.52
4H-3, 75	25.85	3.88	32.3	4.68	0.650	0.040	0.80	1.00	1.23	19.99
4H-4, 101	27.61	3.98	33.2	3.91	0.630	0.010	–0.07	0.58	ND	ND
5H-2, 26	29.79	0.27	2.3	0.32	0.550	0.040	0.05	0.38	0.09	1.20
5H-3, 26	31.23	4.80	40.0	5.19	0.650	0.050	0.39	0.66	0.60	7.74
6H-1, 128	33.48	0.23	1.9	0.35	0.620	0.120	0.12	0.28	0.20	1.02
6H-4, 99	37.69	0.60	5.0	0.81	0.720	0.180	0.21	0.68	0.29	1.17
7H-3, 112	43.32	2.38	19.8	2.57	0.600	0.070	0.19	0.88	0.32	2.78
7H-4, 68	44.38	2.76	23.0	2.77	0.720	0.050	0.01	0.75	0.01	0.15
8H-3, 81	51.51	3.77	31.4	4.54	0.570	0.000	0.77	1.43	1.35	ND
8H-4, 81	53.01	0.69	5.8	0.88	0.520	0.060	0.19	0.56	0.36	3.14
9H-2, 81	59.51	0.48	4.0	0.68	0.690	0.040	0.20	0.91	0.29	4.92
9H-6, 100	65.70	1.70	14.1	2.21	0.550	0.040	0.51	1.11	0.93	12.86
11H-2, 78	71.98	2.58	21.5	2.93	0.550	0.010	0.35	1.18	0.64	35.10
11H-3, 5	72.75	0.57	4.7	0.82	0.680	0.010	0.25	1.28	0.37	25.25
13H-2, 11	86.29	0.17	1.4	0.36	0.760	0.010	0.19	0.52	0.25	19.26
13H-3, 108	88.76	0.10	0.8	0.22	0.640	0.170	0.12	0.46	0.19	0.72
14X-1, 89	95.59	0.23	1.9	0.41	0.640	0.110	0.18	0.26	0.28	1.62
14X-2, 10	96.30	0.12	1.0	0.28	0.640	0.140	0.16	0.54	0.25	1.13
16X-3, 64	116.54	0.34	2.8	0.66	0.810	0.000	0.32	0.52	0.40	ND
16X-4, 107	118.46	0.46	3.9	0.79	0.520	0.290	0.33	0.68	0.62	1.13
18X-1, 25	132.25	0.30	2.5	0.50	0.720	0.040	0.20	0.44	0.27	4.93
18X-1, 110	133.10	0.63	5.2	0.99	0.670	0.000	0.36	0.61	0.54	ND
19X-1, 51	142.11	0.73	6.1	0.89	0.600	0.120	0.16	0.65	0.27	1.33
19X-2, 77	143.87	6.62	55.2	6.40	0.730	0.000	–0.22	0.43	ND	ND
19X-3, 71	145.31	0.20	1.7	0.47	0.710	0.010	0.27	0.54	0.37	26.54
20X-2, 85	153.55	0.07	0.6	0.25	0.670	0.000	0.18	0.38	0.27	ND
21X-2, 71	163.01	0.17	1.4	0.42	0.600	0.000	0.25	0.57	0.42	ND
21X-CC, 7	168.17	3.33	27.7	4.48	0.270	0.220	1.15	0.95	4.25	5.24
22X-2, 13	172.03	5.56	46.3	ND	ND	ND	ND	1.36	ND	ND
25X-1, 61	199.81	0.11	0.9	0.27	0.310	0.300	0.16	0.78	0.52	0.53
25X-2, 53	201.23	4.16	34.6	4.68	0.300	0.240	0.52	1.01	ND	ND
27X-2, 76	220.66	0.17	1.4	ND	ND	ND	ND	1.07	ND	ND
27X-5, 72	225.12	0.54	4.5	ND	ND	ND	ND	0.86	ND	ND
28X-1, 9	228.09	0.18	1.5	0.31	0.270	0.240	0.13	0.59	0.47	0.52
28X-5, 52	234.52	0.22	1.9	ND	ND	ND	ND	0.74	ND	ND
28X-6, 12	235.32	0.44	3.7	0.55	0.280	0.340	0.11	0.78	0.38	0.31
29X-2, 101	240.01	0.24	2.0	ND	ND	ND	ND	1.14	ND	ND
29X-2, 139	240.39	0.27	2.3	0.47	0.280	0.280	0.20	0.79	0.72	0.71
30X-3, 69	250.79	7.49	62.4	ND	ND	ND	ND	0.60	ND	ND
30X-6, 37	254.57	0.24	2.0	ND	ND	ND	ND	0.60	ND	ND
31X-3, 108	260.78	1.06	8.8	1.52	0.290	0.330	0.46	0.84	1.57	1.40
31X-4, 67	261.87	0.22	1.9	ND	ND	ND	ND	1.46	ND	ND
32X-1, 69	266.99	0.56	4.7	0.75	0.310	0.440	0.19	0.76	0.62	0.44
32X-2, 71	268.51	ND	ND	0.95	0.290	0.830	ND	1.15	ND	ND

Table T17 (continued). (Continued on next page.)

Core, section, interval (cm)	Depth CSF-A (m)	IC (wt%)	CaCO₃ (wt%)	TC (wt%)	TN (wt%)	TS (wt%)	TOC_DIFF (wt%)	TOC_SRA (wt%)	TOC_DIFF/TN	TOC_DIFF/TS
33X-2, 36	277.76	1.48	12.3	0.95	0.290	0.830	−0.53	0.87	ND	ND
34X-1, 51	286.01	0.48	4.0	ND	ND	ND	ND	0.59	ND	ND
36X-2, 37	306.57	0.35	2.9	0.57	0.330	0.470	0.22	1.07	0.65	0.46
36X-4, 37	309.07	0.86	7.1	ND	ND	ND	ND	0.71	ND	ND
37X-1, 73	314.63	0.35	2.9	ND	ND	ND	ND	1.01	ND	ND
37X-2, 73	316.13	0.26	2.1	0.64	0.310	0.620	0.38	ND	1.22	0.62
39X-1, 76	333.86	0.51	4.2	ND	ND	ND	ND	1.36	ND	ND
39X-3, 76	336.86	0.96	8.0	ND	ND	ND	ND	0.71	ND	ND
40X-1, 76	343.46	0.59	4.94	0.77	0.250	0.490	0.18	1.09	ND	ND
40X-CC, 7	345.41	0.58	4.8	0.63	0.310	0.500	0.05	0.68	0.16	0.10
41X-1, 76	353.06	0.33	2.7	0.55	0.290	0.540	0.22	0.49	0.78	0.41
41X-CC, 3	353.88	0.49	4.1	ND	ND	ND	ND	ND	ND	ND
43X-1, 17	371.67	0.76	6.3	0.95	0.300	0.420	0.19	1.08	0.64	0.46
44X-1, 55	381.65	0.73	6.1	0.85	0.240	0.360	0.12	0.66	0.49	0.33
44X-CC, 13	382.54	0.75	6.2	0.94	0.310	0.550	0.19	0.62	0.63	0.35
45X-1, 61	391.31	0.72	6.0	1.08	0.320	0.730	0.36	0.70	1.14	0.49
45X-1, 136	392.06	0.78	6.5	1.16	0.310	0.610	0.38	1.02	1.21	0.62
47X-1, 59	410.39	0.87	7.2	1.20	0.280	0.570	0.33	0.62	1.18	0.58
48X-1, 111	420.51	0.59	4.9	0.79	0.320	0.530	0.20	0.62	0.63	0.37
59H-1, 106	509.46	0.31	2.5	0.37	0.240	0.380	0.06	0.73	0.27	0.17
61X-1, 28	524.78	0.32	2.6	0.49	0.330	0.850	0.17	0.60	0.53	0.20
63X-CC, 8	543.88	0.95	7.9	0.90	0.320	0.280	−0.05	0.87	ND	ND
64X-1, 5	553.45	0.30	2.5	0.48	0.350	0.320	0.18	0.70	0.52	0.56
64X-1, 28	553.68	0.35	2.9	0.50	0.340	0.340	0.15	1.24	0.45	0.45
65H-CC, 8	563.65	0.26	2.2	0.42	0.300	0.380	0.16	ND	0.54	0.43
67X-CC, 8	572.68	0.46	3.8	0.55	0.290	0.410	0.09	1.04	0.31	0.22
67X-CC, 17	572.77	0.45	3.7	0.58	0.290	0.400	0.13	0.72	0.47	0.34
70X-2, 10	602.90	1.17	9.8	1.43	0.290	0.320	0.26	1.17	0.90	0.80
70X-2, 37	603.17	1.17	9.7	1.28	0.280	0.380	0.11	1.01	0.39	0.29
72X-1, 101	621.61	1.22	10.1	1.63	0.360	0.620	0.41	1.14	1.15	0.67
72X-2, 52	622.62	0.97	8.1	1.30	0.360	0.510	0.33	1.55	0.92	0.64
73X-1, 49	630.69	1.06	8.9	1.43	0.360	0.500	0.37	0.89	1.02	0.73
73X-1, 87	631.07	1.06	8.8	1.40	0.350	0.430	0.34	1.31	0.98	0.79
76X-CC, 41	659.41	0.48	4.0	0.64	0.320	0.380	0.16	0.97	0.52	0.43
77X-1, 6	668.66	0.46	3.9	0.69	0.310	0.350	0.23	0.93	0.73	0.65
77X-1, 52	669.12	0.51	4.2	0.73	0.340	0.440	0.22	0.93	0.65	0.50
88X-1, 120	756.10	0.42	3.5	ND	ND	ND	ND	ND	ND	ND
88X-2, 19	756.59	0.24	2.0	0.39	0.350	0.400	0.15	0.59	0.44	0.38
89X-1, 101	765.51	0.66	5.5	0.89	0.360	0.390	0.23	0.94	0.64	0.59
89X-2, 50	766.50	0.79	6.6	1.08	0.330	0.440	0.29	0.81	0.86	0.65
90X-2, 101	776.61	0.68	5.7	0.95	0.340	0.620	0.27	0.90	0.80	0.43
90X-3, 63	777.73	0.80	6.7	1.08	0.330	0.490	0.28	1.15	0.84	0.57
92X-1, 100	794.30	1.29	10.7	1.55	0.310	0.430	0.26	1.09	0.84	0.61
92X-2, 103	795.83	1.35	11.3	2.62	0.300	0.270	1.27	1.27	4.29	4.69
93X-1, 37	803.37	0.70	5.8	1.03	0.330	0.450	0.33	0.66	1.01	0.73
93X-4, 80	808.30	0.52	4.3	1.10	0.290	0.470	0.58	0.90	2.02	1.23
94X-4, 72	817.82	1.49	12.4	1.96	0.360	0.500	0.47	1.27	1.32	0.94
95X-CC, 10	822.40	1.29	10.8	1.65	0.320	0.440	0.36	1.06	1.11	0.81
97X-1, 96	842.36	1.41	11.8	1.62	0.350	0.520	0.21	1.02	0.58	0.40
97X-4, 22	845.72	0.55	4.6	1.51	0.340	0.430	0.96	0.95	2.84	2.24
98X-1, 23	851.23	0.86	7.2	1.16	0.320	0.490	0.30	0.96	0.94	0.60
99X-1, 15	860.85	0.71	5.9	0.99	0.330	0.500	0.28	0.73	0.86	0.56
100X-1, 132	871.62	0.69	5.7	0.94	0.330	0.440	0.25	0.59	0.77	0.58
101X-1, 103	880.93	0.60	5.0	0.70	0.340	0.540	0.10	0.76	0.31	0.19
103X-1, 84	900.04	1.05	8.7	1.26	0.320	0.370	0.21	0.87	0.66	0.58
104X-1, 17	908.97	0.99	8.2	1.35	0.320	0.510	0.36	0.68	1.11	0.71
104X-3, 12	911.92	0.90	7.5	1.19	0.280	0.450	0.29	ND	1.04	0.64
106X-1, 141	929.41	1.01	8.4	1.29	0.290	0.510	0.28	0.78	0.96	0.55
106X-3, 40	931.40	1.72	14.4	1.94	0.360	0.480	0.22	1.08	0.60	0.45
107X-1, 10	937.70	0.95	7.9	1.26	0.260	0.390	0.31	0.80	1.20	0.80
107X-1, 13	937.73	0.93	7.8	1.20	0.270	0.390	0.27	0.70	1.00	0.69
109X-2, 75	959.05	0.59	4.9	0.92	0.350	0.540	0.33	0.57	0.93	0.61
109X-3, 124	961.04	1.71	14.2	1.86	0.340	0.350	0.15	1.10	0.44	0.43
111X-1, 31	976.21	1.49	12.5	1.83	0.320	0.500	0.34	1.04	1.08	0.68
111X-1, 35	976.25	1.55	12.9	1.83	0.280	0.430	0.28	0.90	1.02	0.66

Table T17 (continued).

Core, section, interval (cm)	Depth CSF-A (m)	IC (wt%)	CaCO$_3$ (wt%)	TC (wt%)	TN (wt%)	TS (wt%)	TOC$_{DIFF}$ (wt%)	TOC$_{SRA}$ (wt%)	TOC$_{DIFF}$/TN	TOC$_{DIFF}$/TS
112X-3, 68	989.18	1.40	11.7	1.71	0.310	0.420	0.31	0.91	1.00	0.74
113X-2, 114	997.74	1.39	11.6	1.67	0.270	0.350	0.28	1.01	1.03	0.81
115X-CC, 3	1014.33	1.38	11.5	1.70	0.340	0.410	0.32	0.71	0.95	0.78

Notes: Inorganic carbon (IC) is from coulometric measurement of acid-evolved CO_2. CaCO$_3$ is calculated from IC × 8.33. Total carbon (TC), total nitrogen (TN), and total sulfur (TS) are from elemental analysis of sediments. TOC$_{DIFF}$ = total organic carbon from difference of TC and IC, TOC$_{SRA}$ = total organic carbon from source rock analyzer pyrolysis (see Table T18). ND = not determined.

Table T18. Source rock analyzer pyrolysis evaluation of organic matter in sediments, Site U1351. (**See table notes.**) (**Continued on next two pages.**)

Core, section, interval (cm)	Depth CSF-A (m)	S_1 (mg HC/g rock)	S_2 (mg HC/g rock)	S_3 (mg CO$_2$/g rock)	T_{max} (°C)	TOC$_{SRA}$ (wt%)	Hydrogen index (mg S$_2$/g TOC)	Oxygen index (mg S$_3$/g TOC)	Pyrolysis carbon	Production index
317-U1351A-										
1H-1, 11	0.11	0.27	1.13	1.25	429.7	1.31	86.3	95.4	0.116	19.3
1H-1, 25	0.25	0.22	1.01	1.16	422.0	1.37	73.7	84.7	0.102	17.9
1H-2, 43	1.92	0.22	1.05	1.19	422.5	1.35	77.8	88.1	0.105	17.3
2H-3, 98	6.68	0.05	0.20	0.23	416.4	0.83	24.1	27.7	0.021	20.0
2H-4, 50	7.70	0.05	0.21	0.29	419.4	1.07	19.6	27.1	0.022	19.2
3H-2, 77	14.47	0.10	0.52	0.71	421.1	1.05	49.5	67.6	0.051	16.1
3H-4, 56	17.26	0.03	0.12	0.09	426.5	0.62	19.4	14.5	0.012	20.0
4H-2, 127	20.97	0.04	0.15	0.25	401.6	1.00	15.0	25.0	0.016	21.1
4H-3, 76	21.96	0.10	0.57	0.94	423.1	1.42	40.1	66.2	0.056	14.9
5H-2, 34	26.94	0.07	0.35	0.69	413.7	1.01	34.7	68.3	0.035	16.7
5H-2, 54	27.14	0.06	0.36	0.69	425.7	0.98	36.7	70.4	0.035	14.3
6H-1, 35	27.85	0.01	0.06	0.04	419.9	0.65	9.2	6.2	0.006	14.3
317-U1351B-										
1H-1, 50	0.50	0.27	1.50	1.53	420.4	1.20	125.0	127.5	0.147	15.3
1H-1, 78	0.78	0.23	1.13	1.19	412.5	1.35	83.7	88.1	0.113	16.9
1H-5, 41	6.41	0.06	0.22	0.35	403.3	0.72	30.6	48.6	0.023	21.4
2H-4, 69	12.99	0.00	0.01	0.70	ND	0.84	1.2	83.3	0.001	0.0
2H-4, 101	13.31	0.12	0.71	0.76	419.5	1.30	54.6	58.5	0.069	14.5
3H-2, 101	19.22	0.03	0.10	0.32	411.4	0.94	10.6	34.0	0.011	23.1
3H-4, 88	22.08	0.03	0.14	0.17	403.3	0.61	23.0	27.9	0.014	17.6
4H-1, 40	22.50	0.04	0.15	0.24	412.3	0.72	20.8	33.3	0.016	21.1
4H-3, 75	25.85	0.10	0.74	0.78	422.9	1.00	74.0	78.0	0.070	11.9
4H-4, 101	27.61	0.06	0.37	0.73	421.2	0.58	63.8	125.9	0.036	14.0
5H-2, 26	29.79	0.01	0.04	0.06	ND	0.38	10.5	15.8	0.004	20.0
5H-3, 26	31.23	0.07	0.43	0.85	423.3	0.66	65.2	128.8	0.042	14.0
6H-1, 128	33.48	0.02	0.05	0.12	418.9	0.28	17.9	42.9	0.006	28.6
6H-4, 99	37.69	0.05	0.22	0.41	414.9	0.68	32.4	60.3	0.022	18.5
7H-3, 112	43.32	0.09	0.52	0.67	411.1	0.88	59.1	76.1	0.051	14.8
7H-4, 68	44.38	0.08	0.48	0.63	417.9	0.75	64.0	84.0	0.046	14.3
8H-3, 81	51.51	0.19	1.59	1.25	417.7	1.43	111.2	87.4	0.148	10.7
8H-4, 81	53.01	0.03	0.15	0.41	418.0	0.56	26.8	73.2	0.015	16.7
9H-2, 81	59.51	0.05	0.26	0.38	422.3	0.91	28.6	41.8	0.026	16.1
9H-6, 100	65.70	0.07	0.38	0.43	418.5	1.11	34.2	38.7	0.037	15.6
11H-2, 78	71.98	0.11	0.63	0.49	416.6	1.18	53.4	41.5	0.061	14.9
11H-3, 5	72.75	0.05	0.22	0.20	417.6	1.28	17.2	15.6	0.022	18.5
13H-2, 11	86.29	0.04	0.13	0.07	ND	0.52	25.0	13.5	0.014	23.5
13H-3, 108	88.76	0.01	0.05	0.03	ND	0.46	10.9	6.5	0.005	16.7
14X-1, 89	95.59	0.02	0.10	0.23	417.0	0.26	38.5	88.5	0.010	16.7
14X-2, 10	96.30	0.03	0.11	0.12	417.8	0.54	20.4	22.2	0.012	21.4
16X-3, 64	116.54	0.05	0.21	0.50	399.8	0.52	40.4	96.2	0.022	19.2
16X-4, 107	118.46	0.00	0.02	0.43	ND	0.68	2.9	63.2	0.002	0.0
18X-1, 25	132.25	0.00	0.01	0.24	ND	0.44	2.3	54.5	0.001	0.0
18X-1, 110	133.10	0.05	0.23	0.46	408.4	0.61	37.7	75.4	0.023	17.9
19X-1, 51	142.11	0.04	0.20	0.49	404.5	0.65	30.8	75.4	0.020	16.7
19X-2, 77	143.87	0.02	0.10	ND	405.6	0.43	23.3	ND	0.010	16.7
19X-3, 71	145.31	0.05	0.20	0.25	400.0	0.54	37.0	46.3	0.021	20.0
20X-2, 85	153.55	0.03	0.10	0.03	ND	0.38	26.3	7.9	0.011	23.1
21X-2, 71	163.01	0.02	0.10	0.12	421.3	0.57	17.5	21.1	0.010	16.7
21X-CC, 7	168.17	0.11	0.56	0.64	412.9	0.95	58.9	67.4	0.056	16.4

Core, section, interval (cm)	Depth CSF-A (m)	S_1 (mg HC/g rock)	S_2 (mg HC/g rock)	S_3 (mg CO_2/g rock)	T_{max} (°C)	TOC_{SRA} (wt%)	Hydrogen index (mg S_2/g TOC)	Oxygen index (mg S_3/g TOC)	Pyrolysis carbon	Production index
22X-2, 13	172.03	0.12	0.59	0.70	421.1	1.36	43.4	51.5	0.059	16.9
25X-1, 61	199.81	0.06	0.12	0.05	ND	0.78	15.4	6.4	0.015	33.3
25X-2, 53	201.23	0.13	0.39	0.58	407.0	1.01	38.6	57.4	0.043	25.0
27X-2, 76	220.66	0.05	0.17	0.23	398.1	1.07	15.9	21.5	0.018	22.7
27X-5, 72	225.12	0.05	0.14	0.09	416.2	0.86	16.3	10.5	0.016	26.3
28X-1, 9	228.09	0.03	0.10	0.06	432.7	0.59	16.9	10.2	0.011	23.1
28X-5, 52	234.52	0.05	0.09	0.18	ND	0.74	12.2	24.3	0.012	35.7
28X-6, 12	235.32	0.05	0.16	0.16	408.3	0.78	20.5	20.5	0.017	23.8
29X-2, 101	240.01	0.11	0.52	0.39	416.3	1.14	45.6	34.2	0.052	17.5
29X-2, 139	240.39	0.04	0.17	0.19	411.0	0.79	21.5	24.1	0.017	19.0
30X-3, 69	250.79	0.09	0.35	0.81	412.0	0.60	58.3	135.0	0.037	20.5
30X-6, 37	254.57	0.03	0.14	0.11	401.1	0.60	23.3	18.3	0.014	17.6
31X-3, 108	260.78	0.03	0.12	0.09	420.9	0.84	14.3	10.7	0.012	20.0
31X-4, 67	261.87	0.03	0.09	0.22	423.4	1.46	6.2	15.1	0.010	25.0
32X-1, 69	266.99	0.07	0.21	0.29	415.4	0.76	27.6	38.2	0.023	25.0
32X-1, 71	268.51	0.10	0.35	0.41	407.4	1.15	30.4	35.7	0.037	22.2
33X-2, 36	277.76	0.05	0.15	0.28	396.7	0.87	17.2	32.2	0.017	25.0
34X-1, 51	286.01	0.05	0.10	0.18	ND	0.59	16.9	30.5	0.012	33.3
36X-2, 37	306.57	0.05	0.15	0.37	396.5	1.07	14.0	34.6	0.017	25.0
36X-4, 37	309.07	0.07	0.22	0.20	417.8	0.71	31.0	28.2	0.024	24.1
37X-1, 73	314.63	0.09	0.41	0.36	409.5	1.01	40.6	35.6	0.042	18.0
39X-1, 76	333.86	0.05	0.18	0.28	392.3	1.36	13.2	20.6	0.019	21.7
39X-3, 76	336.86	0.05	0.19	0.25	407.6	0.71	26.8	35.2	0.020	20.8
40X-1, 76	343.46	0.04	0.17	0.24	414.0	1.09	15.6	22.0	0.017	19.0
40X-CC, 7	345.41	0.05	0.17	0.15	413.9	0.68	25.0	22.1	0.018	22.7
41X-1, 76	353.06	0.06	0.18	0.24	401.2	0.49	36.7	49.0	0.020	25.0
43X-1, 17	371.67	0.07	0.26	0.28	415.2	1.08	24.1	25.9	0.027	21.2
44X-1, 55	381.65	0.05	0.12	0.21	407.5	0.66	18.2	31.8	0.014	29.4
44X-CC, 13	382.54	0.11	0.36	0.22	407.7	0.62	58.1	35.5	0.039	23.4
45X-1, 61	391.31	0.09	0.41	0.43	411.1	0.70	58.6	61.4	0.042	18.0
45X-1, 136	392.06	0.04	0.12	0.13	411.0	1.02	11.8	12.7	0.013	25.0
47X-1, 59	410.39	0.06	0.19	0.20	399.3	0.62	30.6	32.3	0.021	24.0
48X-1, 111	420.51	0.06	0.24	0.22	421.8	0.62	38.7	35.5	0.025	20.0
59H-1, 106	509.46	0.04	0.15	0.18	414.1	0.73	20.5	24.7	0.016	21.1
61X-1, 28	524.78	0.04	0.15	0.08	419.1	0.60	25.0	13.3	0.016	21.1
63X-CC, 8	543.88	0.04	0.09	0.30	ND	0.87	10.3	34.5	0.011	30.8
64X-1, 5	553.45	0.05	0.12	0.27	ND	0.70	17.1	38.6	0.014	29.4
64X-1, 28	553.68	0.04	0.16	0.27	412.2	1.24	12.9	21.8	0.017	20.0
67X-CC, 8	572.68	0.04	0.17	0.17	421.4	1.04	16.3	16.3	0.017	19.0
67X-CC, 17	572.77	0.04	0.17	0.17	418.4	0.72	23.6	23.6	0.017	19.0
70X-2, 10	602.90	0.06	0.14	0.16	ND	1.17	12.0	13.7	0.017	30.0
70X-2, 37	603.17	0.04	0.27	0.25	409.4	1.01	26.7	24.8	0.026	12.9
72X-1, 101	621.61	0.10	0.61	0.50	422.0	1.14	53.5	43.9	0.059	14.1
72X-2, 52	622.62	0.08	0.60	0.32	419.6	1.55	38.7	20.6	0.056	11.8
73X-1, 49	630.69	0.07	0.39	0.44	417.6	0.89	43.8	49.4	0.038	15.2
73X-1, 87	631.07	0.08	0.43	0.51	424.2	1.31	32.8	38.9	0.042	15.7
76X-CC, 41	659.41	0.04	0.18	0.19	412.7	0.97	18.6	19.6	0.018	18.2
77X-1, 6	668.66	0.06	0.21	0.20	421.5	0.93	22.6	21.5	0.022	22.2
77X-1, 52	669.12	0.06	0.21	0.20	421.5	0.93	22.6	21.5	0.022	22.2
88X-2, 19	756.59	0.05	0.18	0.09	408.0	0.59	30.5	15.3	0.019	21.7
89X-1, 101	765.51	0.07	0.35	0.26	420.5	0.94	37.2	27.7	0.035	16.7

Table T18 (continued).

Core, section, interval (cm)	Depth CSF-A (m)	S_1 (mg HC/g rock)	S_2 (mg HC/g rock)	S_3 (mg CO_2/g rock)	T_{max} (°C)	TOC_{SRA} (wt%)	Hydrogen index (mg S_2/g TOC)	Oxygen index (mg S_3/g TOC)	Pyrolysis carbon	Production index
89X-2, 50	766.50	0.05	0.23	0.25	423.3	0.81	28.4	30.9	0.023	17.9
90X-2, 101	776.61	0.07	0.31	0.23	415.6	0.90	34.4	25.6	0.032	18.4
90X-3, 63	777.73	0.06	0.38	0.34	402.2	1.15	33.0	29.6	0.037	13.6
92X-1, 100	794.30	0.06	0.44	0.28	418.5	1.09	40.4	25.7	0.042	12.0
92X-2, 103	795.83	0.07	0.51	0.46	426.2	1.27	40.2	36.2	0.048	12.1
93X-1, 37	803.37	0.06	0.26	0.26	424.5	0.66	39.4	39.4	0.027	18.8
93X-4, 80	808.30	0.11	0.44	0.32	413.7	0.90	48.9	35.6	0.046	20.0
94X-4, 72	817.82	0.08	0.56	0.40	422.7	1.27	44.1	31.5	0.053	12.5
95X-CC, 10	822.40	0.07	0.39	0.38	427.1	1.06	36.8	35.8	0.038	15.2
97X-1, 96	842.36	0.06	0.44	0.37	424.9	1.02	43.1	36.3	0.042	12.0
97X-4, 22	845.72	0.08	0.41	0.34	416.4	0.95	43.2	35.8	0.041	16.3
98X-1, 23	851.23	0.11	0.26	0.28	423.9	0.96	27.1	29.2	0.031	29.7
99X-1, 15	860.85	0.06	0.21	0.23	419.1	0.73	28.8	31.5	0.022	22.2
100X-1, 132	871.62	0.07	0.19	0.24	403.0	0.59	32.2	40.7	0.022	26.9
101X-1, 103	880.93	0.29	0.20	0.34	408.7	0.76	26.3	44.7	0.041	59.2
103X-1, 84	900.04	0.05	0.19	0.25	415.7	0.87	21.8	28.7	0.020	20.8
104X-1, 17	908.97	0.06	0.27	0.47	412.8	0.68	39.7	69.1	0.027	18.2
106X-1, 141	929.41	0.07	0.32	0.33	400.1	0.78	41.0	42.3	0.032	17.9
106X-3, 40	931.40	0.10	0.55	0.49	410.3	1.08	50.9	45.4	0.054	15.4
107X-1, 10	937.70	0.07	0.25	0.39	417.8	0.80	31.2	48.8	0.027	21.9
107X-1, 13	937.73	0.08	0.22	0.25	417.0	0.70	31.4	35.7	0.025	26.7
109X-2, 75	959.05	0.08	0.27	0.33	410.0	0.57	47.4	57.9	0.029	22.9
109X-3, 124	961.04	0.13	0.34	0.31	418.2	1.10	30.9	28.2	0.039	27.7
111X-1, 31	976.21	0.07	0.41	0.35	418.8	1.04	39.4	33.7	0.040	14.6
111X-1, 35	976.25	0.05	0.23	0.40	416.5	0.90	25.6	44.4	0.023	17.9
112X-3, 68	989.18	0.07	0.32	0.29	403.3	0.91	35.2	31.9	0.032	17.9
113X-2, 114	997.74	0.07	0.32	0.25	417.5	1.01	31.7	24.8	0.032	17.9
115X-CC, 3	1014.33	0.07	0.27	0.23	417.4	0.71	38.0	32.4	0.028	20.6

Notes: T_{max} is the pyrolysis temperature at which the evolution rate of S_2 is at a maximum. TOC_{SRA} = total organic carbon from source rock analyzer pyrolysis. Pyrolysis carbon = [0.83 × (S_1 + S_2)/10], production index = [S_1/(S_1 + S_2)] × 100. ND = not determined.

Table T19. Composition of interstitial waters, Site U1351.

Core, section, interval (cm)	Depth CSF-A (m)	Salinity	pH	Alkalinity (mM)	Ion chromatograph data (mM)						Mg/Ca
					Cl⁻	SO₄²⁻	Mg²⁺	Ca²⁺	Na⁺	K⁺	
317-U1351A-											
1H-1, 110	1.10	3.8	7.58	2.86	545	28.0	52.3	10.8	469	11.0	4.86
2H-1, 110	3.80	3.5	7.49	3.15	538	26.5	50.6	10.3	463	10.9	4.92
2H-3, 110	6.80	3.3	7.70	5.79	546	19.5	46.9	8.9	470	10.0	5.24
2H-5, 130	10.00	3.3	7.30	7.83	561	12.4	43.8	7.6	483	8.8	5.78
3H-1, 110	13.30	3.3	7.34	9.11	565	5.8	39.9	6.0	485	8.1	6.64
3H-3, 110	16.30	3.3	7.50	10.11	546	0.31	35.0	5.3	466	7.1	6.67
4H-1, 110	19.30	3.3	7.38	8.63	577	0.54	36.2	7.1	493	6.8	5.13
4H-3, 110	22.30	3.3	7.44	7.92	591	0.00	35.8	8.7	503	6.3	4.10
4H-5, 140	24.74	3.4	7.26	7.25	591	0.00	35.2	9.6	501	5.9	3.67
5H-1, 110	26.20	3.4	7.40	7.36	597	0.00	35.5	9.8	509	6.0	3.62
5H-2, 80	27.40	3.4	7.39	6.93	589	0.00	34.8	9.7	501	5.7	3.59
317-U1351B-											
8H-3, 130	52.00	3.4	7.34	5.10	612	0.00	32.7	12.5	522	4.8	2.62
9H-2, 130	60.10	3.4	7.35	4.44	599	0.00	31.7	12.9	510	4.2	2.47
11H-1, 140	71.10	3.4	7.39	3.79	602	0.00	32.1	13.4	511	3.8	2.39
11H-2, 140	72.60	3.2	7.41	3.39	591	0.00	31.3	13.0	500	3.8	2.40
11H-3, 140	74.10	3.4	7.49	3.20	609	0.00	32.3	13.4	516	4.1	2.42
11H-4, 107	75.27	3.4	7.37	3.23	604	0.00	31.8	13.5	512	3.8	2.35
14X-1, 140	96.10	3.3	7.54	2.38	572	0.54	30.6	16.6	476	3.2	1.84
16X-3, 130	117.20	3.4	7.48	2.09	594	0.95	32.5	18.1	490	2.9	1.79
18X-1, 140	133.40	3.3	7.56	1.96	601	0.00	32.5	19.6	496	2.8	1.66
19X-2, 140	144.50	3.4	7.33	1.88	573	0.00	30.5	18.4	470	2.9	1.66
20X-2, 140	154.10	3.3	7.34	1.98	567	0.00	30.2	17.0	466	3.0	1.78
21X-3, 130	165.10	3.4	7.38	2.03	602	0.00	32.5	17.0	501	2.9	1.91
22X-2, 140	173.30	3.3	7.50	1.80	599	0.00	32.0	17.1	505	2.5	1.87
25X-1, 130	200.50	3.2	7.41	2.16	588	0.00	32.5	16.0	493	2.3	2.04
27X-2, 140	221.30	3.3	7.32	1.73	579	0.00	27.1	30.7	469	2.3	0.88
28X-2, 140	230.90	3.1	7.30	1.62	572	0.42	24.2	37.2	455	2.2	0.65
29X-3, 140	241.90	3.2	7.37	1.59	545	0.00	22.2	38.4	427	2.4	0.58
30X-3, 140	251.50	3.1	7.51	1.47	540	0.50	22.1	39.0	423	2.0	0.57
31X-3, 125	260.95	3.2	7.41	1.40	541	0.00	22.0	39.7	419	2.2	0.55
32X-2, 135	269.15	3.1	7.49	1.44	562	0.00	22.3	42.2	437	2.1	0.53
36X-2, 125	307.45	3.2	7.39	1.32	547	0.00	21.6	41.5	425	2.3	0.52
37X-1, 135	315.25	3.1	n.d.	n.d.	539	0.00	21.3	40.8	418	2.5	0.52
39X-2, 135	335.95	3.2	7.47	1.52	542	0.00	21.2	41.2	420	2.3	0.51
40X-1, 135	344.05	3.2	7.35	1.31	539	0.90	22.2	40.2	419	2.6	0.55
44X-1, 116	382.26	3.2	7.60	1.57	571	0.40	23.3	42.7	443	3.1	0.54
47X-1, 85	410.65	3.3	7.49	1.39	545	3.95	22.2	40.4	419	3.1	0.55
64X-1, 135	554.75	3.2	7.22	1.40	572	0.00	20.6	34.0	446	2.6	0.61
72X-1, 135	621.95	3.2	7.08	1.09	536	0.00	19.0	33.2	418	2.2	0.57
88X-1, 135	756.25	3.2	7.42	1.26	566	0.75	20.3	33.6	436	3.9	0.60
89X-1, 135	765.85	3.1	7.42	1.46	563	0.00	19.8	34.0	438	2.6	0.58
92X-1, 125	794.55	3.2	7.37	1.39	557	0.00	19.2	33.3	425	1.9	0.57
93X-3, 135	807.35	3.2	7.39	1.32	567	0.00	20.3	34.8	437	2.1	0.58
97X-2, 125	844.15	3.3	7.29	1.17	548	2.65	23.0	33.4	421	3.2	0.69
100X-3, 135	874.65	3.3	7.50	1.30	565	1.63	23.9	40.3	428	4.2	0.59
104X-2, 135	911.65	3.4	7.42	1.17	563	1.32	23.5	42.7	419	3.0	0.55
106X-2, 125	930.75	3.4	7.36	1.10	586	1.19	24.8	44.9	432	4.2	0.55
109X-1, 135	958.15	3.4	7.56	1.21	569	2.22	24.8	44.6	424	2.5	0.56
112X-3, 125	989.75	3.3	7.20	1.32	580	1.66	22.3	46.8	436	1.8	0.48

Table T20. Composition of interstitial waters, Site U1351. (**See table notes.**)

Core, section, interval (cm)	Depth CSF-A (m)	Spectrophotometry data			ICP-AES data					
		NH_4^+ (mM)	HPO_4^{2-} (µM)	$HSiO_4$ (µM)	B (mM)	Sr^{2+} (mM)	Ba (µM)	Si (µM)	Li^+ (µM)	Sr/Ca*
317-U1351A-										
1H-1, 110	1.10	0.0	1.90	139	0.52	0.090	15.80	268	29	0.010
2H-1, 110	3.80	0.0	1.30	314	0.56	0.110	19.70	387	31	0.010
2H-3, 110	6.80	0.0	4.50	688	0.71	0.320	23.50	642	34	0.040
2H-5, 130	10.00	0.0	8.50	818	0.93	0.510	21.20	756	36	0.070
3H-1, 110	13.30	1.7	8.60	671	1.06	0.600	6.60	606	35	0.100
3H-3, 110	16.30	2.2	3.40	625	1.23	0.670	2.70	625	37	0.130
4H-1, 110	19.30	2.2	1.50	600	1.38	0.770	3.20	626	39	0.110
4H-3, 110	22.30	2.4	2.30	594	1.41	0.790	3.20	568	38	0.090
4H-5, 140	24.74	2.6	2.10	427	1.58	0.870	3.10	602	39	0.090
5H-1, 110	26.20	2.6	2.20	592	1.58	0.860	3.20	586	39	0.090
5H-2, 80	27.40	2.8	1.10	524	1.62	0.910	5.10	576	40	0.090
317-U1351B-										
8H-3, 130	52.00	2.9	0.60	705	1.80	0.910	5.40	697	33	0.070
9H-2, 130	60.10	3.0	0.30	740	1.87	0.930	7.00	742	32	0.070
11H-1, 140	71.10	2.7	0.30	736	1.99	0.920	8.10	723	29	0.070
11H-2, 140	72.60	2.9	0.30	598	1.94	0.920	5.90	687	30	0.070
11H-3, 140	74.10	2.8	0.30	620	1.96	0.910	7.10	625	29	0.070
11H-4, 107	75.27	2.9	0.20	456	1.91	0.860	10.10	595	28	0.060
14X-1, 140	96.10	2.8	0.20	403	2.14	0.870	5.90	528	32	0.050
16X-3, 130	117.20	2.7	0.10	451	2.44	0.920	7.30	581	32	0.050
18X-1, 140	133.40	2.8	0.30	402	2.64	0.960	12.10	580	36	0.050
19X-2, 140	144.50	2.9	0.00	411	2.47	0.910	6.30	507	39	0.050
20X-2, 140	154.10	2.8	0.00	188	2.43	0.860	4.70	385	43	0.050
21X-3, 130	165.10	2.8	0.00	231	2.38	0.840	5.50	423	45	0.050
22X-2, 140	173.30	3.1	0.10	311	2.46	0.840	4.90	505	45	0.050
25X-1, 130	200.50	2.8	0.10	206	2.65	0.810	5.30	390	53	0.050
27X-2, 140	221.30	3.0	0.00	222	3.54	0.970	3.90	407	79	0.030
28X-2, 140	230.90	3.1	0.00	233	4.17	1.030	4.00	423	96	0.030
29X-3, 140	241.90	2.8	0.00	258	4.67	1.100	3.80	395	117	0.030
30X-3, 140	251.50	3.0	0.20	339	4.44	1.060	5.70	398	129	0.030
31X-3, 125	260.95	2.8	0.00	373	4.53	1.110	5.10	477	152	0.030
32X-2, 135	269.15	2.9	0.00	320	4.55	1.080	5.30	407	156	0.030
36X-2, 125	307.45	2.7	0.00	325	3.66	1.190	5.00	400	223	0.030
37X-1, 135	315.25	2.9	0.00	278	4.56	1.140	5.50	475	199	0.030
39X-2, 135	335.95	2.7	0.00	276	4.99	1.260	5.60	479	227	0.030
40X-1, 135	344.05	ND	0.00	280	4.20	1.160	4.80	408	209	0.030
44X-1, 116	382.26	ND	0.00	226	4.18	1.160	5.40	460	213	0.030
47X-1, 85	410.65	ND	0.00	243	3.81	1.260	6.50	435	233	0.030
64X-1, 135	554.75	ND	0.00	242	2.43	0.920	6.70	577	30	0.030
72X-1, 135	621.95	ND	0.00	264	3.83	1.480	7.10	497	172	0.040
88X-1, 135	756.25	ND	0.00	254	3.62	1.960	0.60	439	149	0.060
89X-1, 135	765.85	ND	0.00	301	4.22	2.050	1.20	497	137	0.060
92X-1, 125	794.55	ND	0.00	359	4.50	2.050	1.40	556	136	0.060
93X-3, 135	807.35	ND	0.00	355	4.47	2.140	2.40	548	147	0.060
97X-2, 125	844.15	ND	0.00	367	3.60	1.850	3.00	532	160	0.060
100X-3, 135	874.65	ND	0.00	259	3.72	1.850	5.50	493	164	0.050
104X-2, 135	911.65	ND	0.00	443	3.67	1.800	6.10	523	183	0.040
106X-2, 125	930.75	ND	0.00	325	3.40	1.630	4.50	533	204	0.040
109X-1, 135	958.15	ND	0.00	381	3.30	1.570	5.40	544	210	0.040
112X-3, 125	989.75	ND	0.00	538	3.89	1.580	2.30	645	204	0.030

Notes: * = Ca data from ion chromatography (see Table **T19**). ICP-AES = inductively coupled plasma–atomic emission spectroscopy. ND = not determined.

Table T21. Mass balance in sulfate reduction zone, Site U1351.

	Ions (mM)		
Process	Surface	16–20 m	Change
Generation of bicarbonate during sulfate reduction (alkalinity increase)	2.9	10.1	7.2
Precipitation of Ca^{2+} as carbonate (Ca^{2+} removal)	10.8	5.3	5.5
Precipitation of Mg^{2+} as carbonate (Mg^{2+} removal)	52.3	35.1	17.2
Total bicarbonate generated:			29.9
Sulfate reduction and removal	28	0	28

Table T22. Degree of sediment sample contamination (particulate tracer), Site U1351. (**See table notes.**)

Core, section	Depth CSF-A (m)	Microsphere count (beads/cm^3 sediment) Inner	Outer	Delivery confirmed
317-U1351A-				
1H-1	1.5	0	2,010	No
2H-1	4.2	0	779,000	Yes
2H-3	7.2	0	0	Yes
2H-5	10.2	0	2,010	Yes
3H-1	13.7	0	476,000	Yes
3H-3	16.7	0	4,020	Yes
4H-1	19.7	0	454,000	Yes
4H-3	22.7	0	4,020	Yes
4H-5	24.8	0	8,040	Yes
5H-1	26.6	0	36,200	Yes
5H-2	27.5	10	56,300	Yes
317-U1351B-				
8H-3	52.2	10	ND	Yes
16X-3	117.4	50	233,000	Yes
21X-3	165.3	0	22,100	Yes
25X-1	200.7	100	245,000	Yes
31X-3	261.2	0	28,100	Yes
36X-2	307.7	0	52,200	Yes
92X-1	794.8	10	56,300	Yes
97X-2	844.4	20	84,400	Yes
106X-2	931.0	0	229,000	Yes
112X-3	990.0	0	189,000	Yes

Notes: Inner = center part of core, outer = part of core in contact with core liner. ND = not determined.

Table T23. Temperature data, Site U1351. (**See table notes.**)

Core	Tool	Depth CSF-A (m)	Temperature (°C)	t_i (s)	t_f (s)	$t_f - t_i$ (s)	Reliability
317-U1351A-							
4H	APCT-3	25.1	11.61	90	734	644	Good
317-U1351B-							
10H	SET	70.7	9.03	34	167	133	Poor
12H	SET	86.2	12.78	52	316	264	Poor
16X	SET	123.4	11.51	27	108	81	Poor
42X	SET	372.5	15.59	459	689	230	Poor

Notes: Times t_i and t_f are the initial and final times of the interval, respectively, picked to estimate asymptotic temperature for each data set. Estimated temperatures are considered reliable when the picked interval, $t_f - t_i$, is >300 s. APCT-3 = third-generation advanced piston corer temperature tool, SET = Sediment Temperature tool. APCT-3 measurement depth is the bottom of the cored interval. SET measurement depth is the bottom of the last cored interval plus 1 m, the approximate distance the temperature sensor advances beneath the bit.

Table T24. Thermal conductivity data, Site U1351. (**See table note.**)

| Hole | Measurement (*N*) | | Depth CSF-A (m) | Lab-measured thermal conductivity (harmonic mean/range; W/[m·K]) | |
	Good*	Total		Laboratory	In situ
317-					
U1351A	11	19	0.3–27.9	1.474/0.962–2.233	1.467/0.959–2.215
U1351B	107	212	0.7–1004.9		

Note: * = thermal conductivity data were discarded when (1) contact between the probe and sediment was poor, (2) thermal conductivity was close to that of water (0.6 W/[m·K]) because of sediment dilution during coring, or (3) measurements were taken in caved-in layers such as shell hash.